

Extension of a VCI program for the calculation of rovibrational intensities

Von der Fakultät Chemie der Universität Stuttgart
zur Erlangung der Würde eines Doktors der
Naturwissenschaften (Dr. rer. nat.) genehmigte Abhandlung.

Vorgelegt von

Martin Tschöpe

aus Quierschied

Hauptberichter:	apl. Prof. Dr. Guntram Rauhut
Mitberichter:	Prof. Dr. Ronny Nawrodt
Prüfungsausschussvorsitzender:	Prof. Dr. Johannes Kästner
Tag der mündlichen Prüfung:	22. Juni 2023

Institut für Theoretische Chemie
Universität Stuttgart

2023

Abstract

The identification of molecules in the interstellar medium (ISM), circumstellar spheres and low-temperature exoplanet atmospheres is a major challenge in astrophysics and is mainly based on highly accurate rotational and rovibrational infrared reference spectra. One way to determine these reference spectra is through *ab initio* calculations, since they allow for an efficient simulation of a wide range of conditions, including extremely low pressure and temperature.

In this thesis, a new realization of rovibrational configuration interaction (RVCI) theory for the calculation of rovibrational infrared spectra via configuration interaction theory has been developed and implemented to allow for the calculation of these reference spectra. The approach is based on a multi-mode expansion of the multi-dimensional potential energy surface (PES) and dipole moment surface (DMS), vibrational self-consistent field (VSCF) and vibrational configuration interaction (VCI) theory. A direct product between vibrational basis functions (VCI wave functions) and rotational basis functions is used. Thus, in contrast to the previously introduced rotational configuration interaction (RCI), the interaction between rotational and vibrational bands is taken into account. This is done with high accuracy by including the higher order term of the inverse effective moment of inertia tensor μ for the rotational term and the Coriolis coupling term in the Watson Hamiltonian. Moreover, a new rotational basis called molecule specific rotational basis (MSRB) is introduced.

The convergence behavior of several different series expansions within RVCI theory showed very individual effects for the five parameters investigated. If the maximum total angular momentum quantum number J_{\max} or the vibrational basis set is not sufficiently converged, large artifacts occur. Efficient ways to detect and avoid these issues are presented. The CI space in the VCI calculations is another crucial parameter in terms of quantitative convergence. It was found that the best indicator for convergence of the coupling strength is the spectral separation between the vibrational bands. For the two quasi-degenerate vibrational modes of H₂CS the 0th order Coriolis coupling is significant, while the 1st order terms show only small changes. Compared to the Coriolis coupling terms, the rotational terms require a one order higher μ -tensor expansion for the same accuracy. The 1st order introduces at most energy shifts for

entire progressions of 5 cm^{-1} . The changes induced by the 2nd order terms are more than one order of magnitude smaller. Since the absence of higher order coupling terms does not cause artifacts in the spectrum, an insufficient convergence is hard to detect in the resulting spectra.

The calculation for the first paper in this thesis relied on a number of approximations, that could be removed in the further course of this thesis. Most of these approximations did not drastically affect the spectra of ketenimine, as there are only minor changes in the spectrum up to 2900 cm^{-1} . Above that, however, the ν_1 band and the coupling between $\nu_8 + \nu_{12}$ and ν_{11} show that the quality of the quantum number assignment, the consideration of the coupling and the consistency of the intensities improved significantly over the last three years. The new calculations also revealed an interesting turnaround progression in this region. The line broadening study using propynal as a benchmark molecule gives evidence for the assumption that for molecules with 6 – 10 atoms there is no need to consider sophisticated beyond Voigt profiles, as they are used for small molecules (N_2 , H_2O , CH_4 , NH_3 , etc). The reason for this is that the higher mass and the larger moment of inertia tensor lead to a higher rovibrational state density. Therefore, the variation between different broadening profiles is negligible.

At the end of this thesis, several runtime optimizations are analyzed. The parallelization shows an almost perfect scaling in the number of CPU cores for the precalculations and the intensity calculation. In addition, the precalculations of the vibrational integrals save about a factor of 8 in total computation time. The contraction of the MSR coefficients and the RvCI coefficients results in a total reduction of computational time of 50% for H_2CS and 97% for ketenimine.

The current implementation of the RvCI theory in *MOLPRO* is capable of calculating rovibrational infrared and Raman spectra for up to 10 atoms, up to room temperature and over a broad spectral range. However, combining all these features together requires large computational resources. A list of optimizations to increase the computational efficiency is presented in the outlook. Moreover, a number of possible additional functionalities and methods to increase the robustness of the code are provided.

Zusammenfassung

Die Identifizierung von Molekülen im interstellaren Medium, in zirkumstellaren Scheiben und in den Atmosphären kalter Exoplaneten ist eine große Herausforderung in der Astrophysik und basiert hauptsächlich auf hochgenauen Rotations- und Rotationsschwingungs-Referenzspektren. Eine Möglichkeit, diese Referenzspektren zu bestimmen, sind *ab initio*-Berechnungen, da sie eine effiziente Simulation eines breiten Bereichs von Bedingungen (einschließlich extrem niedriger Drücke und Temperaturen) ermöglichen.

In dieser Arbeit wurde eine neue und besonders effiziente Implementierung der Rotationsschwingungskonfigurationswechselwirkungstheorie für die Berechnung von Infrarot-Rotationsschwingungsspektren entwickelt, um die Berechnung dieser Referenzspektren zu ermöglichen. Der Ansatz basiert auf Normalkoordinaten und einer Mehrmodenentwicklung der mehrdimensionalen Potential- und Dipolmomentflächen sowie Schwingungs-Selbstkonsistentes-Feld-Verfahren und Schwingungskonfigurationswechselwirkungstheorie. Dabei wird ein direktes Produkt zwischen Schwingungsbasisfunktionen und Rotationsbasisfunktionen verwendet. So kann im Gegensatz zu der zuvor eingeführten Rotationskonfigurationswechselwirkungstheorie die Wechselwirkung zwischen Rotations- und Vibrationsbanden berücksichtigt werden. Dies geschieht mit hoher Genauigkeit, indem die Terme höherer Ordnung des inversen effektiven Trägheitsmomententensors μ für den Rotationsterm und die Coriolis-Kopplung im Watson Hamiltonian berücksichtigt werden. Darüber hinaus werden eine neue Rotationsbasis namens Molekülspezifische Rotationsbasis (MSRB) und eine neue Art der Zuweisung von Rotationsschwingungsquantenzahlen eingeführt.

Das Konvergenzverhalten verschiedener Entwicklungen für die Rotationsschwingungskonfigurationswechselwirkungstheorie (RVCI) zeigte sehr individuelle Effekte für die fünf untersuchten Parameter. Wenn die maximale Gesamtdrehimpulsquantenzahl J_{\max} oder die Größe der Schwingungsbasis nicht ausreichend konvergiert, treten besonders große Artefakte auf. Es werden effiziente Methoden zur Erkennung und Vermeidung dieser Probleme vorgestellt. Auch die Größe des Schwingungsbasisatzes ist ein entscheidender Parameter für die Konvergenz des Spektrums. Der beste Indikator für die Konvergenz bezüglich dieses Parameters und für die Stärke der Kopplung ist der spektrale Abstand zwischen den

Schwingungsbanden. Für die beiden quasi-entarteten Schwingungsmoden von H_2CS ist die Coriolis-Kopplung nullter Ordnung sehr entscheidend, während die Terme erster Ordnung nur geringe Änderungen verursachen. Im Vergleich zu den Coriolis-Kopplungstermen erfordern die Rotationsterme eine um eine Ordnung höhere μ -Tensorentwicklung für die gleiche Genauigkeit. Die erste Ordnung führt für ganze Progressionen zu Energieverschiebungen von höchstens 5 cm^{-1} . Die durch die Terme der zweiten Ordnung hervorgerufenen Änderungen sind um mehr als eine Größenordnung geringer. Da das Fehlen von Kopplungstermen höherer Ordnung keine Artefakte im Spektrum verursacht, ist eine unzureichende Konvergenz in den resultierenden Spektren sehr schwierig zu erkennen.

Die Berechnungen für die erste Veröffentlichung in dieser Dissertation beruhen auf einer Reihe von Näherungen, die im weiteren Verlauf dieser Arbeit entfernt werden konnten. Die meisten dieser Näherungen hatten kaum Auswirkungen auf die Spektren von Ketenimin, da sie bis 2900 cm^{-1} nur zu geringfügigen Änderungen des Spektrums führten. Oberhalb dieser Grenze zeigen jedoch die ν_1 -Bande und die Kopplung zwischen $\nu_8 + \nu_{12}$ und ν_{11} , dass sich die Qualität der Quantenzahlzuordnung und die Konsistenz der Intensitäten in den letzten drei Jahren deutlich verbessert haben. Die neuen Berechnungen zeigen auch eine interessante *turnaround* Progression in diesem Bereich. Die Studie zur Linienverbreiterung unter Verwendung von Propynal als Anwendungsmolekül bestätigte die Annahme, dass für Moleküle mit 6 – 10 Atomen keine Notwendigkeit besteht, *beyond Voigt*-Profile zu verwenden, wie sie für kleine Moleküle (N_2 , H_2O , CH_4 , NH_3 , etc.) benutzt werden. Der Grund dafür ist, dass die höhere Masse und der größere Trägheitstensor zu einer hohen Schwingungszustandsdichte führen, wodurch die genaue Form des Verbreiterungsprofil weniger relevant wird.

Am Ende dieser Arbeit werden verschiedene Laufzeitoptimierungen analysiert. Die Parallelisierung zeigt eine nahezu perfekte Skalierung in der Anzahl der CPU-Kerne für die Vorberechnungen der Schwingungsintegrale und für die Intensitätsberechnung. Darüber hinaus sparen die Vorberechnungen der Schwingungsintegrale etwa einen Faktor von 8 an Gesamtrechenzeit ein. Die Kontraktion der MSRB-Koeffizienten mit den RVCI-Koeffizienten führt zu einer Gesamtrechenzeitreduktion von 50% für H_2CS und 97% für Ketenimin.

Die derzeitige Implementierung der RVCI-Theorie in *MOLPRO* ist in der Lage, Infrarot- und Raman-Spektren für bis zu 10 Atome, von $T = 0 \text{ K}$ bis zu Raumtemperatur und über einen weiten Spektralbereich zu berechnen. Die Kombination all dieser Eigenschaften erfordert jedoch große Rechenressourcen. Im Ausblick wird daher eine Liste von Optimierungen zur Steigerung der Recheneffizienz vorgestellt. Darüber hinaus wird eine Reihe von möglichen zusätzlichen Funktionalitäten und Methoden zur Erhöhung der Robustheit des Programms aufgelistet.

Danksagung

In den letzten vier Jahren haben mich viele Menschen in vielfältiger Weise unterstützt und dazu beigetragen, diese Arbeit zu ermöglichen. Ihnen möchte ich nun an dieser Stelle meinen Dank aussprechen. Als Erstes möchte ich mich bei Prof. Dr. Guntram Rauhut bedanken. Er hat mir nicht nur diese Promotion ermöglicht, sondern mich auch fachlich und beim Schreiben der zahlreichen Berichte und Paper viel gelehrt. Besonders froh bin ich darüber, dass er mir die Freiheiten gelassen hat, unsere Forschung in Richtung astrophysikalischer Anwendungen voranzutreiben und er mir meine Reise in die USA ermöglichte.

Mein Dank gilt auch Prof. Dr. Ronny Nawrodt als Mitberichter und Prof. Dr. Johannes Kästner als Prüfungsausschussvorsitzender, die beide ohne Zögern und auf sehr unkompliziert Weise bereit waren, diese Aufgaben zu übernehmen.

Darüber hinaus danke ich Prof. Dr. Laura Kreidberg, Dr. Iouli Gordan und Prof. Dr. Heather A. Knutson für Ihre Gastfreundschaft und dafür, dass ich meine Ergebnisse in Ihren Arbeitsgruppen präsentieren durfte. Der Studienstiftung des deutschen Volkes danke ich für die finanzielle Unterstützung in den letzten drei Jahren und für die Möglichkeit, in die USA zu reisen.

Auch einige Arbeitskollegen möchte ich nicht unerwähnt lassen. So habe ich die enge Zusammenarbeit mit Sebastian Erfort sehr genossen. Von ihm habe ich nicht nur viel über Rotationen und Schwingungen gelernt, sondern auch so manches beim Bouldern. Ein weiterer, ehemaliger Zimmerkollege, mit dem ich viele gesellige Stunden verbracht habe, ist Moritz Schneider. Ich kenne wenig andere Menschen, mit denen ich so gut über Themen diskutieren kann, egal ob wir einer Meinung waren oder nicht. Von Dr. Benjamin Ziegler habe ich nicht nur die Phrase "Um Gottes willen! Wie konnte das jemals funktionieren?" zu schätzen und zu fürchten gelernt, sondern auch viele Kniffe in Fortran. Mit Dr. Taras Petrenko verbinde ich viele, sehr gesellige Stunden, auch wenn er meistens eine Spur aus Kekskrümeln hinterlassen hatte. Unserem ehemaligen Post Doc Dr. Benjamin Schröder möchte ich dafür danken, dass er mich an seinem allumfassenden Wissen zu Rotationsschwingungsspektren hat teilhaben lassen und Dr. Tina Mathea für die schöne Zeit und die angenehme Arbeitsatmosphäre. Den Abschluss dieser Runde aus ehemaligen Arbeitskollegen darf Dennis Dinu bereiten. Auch

wenn die Zeit mit ihm in Stuttgart nur sehr kurz war, so war sie doch sehr intensiv und bleibt mir überaus positiv in Erinnerung.

Ebenfalls in meinem Universitätsalltag, wenn auch nicht in Form von Arbeitskollegen, haben mich einige weitere Personen begleitet. Als Erstes möchte ich Juliane Heitkämper und Tizian Wenzel für manch mächtig munteres Mensa-Mahl merci mitteilen. Meinem ehemaligen Betreuer während der Bachelorarbeit, Dr. Nicolai Lang, möchte ich besonders herzlich dafür danken, dass er meine Frage “Hast du kurz Zeit?” stets bejahte, obschon er wusste, dass ich damit seine Abendplanung über den Haufen geworfen hatte. Ich schätze an dir nicht nur, dass du mir geduldig, die abstraktesten physikalischen Zusammenhänge wieder und wieder erklärt hast, sondern auch, dass du mich dazu ermutigt hast, die Forschungsreise in die USA anzutreten. Für viele musikalische und kulinarische Stunden, so wie einige der wichtigsten Unterhaltungen in meinem Leben kurz vor Beginn der Promotion danke ich Dr. Daniel Dizdarevic. Darüber hinaus möchte ich Dr. Johannes Reiff danken für 9 Jahre in denen wir uns durch Praktikumsprotokolle, Übungsblätter und die Masterarbeit gekämpft haben.

Nun möchte ich drei ganz besonderen Männern danken, die mich in den letzten fünf Jahren, weniger in meiner fachlichen als vielmehr in meiner persönlichen Entwicklung unterstützt haben. Beginnen möchte ich mit Mario Zinßer. Er ist ein schier unerschöpflicher Quell positiver Energie und schafft es immer, in allem das Gute zu sehen. Dies hat mir in vielen schwierigen Phasen meiner Promotion, aber auch darüber hinaus sehr geholfen. Auch du hast mich dazu ermutigt, die Reise in die USA anzutreten und vielleicht warst du mit deiner Reise nach Hawaii sogar ein weiteres Mal eine Quelle der Inspiration. Wir waren in den letzten Jahren nicht nur gemeinsam auf der Wildspitze, in Hawaii (mit einem *Jeep*), beim Klettern und Ski fahren, sondern haben auch so manche persönliche Herausforderung gemeistert. Trotzdem glaube ich, dass unser mit Abstand größtes Abenteuer noch vor uns liegt.

Auch wenn das zeitliche Zusammenfallen mit meiner Promotion ein Zufall war, so hat mir Dr. Manfred Schrode in den letzten fünf Jahren maßgeblich mit meiner Persönlichkeitsentwicklung geholfen. Fast noch wichtiger ist aber, dass er mir das Handwerkszeug gegeben hat, um diesen Prozess in Zukunft alleine weiterführen zu können und dafür möchte ich mich an dieser Stelle in aller Form bedanken. Auch wenn mein nächster Dank über die Maßen exzentrisch wirken mag, geht dieser an Elon Musk. Die Entwicklung der *Falcon 9* und *Starship* Raketen und das zugehörige Raumfahrtprogramm hatte auch den Zweck, die Menschen zu motivieren und ihnen etwas zu geben, worauf sie sich freuen können, weil es im Leben nicht nur darum gehen kann, Probleme zu lösen. Das größte Abenteuer in der Geschichte der Menschheit hat dies definitiv bei mir bewirkt.

Zu guter Letzt möchte ich mich bei meiner Familie bedanken. Gabi Tschöpe und Michael Tschöpe, ihr habt mich in den 13 Jahren meiner akademischen Ausbildung auf dem Weg vom mittelmäßigen Realschüler zum *Dr. rer. nat.* immer bedingungslos unterstützt und dafür

bin ich euch unendlich dankbar. Meinem Bruder Matthias Tschöpe bin ich nicht nur dafür dankbar, dass er mich an seinem Wissen über theoretische Informatik und künstliche Intelligenz hat teilhaben lassen. Ich bin dir auch dafür dankbar, dass du den Mut hattest, mit mir zahlreiche Projekte in Angriff zu nehmen, sei es handwerklicher Art (unsere Jahrhundert-Betonage *im Stick* oder die selbst-geschweißten Gartentore) oder automobiler Art (die Fahrten an der Nordschleife). Zuletzt möchte ich Dr. Andreas Tschöpe danken. Du bist für mich seit langem ein Vorbild, weil du der erste in unserer Familie warst, der promoviert hat, du trotzdem einer der bodenständigsten Menschen geblieben bist, den ich mir vorstellen kann und du mich damals ermutigt hast, diese Promotion hier anzutreten.

Peer-reviewed publications

This cumulative dissertation summarizes results that have been published in

- (I) **Martin Tschöpe**, Benjamin Schröder, Sebastian Erfort and Guntram Rauhut *High-Level Rovibrational Calculations on Ketenimine*. *Frontiers in Chemistry, Section Astrochemistry*, **8**, 623641 (2021)

Copyright: Reprinted from Ref. [1], Copyright 2021, CC-BY 4.0.

Contributions: M.T.: Implementation (RVCI), Simulation, Data curation, Visualization, Formal analysis (partially), Project administration (partially), Writing – original draft sections *Abstract, Theory and Computational Details, Results, Discussion and Summary (partially)*, Writing – review & editing (partially)

B.S.: Formal analysis (partially), Writing – original draft sections *Introduction, Discussion and Summary (partially)*, Writing – review & editing (partially)

S.E.: Conceptualization, Methodology, Implementation (RCI), Writing – review & editing (partially)

G.R.: Project administration (partially), Funding acquisition, Resources, Writing – review & editing (partially)

DOI: <https://doi.org/10.3389/fchem.2020.623641>

- (II) **Martin Tschöpe** and Guntram Rauhut *Convergence of series expansions in rovibrational configuration interaction (RVCI) calculations*. *The Journal of Chemical Physics*, **157**, 234105 (2022)

Copyright: Reprinted from [2], with the permission of AIP Publishing,

Contributions: M.T.: Methodology, Implementation, Simulation, Data curation, Visualization, Writing – original draft sections *Theory (RVCI), Computational Details, Results, Discussion and Summary* and Writing – review & editing (partially)

G.R.: Project administration, Funding acquisition, Writing – original draft sections *Abstract, Introduction, Theory (PES and VCI)* and Writing – review & editing (partially)

DOI: <https://doi.org/10.1063/5.0129828>

- (III) **Martin Tschöpe** and Guntram Rauhut *A theoretical study of propynal under interstellar conditions and beyond, covering low-frequency infrared spectra, spectroscopic constants, and hot bands*. Monthly Notices of the Royal Astronomical Society, **520**, 3345–3354 (2023), Issue 3

Copyright: Reprinted with the permission from Ref. [3]. Copyright 2023, Oxford University Press.

Contributions: M.T.: Methodology, Implementation, Simulation, Data curation, Visualization, Writing – original draft and Writing – review & editing (partially)

G.R.: Project administration, Funding acquisition, Resources, Writing – review & editing (partially)

DOI: <https://doi.org/10.1093/mnras/stad251>

- (IV) **Martin Tschöpe** and Guntram Rauhut *Spectroscopic Characterization of Diazophosphane – A Candidate for Astrophysical Observations*. The Astrophysical Journal, **949**, 1 (2023)

Copyright: Reprinted from Ref. [4], Copyright 2023, CC-BY 4.0.

Contributions: M.T.: Methodology, Implementation, Simulation, Data curation, Visualization, Project administration, Writing – original draft and Writing – review & editing (partially)

G.R.: Funding acquisition, Resources, Writing – review & editing (partially)

DOI: <https://doi.org/10.3847/1538-4357/acc9ad>

Other publications by the author, not included in this thesis:

- (V) Erfort, S., **Tschöpe, M.**, & Rauhut, G. *Toward a fully automated calculation of rovibrational infrared intensities for semi-rigid polyatomic molecules.* J. Chem. Phys. **152**, 244104 (2020)
DOI: <https://doi.org/10.1063/5.0011832>
- (VI) Erfort, S., **Tschöpe, M.**, Rauhut, G., Zeng, X., & Tew, D. P. *Ab initio calculation of rovibrational states for non-degenerate double-well potentials: cis–trans isomerization of HOPO.* J. Chem. Phys. **152**, 174306 (2020)
DOI: <https://doi.org/10.1063/5.0005497>
- (VII) Erfort, S., **Tschöpe, M.**, & Rauhut, G. *Efficient and automated quantum chemical calculation of rovibrational nonresonant Raman spectra.* J. Chem. Phys. **156**, 124102 (2022)
DOI: <https://doi.org/10.1063/5.0087359>
- (VIII) Dinu, D. F., **Tschöpe, M.**, Schröder, B., Liedl, K. R., & Rauhut, G. *Determination of spectroscopic constants from rovibrational configuration interaction calculations.* J. Chem. Phys. **157**, 154107 (2022)
DOI: <https://doi.org/10.1063/5.0116018>

The results of this thesis have also been presented in the following talks and conferences:

- (I) **Martin Tschöpe**, Benjamin Schröder, Sebastian Erfort, Guntram Rauhut, *High-Level Rovibrational Calculations on Ketenimine*.
Online presentation at 75th International Symposium on Molecular Spectroscopy virtual, June 2021
- (II) **Martin Tschöpe**, *Adaptable High-Level Rovibrational Calculations*.
Seminar presentation, invited by Prof. Laura Kreidberg
Max-Planck-Institute, APEX, Heidelberg, Germany
March 2022
- (III) **Martin Tschöpe**, *Adaptable Infrared Line List Calculation for Medium Sized Molecules*
Seminar presentation, invited by Dr. Iouli E. Gordon
Harvard-Smithsonian Center for Astrophysics, Boston, Massachusetts, USA
April 2022
- (IV) **Martin Tschöpe**, Guntram Rauhut, *Efficient and Automated Ab Initio Calculation of Infrared Spectra for Medium Sized Molecules*.
Poster presentation at *Exoplanet IV* conference
Las Vegas, Nevada, USA
May 2022
- (V) **Martin Tschöpe**, *Adaptable Infrared Line List Calculation for Medium Sized Molecules*.
Several presentations in different groups, invited by Prof. Heather A. Knutson
California Institute of Technology, Pasadena, California, USA
May 2022
- (VI) **Martin Tschöpe**, *Adaptable Infrared Line List Calculation for Medium Sized Molecules*.
Online seminar presentation, invited by Prof. Sara Seager
Massachusetts Institute of Technology, virtual
July 2022
- (VII) **Martin Tschöpe**, Sebastian Erfort, Guntram Rauhut, *Efficient and Automated Ab Initio Simulation of Rovibrational Infrared Spectra for Medium-Sized Molecules*.
Poster presentation at 58th Symposium on Theoretical Chemistry
Heidelberg, Germany, September 2022

Contents

ABSTRACT	iii
ZUSAMMENFASSUNG	v
DANKSAGUNG	vii
PEER-REVIEWED PUBLICATIONS	xi
CONTENTS	xv
1 INTRODUCTION	I
1.1 Motivation	1
1.2 Scope of the Thesis	4
1.2.1 Delimitation to other program parts in Molpro	4
1.2.2 Delimitation to rovibrational theory literature	7
1.2.3 Delimitation to other rovibrational software	7
2 THEORY	II
2.1 Watson Hamiltonian	11
2.1.1 Vibrational term	13
2.1.2 Rotational term	17
2.1.3 Coriolis coupling term	24
2.1.4 RVCi Implementation	29
2.2 Infrared Intensities	33
2.3 Raman Intensities	37
2.4 Line Broadening	40
2.4.1 Natural linewidth	40
2.4.2 Doppler broadening	41
2.4.3 Pressure broadening	42

2.4.4	Voigt broadening	45
3	RESULTS	47
3.1	Convergence analysis	48
3.1.1	Total angular momentum	50
3.1.2	VCI space	52
3.1.3	Vibrational basis set size	52
3.1.4	Coriolis coupling term order	54
3.1.5	Rotational term order	57
3.1.6	Influence of NSSWs	57
3.2	Ketenimine	58
3.3	Line broadening	68
3.4	Runtime optimizations	72
3.4.1	Parallelization	72
3.4.2	Precalculations	75
3.4.3	Contraction	76
3.4.4	RVCI Coefficient Threshold	77
4	SUMMARY AND CONCLUSION	81
5	OUTLOOK	85
5.1	Runtime and memory savings	86
5.2	Additional functionality	88
5.3	Miscellaneous	90
	ABBREVIATIONS	93
	LIST OF FIGURES	95
	LIST OF TABLES	97
	BIBLIOGRAPHY	99
	PUBLICATION 1: HIGH-LEVEL ROVIBRATIONAL CALCULATIONS ON KETENIMINE	111
	PUBLICATION 2: CONVERGENCE OF SERIES EXPANSIONS IN ROVIBRATIONAL CONFIGURATION INTERACTION (RVCI) CALCULATIONS	127

PUBLICATION 3: A THEORETICAL STUDY OF PROPYNAL UNDER INTERSTELLAR CONDITIONS AND BEYOND, COVERING LOW-FREQUENCY INFRARED SPECTRA, SPECTROSCOPIC CONSTANTS, AND HOT BANDS	139
PUBLICATION 4: SPECTROSCOPIC CHARACTERIZATION OF DIAZOPHOSPHANE - A CANDIDATE FOR ASTROPHYSICAL OBSERVATIONS	151
DECLARATION OF AUTHORSHIP	161

1

Introduction

Choosing a subject for a PhD is a difficult decision and above all it depends on personal preferences. Section 1.1 describes, from my subjective perspective, why my topic is so important and motivating these days. The Section 1.2 addresses the scope of the thesis. Since a PhD thesis is build upon previous research, it is important to precisely define the border between the previous status quo and the own new research. This will be given in Subsec. 1.2.1 and 1.2.2, along with a short overview what distinguishes the approach in this thesis from other rovibrational research groups in Subsec. 1.2.3.

1.1 MOTIVATION

The question of whether places outside the solar system are habitable has long preoccupied mankind [5–9]. The most promising extraterrestrial places are planets orbiting other stars and their moons (exoplanet (EP) and exomoon (EM))[9–13]. Over the last three decades more than 3500 systems with altogether more than 5000 confirmed EPs and about 3000 candidates were found [14]. In contrast to that, so far no EM has been confirmed, although there were several promising candidates [15–17], therefore the subsequent discussion focuses on EPs. After the planets are discovered, the usual procedure is to study them in more detail. Parameters like the radius of the planet, the mass, the mean distance to the star (semi-major axis) and the calculated average temperature on the planet are determined [14, 18, 19]. The latter

depends on the one hand on the distance to the star. On the other hand it depends on the existence and the composition of the atmosphere. More atmospheric greenhouse gases cause higher temperatures, as can be seen on Venus in a very extreme way. This is one of the reasons, why the investigation of exoplanet atmosphere (EPA) is very important for the habitability of planets beyond earth. Other reasons are, that the atmosphere protects the surface of a planet against radiation and meteorites. Hence, EP research relies heavily on the spectroscopy investigation of the atmospheres and therefore also accurate reference spectra. Due to the temperature of EPA, microwave and infrared (IR) spectroscopy are widely used. For very hot planets, there is a significant number of electronic excitations that also allow spectroscopy in the visible or ultraviolet wavelengths.

There are many different methods to detect EPs, but not all of them allow for a subsequent analysis of the atmosphere [20]. Only 3% of the planets are detected by the direct imaging method (DIM) [14, 21], meaning that the planet is far enough away from the star and the resolving power of the telescope is high enough to distinguish the star and the planet on images. With this method an analysis of the atmosphere is in principle possible. In this case *emission spectroscopy* can be used. There are also indirect methods to detect exoplanets, where the planet and the star are too close to spatially resolve them, but only the influence of the planet on the host star can be detected [20]. One indirect detection method, that also allows for an analysis of the atmosphere is for example the transit method (TM). It can be applied, when coincidentally the star, the EP and the observer are in a straight line. In that case there is a primary eclipse (earth - planet - star) that can be used for detection via *absorption spectroscopy*. The opposite case is called secondary eclipse (earth - star - planet), which can be used for *emission spectroscopy* [22]. Another detection method that contributed to the majority of the detections in the early days of EP discovery (between 1990 and 2010) is the radial velocity method (RVM) [14, 21]. It uses the fact that the star and planet orbit around their common center of gravity. This causes a red and blue shift of the star, that can be detected and yields for example the mass of the EP. However, it does not provide any information about the EPA. The most promising methods for the investigation of EPA are therefore the DIM and the TM.

In general, a larger planet yields a higher signal-to-noise ratio (SNR) of the atmospheric signals due to the larger volume causing scattering or emission (depending on the detection method). For this reason, atmospheres have been detected in most cases for Jupiter-like and Neptune-like planets, some have been found for super-Earth planets [23], but no EPA detection has been successful for Earth-sized EPs [24–27], like for example rocky planets. However, this is mainly due to two experimental limitations. The first is that for Earth-like planets, the majority of the shading effect during the eclipse is due to the core shadow and not due to the atmosphere. The core of the planet simply reduces all the light from the star (called a flat transmission spectrum) [28–30], without any measurable spectral signature. In contrast, an atmo-

sphere shows a frequency dependent dimming, i.e. spectral features, due to the absorption lines of the molecules in the atmosphere. Therefore measuring the atmosphere of a rocky, icy or watery planet simply requires a better telescope. The second experimental limitation, that prevents the detection of Earth-like EPA is a systematic observational bias in the TM, meaning that the SNR is higher when the planet is closer to the star [22]. Therefore the vast majority of planets observed by TM are closer to their star, than the distance between Mercury and the Sun [14]. Hence, the stellar pressure is strong and in most cases stronger than the gravity of small planets and therefore these planets can not hold their atmosphere. This effect is known as photoevaporation-driven atmosphere loss/mass loss and is related to the explanation of the small planet radius gap [31, 32]. Since, better telescopes allow to apply the TM to EP further away from their host star, these planets should be able to protect their atmosphere against the stellar pressure, even if these planets are relatively light. This means that the reason, why the majority of the EPAs discovered so far are around gas giants is that they are the easiest targets to probe new methods.

However, the future EP and EPA research strives to smaller and colder planets, as can be seen in the following: In 2001 the first detection of a chemical substance (sodium) in an EPA was achieved for the hot Jupiter HD 209458 b, which has a diameter of about 1.35 times that of Jupiter and it orbits its star on a very narrow orbit (about 1/8 of the distance Mercury-Sun). As a result, a year on the planet lasts only 3.5 Earth days and the surface temperature is about 1000 K [33]. Many organic compounds are destroyed at such high temperatures. After that, a number of other molecules such as, water, carbon monoxide, carbon dioxide, methane, ozone were also detected on other hot Jupiters [34, 35]. In addition, the limit for the lightest planet where an atmosphere could be detected was lowered from the hot Jupiter HD 209458 b with 220 times the mass of Earth to Neptune-sized planets (HAT-P-11b, 23 times the mass of Earth) [36] to super-Earths (55 Cancri e, 8 Earth masses) [37]. Another super-Earth with a detected atmosphere is K2-18b with 8.6 Earth masses [38]. This planet is also in the habitable zone, making its atmospheric detection even more groundbreaking [38], since organic compounds can exist there.

The results mentioned above show that enormous progress has been made in this field in the last two decades. Within the community it seems to be common sense that the next step is the investigation of these atmospheres in respect to biological relevant molecules [39–41]. There are different definitions and an ongoing discussion about how to properly define these gases. Deciding which molecules are suitable for this task is a very difficult interdisciplinary challenge. The contribution that spectroscopists can make is primarily to provide highly accurate reference spectra. To summarize this task a bit more precisely: We need to provide highly accurate reference spectra for temperatures up to 370 K (upper end of the habitable zone) for a

large number of relatively small molecules (typically 13 atoms at most [40]) with a potentially high abundance in the atmosphere.

However, the detection of these gases is still in the distant future because it requires a completely new type of space-based telescopes [42, 43], using either a starshade/coronagraph (e.g. *New Worlds Mission*, *LUVOIR* or *Terrestrial Planet Finder-C*) or an optical interferometer (e.g. *Large Interferometer For Exoplanets (LIFE)* or *Terrestrial Planet Finder-I*) [44–47]. This is also the reason why it is a relatively new and small field of research and therefore there is not yet a consensus on which molecules to study [39–41]. Fortunately, there is a related field of research where biologically relevant molecules have already been found, albeit under very different conditions. In the interstellar medium (ISM) and in circumstellar shells more than 200 molecules have been detected [48–50]. These regions represent a wide chemical diversity, from rather stable to highly reactive species, from simple diatomics (e.g. CO, N₂ and OH), to simple organic molecules such as methanol (CH₃OH; [51]) and up to even larger compounds such as polycyclic aromatic hydrocarbons (PAHs; [52]) and fullerenes (C₆₀; [53]). For this reason, the ISM and circumstellar shells are a very interesting test case for the detection of biologically relevant molecules in EPs. In this context, *complex organic molecules* (COMs; [54]) are of particular interest. These are molecules with 6 or more atoms, including at least one carbon molecule. Such compounds are thought to be important building blocks for biologically relevant molecules [55–57]. Two examples of such COMs are ketenimine and propynal. Both of them were studied in the course of this PhD [1, 3].

1.2 SCOPE OF THE THESIS

Since a dissertation builds on previous research, it is important to clearly define the boundary between the previous state of the art and the own new research. This will be done in Subsec. 1.2.1 and 1.2.2, along with a brief overview of what distinguishes the approach in this thesis from other rovibrational research groups in Subsec. 1.2.3.

1.2.1 DELIMITATION TO OTHER PROGRAM PARTS IN MOLPRO

The rovibrational configuration interaction (RVCI) theory developed in the context of this thesis and the according algorithms is at the very end of a long sequence of theoretical methods. Hence, the question appears which of these methods should and need to be explained in this thesis. The overview of the program structure in Fig. 1.1 allows for a rough understanding of the different subprograms. The black arrows guide the main information flow. However, the illustration is by no means complete, as there are many more minor dependencies. The main information within this graphic is encoded in the color of the boxes. The algorithms in the red boxes are not explained at all, but only some computational details are

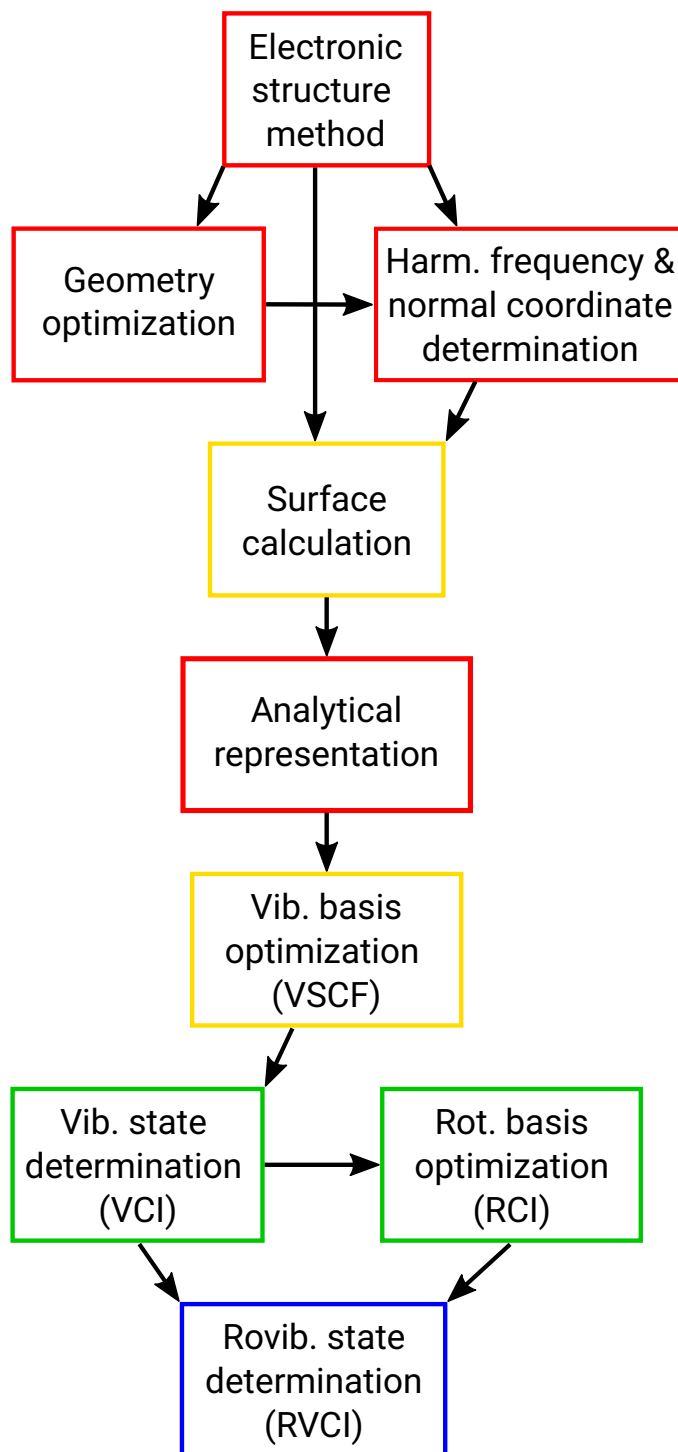


Figure 1.1: Overview of the program structure with the level of detail for the explanations within this thesis. Algorithms in red boxes are not explained, but sometimes computational details are given. The yellow boxes denote algorithms that are briefly discussed, program parts in the green boxes will be explained in more detail and the algorithm in the blue box in the bottom represents the main content of the thesis.

mentioned. For example the specific electronic structure theory method and the corresponding basis set, will be given for some of the calculations. The details behind it are not necessary for the understanding of the rest of the thesis. The same holds true for the geometry optimization algorithms. The harmonic frequency calculation is to a certain extent important for the understanding because it yields the coordinate system. However, this will be explained along with the surface calculation. The fitting of the potential energy surface is a non-trivial and crucial part in the code. However, to understand the RVCi theory, it is sufficient to know that the grid representation is replaced by analytical functions, to save computational time. For the algorithms in the yellow boxes, the basic ideas will be explained. This is because the design decision made there affects the latter calculations, namely the choice of the coordinates and multi-mode expansion in the surface calculation and the basis set for the vibrational configuration interaction (VCI) program depends on the vibrational self-consistent field (VSCF) program. The VCI theory and rotational configuration interaction (RCI) theory in green require a more detailed explanation. They provide the basis functions for the RVCi theory (in blue), which is the main topic of this thesis.

VCI theory is briefly described in this thesis, but since the vibrational theory is the primary research object of the Rauhut Group for the last decades, there are many theses from previous PhD students, that are more suited to give a deeper understanding. Another reason why I want to keep the VCI theory very short. For the RVCi theory, I derived all equations again, if they were identical to the RCI theory (such as for the partition functions, rotational integrals or in parts for the intensity calculation) or the equations were derived by me for the first time.

For most of the *MOLPRO* program it is easy to drawing a clear line between my own work and the previous status quo. However, the transition between the RCI implementation of Erfort and my RVCi program is more involved and will be explained in the following: The calculation of the partition functions and the RCI are both implemented by Erfort. In contrast, the calculation and diagonalization of the RVCi matrix, including all higher order μ -tensor coupling terms (Coriolis-coupling and rotational terms), is my work. The rigid rotor basis (RRB) and the Wang basis (WB) were introduced decades ago in the literature and implemented in *MOLPRO* by Erfort. The molecule specific rotational basis (MSRB) was introduced and implemented by me in the course of this PhD. The assignment of the k and ν quantum number only occurred in the RVCi program and the two algorithms (leading coefficient method and partial trace method) were implemented by me. The same holds true for the two assignment algorithms for the rovibrational irrep (based on the rovibrational wave function and based on a partial trace on the rovibrational basis functions).

The infrared intensity calculations for RCI were the work of Erfort. The necessary adjustments for the RVCi intensities and the introduction of the intensity calculations with the MSRB were done within this thesis. The different broadening profiles were introduced by me

and later combined by Erfort in the DAT2GRAPH program. For the hot bands, Erfort introduced the vibrational transition moment integrals and I did the rest of the programming. The majority of runtime optimization was implemented by me (see Section 3.4), besides, a symmetry optimization for the rotational integrals.

1.2.2 DELIMITATION TO ROVIBRATIONAL THEORY LITERATURE

There are a number of books and publications on the subject of rovibrational spectroscopy. Usually several assumptions are made at the beginning (choice of coordinate origin, space fixed or molecule fixed coordinate system, internal or normal coordinates, grid based calculations or the use of fit functions, Taylor series expansion or multi-mode expansion, RRB or WB etc). Only if many of these assumptions match with the own implementation and additionally the derivation is as close as possible to equations, which can be programmed later, there is a substantial benefit of following this literature. For the *MOLPRO* software, a comparison with the book of Bunker and Jensen [58] is most suitable. It also uses the Eckart conditions, the transition between space-fixed and molecule-fixed coordinates is also described by means of Wigner rotation matrix elements, and normal coordinates and equivalent rotations are used to determine the rotational irreps and thus the nuclear spin statistical weights (NSSW). In addition, intensities are addressed fairly detailed. However, neither the multi-mode expansion and nor a specific vibrational basis set is selected. Thus, the expressions for the vibrational integrals cannot be simplified at an early point in the analytic calculation, and thus the derivation is also terminated early. Moreover, the rotational integrals are not even computed in the RRB. The Wigner 3-J symbols are introduced as a general concept, but the calculation of individual elements is not included. Hence, they were also self-derived and then compared with the tabulated results in the appendix of [59]. There is various literature about partition functions, but little about the actual and efficient implementation. The same is true for the assignment of quantum numbers and rovibrational irreps. Most literature either refers to uncoupled systems, or uses the Hore-Taylor theorem [60], which is a rather academic but not very practical approach. (If the leading coefficient is smaller than 0.5, then an unambiguous assignment is not possible.) The issues regarding runtime optimization are either analogous to other places in the code, which makes similar methods possible (parallelization, thresholds) or so specialized that there is also no literature about them.

1.2.3 DELIMITATION TO OTHER ROVIBRATIONAL SOFTWARE

Over the last decades a number of quantum chemical programs describing nuclear motions appeared. Of course, it is not possible to present all the groups working on this topic, but some of them will be introduced. For example Bowman and Carter *et al.* did some early work on

the VSCF and VCI theory and developed the *MULTIMODE* software [61, 62]. However, since they focus on a different accuracy regime and usually do not calculate complete rovibrational spectra, but some selected lines for small J it is not really comparable to *MOLPRO* [63]. Carrington *et al.* developed a lot of different, out of the box approaches [64–66]. However, a comparison to *MOLPRO* is also difficult, since it is not a software package, but more a set of independent algorithms. Furthermore, the focus is more on innovative, academic problem solving than on broad applicability. In contrast, the groups of Mátyus and Császár *et al.* developed the software packages *GENUISH* and *MARVEL* [67–70]. The former is an *ab initio* program using internal coordinates and it also allows for the calculation of rovibrational spectra. The latter is an empirical software, that relies on high quality experimental data. In addition to that there are some very successful programs making use of fitting a model Hamiltonian. One example is the *SPFIT/SPCAT* program introduced by Pickett *et al.* [71, 72]. Another example is *PGOPHER*, which was invented by Western [73]. Moreover, the methods of Stanton and Franke *et al.* [74] rely on VPT₂ using a large effective model Hamiltonian.

A group that has so far specialized in a low number of small molecules (e.g. water, methane and ozone), but with a very high accuracy demand is Tyuterev *et al.* [75–77]. Over decades they successively improve the quality of their potential energy surface (PES) with more and more experimental results. Since *MOLPRO* is a pure *ab initio* program, allowing for the simulation of molecules for which no or only scarce experimental data exist, this is again not really a suitable comparison. However, one of the members of the latter group developed its own more generalized software [78]. Similarities to *MOLPRO* are the use of the Born-Oppenheimer approximation and therefore the use of a PES and dipole moment surface (DMS). Moreover, it is in principle an *ab initio* method relying on a non-empirical effective Hamiltonian, that exploits symmetry properties. The basic idea is to combine the *Van Vleck perturbation theory* (also known as *contact transformation*) with the *polyad scheme*. Both the contact transformation and the new method of Ref. [78] apply a series of unitary transformations on the nuclear motion Hamiltonian. However, the former results in an expansion of the Hamiltonian in a power series and the latter uses an expansion in the polyad scheme. Furthermore, the approach of Ref. [78] does also allow for empirical corrections, if this is requested.

The program *TROVE* [79] was developed by Yurchenko, Thiel and Jensen and is since then extensively used by Yurchenko, Yachmenev and Tennyson [80–83] for calculations for their *EXOMOL* [84] database. Similarities to *MOLPRO* are again the use of the Born-Oppenheimer approximation and hence of an electronic PES and DMS. Moreover, they use a variationally computed eigenvector matrix. In principle they use an *ab initio* approach that can be refined using semi-empirical PES, an empirical basis set correction [85] or similar methods [86]. However, there are much more differences: For example, in *TROVE*, the rovibra-

tional Hamiltonian is represented by a Taylor series expansion in terms of linearized coordinates around the non-rigid reference configuration that is treated explicitly on a grid. In contrast, *MOLPRO* relies on an analytic representation of the PES and DMS in terms of polynomials or B-splines, represented in normal coordinates, a multi mode expansion and VCI theory.

A particular good comparison is possible for H_2CS , which was calculated with both approaches [81, 87]. In *TROVE*, the kinetic energy operator was terminated after the 6th order and the PES after the 8th order. However, this cannot be directly compared with our values because the 8th order Taylor series contains different terms than our 4th order multi-mode expansion. In both cases there are terms which are not included in the other method. Yachmenev *et al.* control the size of the vibrational basis set by the polyad number P and its maximum value P_{max} . Then they define a function that defines how important the different vibrational modes are for the convergence. For example, for H_2CS they define

$$P = n_{\text{CS}} + 2(n_{\text{CH}_1} + n_{\text{CH}_2}) + n_{\text{H}_1\text{CS}} + n_{\text{H}_2\text{CS}} + n_{\tau} < P_{\text{max}} \quad (\text{I.1})$$

This means for example that the level of excitation n_{CH_1} of the C – H₁ stretching mode is weighted twice as much as the level of excitation n_{CS} for the C – S mode, due to the prefactor 2. In contrast, in *MOLPRO* the selection of the vibrational basis functions in the rovibrational code is either set manually via a user input or giving by an upper energetic bound.

This shows that although there are a large number of methods for calculating rovibrational infrared spectra, they are so different that the theory has to be recalculated from scratch each time, besides the basics already developed decades ago and summarized for example in [58, 59, 88, 89], as mentioned above.

2

Theory

The goal of this thesis is to calculate rovibrational spectra. Therefore we need to determine two quantities: 1. The frequencies $\nu_{i,f}$ (i for initial state, f for final state) and 2. the intensities $I_{i,f}$ of each transition. This means that in a first step, the rovibrational state energies and wave functions need to be determined. This is done by using the Schrödinger equation, determining a Hamiltonian that describes the rovibrational problem, choosing a rovibrational basis set, building up the corresponding matrix and diagonalizing it. The second quantity that is needed for the spectrum is a measurement for the strength of the transition. This is the intensity for IR spectra and the differential cross-sections for Raman spectra.

As mentioned in Subsec. 1.2.1, there is a long series of programs and algorithms in the *MOLPRO* software that is required before the rovibrational calculations can be done. However, for the understanding of the RVCI theory that is developed in the course of this thesis, it is sufficient to explain the basics about the surface calculation (PES, DMS and polarisability surface (PS)), VCI and RCI theory. This is done while introducing the Watson Hamiltonian.

2.1 WATSON HAMILTONIAN

There are many different ways to describe the nuclear motion of molecules. Many of them are using the Born-Oppenheimer approximation to separate the nuclear motion and the electronic motion, making use of the different time scale of these processes and yielding a PES

term in the Hamiltonian. Determining the Euler angles and applying the Eckart conditions allows to separate the rotational and the vibrational motion as much as possible. The vibrational motion of the cores corresponds to a physical angular momentum and is not due to the choice of the coordinate system. Therefore, a complete decoupling is not possible. The Coriolis coupling term describes this effect. In a second step, the different vibrational modes can now also be separated as far as possible. For this purpose, the potential is approximated quadratically in the vicinity of the minimum. This harmonic approximation allows then to set up and diagonalize the Hessian matrix. The resulting eigenvalues are proportional to the harmonic frequencies and the eigenvectors correspond to the so-called normal coordinates q_i , which are used in the following. Combining these steps leads to the Watson Hamiltonian [90]

$$\mathcal{H}_W = \frac{1}{2} \sum_{\alpha\beta} (J_\alpha - \pi_\alpha) \mu_{\alpha\beta} (J_\beta - \pi_\beta) - \frac{1}{8} \sum_{\alpha} \mu_{\alpha\alpha} - \frac{1}{2} \sum_{i=1}^{3N-6} \frac{\partial^2}{\partial q_i^2} + V(q_1, \dots, q_{3N-6}). \quad (2.1)$$

Here μ denotes the *inverse of the effective moment of inertia tensor*, J_α the *total angular momentum*, the indices α and β correspond to the Cartesian coordinates $\{x, y, z\}$, π_α describes the *vibrational angular momentum* and N is the number of atoms. Hence, there are $M = 3N - 6$ vibrational modes, since we only consider non-linear molecules. This results in M normal coordinates, which span the potential energy surface (PES) $V(q_1, \dots, q_M)$. The Watson Hamiltonian can be split in the following three parts

1. Vibrational term (subsection 2.1.1)

$$\mathcal{H}_{\text{vib}} = \frac{1}{2} \sum_{\alpha\beta \in \{x,y,z\}} \pi_\alpha \mu_{\alpha\beta} \pi_\beta - \frac{1}{8} \sum_{\alpha \in \{x,y,z\}} \mu_{\alpha\alpha} - \frac{1}{2} \sum_{i=1}^M \frac{\partial^2}{\partial q_i^2} + V(q_1, \dots, q_M)$$

2. Rotational term (subsection 2.1.2)

$$\mathcal{H}_{\text{rot}} = \frac{1}{2} \sum_{\alpha\beta \in \{x,y,z\}} J_\alpha \mu_{\alpha\beta} J_\beta$$

3. Coriolis coupling term (subsection 2.1.3)

$$\mathcal{H}_{\text{cc}} = -\frac{1}{2} \sum_{\alpha\beta \in \{x,y,z\}} (J_\alpha \mu_{\alpha\beta} \pi_\beta + \pi_\alpha \mu_{\alpha\beta} J_\beta)$$

$$\mathcal{H}_W = \mathcal{H}_{\text{vib}} + \mathcal{H}_{\text{rot}} + \mathcal{H}_{\text{cc}}.$$

2.1.1 VIBRATIONAL TERM

The Watson Hamiltonian for non-rotating molecules has the form [90]

$$\mathcal{H}_{\text{vib}} = \frac{1}{2} \sum_{\alpha, \beta \in \{x, y, z\}} \pi_{\alpha} \mu_{\alpha\beta} \pi_{\beta} - \frac{1}{8} \sum_{\alpha \in \{x, y, z\}} \mu_{\alpha\alpha} - \frac{1}{2} \sum_{i=1}^M \frac{\partial^2}{\partial q_i^2} + V(q_1, \dots, q_M). \quad (2.2)$$

For didactic reasons it is most useful to start with the PES term

$$V(q_1, \dots, q_M). \quad (2.3)$$

This is due to the fact that it relies on a multi-mode expansion, which is also used for another part of the Watson Hamiltonian. Since the calculation of an equidistant grid is not computationally feasible for large molecules, an expansion that is truncated after a certain order is an intuitive solution for this issue. In addition, it is advantageous to use difference surfaces, since this leads to decreasing contributions for the higher order terms, which is essential for the convergence of the expansion. A Taylor expansion and a multi-mode expansion are closely related in that sense, that they consist of the same terms, but their assignment to the specific expansion orders is differently.

The PES described by a multi-mode expansion is given by

$$V(q_1, \dots, q_M) = \sum_i^M V_i(q_i) + \sum_{i < j}^M V_{ij}(q_i, q_j) + \sum_{i < j < k}^M V_{ijk}(q_i, q_j, q_k) + \dots \quad (2.4)$$

$$V_i(q_i) = V_i^0(q_i) - V_0 \quad (2.5)$$

$$V_{ij}(q_i, q_j) = V_{ij}^0(q_i, q_j) - \sum_{r \in \{i, j\}}^M V_r(q_r) - V_0 \quad (2.6)$$

$$V_{ijk}(q_i, q_j, q_k) = V_{ijk}^0(q_i, q_j, q_k) - \sum_{\substack{r < s \\ r, s \in \{i, j, k\}}}^M V_r(q_r, q_s) - \sum_{r \in \{i, j\}}^M V_r(q_r) - V_0. \quad (2.7)$$

To determine the PES, *ab initio* electronic structure theory is used to determine energies along the required directions. While a naive implementation of the surface calculation for one molecule is relatively straight forward, the generalization over all symmetry groups and many molecules is very demanding. Furthermore, the efficient calculation, using an iterative construction of the surfaces, a multi-level scheme, screening, parallelization, symmetry properties turns the implementation into a very challenging undertaking. The determination of the grid representation of the PES is done in *MOLPRO* in the *XSURF* program [91–94]. Subsequently, the grid representation is transformed into an analytical representation, such

as polynomials or B-splines. This accelerates the later determination of the integrals within the vibrational calculations. Within *MOLPRO* this is done in the POLY program, with a very efficient Kronecker product fitting [95]. It should be noted that the property surfaces, i.e. the dipole moment surface (DMS) and polarisability surface (PS), are constructed in the same way.

The first part in Eq. (2.2) describes the vibrational angular momentum (VAM) term

$$\mathcal{H}_{\text{VAM}} = \frac{1}{2} \sum_{\alpha\beta \in \{x,y,z\}} \pi_\alpha \mu_{\alpha\beta} \pi_\beta \quad (2.8)$$

including the *vibrational angular momentum operator* [90]

$$\pi_\alpha := -i \sum_{kl} \zeta_{kl}^\alpha q_l \partial_{q_k}, \quad (2.9)$$

which consists of the *Coriolis- ζ constants* [90]

$$\zeta_{lk}^\alpha := \sum_{j=1}^N (\mathbf{L}_{jk} \times \mathbf{L}_{jl})_\alpha = -\zeta_{kl}^\alpha. \quad (2.10)$$

Thereby \mathbf{L} denotes the transformation matrix from mass-weighted elongation vectors in normal coordinates. Moreover, the Coriolis- ζ constants fulfill the relation $\zeta_{kk}^\alpha = 0$. The VAM term also includes the inverse of the effective moment of inertia tensor μ , which is defined as

$$\mu_{\alpha\beta} := (I')_{\alpha\beta}^{-1}, \quad I'_{\alpha\beta} := I_{\alpha\beta} - \sum_{k,l,m=1}^M \zeta_{lk}^\alpha \zeta_{mk}^\beta q_l q_m. \quad (2.11)$$

The μ -tensor is also represented in a multi-mode expansion

$$\mu_{\alpha\beta} := \mu_{\alpha\beta}^0 + \sum_{k=1}^M \mu_{\alpha\beta}(q_k) + \sum_{k=1}^M \sum_{l=1}^{k-1} \mu_{\alpha\beta}(q_k, q_l) + \dots \quad (2.12)$$

describing the inverse effective moment of inertia tensor in terms of difference surfaces. Empirical studies have shown that this expansion converges faster than the multi-mode expansion for the PES. For example, most semi-rigid molecules require a 4D multi-mode expansion for the potential to converge, while the 0th order μ -tensor terms are sufficient for the VAM terms [96].

The second term in Eq. (2.2) describes the Watson correction term

$$\frac{1}{8} \sum_{\alpha \in \{x,y,z\}} \mu_{\alpha\alpha}. \quad (2.13)$$

It is a pure quantum mechanical term, i.e. it has no classical equivalent. For the later vibrational calculations, this term can be combined with the PES. It corresponds to a mass-dependent pseudo-potential.

The third part of Eq. (2.2)

$$\frac{1}{2} \sum_{i=1}^M \frac{\partial^2}{\partial q_i^2} \quad (2.14)$$

describes the main contribution of the kinetic energy operator. In the analogy to classical mechanics, this term corresponds to the kinetic energy of the vibrational modes.

In general, there are many different methods to solve the vibrational problem, such as VMP2, VMP4 [97], VPT2 [98], VSCF [99], VCI [100, 101], VMCSF [102], VM-RCI [103], VCC [104, 105], etc. In the following two of these methods will be described briefly, since they are used in the course of this thesis.

VIBRATIONAL SELF-CONSISTENT FIELD THEORY

The vibrational self-consistent field (VSCF) theory is the vibrational equivalent to the Hartree-Fock theory in electronic structure theory. It is a variational method relying on a mean-field approximation. Hence, it does not consider correlation effects and is therefore only used to provide optimized vibrational basis functions for the subsequent VCI calculation. The VSCF implementation in *MOLPRO* allows to use

- either distributed Gaussian basis functions, which are local, but not pairwise orthogonal
- or harmonic oscillator basis functions, which are pairwise orthogonal, but global functions.

A linear combination of these basis functions yields one mode wave functions $\varphi_a^{n_a^I}(q_a)$, which are called *modals*. In the following, n_a^I denotes the *quantum number* for the normal coordinate q_a and the full set of occupation numbers is given by $I = (n_1^I, \dots, n_M^I)$. Based on that, the VSCF wave functions are given by Hartree-product of modals

$$\phi_I^{\text{VSCF}}(q_1, \dots, q_M) = \prod_a^M \varphi_a^{n_a^I}(q_a). \quad (2.15)$$

Within the later derivation of the RVC theory it will be necessary to understand the VSCF wave functions, but the specific choice for the VSCF basis functions will not be important. The reason for that is the following: The rovibrational integrals can be separated in vibrational and rotational integrals. While the latter are completely independent of any vibrational wave functions, the former are obviously not. Moreover, all operators in the later calculations can be decomposed in sums and products of the position operators q_i^d and the momentum operators ∂_i . Hence, they are acting only on one coordinate and therefore allow to separate the calculation in one dimensional integrals. It should be noted, that coupling between different vibrational modes is still considered due to multi-dimensional polynomial coefficients and the corresponding summations introduced in the polynomial expansion. However, this individual treatment of one dimensional integrals requires to consider the one mode wave functions which are modals.

VIBRATIONAL CONFIGURATION INTERACTION THEORY

Analogously to VSCF theory, VCI theory does also rely on the variational principle, but in contrast no mean field approach is used. Therefore, it allows to consider correlation effects between different modes. As a consequence, the resulting transition frequencies are much more accurate. The basic idea is to use the Schrödinger equation, the Watson Hamiltonian and the VSCF wave functions as VCI basis functions to build up the correlation matrix. The diagonalization of this matrix yields the vibrational state energies and wave functions

$$|\phi_I^{\text{VCI}}\rangle = \sum_I c_I^{\tilde{I}} |\phi_I^{\text{VSCF}}\rangle = \sum_I c_I^{\tilde{I}} \left| \prod_a^M \varphi_a^{n_a^I} \right\rangle. \quad (2.16)$$

The $|\phi_I^{\text{VSCF}}\rangle$ wave functions will be referred to as configurations in the following. It should be noted that the used VCI implementation used relies on state specific, symmetry-blocked matrices relying on prescreening. This means for every vibrational state of interest a VCI matrix is built iteratively by adding more basis functions of the same irreducible representation. Then only one eigenpair is determined by a special algorithm [106]. Prior to the prescreening, the number of considered configurations spanning the configuration interaction (CI) space is limited by three quantities:

- LEVEX determines the largest quantum number within one mode, i.e. $0 \rightarrow 1, 0 \rightarrow 2, 0 \rightarrow 3, \dots$ The default is LEVEX = 5.
- CITYPE defines the maximum number of simultaneous excitations with respect to the different modes, i.e. Singles, Doubles, Triples, ...and thus determines the kind of calcula-

tions, i.e. VCIS, VCISD, VCISDT, ... The default is CITYPE = 5, VCI(5) if a 4D surface is used.

- CIMAX is the maximum excitation level (maximum sum of quantum numbers) of configurations within the limits of LEVEX and CITYPE. The default is CIMAX = 15.

The coupling through the Watson Hamiltonian is usually stronger between configurations with similar quantum numbers or transition frequencies. For the later RVCIs calculations it is important to keep in mind, that the VCI wave functions $|\phi_{\tilde{I}}^{\text{VCI}}\rangle$ are solutions for the Schrödinger equation with the vibrational Watson Hamiltonian \mathcal{H}_{vib} . For this reason, they are an excellent choice for the vibrational part in a product ansatz for the RVCIs basis functions.

ROVIBRATIONAL WAVE FUNCTIONS

Since the vibrational part of the RCI and RVCIs basis functions consists of VCI wave functions, the former can be introduced now. The main difference between RCI and RVCIs theory is that the former does not consider coupling terms between different vibrational modes. As a consequence, the resulting RCI wave functions are only a linear combination of different k values (z-component of the total angular momentum), but not a linear combination of different vibrational states. This can be seen in the following comparison:

$$|\phi_{\tilde{I}}^{\text{VCI}}\rangle = \sum_I c_{\tilde{I}}^I |\phi_I^{\text{VSCF}}\rangle \quad (2.17)$$

$$|\Phi_{J,r,\tilde{I}}^{\text{RCI}}\rangle := \left(\sum_k c_k^{J,r,\tilde{I}} |J, k\rangle \right) |\phi_{\tilde{I}}^{\text{VCI}}\rangle = \left(\sum_k c_k^{J,r,\tilde{I}} |J, k\rangle \right) \left(\sum_I c_{\tilde{I}}^I |\phi_I^{\text{VSCF}}\rangle \right) \quad (2.18)$$

$$|\Psi_{J,r,\tilde{I}}^{\text{RVCIs}}\rangle := \sum_{k,\tilde{I}} c_{k,\tilde{I}}^{J,r,\tilde{I}} |J, k\rangle |\phi_{\tilde{I}}^{\text{VCI}}\rangle = \sum_{k,\tilde{I}} c_{k,\tilde{I}}^{J,r,\tilde{I}} |J, k\rangle \sum_I c_{\tilde{I}}^I |\phi_I^{\text{VSCF}}\rangle \quad (2.19)$$

The RVCIs wave functions are also a linear combination of different vibrational states and therefore allow to consider inter-vibrational state coupling. In the upper equations, the rotational basis functions are for example provided by the primitive rigid rotor basis functions (also called symmetric top basis functions). However, this can be any pure rotational wave function, which will be discussed later.

2.1.2 ROTATIONAL TERM

A vibrational $|\phi_{\text{vib}}''\rangle$ and rotational $|\phi_{\text{rot}}''\rangle$ basis function can be combined in a direct product $|\Phi''\rangle = |\phi_{\text{vib}}''\rangle |\phi_{\text{rot}}''\rangle$. In the following, an abstract vibrational basis function will be denoted $|\phi_{\text{vib}}''\rangle$ while a specific basis function such as a VCI wave functions will be denoted $|\phi_{\tilde{I}}^{\text{VCI}}\rangle$. The same holds for the rotational basis function with $|\phi_{\text{rot}}''\rangle$ denoting the general form and

$|J'', k''\rangle$ denoting the rigid rotor basis (RRB). Moreover, the initial states are marked with a '' and the final states with a ', since this is sufficient for the distinctions. However, the specific form of the vibrational basis requires more information. Therefore, different indices are used to distinguish the initial and final state.

It should also be mentioned that it is very difficult to find a notation that makes sense for both the derivation of the eigenstates and the derivation of the intensities. Furthermore, the notation should not contradict the usual conventions of the literature from the vibrational spectroscopy community nor the literature from the rotational spectroscopy. This was not always possible, but was attempted to the best of our ability.

The rotational term can be written as

$$\mathcal{H}_{\text{rot}} = \frac{1}{2} \sum_{\alpha\beta \in \{x,y,z\}} J_{\alpha} \mu_{\alpha\beta} J_{\beta}. \quad (2.20)$$

Using the direct product basis yields

$$\langle \Phi' | \mathcal{H}_{\text{rot}} | \Phi'' \rangle = \frac{1}{2} \sum_{\alpha\beta \in \{x,y,z\}} \langle \phi'_{\text{vib}} | \langle \phi'_{\text{rot}} | J_{\alpha} \mu_{\alpha\beta} J_{\beta} | \phi''_{\text{vib}} \rangle | \phi''_{\text{rot}} \rangle = \quad (2.21)$$

$$\frac{1}{2} \sum_{\alpha\beta \in \{x,y,z\}} \langle \phi'_{\text{vib}} | \mu_{\alpha\beta} | \phi''_{\text{vib}} \rangle \langle \phi'_{\text{rot}} | J_{\alpha} J_{\beta} | \phi''_{\text{rot}} \rangle. \quad (2.22)$$

This is due to the fact that the effective inverse moment of inertia tensor operator μ has no effect on the rotational basis functions and total angular momentum operators J_{α}, J_{β} have no effect on vibrational basis functions. Therefore we can split the analysis in two parts: The vibrational integral and the rotational integral.

VIBRATIONAL INTEGRALS

The study of similar vibrational integrals for the VAM terms has been presented in a previous thesis in the Rauhut group by Neff [107]. However, the vibrational basis corresponded to the VCI basis and not to the VCI wave functions. For the sake of completeness and a better understanding, it will be started with the vibrational integrals, as they appear in VCI and RCI. (Note, that this exact term is not determined in VCI theory, since the VAM terms have an additional π_{α} operator.) After that, the equations will be derived in the form in which they appear in RVCI.

If we use Eq. (2.12) and consider the vibrational integral of Eq. (2.22) it yields:

$$\begin{aligned} \langle \phi'_{\text{vib}} | \mu_{\alpha\beta} | \phi''_{\text{vib}} \rangle &= \mu_{\alpha\beta}^0 \langle \phi'_{\text{vib}} | \phi''_{\text{vib}} \rangle + \sum_{k=1}^M \langle \phi'_{\text{vib}} | \mu_{\alpha\beta}(q_k) | \phi''_{\text{vib}} \rangle \\ &+ \sum_{k=1}^M \sum_{l=1}^{k-1} \langle \phi'_{\text{vib}} | \mu_{\alpha\beta}(q_k, q_l) | \phi''_{\text{vib}} \rangle + \dots \end{aligned} \quad (2.23)$$

Without an assumptions about the basis functions, it is not possible to simplify this expression. For VCI theory it follows

$$\begin{aligned} \langle \phi_I^{\text{VSCF}} | \mu_{\alpha\beta} | \phi_J^{\text{VSCF}} \rangle &= \\ \mu_{\alpha\beta}^0 \underbrace{\langle \phi_I^{\text{VSCF}} | \phi_J^{\text{VSCF}} \rangle}_{=\delta_{I,J}} &+ \sum_{k=1}^M \langle \phi_I^{\text{VSCF}} | \mu_{\alpha\beta}(q_k) | \phi_J^{\text{VSCF}} \rangle \\ + \sum_{k=1}^M \sum_{l=1}^{k-1} \langle \phi_I^{\text{VSCF}} | \mu_{\alpha\beta}(q_k, q_l) | \phi_J^{\text{VSCF}} \rangle &+ \dots \end{aligned} \quad (2.24)$$

Using that the VCI basis functions are described by the VSCF wave functions, consisting of modals (see Eq. (2.15)) yields

$$\begin{aligned} \mu_{\alpha\beta}^0 \delta_{I,J} + \sum_{k=1}^M \left\langle \prod_a^M \varphi_a^{n_a^I} \middle| \mu_{\alpha\beta}(q_k) \middle| \prod_a^M \varphi_a^{n_a^J} \right\rangle \\ + \sum_{k=1}^M \sum_{l=1}^{k-1} \left\langle \prod_a^M \varphi_a^{n_a^I} \middle| \mu_{\alpha\beta}(q_k, q_l) \middle| \prod_a^M \varphi_a^{n_a^J} \right\rangle + \dots \end{aligned} \quad (2.25)$$

This can be simplified by using the orthonormality of the wave functions, that are not effected by an operator

$$\mu_{\alpha\beta}^0 \delta_{I,J} + \sum_{k=1}^M \left\langle \varphi_k^{n_k^I} \middle| \mu_{\alpha\beta}(q_k) \middle| \varphi_k^{n_k^J} \right\rangle \prod_{i \neq k} \left\langle \varphi_i^{n_i^I} \middle| \varphi_i^{n_i^J} \right\rangle \quad (2.26)$$

$$+ \sum_{k=1}^M \sum_{l=1}^{k-1} \left\langle \varphi_l^{n_l^I} \middle| \left\langle \varphi_k^{n_k^I} \middle| \mu_{\alpha\beta}(q_k, q_l) \middle| \varphi_k^{n_k^J} \right\rangle \middle| \varphi_l^{n_l^J} \right\rangle \prod_{i \neq \{k,l\}} \left\langle \varphi_i^{n_i^I} \middle| \varphi_i^{n_i^J} \right\rangle + \dots \quad (2.27)$$

Note, that there is no summation over VCI coefficients, as these are VCI integrals of VCI basis functions, not wave functions.

There are some changes if compared with an RCI calculation. Using Eq. (2.18) adds two sums over the VCI wave functions. However, since the implementation is limited to a 0th order μ -tensor these sums vanish due to the orthonormality of the VCI wave functions resulting in a very simple integral

$$\langle \phi_I^{\text{RCI}} | \mu_{\alpha\beta} | \phi_J^{\text{RCI}} \rangle = \langle \phi_I^{\text{RCI}} | \mu_{\alpha\beta}^0 | \phi_J^{\text{RCI}} \rangle = \mu_{\alpha\beta}^0 \delta_{I,J} \quad (2.28)$$

In contrast, within RVCI theory, these integrals are much more involved. This is due to

1. the higher order terms
2. the different basis functions, and
3. the fact that the selected configurations for left and right wave functions are no longer identical.

In the previous calculations it was assumed that the modals are ground state based. However, in the most general case, they can be optimized for each vibrational state and therefore they are not orthonormal to each other.

Inserting the VCI wave functions for the vibrational part of the RVCI basis functions yields

$$\begin{aligned} \langle \phi_{\tilde{I}}^{\text{RVCI}} | \mu_{\alpha\beta} | \phi_{\tilde{J}}^{\text{RVCI}} \rangle &= \mu_{\alpha\beta}^0 \left(\sum_{I=1}^{N'_{\text{conf}}} c_{\tilde{I}}^{\tilde{I}} \langle \phi_I^{\text{VSCF}} | \right) \left(\sum_{J=1}^{N_{\text{conf}}} c_{\tilde{J}}^{\tilde{J}} | \phi_J^{\text{VSCF}} \rangle \right) \\ &+ \sum_{k=1}^M \left(\sum_{I=1}^{N'_{\text{conf}}} c_{\tilde{I}}^{\tilde{I}} \langle \phi_I^{\text{VSCF}} | \right) \mu_{\alpha\beta}(q_k) \left(\sum_{J=1}^{N_{\text{conf}}} c_{\tilde{J}}^{\tilde{J}} | \phi_J^{\text{VSCF}} \rangle \right) \\ &+ \sum_{k=1}^M \sum_{l=1}^{k-1} \left(\sum_{I=1}^{N'_{\text{conf}}} c_{\tilde{I}}^{\tilde{I}} \langle \phi_I^{\text{VSCF}} | \right) \mu_{\alpha\beta}(q_k, q_l) \left(\sum_{J=1}^{N_{\text{conf}}} c_{\tilde{J}}^{\tilde{J}} | \phi_J^{\text{VSCF}} \rangle \right), \quad (2.29) \end{aligned}$$

with the number of selected configurations N_{conf} . Replacing the VCI basis functions by VSCF wave functions and using the overlap integrals $S_a^{IJ} := \langle \varphi_a^{n_a^I} | \varphi_a^{n_a^J} \rangle$ yields

$$\begin{aligned} &\mu_{\alpha\beta}^0 \sum_{I,J} c_{\tilde{I}}^{\tilde{I}} c_{\tilde{J}}^{\tilde{J}} \underbrace{\left\langle \prod_a \varphi_a^{n_a^I} \middle| \prod_a \varphi_a^{n_a^J} \right\rangle}_{=\prod_a S_a^{IJ}} \\ &+ \sum_{k,I,J} c_{\tilde{I}}^{\tilde{I}} c_{\tilde{J}}^{\tilde{J}} \underbrace{\left\langle \prod_a \varphi_a^{n_a^I} \middle| \mu_{\alpha\beta}(q_k) \middle| \prod_a \varphi_a^{n_a^J} \right\rangle}_{=\langle \varphi_k^{n_k^I} | \mu_{\alpha\beta}(q_k) | \varphi_k^{n_k^J} \rangle \prod_{a \neq k} S_a^{IJ}} \end{aligned}$$

$$\begin{aligned}
& + \sum_{m < k, I, J} c_I^{\tilde{I}} c_J^{\tilde{J}} \left\langle \prod_a \varphi_a^{n_a^I} \middle| \mu_{\alpha\beta}(q_k, q_l) \middle| \prod_a \varphi_a^{n_a^J} \right\rangle \\
& = \left\langle \varphi_k^{n_k^I} \varphi_l^{n_l^I} \middle| \mu_{\alpha\beta}(q_k, q_l) \middle| \varphi_k^{n_k^J} \varphi_l^{n_l^J} \right\rangle \prod_{a \neq \{k, l\}} S_a^{IJ}
\end{aligned} \tag{2.30}$$

The μ -tensor integrals are already implemented in *MOLPRO*. Therefore we use the following notation of Ref. [107]

$$X_{kg}^{n_k^I n_k^J} = \left\langle \varphi_k^{n_k^I} \middle| q_k^g \middle| \varphi_k^{n_k^J} \right\rangle \tag{2.31}$$

to yield

$$\left\langle \varphi_k^{n_k^I} \middle| \mu_{\alpha\beta}(q_k) \middle| \varphi_k^{n_k^J} \right\rangle = \sum_{g=1}^{N_{\text{poly}}} p_{g,\alpha\beta}^{(k)} X_{kg}^{n_k^I n_k^J} \tag{2.32}$$

$$\left\langle \varphi_k^{n_k^I} \varphi_l^{n_l^I} \middle| \mu_{\alpha\beta}(q_k, q_l) \middle| \varphi_k^{n_k^J} \varphi_l^{n_l^J} \right\rangle = \sum_{g=1}^{N_{\text{poly}}} \sum_{h=1}^{N_{\text{poly}}} p_{gh,\alpha\beta}^{(k,l)} X_{kg}^{n_k^I n_k^J} X_{lh}^{n_l^I n_l^J}. \tag{2.33}$$

Here, N_{poly} describes the maximum order of the polynomial, $p_{g,\alpha\beta}^{(k)}$ describes a one dimensional expansion coefficient for an analytic description of the μ -tensor. In two dimensions it is given by $p_{gh,\alpha\beta}^{(k,l)}$. By combining the equations (2.30) and (2.33) it follows:

$$\begin{aligned}
& \mu_{\alpha\beta}^0 \sum_{I,J} c_I^{\tilde{I}} c_J^{\tilde{J}} \prod_a S_a^{IJ} + \sum_{k,I,J} c_I^{\tilde{I}} c_J^{\tilde{J}} \sum_g p_{g,\alpha\beta}^{(k)} X_{kg}^{n_k^I n_k^J} \prod_{a \neq k} S_a^{IJ} \\
& + \sum_{l < k, I, J} c_I^{\tilde{I}} c_J^{\tilde{J}} \sum_g \sum_h p_{gh,\alpha\beta}^{(kl)} X_{kg}^{n_k^I n_k^J} X_{lh}^{n_l^I n_l^J} \prod_{a \neq \{k, l\}} S_a^{IJ}
\end{aligned} \tag{2.34}$$

This shows that the vibrational integral of the rotational term can be implemented based on existing integrals and summation.

ROTATIONAL INTEGRALS

After determining the vibrational integral of the rotational term, it is necessary to derive the rotational integral

$$\left\langle \phi'_{\text{rot}} \middle| J_{\alpha} J_{\beta} \middle| \phi''_{\text{rot}} \right\rangle. \tag{2.35}$$

At first, a rotational basis has to be chosen. The simplest basis is the rigid rotor basis (RRB) $|J, k\rangle$ fulfilling the relations

$$\mathbf{J}^2 |J, k\rangle = J(J+1) |J, k\rangle \quad (2.36)$$

$$J_z |J, k\rangle = k |J, k\rangle \quad (2.37)$$

$$(2.38)$$

The angular momentum ladder operator

$$J_{\pm} |J, k\rangle = \sqrt{J(J+1) - k(k \pm 1)} |J, k \pm 1\rangle \text{ with } J_{\pm} = J_x \pm iJ_y. \quad (2.39)$$

can be very helpful for the determination of the rotational integrals.

Another very common basis is the Wang basis that appears in different variants. Instead of the quantum number $k \in \{-J, \dots, +J\}$ the Wang basis uses the parity τ of k and the absolute value of $K = |k|$. *MOLPRO* uses the version introduced in Ref. [108]

$$\tau := \begin{cases} 0 & \text{for } k < 0 \\ 1 & \text{for } k \geq 0 \end{cases} \quad (2.40)$$

$$\sigma := \begin{cases} 0 & \text{for } \tau = 0 \\ K \bmod 3 & \text{for } \tau = 1 \end{cases} \quad (2.41)$$

$$|J0\tau\rangle = \begin{cases} |J0\rangle & \text{for } \tau = 0 \\ 0 & \text{for } \tau = 1 \end{cases} \quad \text{for } K = 0 \quad (2.42)$$

$$|JK\tau\rangle = \frac{i^{\sigma}}{\sqrt{2}} (|JK\rangle + (-1)^{J+K+\tau} |J-K\rangle) \quad \text{for } K \neq 0 \quad (2.43)$$

Since it is a linear combination it is also called Wang combination.

Both types of basis functions are available in *MOLPRO*, but the analytical integrals are only implemented for RRB and the integrals in the Wang basis (WB) are determined by adding the different rigid rotor terms. This is the reason, why we will only use the RRB for the derivation of equations.

Using the RRB gives

$$\langle J', k' | J_{\alpha} J_{\beta} | J'', k'' \rangle, \quad (2.44)$$

which has only non-vanishing values for $J' = J''$ due to the selection rules. Since $\alpha, \beta \in \{x, y, z\}$ there are 15 different combinations of operators, that need to be considered. By using

Eqs. (2.36)-(2.39) it follows

$$\langle J, k | J_z^2 | J, k \rangle = k^2 \quad (2.45)$$

$$\langle J, k | J_x^2 | J, k \rangle = \langle J, k | J_y^2 | J, k \rangle \quad (2.46)$$

$$= \frac{1}{2} [J(J+1) - k^2] \quad (2.47)$$

$$\langle J, k | J_x J_y | J, k \rangle = - \langle J, k | J_y J_x | J, k \rangle \quad (2.48)$$

$$= -\frac{i}{2} k \quad (2.49)$$

$$\langle J, k \pm 1 | J_x J_z | J, k \rangle = \mp i \langle J, k \pm 1 | J_y J_z | J, k \rangle \quad (2.50)$$

$$= \frac{1}{2} k \sqrt{J(J+1) - k(k \pm 1)} \quad (2.51)$$

$$\langle J, k \pm 1 | J_z J_x | J, k \rangle = \mp i \langle J, k \pm 1 | J_z J_y | J, k \rangle \quad (2.52)$$

$$= \frac{1}{2} (k \pm 1) \sqrt{J(J+1) - k(k \pm 1)} \quad (2.53)$$

$$\langle J, k \pm 2 | J_x^2 | J, k \rangle = - \langle J, k \pm 2 | J_y^2 | J, k \rangle \quad (2.54)$$

$$= \mp i \langle J, k \pm 2 | J_x J_y | J, k \rangle \quad (2.55)$$

$$= \mp i \langle J, k \pm 2 | J_y J_x | J, k \rangle \quad (2.56)$$

$$= -\frac{1}{4} \sqrt{J(J+1) - k(k \pm 1)} \sqrt{J(J+1) - (k \pm 1)(k \pm 2)} \quad (2.57)$$

All integrals with two angular momentum operators not mentioned above vanish. As can be seen, the elements of the total angular momentum operators are not commuting. However, there is a simplification if the combined integral Eq. (2.22) (including the summation over α, β) is considered. For example, Eq. (2.48) can be used together with the symmetry of $\mu_{\alpha, \beta}$ to show that

$$\langle J, k | J_x J_y \mu_{xy} + J_y J_x \mu_{yx} | J, k \rangle = \quad (2.58)$$

$$\langle J, k | J_x J_y \mu_{xy} - J_x J_y \mu_{yx} | J, k \rangle = \quad (2.59)$$

$$\langle J, k | J_x J_y \mu_{xy} - J_x J_y \mu_{yx} | J, k \rangle = 0 \quad (2.60)$$

The vibrational basis is not explicitly given for the sake of simplicity. The resulting integral for $k' = k''$ is

$$\langle J, k | \mathcal{H}_{\text{rot}} | J, k \rangle = \frac{1}{2} \langle J, k | J_x^2 \mu_{xx} + J_y^2 \mu_{yy} + J_z^2 \mu_{zz} | J, k \rangle \quad (2.61)$$

$$= \frac{1}{2} \left\{ \frac{1}{2} [J(J+1) - k^2] (\mu_{xx} + \mu_{yy}) + k^2 \mu_{zz} \right\} \quad (2.62)$$

and for the other non-vanishing cases

$$\langle J, k \pm 1 | \mathcal{H}_{\text{rot}} | J, k \rangle = \frac{1}{2} \langle J, k \pm 1 | J_x J_y \mu_{xy} + J_y J_z \mu_{yz} + J_z J_x \mu_{zx} + J_z J_y \mu_{zy} | J, k \rangle \quad (2.63)$$

$$= \frac{1}{4} \sqrt{J(J+1) - k(k \pm 1)} (2k \pm 1) (\mu_{xz} \pm i\mu_{yz}). \quad (2.64)$$

$$\langle J, k \pm 2 | \mathcal{H}_{\text{rot}} | J, k \rangle = \frac{1}{2} \langle J, k \pm 2 | J_x^2 \mu_{xx} + J_y^2 \mu_{yy} + J_x J_y \mu_{xy} + J_y J_x \mu_{yx} | J, k \rangle \quad (2.65)$$

$$= \frac{1}{8} \sqrt{J(J+1) - k(k \pm 1)} \sqrt{J(J+1) - (k \pm 1)(k \pm 2)} \\ \times (\mu_{xx} - \mu_{yy} \pm 2i\mu_{xy}). \quad (2.66)$$

2.1.3 CORIOLIS COUPLING TERM

The Coriolis coupling term can be written as

$$\mathcal{H}_{\text{cc}} = -\frac{1}{2} \sum_{\alpha\beta \in \{x,y,z\}} (J_\alpha \mu_{\alpha\beta} \pi_\beta + \pi_\alpha \mu_{\alpha\beta} J_\beta). \quad (2.67)$$

Using the aforementioned separation between rotational and vibrational basis functions yields

$$\begin{aligned} \langle \Phi' | \mathcal{H}_{\text{cc}} | \Phi'' \rangle &= -\frac{1}{2} \sum_{\alpha\beta \in \{x,y,z\}} \langle \phi'_{\text{vib}} | \langle \phi'_{\text{rot}} | J_\alpha \mu_{\alpha\beta} \pi_\beta + \pi_\alpha \mu_{\alpha\beta} J_\beta | \phi''_{\text{vib}} \rangle | \phi''_{\text{rot}} \rangle \\ &= \frac{1}{2} \sum_{\alpha} \langle \phi'_{\text{rot}} | J_\alpha | \phi''_{\text{rot}} \rangle \langle \phi'_{\text{vib}} | \sum_{\beta} \mu_{\alpha\beta} \pi_\beta | \phi''_{\text{vib}} \rangle \\ &\quad + \frac{1}{2} \sum_{\beta} \langle \phi'_{\text{vib}} | \sum_{\alpha} \pi_\alpha \mu_{\alpha\beta} | \phi''_{\text{vib}} \rangle \langle \phi'_{\text{rot}} | J_\beta | \phi''_{\text{rot}} \rangle. \end{aligned} \quad (2.68)$$

Note that both the μ and the π_β operators commute with the J_α operator, since they act on the vibrational basis and the J_α operator acts purely on the rotational basis. Moreover, the μ operator also commutes with the π_β operator, as has been shown by Ref. [90]. However, it was shown that the commutation does not hold if the μ tensor is expanded in a multi-mode expansion and truncated after a certain order. During the recent optimization of the VAM term implementation in Ref. [109] this was not considered for the following reason: Considering the commutator between π_β and all μ -tensor orders yields

$$\left[\sum_m^{\infty} \mu_{\alpha\beta}^{(m)}, \pi_\beta \right] = 0, \quad (2.69)$$

but for a truncation after the n -th order term it gives

$$\left[\sum_m^n \mu_{\alpha\beta}^{(m)}, \pi_\beta \right] = \mathcal{O}(n+1). \quad (2.70)$$

This means that the missing contributions are either zero or correspond to a higher order term and are therefore less important. In the course of this thesis these terms are explicitly derived, thus allowing for an investigation of this issue.

VIBRATIONAL INTEGRAL

Compared to the rotational term, the rotational integrals in the Coriolis coupling term are much simpler, since only a single angular momentum operator occurs. However, the vibrational integral is much more involved, since the additional vibrational angular momentum operator π_α occurs. It requires to employ the definitions Eqs. (2.9), (2.10), (2.12).

The different orders of the multi-mode expansion are analyzed separately. As the 0th order μ -tensor is only a scalar number, but not an operator, it yields

$$\frac{1}{2} \sum_{\alpha\beta} \langle \phi'_{\text{vib}} | \mu_{\alpha\beta}^0 \pi_\beta + \pi_\alpha \mu_{\alpha\beta}^0 | \phi''_{\text{vib}} \rangle = \sum_{\alpha\beta} \langle \phi'_{\text{vib}} | \mu_{\alpha\beta}^0 \pi_\beta | \phi''_{\text{vib}} \rangle, \quad (2.71)$$

by swapping and renaming the α and β sums in the second term and utilizing the symmetry of $\mu_{\alpha\beta}^0$. In the following, the summation over α, β gives no further insights and is therefore not explicitly given. Applying Eq. (2.9) gives

$$-i \sum_{kl} \zeta_{kl}^\alpha \mu_{\alpha\beta}^0 \langle \phi'_{\text{vib}} | q_l \partial_{q_k} | \phi''_{\text{vib}} \rangle. \quad (2.72)$$

Using the definition of the vibrational part of the RVCi basis functions Eq. (2.19) yields

$$-i \sum_{kl} \zeta_{kl}^\alpha \mu_{\alpha\beta}^0 \sum_{I,J} c_I^{\tilde{I}} c_J^{\tilde{J}} \left\langle \prod_a \varphi_a^{n_a^I} \left| q_l \partial_{q_k} \right| \prod_a \varphi_a^{n_a^J} \right\rangle \quad (2.73)$$

with VCI coefficients $c_I^{\tilde{I}}$ and $c_J^{\tilde{J}}$. Since ζ_{kl}^α vanishes when $k = l$, the two normal coordinates l and k are unequal and therefore the integral can be split

$$\left\langle \prod_a \varphi_a^{n_a^I} \left| q_l \partial_{q_k} \right| \prod_a \varphi_a^{n_a^J} \right\rangle = \left\langle \varphi_l^{n_l^I} \left| q_l \right| \varphi_l^{n_l^J} \right\rangle \left\langle \varphi_k^{n_k^I} \left| \partial_{q_k} \right| \varphi_k^{n_k^J} \right\rangle \prod_{a \neq \{k,l\}} S_a^{IJ} \quad (2.74)$$

with $S_a^{IJ} := \left\langle \varphi_a^{n_a^I} \left| \varphi_a^{n_a^J} \right\rangle$

It is helpful to define

$$\Delta_{k,g}^{n_k^I n_k^J} := \left\langle \varphi_k^{n_k^I} \left| q_k^g \partial_{q_k} \right| \varphi_k^{n_k^J} \right\rangle. \quad (2.75)$$

analogously to Neff in Ref. [107]. The two non-trivial integrals in Eq. (2.74) can be given this notation as

$$\left\langle \varphi_l^{n_l^I} \left| q_l \right| \varphi_l^{n_l^J} \right\rangle \left\langle \varphi_k^{n_k^I} \left| \partial_{q_k} \right| \varphi_k^{n_k^J} \right\rangle = X_{l1}^{n_l^I n_l^J} \Delta_{k0}^{n_k^I n_k^J} \quad (2.76)$$

For the 1D vibrational term in Eq. (2.68)

$$\frac{1}{2} \sum_{\alpha\beta} \left\langle \phi'_{\text{vib}} \left| \sum_r \mu_{\alpha\beta}(q_r) \pi_\beta + \sum_r \pi_\alpha \mu_{\alpha\beta}(q_r) \right| \phi''_{\text{vib}} \right\rangle \quad (2.77)$$

the $\mu_{\alpha\beta}(q_r) \pi_\beta$ part will be considered first and afterwards it will be checked which additional terms have to be added for $\pi_\alpha \mu_{\alpha\beta}(q_r)$.

Using Eq. (2.9) (2.19) again yields an integral of the form

$$\left\langle \prod_a \varphi_a^{n_a^I} \left| \mu_{\alpha\beta}(q_r) q_l \partial_{q_k} \right| \prod_a \varphi_a^{n_a^J} \right\rangle. \quad (2.78)$$

To separate this integral in different normal coordinates, a case analysis for the different labels r, l, k is required. There are five different cases to be considered:

1. $r = l = k$, vanishes since $\zeta_{kk}^\alpha = 0$

2. $r = l \neq k$, yields:

$$\left\langle \varphi_r^{n_r^I} \left| \mu_{\alpha\beta}(q_r) q_r \right| \varphi_r^{n_r^J} \right\rangle \left\langle \varphi_k^{n_k^I} \left| \partial_{q_k} \right| \varphi_k^{n_k^J} \right\rangle = \sum_{a=1}^{N_{\text{Poly}}} p_{a,\alpha\beta}^{(r)} X_{r,(a+2)}^{n_r^I n_r^J} \Delta_{k,0}^{n_k^I n_k^J} \quad (2.79)$$

3. $r \neq l = k$, vanishes since $\zeta_{kk}^\alpha = 0$

4. $r \neq l \neq k = n$, yields:

$$\left\langle \varphi_r^{n_r^I} \left| \mu_{\alpha\beta}(q_r) \partial_{q_r} \right| \varphi_r^{n_r^J} \right\rangle \left\langle \varphi_k^{n_k^I} \left| q_k \right| \varphi_k^{n_k^J} \right\rangle = \left(-2 \sum_{a=1}^{N_{\text{Poly}}} p_{a,\alpha\beta}^{(r)} \Delta_{r,a}^{n_r^I n_r^J} \right) X_{k,1}^{n_k^I n_k^J} \quad (2.80)$$

5. $r \neq l \neq k \neq n$, yields:

$$\left\langle \varphi_r^{n_r^I} \left| \mu_{\alpha\beta}(q_r) \right| \varphi_r^{n_r^J} \right\rangle \left\langle \varphi_l^{n_l^I} \left| q_l \right| \varphi_l^{n_l^J} \right\rangle \left\langle \varphi_k^{n_k^I} \left| \partial_{q_k} \right| \varphi_k^{n_k^J} \right\rangle$$

$$= \left(\sum_{a=1}^{N_{\text{poly}}} p_{a,\alpha\beta}^{(r)} X_{r,a}^{n_r^I n_r^J} \right) X_{l,1}^{n_l^I n_l^J} \Delta_{k,0}^{n_k^I n_k^J} \quad (2.81)$$

Determining the analytical expressions in terms of Neff's notation requires a rather lengthy, but straightforward derivation, especially later for the 2D terms.

Considering the commutated terms in Eq. (2.68) gives the same result for the 2nd case (since $[\mu_{\alpha\beta}(q_r), q_r \partial_{q_k}] = 0$ for $r \neq k$) and for the 5th case (since $[\mu_{\alpha\beta}(q_r), q_l \partial_{q_k}] = 0$ for r, l, k pairwise distinct). However, the integral in the 4th case can be expressed by its non-commutated integral plus an additional term:

$$\left\langle \varphi_r^{n_r^I} \left| \partial_{q_r} \mu_{\alpha\beta}(q_r) \right| \varphi_r^{n_r^J} \right\rangle = \sum_a p_{a,\alpha\beta}^{(r)} a q_r^{(a-1)} + \left\langle \varphi_r^{n_r^I} \left| \mu_{\alpha\beta}(q_r) \partial_{q_r} \right| \varphi_r^{n_r^J} \right\rangle \quad (2.82)$$

Similarly to the 1D terms in Eq. (2.78), the 2D terms can be expressed as

$$\left\langle \prod_a \varphi_a^{n_a^I} \left| \mu_{\alpha\beta}(q_r, q_t) q_l \partial_{q_k} \right| \prod_a \varphi_a^{n_a^J} \right\rangle \quad (2.83)$$

resulting in another case analysis. The modes r and t cannot be equal, since this would correspond to the 1D μ -tensor. Moreover, l and k cannot be equal, due to $\zeta_{kk}^\alpha = 0$. There are 7 cases left to distinguish:

1. r, t, l, k all pairwise distinct:

$$\begin{aligned} & \left\langle \varphi_r^{n_r^I} \varphi_t^{n_t^I} \left| \mu_{\alpha\beta}(q_r, q_t) \right| \varphi_r^{n_r^J} \varphi_t^{n_t^J} \right\rangle \left\langle \varphi_l^{n_l^I} \left| q_l \right| \varphi_l^{n_l^J} \right\rangle \left\langle \varphi_k^{n_k^I} \left| \partial_{q_k} \right| \varphi_k^{n_k^J} \right\rangle \\ &= \left(\sum_{a,b} p_{ab,\alpha\beta}^{(r,t)} X_{r,a}^{n_r^I n_r^J} X_{t,b}^{n_t^I n_t^J} \right) X_{l,1}^{n_l^I n_l^J} \Delta_{k,0}^{n_k^I n_k^J} \end{aligned} \quad (2.84)$$

2. $r = l$ (rest pairwise distinct):

$$\begin{aligned} & \left\langle \varphi_r^{n_r^I} \varphi_t^{n_t^I} \left| \mu_{\alpha\beta}(q_r, q_t) q_r \right| \varphi_r^{n_r^J} \varphi_t^{n_t^J} \right\rangle \left\langle \varphi_k^{n_k^I} \left| \partial_{q_k} \right| \varphi_k^{n_k^J} \right\rangle \\ &= \left(\sum_{a,b} p_{ab,\alpha\beta}^{(r,t)} X_{r,(a+1)}^{n_r^I n_r^J} X_{t,b}^{n_t^I n_t^J} \right) \Delta_{k,0}^{n_k^I n_k^J} \end{aligned} \quad (2.85)$$

3. $t = l$ (rest pairwise distinct): Corresponds to the previous case by swapping r and t .

4. $r = k$ (rest pairwise distinct):

$$\begin{aligned} & \left\langle \varphi_r^{n_r^I} \varphi_t^{n_t^I} \left| \mu_{\alpha\beta}(q_r, q_t) \partial_{q_r} \right| \varphi_r^{n_r^J} \varphi_t^{n_t^J} \right\rangle \left\langle \varphi_l^{n_l^I} \left| q_l \right| \varphi_l^{n_l^J} \right\rangle \\ &= \left(-2 \sum_{a,b} p_{ab,\alpha\beta}^{(r,t)} \Delta_{r,a}^{n_r^I n_r^J} X_{t,b}^{n_t^I n_t^J} \right) X_{l,1}^{n_l^I n_l^J} \end{aligned} \quad (2.86)$$

5. $t = k$ (rest pairwise distinct): Corresponds to the previous case by swapping r and t .

6. $r = l, t = k$:

$$\left\langle \varphi_r^{n_r^I} \varphi_t^{n_t^I} \left| \mu_{\alpha\beta}(q_r, q_t) q_r \partial_{q_t} \right| \varphi_r^{n_r^J} \varphi_t^{n_t^J} \right\rangle = -2 \sum_{a,b} p_{ab,\alpha\beta}^{(r,t)} X_{r,(a+1)}^{n_r^I n_r^J} \Delta_{t,b}^{n_t^I n_t^J} \quad (2.87)$$

7. $r = k, t = l$: Corresponds to the previous case by swapping r and t .

For the discussion about the commutated term, there is no need to consider the 3rd, 5th or 7th case, because they can be reduced to other cases by switching the two coordinates of the 2D μ -tensor. The cases 1 and 2 commute, as either all considered normal coordinates are different, or it can be used that the q_r operator commutes with $\mu(q_r, q_t)$.

However, the integral in the 4th case

$$\begin{aligned} & \left\langle \varphi_r^{n_r^I} \varphi_t^{n_t^I} \left| \partial_{q_r} \mu_{\alpha\beta}(q_r, q_t) \right| \varphi_r^{n_r^J} \varphi_t^{n_t^J} \right\rangle \\ &= \sum_{a,b} p_{ab,\alpha\beta}^{(r,t)} a q_r^{(a-1)} q_t^b + \left\langle \varphi_r^{n_r^I} \varphi_t^{n_t^I} \left| \mu_{\alpha\beta}(q_r, q_t) \partial_{q_r} \right| \varphi_r^{n_r^J} \varphi_t^{n_t^J} \right\rangle \end{aligned} \quad (2.88)$$

and in the 6th case gives

$$\begin{aligned} & \left\langle \varphi_r^{n_r^I} \varphi_t^{n_t^I} \left| q_r \partial_{q_t} \mu_{\alpha\beta}(q_r, q_t) \right| \varphi_r^{n_r^J} \varphi_t^{n_t^J} \right\rangle \\ &= \sum_{a,b} p_{ab,\alpha\beta}^{(r,t)} q_r^{a+1} b q_r^{b-1} X_{k,1}^{n_k^I n_k^J} + \left\langle \varphi_r^{n_r^I} \varphi_t^{n_t^I} \left| \mu_{\alpha\beta}(q_r, q_t) q_r \partial_{q_t} \right| \varphi_r^{n_r^J} \varphi_t^{n_t^J} \right\rangle. \end{aligned} \quad (2.89)$$

ROTATIONAL INTEGRAL

In comparison to the rotational term, the rotational integral in the Coriolis coupling term is much simpler. Since there is never a product of angular momentum operators, there are only

three cases to consider

$$\langle J, k | J_z | J, k \rangle = k \quad (2.90)$$

$$\langle J, k \pm 1 | J_x | J, k \rangle = \pm i \langle J, k \pm 1 | J_x | J, k \rangle \quad (2.91)$$

$$= \frac{1}{2} \sqrt{J(J+1) - k(k \pm 1)} \quad (2.92)$$

The resulting integrals of Eq. (2.68) are

$$\langle J, k | \mathcal{H}_{\text{rot}} | J, k \rangle = \frac{1}{2} \langle J, k | J_z \sum_{\beta} \mu_{z\beta} \pi_{\beta} | J, k \rangle = \frac{1}{2} k \sum_{\beta} \mu_{z\beta} \pi_{\beta} \quad (2.93)$$

for $k' = k''$ and for $k' = k'' \pm 1$

$$\langle J, k \pm 1 | \mathcal{H}_{\text{rot}} | J, k \rangle = \frac{1}{2} \langle J, k \pm 1 | J_x \sum_{\beta} \mu_{x\beta} \pi_{\beta} + J_y \sum_{\beta} \mu_{y\beta} \pi_{\beta} | J, k \rangle \quad (2.94)$$

$$= \frac{1}{4} \sqrt{J(J+1) - k(k \pm 1)} \sum_{\beta} (\mu_{x\beta} \pm i \mu_{y\beta}) \pi_{\beta}. \quad (2.95)$$

2.1.4 RVC IMPLEMENTATION

Combining all the information from the previous sections, it is possible to give an explicit expression for the Watson Hamiltonian matrix elements. However, it is a very long equation that does not provide any new insights. Moreover, there is no single place in the program code, where this equation can be found, since the two types of vibrational integrals are precalculated separately.

Instead, the structure of the RVC matrix can be understood by considering the following representation:

$$\mathcal{H}_{\text{Watson}} = \underbrace{\frac{1}{2} \sum_{\alpha\beta} J_{\alpha} \mu_{\alpha\beta} J_{\beta}}_{\text{RCI/RVC}} + \underbrace{\frac{1}{2} \sum_{\alpha\beta} (J_{\alpha} \mu_{\alpha\beta} \pi_{\beta} + \pi_{\alpha} \mu_{\alpha\beta} J_{\beta})}_{\text{RVC}} + \underbrace{\mathcal{H}_{\text{vib}}}_{\text{VCI}}$$

$$\begin{array}{cc}
 \text{1st vib. state} & \text{2nd vib. state} \\
 \left(\begin{array}{c} \left(\begin{array}{ccc} \mathcal{H}_{\text{vib}}^{00} + \mathcal{H}_{\text{rot}}^{00} & \mathcal{H}_{\text{rot}}^{01} & \dots \\ \mathcal{H}_{\text{rot}}^{10} & \mathcal{H}_{\text{vib}}^{00} + \mathcal{H}_{\text{rot}}^{11} & \\ \vdots & & \ddots \end{array} \right) & \left(\begin{array}{ccc} \mathcal{H}_{\text{cc}}^{00,10} + \mathcal{H}_{\text{rot}}^{00} & \mathcal{H}_{\text{cc}}^{00,11} + \mathcal{H}_{\text{rot}}^{01} & \dots \\ \mathcal{H}_{\text{cc}}^{01,10} + \mathcal{H}_{\text{rot}}^{10} & \mathcal{H}_{\text{cc}}^{01,11} + \mathcal{H}_{\text{rot}}^{11} & \\ \vdots & & \ddots \end{array} \right) & \dots \\ \left(\begin{array}{ccc} \mathcal{H}_{\text{cc}}^{10,00} + \mathcal{H}_{\text{rot}}^{00} & \mathcal{H}_{\text{cc}}^{10,01} + \mathcal{H}_{\text{rot}}^{01} & \dots \\ \mathcal{H}_{\text{cc}}^{11,00} + \mathcal{H}_{\text{rot}}^{10} & \mathcal{H}_{\text{cc}}^{11,01} + \mathcal{H}_{\text{rot}}^{11} & \\ \vdots & & \ddots \end{array} \right) & \left(\begin{array}{ccc} \mathcal{H}_{\text{vib}}^{11} + \mathcal{H}_{\text{rot}}^{00} & \mathcal{H}_{\text{rot}}^{01} & \dots \\ \mathcal{H}_{\text{rot}}^{10} & \mathcal{H}_{\text{vib}}^{11} + \mathcal{H}_{\text{rot}}^{11} & \\ \vdots & & \ddots \end{array} \right) \\ \vdots & & \ddots
 \end{array} \right)
 \end{array}$$

The outer block structure of the RVC matrix is given by the vibrational basis functions and the inner structure is defined by the rotational basis functions. The vibrational terms only appear on the main diagonal. The Coriolis coupling terms contribute only for different vibrational modes and only if $\Delta k \in \{0, \pm 1, \pm 2\}$. Finally, the rotational terms are not restricted by the vibrational basis, but they contribute only if $\Delta k \in \{0, \pm 1\}$. Thus, for larger J the matrix is very sparse.

QUANTUM NUMBER ASSIGNMENT

After diagonalizing the RVC matrix, assigning the quantum numbers is an important task. J is a good quantum number and easy to assign because the block-diagonal structure in J of the RVC matrix is used. Therefore, each matrix contains only eigenstates for a particular J . The quantum number k denoting the z component of the angular momentum and the vibrational quantum number ν are not good quantum numbers. However, if the coupling is moderate, these quantum numbers can be assigned approximately, which gives insight into understanding the spectrum.

The rovibrational irrep of the eigenstate can be trivially assigned, if the block diagonal structure in the irrep is used. Since this was not done in the course of this thesis for several reasons, the assignment of the irrep was an issue. The importance of this assignment arises from the closely related NSSWs. At first, the rovibrational irrep was assigned by separately assigning the k and ν quantum number of the eigenstate. This yields the rotational and vibrational irrep, that can be combined using group theory to obtain the rovibrational irrep. This detour based on two non-good quantum numbers was later revised by using the k and ν quantum numbers of the basis functions instead of the resulting wave function, since these are good quantum numbers. This yields the rovibrational irrep of each basis function. Using the eigenvector coefficients gives one irrep that dominates the eigenvector, which is then assigned as the rovibrational irrep of that state.

As mentioned before, although k and ν are not good quantum numbers, they can provide considerable insights in moderately coupled regions of the spectrum. For this reason, two different methods for their assignment are implemented. The first method considers only the

leading coefficient of the eigenvector and assigns the same quantum numbers to the eigenstate as to the corresponding basis function. The second method is related to the *partial trace* as it is known, for example, from quantum information theory. For two finite dimensional Hilbert spaces V (for the vibrational subspace) and R (for the rotational subspace) of size N_{vib} and N_{rot} resulting in a product space $V \otimes R$ the partial trace Tr_R over the rotational space corresponds to a mapping $V \otimes R \rightarrow V$, i.e. the rotational space is traced out. Using a matrix representation with matrix elements $a_{kl,ij}$ (k corresponds to the initial vibrational basis, l to the initial rotational basis, i to the final vibrational basis, j to the final rotational basis) it can be written as

$$b_{k,i} = \sum_j^{N_{\text{rot}}} a_{kj,ij}. \quad (2.96)$$

This method is adapted for the eigenvectors. The summation of the eigenvector over the rotational subspace returns the vibrational quantum number and the summation over the vibrational subspace returns the rotational quantum number. This significantly increases the stability of the assignment compared to the leading coefficients, since it does not only rely on a single coefficient.

ASYMMETRIC TOP QUANTUM NUMBERS

Molecules can be classified depending on their moment of inertia tensor I_α in five groups:

1. Linear molecules: $I_a \ll I_b = I_c$
2. Spherical top molecules $I_a = I_b = I_c$
3. Symmetric top molecules
 - (a) Prolate symmetric top molecules $I_a = I_b < I_c$
 - (b) Oblate symmetric top molecules $I_a < I_b = I_c$
4. Asymmetric top molecules $I_a < I_b < I_c$

The axes a, b, c are molecule fixed and defined by the moment of inertia tensor, with a denoting the axis with the smallest moment of inertia and c denoting the axis with the largest moment of inertia. This definition is particularly meaningful for asymmetric top molecules.

For asymmetric top molecules, the quantum number $k \in \{-J, \dots, 0, \dots, +J\}$ is usually replaced by the two quantum numbers $k_a, k_c \in \{0, \dots, +J\}$. This is due to the fact that asymmetric top molecules can often be described as near-prolate ($I_a \approx I_b < I_c$) or near-oblate ($I_a < I_b \approx I_c$). It should be noted that all four molecules investigated in the course of this thesis are near-prolate molecules. The names can be explained in the following way: The k_a

quantum number can be understood as the z component of the angular momentum, if the (molecule fixed) a axis would correspond to the (space fixed) z axis. If the c axis is oriented in a way that it corresponds to the z axis, than k_c denotes the z component of the total angular momentum. However, the main use of these quantum number are the simpler assignment of the rovibrational irrep, as is discussed in Ref. [58] and in the masters thesis of Schneider[110]. Examples for the conversion between quantum numbers k and k_a, k_c are given in Tab. 2.1.

Table 2.1: Transformation between the quantum numbers k and two asymmetric top quantum numbers k_a and k_c

J	k	k_a	k_c
0	0	0	0
1	-1	0	1
1	0	1	1
1	1	1	0
2	-2	0	2
2	-1	1	2
2	0	1	1
2	1	2	1
2	2	2	0

MOLECULE SPECIFIC ROTATIONAL BASIS

In the course of this thesis a new rotational basis was invented to improve the quantum number assignment of k_a and k_c . This basis is called MSRB and can be expressed as a linear combination of an arbitrary rotational basis function, e.g. the RRB or WB. The linear coefficients are obtained as eigenvectors of an RCI calculation for the ground state. This results in the rotational basis functions

$$|\Phi_{J,r'}^{\text{RCI}}\rangle = \sum_k c_k^{J,r'} |J, k\rangle \quad (2.97)$$

and yields the overall RVCi wave function

$$|\Psi_{J,r,v}^{\text{MSRB}}\rangle = \sum_{r',v'} c_{r',v'}^{J,r,v} \sum_k c_k^{J,r'} |J, k\rangle |\Phi_{v'}^{\text{VCI}}\rangle. \quad (2.98)$$

The calculation of the MSRB coefficients is very efficient, since the RCI matrix construction and diagonalization is not time consuming. In contrast the additional summation needs to be considered in the intensity calculation. However, this problem can be solved by contracting the MSRB coefficients with the RVCi coefficients. The effects of this contraction on the computational time is studied in Subsec. 3.4.3.

2.2 INFRARED INTENSITIES

For a rovibrational IR spectrum intensities are the second quantity that needs to be calculated besides the frequencies. In the following, only electric dipole transitions are derived. Hence, neither magnetic dipole transitions nor electric quadruple transitions will be discussed. Moreover, the discussed selection rules are also only true for electric dipole transitions. However, in the next section Raman transitions will also be derived.

The subsequent derivation is based on [58], who gives a more detailed introduction in this topic. However, the vibrational integrals are not simplified in this literature, since this cannot be done *without loss of generality*. By using the information about multi-mode expansion, VSCF modals and VCI wave functions, these integrals can be derived specifically for the approach in this thesis.

The starting point is the following expression derived by an integral over the absorption coefficient for all transitions:

$$I_{\text{if}} = \frac{2\pi^2}{3} \frac{N_A}{\epsilon_0 h c} \tilde{Q}(T) \nu_{\text{if}} S_{\text{if}}, \quad \text{with } \tilde{Q}(T) = \frac{\exp(-E''/k_B T) [1 - \exp(-hc\nu_{\text{if}}/k_B T)]}{Q} \quad (2.99)$$

It consists of the Avogadro constant N_A , the Boltzmann constant k_B , the vacuum speed of light c , the permittivity of vacuum, the wave number of the transition $\nu_{\text{if}} = (E' - E'')/hc$, the thermal occupation factor $\tilde{Q}(T)$ and the partition function

$$Q = \sum_w g_w \exp\{-E_w/k_B T\}. \quad (2.100)$$

The summation over the different transitions occurs in the line strength

$$S_{\text{if}} = \sum_{\Phi'_{\text{int}}, \Phi''_{\text{int}}} \sum_{A=X,Y,Z} |\langle \Phi'_{\text{int}} | \mu_A | \Phi''_{\text{int}} \rangle|^2 = \sum_{\Phi'_{\text{int}}, \Phi''_{\text{int}}} \sum_{A=\xi,\eta,\zeta} |\langle \Phi'_{\text{int}} | \mu_A | \Phi''_{\text{int}} \rangle|^2, \quad (2.101)$$

with internal wave functions Φ_{int} combining the electronic, vibrational, rotational and nuclear spin contribution of the initial and final state. μ_A denotes the dipole moment operator and the second equations describes the transition from space fixed coordinates X, Y, Z to molecule fixed coordinates ξ, η, ζ . Moreover, a transformation between spherical and Cartesian components is required. Both steps together can be expressed by

$$\mu_s^{(1,\pm 1)} = [\mp \mu_\xi + i\mu_\eta]/\sqrt{2} \quad (2.102)$$

$$\mu_s^{(1,0)} = \mu_\zeta. \quad (2.103)$$

The superscript has the general form (ω, σ) , with ω denoting the order of the transition operator (e.g., 1 for electric dipole transitions and 2 for Raman transitions) and $|\sigma| < \omega$ as explained in Section 2.1. This transformation can also be expressed in terms of Euler angles ϕ, θ, χ using the rotational matrix elements $D_{\sigma\sigma'}^{(1)}(\phi, \theta, \chi)$ as described in Ref. [59] by

$$\mu_s^{(1,\sigma)} = \sum_{\sigma'=-1}^1 [D_{\sigma\sigma'}^{(1)}(\phi, \theta, \chi)]^* \mu_m^{(1,\sigma')} \quad (2.104)$$

The approximation that the wave functions are separable in terms of their electronic, vibrational, rotational, and nuclear spin contributions can be used to separate the line strength

$$S_{if} = \sum_{\Phi'_{\text{int}}, \Phi''_{\text{int}}} \sum_{\sigma=-1}^1 |\langle \Phi'_{\text{int}} | \mu_s^{(1,\sigma)} | \Phi''_{\text{int}} \rangle|^2 \quad (2.105)$$

in terms of a rotational integral

$$\langle \Phi'_{\text{rot}} | D_{\sigma\sigma'}^{(1)*} | \Phi''_{\text{rot}} \rangle = \sum_{k'=-J'}^{J'} \sum_{k''=-J''}^{J''} c_{k'}^{(J')*} c_{k''}^{(J'')} \langle J', k', m' | D_{\sigma\sigma'}^{(1)*} | J'', k'', m'' \rangle, \quad (2.106)$$

which yields for rigid rotor basis functions $|J'', k'', m''\rangle$ the term

$$\langle J', k', m' | D_{\sigma\sigma'}^{(1)*} | J'', k'', m'' \rangle = (-1)^{k'+m'} \sqrt{(2J''+1)(2J'+1)} \begin{pmatrix} J'' & 1 & J' \\ k'' & \sigma & -k' \end{pmatrix} \begin{pmatrix} J'' & 1 & J' \\ m'' & \sigma & -m' \end{pmatrix}. \quad (2.107)$$

This describes a special case of the Wigner-Eckart theorem, as described by Ref. [59], using the Wigner 3J-Symbols. The Wigner 3J-Symbols are defined via the Clebsch-Gordan coefficients. The latter are used to describe a set of coupled angular momentum operators. Let, $J = J_1 + J_2$ denote the total angular momentum of two coupled angular momenta J_1, J_2 , with the uncoupled representation

$$|J_1 k_1\rangle |J_2 k_2\rangle = |J_1 k_1, J_2 k_2\rangle \quad (2.108)$$

and the coupled representation

$$|J_1 J_2 J k\rangle. \quad (2.109)$$

Then the Clebsch-Gordan coefficients are defined as the corresponding transformation coefficients

$$|Jk\rangle = \sum_{k_1, k_2} C(J_1 J_2 J; k_1 k_2 k) |J_1 k_1, J_2 k_2\rangle \quad (2.110)$$

$$|J_1 k_1, J_2 k_2\rangle = \sum_{J, k} C(J_1 J_2 J; k_1 k_2 k) |Jk\rangle. \quad (2.111)$$

The Wigner 3J-Symbols are defined as

$$\begin{pmatrix} J_1 & J_2 & J_3 \\ k_1 & k_2 & k_3 \end{pmatrix} := (-1)^{J_1 - J_2 - k_3} \frac{1}{\sqrt{2J_3 - 1}} \langle J_1 k_1, J_2 k_2 | J_3 - k_3 \rangle. \quad (2.112)$$

This representation is very helpful to identify vanishing integrals or to transform integrals via permutation.

The vibrational integral

$$\langle \Phi'_{\text{vib}} | \mu_m^{(1, \sigma')} | \Phi''_{\text{vib}} \rangle \quad (2.113)$$

cannot be simplified without further assumptions. For the rovibrational part of the integral, this yields

$$\begin{aligned} \langle \Phi'_{\text{rovib}} | \mu_s^{(1, \sigma)} | \Phi''_{\text{rovib}} \rangle &= (-1)^{m'} \sqrt{(2J'' + 1)(2J' + 1)} \begin{pmatrix} J'' & 1 & J' \\ m'' & \sigma & -m' \end{pmatrix} \\ &\times \sum_{k' = -J'}^{J'} \sum_{k'' = -J''}^{J''} (-1)^{k'} c_{k'}^{(J')} c_{k''}^{(J'')} \sum_{\sigma' = -1}^1 \langle \Phi'_{\text{vib}} | \mu_m^{(1, \sigma')} | \Phi''_{\text{vib}} \rangle \begin{pmatrix} J'' & 1 & J' \\ k'' & \sigma' & -k' \end{pmatrix}. \end{aligned} \quad (2.114)$$

Assuming a completely separable wave function results in three types of degeneracies:

- The nuclear spin wave functions can be orthonormalized $\langle \Phi'_{\text{nspin}} | \Phi''_{\text{nspin}} \rangle = \delta_{\Phi'_{\text{nspin}}, \Phi''_{\text{nspin}}}$. Hence, the only non-vanishing contributions are for $\Phi'_{\text{nspin}} = \Phi''_{\text{nspin}}$ resulting in a nuclear spin statistical degeneracy factor g_{ns} . The latter can be determined as described in Ref. [58]. It was implemented by Schneider in his Master's thesis and will not be covered in the PhD thesis.
- Another degeneracy concerns the electronic state quantum number. However, since in this thesis only transitions within the electronic ground state are concerned, the corresponding degeneracy prefactor is equal to 1.
- As the molecular energy does not depend on the m' quantum number if neither electric nor magnetic fields are present, but the matrix element depends on m' via the Wigner 3J-symbols, this degeneracy is considered by

$$\sum_{\sigma = -\omega}^{\omega} \sum_{m' = -J'}^{J'} \sum_{m'' = -J''}^{J''} \left(\begin{pmatrix} J'' & 1 & J' \\ m'' & \sigma & -m' \end{pmatrix} \right)^2 = 1. \quad (2.115)$$

The resulting line strength (for transitions between the electronic ground state) is given by

$$S_{\text{if}} = g_{\text{ns}}(2J'' + 1)(2J' + 1) \left| \sum_{k'=-J'}^{J'} \sum_{k''=-J''}^{J''} (-1)^{k'} \times c_{k'}^{(J')*} c_{k''}^{(J'')} \sum_{\sigma'=-1}^1 \langle \Phi'_{\text{vib}} | \mu_m^{(1,\sigma')} | \Phi''_{\text{vib}} \rangle \begin{pmatrix} J'' & 1 & J' \\ k'' & \sigma' & -k' \end{pmatrix} \right|^2 \quad (2.116)$$

The multi-mode expansion of the DMS

$$\mu_\alpha := \mu_\alpha^0 + \sum_{k=1}^M \mu_\alpha(q_k) + \sum_{k=1}^M \sum_{l=1}^{k-1} \mu_\alpha(q_k, q_l) + \dots \quad (2.117)$$

is analogously to the multi-mode expansion for the PES and the inverse effective moment of inertia tensor μ in Eq. (2.12). (It should be noted, that it is an unfortunate coincidence in literature that there are two completely independent quantities are both denoted as μ , which is the dipole moment operator and the inverse effective moment of inertia.) Since integrals between VSCF and VCI wave functions and a multi-mode tensor has been discussed before (see Eq. (2.30)), only the results are presented:

$$\begin{aligned} \langle \Phi'_{\text{vib}} | \mu_m^{(1,\sigma')} | \Phi''_{\text{vib}} \rangle &= \mu_\alpha^0 \sum_{I,J} c_I^{\tilde{I}} c_J^{\tilde{J}} \prod_a S_a^{IJ} \\ &+ \sum_{k,I,J} c_I^{\tilde{I}} c_J^{\tilde{J}} \langle \varphi_k^{n_k^I} | \mu_\alpha(q_k) | \varphi_k^{n_k^J} \rangle \prod_{a \neq k} S_a^{IJ} \\ &+ \sum_{l < k, I, J} c_I^{\tilde{I}} c_J^{\tilde{J}} \langle \varphi_k^{n_k^I} \varphi_l^{n_l^I} | \mu_\alpha(q_k, q_l) | \varphi_k^{n_k^J} \varphi_l^{n_l^J} \rangle \prod_{a \neq \{k,l\}} S_a^{IJ} \end{aligned} \quad (2.118)$$

All variables are defined as in Subsec. 2.1.2. Using the polynomial coefficients for the DMS expansion, the equation yields an expression, that can be implemented. Note that this subsection showed the derivation for the simplest rotational basis, which is the rigid rotor basis. For the Wang-combinations there would be another summation over the two Wang coefficients. For the MSRB, there would be an additional summation over the MSRB coefficients. However, for the derivation, these coefficients can be *contracted* with the RVCIs coefficients $c_k^{(J)}$. In this case, the meaning of the $c_k^{(J)}$ coefficients in Eq. (2.116) changes, but the equations are identical. Moreover, it should be noted that this contraction is actually implemented in the code to save runtime (see Subsec. 3.4.3).

2.3 RAMAN INTENSITIES

The calculation of Raman intensities is also implemented in *MOLPRO*. The Raman effect is a two photon process with an additional virtual energy level, which is usually much higher than the initial and the final level. The theory will only be described very briefly, with a focus on the difference to IR intensities, since most of the work was already done for the RCI calculations and neither of the four publications of this thesis addresses Raman transitions.

Non-resonant Raman intensities can be determined by [111]

$$I \propto \frac{64\pi^4(\nu + \nu_{if})^4}{3c^3} \sum_{AB} |C_{if}|^2 \quad (2.119)$$

with the Raman scattering radiation frequency ν and the correlation coefficients

$$C_{if}^{AB} = \sum_j \left[\frac{\mu_{ij}^B \mu_{jf}^A}{hc(\nu_{ji} - \nu)} + \frac{\mu_{ij}^A \mu_{jf}^B}{hc(\nu_{jf} + \nu)} \right] \approx \langle \Phi'_{\text{rovib}} | \alpha_{AB} | \Phi''_{\text{rovib}} \rangle. \quad (2.120)$$

The second equation denotes the polarization approximation[58]. This approximation is valid if three conditions are fulfilled.

- The Born-Oppenheimer approximation is valid for the initial, the final and the virtual states.
- Both, the initial and final states of the transition belong to the electronic ground state.
- There must be a large energetic separation between the virtual state and both the initial and final states.

The transition moments of the electric dipole operator

$$\mu_{ij}^A = \langle \Phi_{\text{int}}^{(i)} | \mu_A | \Phi_{\text{int}}^{(j)} \rangle, \quad (2.121)$$

where i is the initial state, j is the virtual state, and f is the final state. Since the space-fixed coordinate axes are used, the variables for Cartesian coordinates are denoted A and B instead of α and β . The total internal wave functions

$$|\Phi_{\text{int}}\rangle = |\Phi_{\text{ns}}\rangle |\Phi_{\text{el}}\rangle |\Phi_{\text{rovib}}\rangle \quad (2.122)$$

are a product of the nuclear spin, electronic, and rovibrational wave functions.

Unlike the first-order DMS tensor, the polarizability tensor α is a second-order tensor. Since it is symmetric and has rank $\omega = 2$, there are six independent elements. Analogous to the IR

intensities, a transformation from space-fixed components to molecule-fixed components is used. First, a spherical representation of the polarizability tensor $\alpha_s^{(\omega,\sigma)}$ with $|\sigma| \leq \omega$ and $\sigma = k'' - k'$ is introduced (see Ref. [58] and Ref. [112])

$$\alpha_s^{(0,0)} = -\frac{1}{\sqrt{3}} [\alpha_{XX} + \alpha_{YY} + \alpha_{ZZ}], \quad (2.123a)$$

$$\alpha_s^{(2,0)} = \frac{1}{\sqrt{6}} [2\alpha_{ZZ} - \alpha_{XX} - \alpha_{YY}], \quad (2.123b)$$

$$\alpha_s^{(2,\pm 1)} = \frac{1}{2} [\mp(\alpha_{XZ} + \alpha_{ZX}) - i(\alpha_{YZ} + \alpha_{ZY})], \quad (2.123c)$$

$$\alpha_s^{(2,\pm 2)} = \frac{1}{2} [\alpha_{XX} - \alpha_{YY} \pm i(\alpha_{XY} + \alpha_{YX})]. \quad (2.123d)$$

Due to symmetry, all elements with $\omega = 1$ vanish [59]. This simplifies Eq. (2.119) to

$$R_\omega := \sum_{AB} |\langle \Phi'_{\text{int}} | \alpha_{AB} | \Phi''_{\text{int}} \rangle|^2 = \sum_{\bar{\sigma}=-\omega}^{\omega} \left| \langle \Phi'_{\text{int}} | \alpha_s^{(\omega,\bar{\sigma})} | \Phi''_{\text{int}} \rangle \right|^2. \quad (2.124)$$

Similar to the IR derivation, the Wigner rotational matrix elements $D_{\bar{\sigma}\sigma}^{(\omega)}(\Omega)$, with Euler angles $\Omega = \chi, \phi, \theta$ [59] can be used to obtain

$$\alpha_s^{(\omega,\bar{\sigma})} = \sum_{\sigma=-\omega}^{\omega} D_{\bar{\sigma}\sigma}^{(\omega)*}(\Omega) \alpha_m^{(\omega,\sigma)}. \quad (2.125)$$

In contrast to IR transitions, there is no $\omega = 1$ term for Raman transitions, but an isotropic Raman transition moment $D_{\bar{\sigma}\sigma}^{(0)}$ for $\omega = 0$ and anisotropic Raman scattering terms $D_{\bar{\sigma}\sigma}^{(2)}$ for $\omega = 2$. This makes the final transition moment dependent on the experimental setup [113].

Analogous to the IR derivation, it is assumed that there are no external electric and magnetic fields, which results in a degeneracy in the m quantum number. Moreover, the $|\Phi_{\text{ns}}\rangle$ wave functions yield the degeneracy factor for the nuclear spin statistical weight g_{ns} [58, 88]. This is described by a sum over degeneracy prefactors. As was derived in Ref. [114], it follows that

$$R_\omega = \sum_{\substack{\text{degenerate} \\ \text{states}}} \sum_{\bar{\sigma}=-\omega}^{\omega} \left| \sum_{\sigma=-\omega}^{\omega} \sum_{v''v'} \langle v' | \alpha_m^{(\omega,\sigma)} | v'' \rangle \sum_{r'r''} c'_{vr} c''_{vr} \langle r' | D_{\bar{\sigma}\sigma}^{(\omega)*}(\Omega) | r'' \rangle \right|^2. \quad (2.126)$$

As it was done for the IR calculations, the integrals are separated in a vibrational and rotational part. While the vibrational part is computed numerically, the rotational parts can be solved analytically [58].

By using rigid-rotor basis functions $|Jkm\rangle \hat{=} \sqrt{\frac{2J+1}{8\pi^2}} D_{mk}^{J*}$ it follows with the integrals of three Wigner D functions from [59]:

$$\begin{aligned} & \langle J'k'm' | D_{\bar{\sigma},\sigma}^{(\omega)*(\Omega)} | J''k''m'' \rangle \\ &= (-1)^{\bar{\sigma}-\sigma+m''+k''} \sqrt{(2J''+1)(2J'+1)} \begin{pmatrix} J'' & \omega & J' \\ m'' & \bar{\sigma} & -m' \end{pmatrix} \begin{pmatrix} J'' & \omega & J' \\ k'' & \sigma & -k' \end{pmatrix} \end{aligned} \quad (2.127)$$

The strict Raman selection rule follows from this equation, since the $3J$ -symbols vanishes if $|\Delta J| \leq \omega$. Hence, for the isotropic transition moment $\omega = 0$ the selection rule results in $J' = J''$, while for the anisotropic part it is less restrictive ($\Delta J \in \{0, \pm 1, \pm 2\}$). Eq. (2.127) also results in a selection rule for k and two selection rules for the parity. For a more detailed discussion see Ref. [58, 59, 113]. Evaluating Eq. (2.127) with the restrictions introduced by the vanishing Wigner $3J$ -symbols and $\omega = 0$ (and therefore also $\sigma = 0$) yields

$$\langle J'k'm' | D_{0,0}^{(0)*} | J''k''m'' \rangle = \delta_{J''J'} \delta_{m''m'} \delta_{k''k'}. \quad (2.128)$$

This gives for the isotropic transition moment

$$R_0 = g_{ns} \sum_{m'',m'} \left| \sum_{v'',v'} \langle v' | \alpha_m^{(0,0)} | v'' \rangle \sum_{k'',k'} c'_{kv} c''_{kv} \langle J'k'm' | D_{0,0}^{(0)*} | J''k''m'' \rangle \right|^2 \quad (2.129)$$

$$= \delta_{J''J'} g_{ns} (2J''+1) \left| \sum_{v'',v'} \langle v' | \alpha_m^{(0,0)} | v'' \rangle \sum_{k'',k'} c'_{kv} c''_{kv} \delta_{k''k'} \right|^2, \quad (2.130)$$

and for the anisotropic transition moment

$$R_2 = g_{ns} (2J''+1)(2J'+1) \left| \sum_{\sigma=-2}^2 \sum_{v'',v'} \langle v' | \alpha_m^{(2,\sigma)} | v'' \rangle \sum_{k'',k'} c'_{kv} c''_{kv} (-1)^{k'} \begin{pmatrix} J'' & 2 & J' \\ k'' & \sigma & -k' \end{pmatrix} \right|^2. \quad (2.131)$$

As mentioned above, the Raman intensities depend on the exact experimental setup. More specifically, it is influenced by the polarization of the probe radiation (linear, circular, or naturally polarized), the polarization of the detected radiation, the position of the detector, etc. In general, the resulting intensity can be described as a linear combination of R_0 and R_2 . This was elaborated in Ref. [113] and also discussed with respect to our implementation in Ref. [115]. However, without a specific application in this thesis, it is not meaningful to provide any experiment specific equations. To avoid as much experimental dependence as possible, the Ra-

man transition strengths are given in terms of differential absorption cross-sections

$$\frac{d\sigma}{d\Omega} = \left(\frac{\pi}{\epsilon_0}\right)^2 \frac{e^{-E''/k_B T}}{Q(T)} \Delta\nu^4 R \quad (2.132)$$

instead of intensities.

2.4 LINE BROADENING

The calculation of accurate line lists is very important for rovibrational infrared spectroscopy. However, the observed spectral lines are broadened by various effects that obscure the details of the underlying molecular motion. There are several types of line broadening that affect rovibrational infrared spectra, including natural linewidth (see Subsec. 2.4.1), pressure broadening (see Subsec. 2.4.3), Doppler broadening (see Subsec. 2.4.2), and Voigt broadening (see Subsec. 2.4.4). These different types of broadening arise from different physical mechanisms and have distinct effects on the observed spectra. Understanding the various types of line broadening is important for accurate interpretation of rovibrational infrared spectra.

2.4.1 NATURAL LINEWIDTH

The most fundamental type of line broadening is the natural linewidth, as it is inevitable and depends only on the life time of a state. It arises from the time-energy uncertainty relation

$$\Delta t \Delta E \geq \hbar/2. \quad (2.133)$$

ΔE denotes the linewidth in units of energy, but it can also be given in units of cm^{-1} , which is denoted by $\Delta\bar{\nu}$. Moreover, Δt describes the life time of a quantum mechanical state. Δt spans many orders of magnitude for different physical processes. For the three most interesting in the course of this thesis exemplary numbers are presented in the following [116–118]:

- Electronic excitations; $\bar{\nu} \approx 3 \times 10^4 \text{ cm}^{-1}$; $\Delta t \approx 1 \times 10^{-8} \text{ s}$; $\Delta\bar{\nu} \approx 5 \times 10^{-4} \text{ cm}^{-1}$
- Vibrational excitations; $\bar{\nu} \approx 1 \times 10^3 \text{ cm}^{-1}$; $\Delta t \approx 1 \times 10^{-3} \text{ s}$; $\Delta\bar{\nu} \approx 5 \times 10^{-9} \text{ cm}^{-1}$
- Rotational excitations; $\bar{\nu} \approx 1 \times 10^1 \text{ cm}^{-1}$; $\Delta t \approx 1 \times 10^3 \text{ s}$; $\Delta\bar{\nu} \approx 5 \times 10^{-15} \text{ cm}^{-1}$

Of course, these numbers are only a rough reference point, and the actual transition energies E and life times Δt can cover a wide range for all three types of transitions. However, the natural linewidth of vibrational and rotational transitions is much smaller than other types of broadening, even at low pressure and low temperature. For this reason, the natural linewidth will not be discussed in this thesis. As a final note, it should be mentioned that the natural

linewidth broadening profile corresponds to a Lorentz profile, as it is also used for pressure broadening. Thus, the algorithms implemented during this PhD allow for the simulation of spectra with natural linewidth.

2.4.2 DOPPLER BROADENING

Doppler broadening is an important factor in rovibrational spectroscopy, causing spectral lines to broaden due to temperature effects in a gas. The Doppler effect results from the relative motion between the molecule and the observer. It causes a shift in the frequency of the radiation emitted or absorbed by the molecule. The superposition of spectral lines from molecules with different velocities creates a statistical distribution that results in the broadening effect. The velocity profile of molecules with mass m in a gas at temperature T corresponds to a Maxwell-Boltzmann distribution. The standard deviation of the broadening is given by

$$\sigma_f = \frac{f_0}{c} \sqrt{\frac{k_B T}{m}}, \quad (2.134)$$

with the Boltzmann-constant k_B , the speed of light in vacuum c and the frequency of the transition f_0 without Doppler effect. Unlike the velocity, the line broadening profile for the Doppler effect is described by a Gaussian function, with a full width at half maximum (FWHM) of

$$\Delta f = 2\sqrt{2 \ln(2)} \sigma_f = \frac{f_0}{c} \sqrt{\frac{8 \ln(2) k_B T}{m}}. \quad (2.135)$$

By using

$$\frac{\Delta f}{f_0} = \frac{\Delta \bar{\nu}}{\bar{\nu}_0} \quad (2.136)$$

it follows

$$\Delta \bar{\nu}(T) = \frac{\bar{\nu}_0}{c} \sqrt{\frac{8 \ln(2) k_B T}{m}}. \quad (2.137)$$

Therefore, it is sufficient to know the temperature of the gas and the mass of the molecule to determine its Doppler broadening. An example for propynal (CHCCHO) at $T_1 = 10$ K and $T_2 = 300$ K is provided to give a sense for the magnitude of the broadening effect. Moreover, these values are later used in Section 3.3.

$$\begin{aligned} m_{\text{H}} &= 1 \text{ u}, & m_{\text{C}} &= 12 \text{ u}, & m_{\text{O}} &= 16 \text{ u} \\ \Rightarrow m &= 2m_{\text{H}} + 3m_{\text{C}} + 1m_{\text{O}} = 54 \text{ u} \\ T_1 &= 10 \text{ K}, & T_2 &= 300 \text{ K} \\ k_{\text{B}} &= 1.380\,649 \times 10^{-23} \text{ J/K} \end{aligned}$$

$$\begin{aligned}
c &= 2.997\,924\,58 \times 10^8 \text{ m/s} \\
\bar{\nu}_0 &= 300 \text{ cm}^{-1} \\
\Delta\bar{\nu}(T_1) &= 7.7 \times 10^{-6} \text{ cm}^{-1} \\
\Delta\bar{\nu}(T_2) &= 4.2 \times 10^{-5} \text{ cm}^{-1}
\end{aligned}$$

This shows that the temperature range covered in this thesis ($T_1 = 10$ to $T_2 = 300$ K) results in a Doppler width that spans less than one order of magnitude. This is in contrast to the pressure broadening discussed later. Note, that an exemplary transition at 300 cm^{-1} was assumed. The linear scaling in $\bar{\nu}_0$ allows for the calculation of a dimensionless relative width

$$\frac{\Delta f}{f_0} = \frac{\Delta\bar{\nu}}{\bar{\nu}_0} = \frac{1}{c} \sqrt{\frac{8 \ln(2) k_B T}{m}}, \quad (2.138)$$

which is independent of the specific line position.

It should also be noted that the limitations of the experimental setup also lead to a broadening effect. In many cases, a Gaussian profile is used to model this broadening. However, since the specific FWHM of this effect crucially depends on the setup itself, there is no general equation to determine the width. In contrast, experimentalists provide values for their specific setup.

2.4.3 PRESSURE BROADENING

Considering pressure broadening is significantly more challenging than considering Doppler broadening. The former results from collisions between molecules, which can shift the energy levels of the molecules and cause the spectral lines to broaden. Unlike Doppler broadening, which is well-described by a Gaussian profile, pressure broadening exhibits a more complex profile, including Lorentzian, Voigt, or related shapes, depending on the pressure and collision cross-sections of the molecules involved [119, 120]. Due to the complex interplay of molecular collisions, pressure broadening is much more difficult to model accurately, and precise measurements require careful consideration of the molecular properties and conditions of the sample. In this thesis pressure broadening is modeled only by a Lorentz profile and, in combination with temperature effects, by a Voigt profile.

The FWHM of the Lorentz profile is often referred to as γ , in contrast to the Gaussian profile, where σ is used. This usually describes dimensionless quantities, in contrast to the previously introduced $\Delta\bar{\nu}$, which describes the FWHM in units of wavenumbers. The width

of the Lorentz profile in wavelength λ can be written as

$$\Delta\lambda = \frac{\lambda^2 A}{\pi c} n \sqrt{\frac{2k_B T}{m}} \quad (2.139)$$

Its calculation requires knowledge of the scattering cross-section A and the particle number density n . Similar to the temperature broadening, it also depends on the mass of the molecule m and the temperature T . The particle number density n is defined by the number of particles N and the gas volume V as follows:

$$n := \frac{N}{V} = \frac{p}{k_B T} \quad (2.140)$$

The latter equation assumes an ideal gas with pressure p and Boltzmann constant k_B . Combining these equations yields

$$\Delta\lambda = \frac{\lambda^2 A}{\pi c} \frac{p}{k_B T} \sqrt{\frac{2k_B T}{m}} = \frac{\lambda^2 A p}{\pi c} \sqrt{\frac{2}{k_B T m}} \quad (2.141)$$

Replacing the transition wavelength λ through wavenumbers

$$\lambda = \frac{1}{\bar{\nu}} \quad (2.142)$$

allows for the last transformation in the following derivation:

$$\frac{\Delta\lambda}{\lambda} = \frac{\Delta\bar{\nu}}{\bar{\nu}} = \frac{A p}{\pi c} \sqrt{\frac{2}{k_B T m}} \lambda = \frac{A p}{\pi c} \sqrt{\frac{2}{k_B T m}} \frac{1}{\bar{\nu}} \quad (2.143)$$

Hence, the Lorentz width

$$\Delta\bar{\nu} = \frac{A p}{\pi c} \sqrt{\frac{2}{k_B T m}} \quad (2.144)$$

in units of wavenumbers is independent of the specific transition frequency. However, it requires information about the cross-sections A , which can be determined experimentally or theoretically. In principle, there are advanced methods to simulate scattering cross-sections of molecules. For several reasons, it was decided that a rough estimate of A would be sufficient:

1. The main result of this PhD is the calculation of accurate line list and bar plot spectra and not on broadened spectra.
2. All research groups interested in highly accurate spectras use line lists and then apply more sophisticated methods to account for line broadening (beyond Voigt profile methods).

3. However, it can be helpful to give a rough estimate of the visual appearance of the broadened spectra. The resulting spectra do not depend crucially on the exact width of the profiles.

In some of the publications of this PhD, the cross-section A was estimated by a geometric approximation of the molecule. Alternatively, a simpler and less accurate, but easily automated method can be used. Since it is not so much the exact value of A that matters, but rather the order of magnitude, the latter method is sufficient and will be demonstrated for the example of propynal (HCCCHO). Propynal consists of three elements for which the atomic radii can be found in Ref. [121]. There are several different ways to determine the radius of an atom (empirical, via calculations, via bond lengths of different interaction types). In the following example, the radii are approximated by a covalent single bond length, although not all bonds in propynal are single bonds. This yields

$$\begin{aligned} r_{\text{H}} &= 0.32 \text{ \AA} ; & r_{\text{C}} &= 0.70 \text{ \AA} ; & r_{\text{O}} &= 0.63 \text{ \AA} ; \\ A_{\text{H}} &= \pi r_{\text{H}}^2 = 0.32 \text{ \AA}^2 ; & A_{\text{C}} &= 1.54 \text{ \AA}^2 ; & A_{\text{O}} &= 1.25 \text{ \AA}^2 ; \\ A &\approx 2A_{\text{H}} + 3A_{\text{C}} + A_{\text{O}} = 6.51 \text{ \AA}^2 \end{aligned}$$

As each molecule is treated individually, the geometry of the molecule is not taken into account, which is a crude approximation. However it allows for a robust and automated calculation.

In the following, one value is given for interstellar conditions ($p_1 = 3 \times 10^{-13}$ Pa), low pressure laboratory conditions ($p_2 = 1$ Pa) and terrestrial conditions ($p_3 = 1 \times 10^5$ Pa). Using the same temperatures and values for the mass and physical constants yields

$$\begin{aligned} \Delta\bar{\nu}(p_1, T = 10 \text{ K}) &\approx 7.0 \times 10^{-21} \text{ cm}^{-1} \\ \Delta\bar{\nu}(p_2, T = 300 \text{ K}) &\approx 4.2 \times 10^{-9} \text{ cm}^{-1} \\ \Delta\bar{\nu}(p_3, T = 300 \text{ K}) &\approx 4.2 \times 10^{-4} \text{ cm}^{-1}. \end{aligned}$$

Hence, the pressure broadening in the ISM can be neglected, since it is many orders of magnitude larger than the natural linewidth. At normal terrestrial conditions (300 K and 1×10^5 Pa) the pressure broadening is larger than the temperature broadening. However, the difference is only one order of magnitude, and since the latter has a linear scaling in the frequency of the transition, there is a break-even point at large frequencies (about 3000 cm^{-1}). Again, it should be noted that these are rough estimates to demonstrate the computational approach, e.g. the ideal gas approximation is used and the scattering cross-section was determined with a very crude approximation.

2.4.4 VOIGT BROADENING

As discussed above, temperature effects can be considered using a Gaussian profile and pressure effects can be considered using a Lorentz profile. For a more accurate description, both effects should be considered together. This is possible by using a Voigt profile, which is obtained by a convolution of a Gaussian and a Lorentzian. The resulting convolution integral has no analytical result. However, there are many ways to either approximate or to determine the Voigt profile numerically, e.g. via the real part of the Faddeeva-function [122] or the pseudo-Voigt approximation. The FWHM of the Voigt profile can be approximated by the FWHM of the Gaussian function $\Delta\bar{\nu}_G$ and the FWHM of the Lorentzian $\Delta\bar{\nu}_L$ using

$$\Delta\bar{\nu}_V \approx \frac{\Delta\bar{\nu}_L}{2} + \sqrt{\frac{\Delta\bar{\nu}_L^2}{4} + \Delta\bar{\nu}_G^2} \quad (2.145)$$

In general the three different line shapes are very similar. The main differences are that a pure Gaussian profile is wider, the Lorentz profile is narrower and the Voigt profile is somewhere in between, depending on the ratio of $\Delta\bar{\nu}_L$ and $\Delta\bar{\nu}_G$. A more detailed discussion is provided in Section 3.3.

These three types of line broadening are implemented in *MOLPRO*. It should be mentioned, that the most recent implementation in *MOLPRO* in terms of the DAT₂GRAPH program was introduced by Erfort in a refactoring project. In contrast, the work and achievements in this thesis concern the implementation of the Lorentz profile, and an efficient evaluation of the Voigt profile, since it is very time consuming. Furthermore, it was necessary to implement a runtime optimization for the Voigt profile in terms of a discretization in the frequency axis and precalculating the Voigt profile. Furthermore, it falls within the scope of this thesis to perform an optimization to achieve the best possible broadening width values for a comparison with experiments.

3

Results

As this is a cumulative thesis, a large part of the results can already be found in the attached publications. Nevertheless, there are some results that could not be presented in the publications and that will be elaborated in the context of this thesis. Here, the four different publications are considered more as a rough reference point to present further work that was done during the PhD. Thus, for example, from a didactic point of view, it makes more sense to discuss the second publication first, since Ref. [2] is about the convergence of different series expansions for the RVCi theory. The publication mainly used various metrics to study the convergence *quantitatively*. In contrast, this thesis mainly shows *qualitative* differences in the spectra. Five different parameters are considered with respect to their convergence behavior. An incomplete convergence for the different parameters leads to very individual phenomena in the spectrum. This is useful for subsequent users to quickly see which parameters have not yet converged sufficiently.

After that, the content of the chronologically first publication Ref. [1] will be discussed and updated. This means that essentially the same spectral ranges are presented again, but with the most recent calculations. Since the original publication is already 3 years old, this is useful for two reasons. First, it shows the progress that has been made in the course of this PhD. On the other hand, some interpretations and assumptions about the limitations of the program at that time, can now be confirmed or disproved. The publication about propynal [3] is the only one that used line broadening. For this reason, this publication is taken as an opportunity to

present and compare the different forms of line broadening implemented. After that, a small selection of runtime optimizations are presented, based on Ref. [4] and calculations for the other molecules.

In this thesis four different molecules have been studied. Three of them have a high astro-physical relevance, either because they have been found in the ISM (ketenimine, propynal) or because a synthesis has recently been achieved which suggests that this molecule could exist in the envelope of an asymptotic giant branch (AGB) star (diazophosphane). The first two are also considered to be a complex organic molecules (COMs), which makes them particularly interesting from a biological point of view. Moreover, all these molecules are near-prolate asymmetric top molecules with point groups C_{2v} or C_s .

3.1 CONVERGENCE ANALYSIS

The second publication in the context of this thesis [2] discusses the convergence of different series expansions for RVC1 theory. As a benchmark molecule, H_2CS is used. It is a 4 atomic molecule with point group C_{2v} , that is a near-prolate asymmetric top ($\kappa = -0.993$) with two different NSSWs (1 and 3). (For more details see Ref. [2].) The paper mainly used different metrics to investigate the convergence behavior quantitatively. In contrast, this thesis mainly shows qualitative differences in the spectra. Five different parameters are considered in terms of their convergence behavior, with each of them showing a very individual phenomenon in the spectrum if not sufficiently converged. After that, the influence of the NSSWs on the spectrum of H_2CS will be discussed briefly.

Before discussing the first convergence parameter, a brief discussion about bands and *band heads* will be given for didactic reasons. In spectroscopy, there are many ways to classify different bands. One is by the number of *band heads*. There are *headless bands*, *single head bands* and *double head bands* [123]. However, the latter case is relatively rare, so the subsequent discussion focuses on the first two. The typical P- and R-branches of a two atomic homonuclear molecule with a gradually increasing and decreasing intensity on both sides of the band are a good example for a headless band. In contrast, there are many examples in the converged spectrum of H_2CS (e.g. the red band in the bottom of Fig. 3.1) where progressions only gradually decrease in intensity in one direction. For the other direction, a sudden end or an abrupt edge of the band is visible. This edge is called band head. A part of the reason for this effect can be understood by analyzing the quantum numbers of each transition of these bands. For example the aforementioned red progression consists of the lines (starting at the band head):

- $J'' = 5, k''_a = 5, k''_c = 0 \rightarrow J' = 6, k'_a = 6, k'_c = 0$
- $J'' = 6, k''_a = 5, k''_c = 1 \rightarrow J' = 7, k'_a = 6, k'_c = 1$

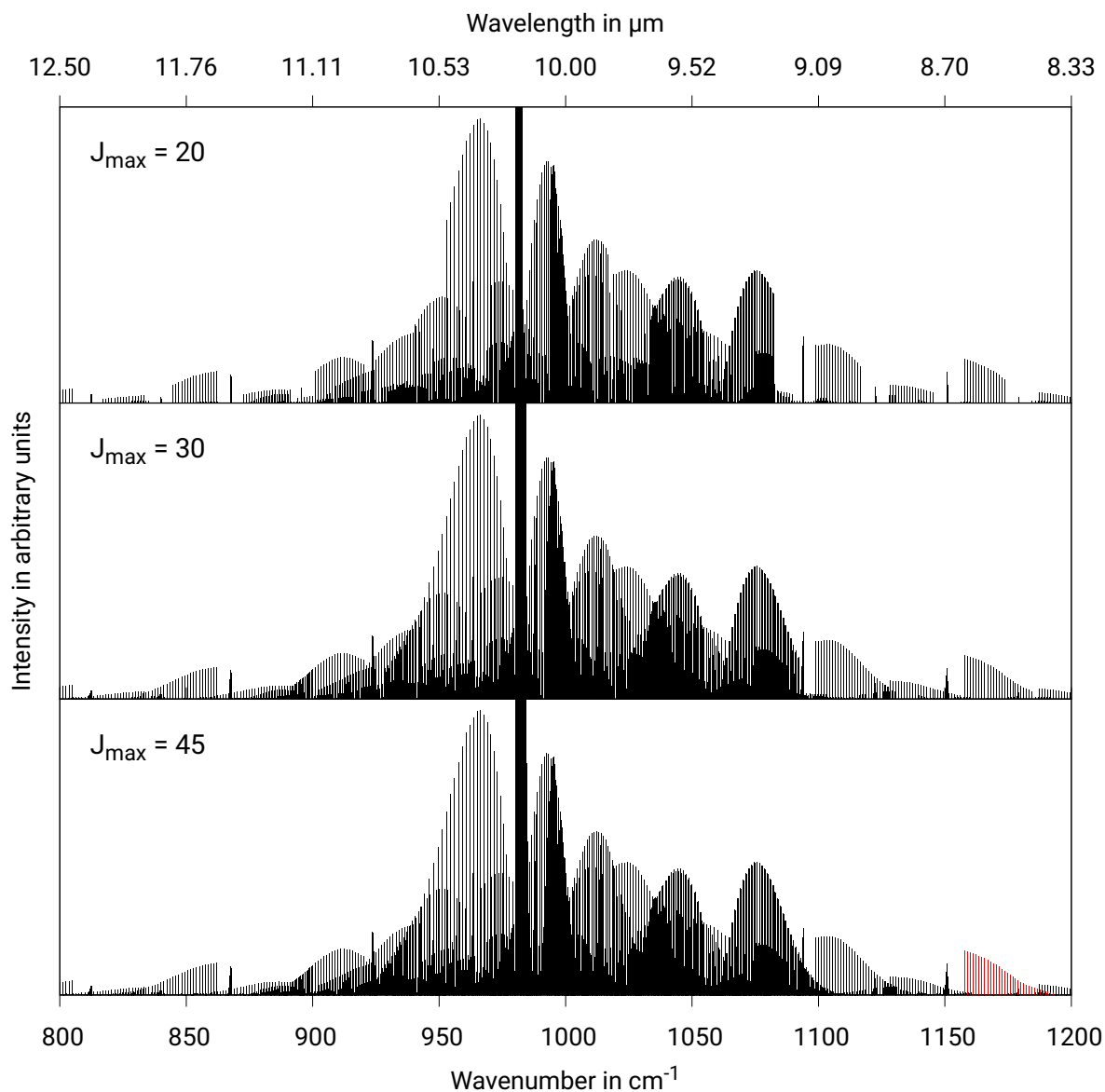


Figure 3.1: Influence of the convergence behavior of J_{\max} on the visual appearance of the rovibrational infrared spectrum. The example shows H_2CS in the strongly coupled region of the quasi degenerate vibrational modes ν_4 and ν_6 at 989.4 cm^{-1} and 989.5 cm^{-1} , respectively. In addition, there is another fundamental band ν_3 at 1060.2 cm^{-1} . The vibrational basis set includes up to second overtones and threefold combination bands up to 5000 cm^{-1} , the μ -tensor was considered up to 2nd order for the rotational terms and 1st order for Coriolis coupling terms and the VCI space was set to its current default value $\text{levex}=5$ $\text{citype}=5$ and $\text{cimax}=15$. The red progression used as an example to describe band heads. (See text.)

- $J'' = 7, k_a'' = 5, k_c'' = 2 \rightarrow J' = 8, k_a' = 6, k_c' = 2$
- $J'' = 8, k_a'' = 5, k_c'' = 3 \rightarrow J' = 9, k_a' = 6, k_c' = 3$
- $J'' = 9, k_a'' = 5, k_c'' = 4 \rightarrow J' = 10, k_a' = 6, k_c' = 4$
- ...

In this case the quantum number k_a is fixed (corresponding to the z -component for the near-prolate molecule H₂CS) and the quantum number k_c as well as the total angular momentum J increase for each line in the band. This also explains the reason for the band head, since there cannot be a line with $J'' = 4, k_a'' = 5, k_c'' = -1$, since the quantum number k_c cannot be negative.

3.1.1 TOTAL ANGULAR MOMENTUM

Within the publication [2], the convergence of the spectrum with respect to the total angular momentum number J was not discussed. This is due to the fact that an improper convergence is easy to detect, easy to solve, and an unacceptable approximation because of the large artifacts, shown in Fig. 3.1. The calculation obtained with $J_{\max} = 20$ shows an artificial second band head. Since this is always the case, it seems relatively easy to detect when J_{\max} is not converged. However, the following situations can make the convergence decision more involved:

- Strong bands can overlap the tail of weaker bands, as can be seen between 950 and 1050 cm⁻¹. This makes it difficult to spot the artifacts. In this case a color coding with respect to the quantum numbers ν, k_a or k_c can be very helpful.
- There are bands with increasing line density towards one direction, which is followed by a turnaround of the band. For example, the lines in an R-branch are expected to have an increasing frequency for increasing the quantum numbers k_a, k_c . However, for asymmetric top molecules, this progression can turnaround, as is for example discussed in Ref. [124] and in this thesis in Section 3.2. To distinguish these bands from J_{\max} artifacts, the calculations can be repeated with an increased J_{\max} . However, this can be very time consuming and therefore it is more advisable, to either reduce J_{\max} during plotting. This makes the artifacts worse if J_{\max} was not converged sufficiently and has no influence on turnaround progressions. Alternatively, all lines that involve a $J = J_{\max}$ can be plotted in red, to identify these transitions quickly.
- Last but not least, there are also bands in strongly coupled regions that rapidly decrease in intensity without a turnaround or an increase in line density. This can also be misinterpreted as an insufficient convergence of J_{\max} . The analysis can be done analogously to the previous case.

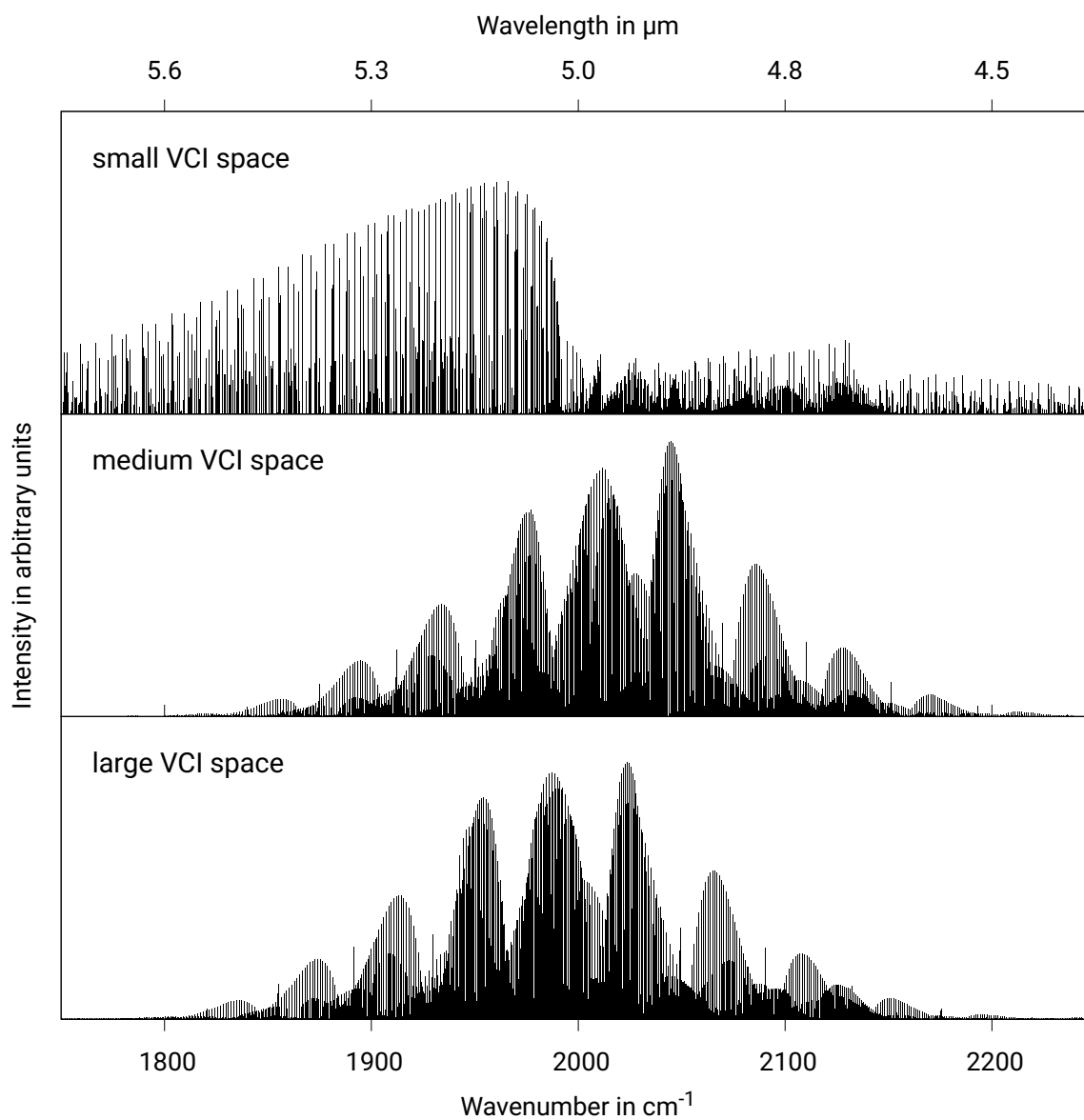


Figure 3.2: Influence of the convergence behavior of the VCI space on the visual appearance of the rovibrational infrared spectrum. The example shows H_2CS in the strongly coupled region of the three overtones and three combination bands of the vibrational modes ν_3 , ν_4 and ν_6 . The vibrational basis set includes up to second overtones and threefold combination bands up to 5000 cm^{-1} , the μ -tensor was considered up to 2nd order for the rotational terms and 1st order for Coriolis coupling terms and $J_{\text{max}} = 45$.

As mentioned before, the artifacts induced by a J_{\max} that was chosen to small are significant and are therefore not a suitable compromise to save computational time. Nevertheless, it should be noted that there are cases where a small number of bands have very slowly converging tails.

3.1.2 VCI SPACE

Another important parameter for the convergence of the rovibrational spectra is the configuration interaction space (CI space) of the VCI calculation. Since H_2CS is a fairly rigid molecule the default CI space (`levex=5 citime=5` and `cimax=15`) is sufficient. Hence, this parameter was also not discussed in Ref. [2]. However, larger molecules such as ketenimine and propynal crucially depend on the convergence of the CI space. This is not only in terms of energies but also in terms of wave functions. For consistency reasons, this phenomenon will also be discussed for H_2CS , but with very small CI spaces. Fig. 3.2 shows that a slightly too small CI space leads only to frequency and intensity shifts (middle vs. bottom). In this case, the VCI wave functions are largely converged. In contrast, the effect of an insufficiently converged VCI wave function can be seen in the top of Fig. 3.2. The artifacts are extreme and there is little resemblance to the correct spectrum. Of course, for H_2CS , the CI space had to be chosen extremely small to yields such results. However, in the case of propynal this could also be seen for a much larger CI space (`levex=7 citime=6` and `cimax=20`). It should be noted that this effect is also present in cases where the VCI energies are converged. Consequently, the VCI energies are an insufficient indicator for the convergence of the corresponding wave functions. A somewhat better indicator is, of course, provided by the VCI intensities. However, there may be an error compensation within the VCI intensities, which can hide an insufficient convergence of the wave functions. Further methods to overcome this problem are discussed in Chapter 5.

3.1.3 VIBRATIONAL BASIS SET SIZE

One parameter that was analyzed in Ref. [2] is the size of the vibrational basis set. One of the results was that this is a crucial parameter in terms of quantitative changes. In contrast, the qualitative changes are much more subtle than for J_{\max} and for the CI space. When viewed on a 400 cm^{-1} wide plot, there are hardly any changes visible. Therefore, Fig. 3.3 shows only a more narrow snippet of 40 cm^{-1} . The overall structure remains relatively unchanged regardless if only 4 or 45 excited vibrational bands are considered. Considering the smaller progression reveals that some of the very dense bands in the upper spectrum split into wider progression, if more vibrational basis functions are used. A further increase in this respect will result in shifts for these bands. Compared to the previously discussed parameters, an insuffi-

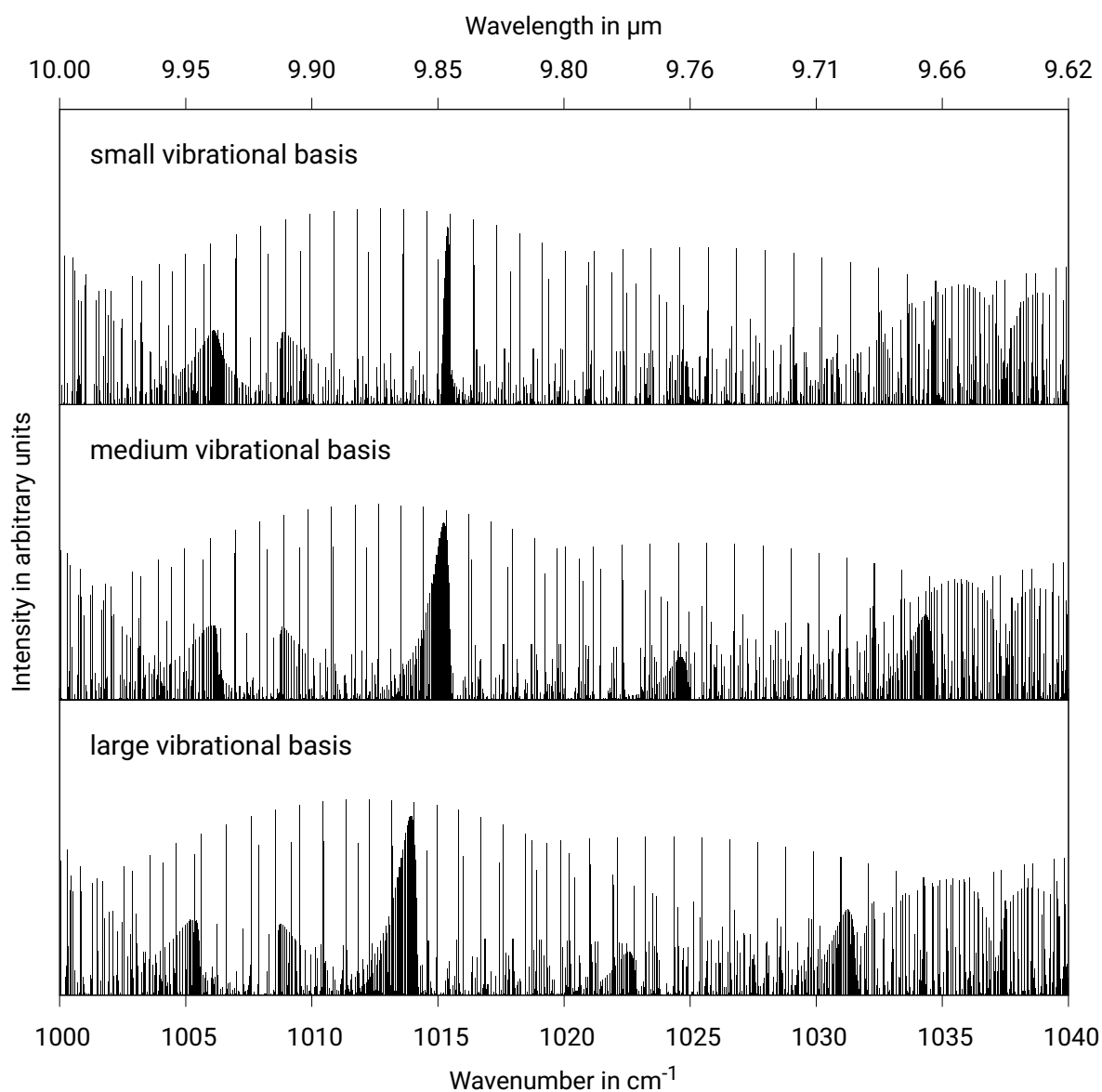


Figure 3.3: Influence of the convergence behavior of the vibrational basis set size on the rovibrational spectrum. The small basis set includes only the ground state and the four lowest vibrational fundamental modes. The medium basis set of 15 vibrational states includes all fundamental bands, single overtones and combination bands up to 3000 cm^{-1} . In the large basis set 45 vibrational states up to double excitations and threefold combination bands up to 5000 cm^{-1} are included. The example shows H_2CS in a narrow spectral range of the strongly coupled region of the two quasi degenerate vibrational modes ν_4 and ν_6 at 989.4 cm^{-1} and 989.5 cm^{-1} , respectively. In addition, there is another fundamental band ν_3 at 1060.2 cm^{-1} . The vibrational basis set includes up to second overtones and threefold combination bands up to subtle, the μ -tensor was considered up to 2nd order for the rotational terms and 1st order for Coriolis coupling terms, the VCI space was set to its current default value $\text{levex}=5$ $\text{citime}=5$ and $\text{cimax}=15$ and $J_{\text{max}} = 45$.

cient convergence in the size of the vibrational basis set is much more difficult to detect. So far, the best practice for this task is increasing the number of vibrational basis functions and visually comparing the spectra. However, it should be mentioned that usually the spectral separation between different vibrational bands is a good indicator for the strength of the coupling. This is also the reason, why the upper figure already yields a very decent approximation for the actual spectrum, since all additional bands are at least 1000 cm^{-1} apart. In the large basis set of 45 vibrational bands all vibrational bands up to 5000 cm^{-1} and up to threefold excitations are already included. Therefore, the lowest additional band that could be considered are threefold overtones and four mode combination bands. However, since normal coordinates and the multi-mode expansion are best suited to describe small nuclear motions, these higher vibrational bands will be described with less accuracy. Therefore, a trade-off has to be found between a larger basis set with some less accurate bands and a smaller vibrational basis set with only very precise bands. It should be mentioned that for larger molecules (e.g. six or more atoms) the aforementioned criteria (vibrational modes up to 5000 cm^{-1} and up to three mode excitations) can already lead to hundreds of vibrational modes. Since this is not yet computationally feasible, more restrictive constraints are necessary. Therefore, the specific choice of the vibrational basis set depends heavily on the specific molecule.

3.1.4 CORIOLIS COUPLING TERM ORDER

A characteristic feature of H_2CS is the particularly strong Coriolis coupling between the two quasi-degenerate vibrational modes ν_4 and ν_6 at 989.4 cm^{-1} and 989.5 cm^{-1} . In this sense, it can be understood as an upper bound for the strength of this type of coupling. Fig. 3.4 shows that the 0th order Coriolis coupling is very significant in this region. However, comparing the 0th order Coriolis coupling with the 1st shows barely any difference on this wide spectral range. This is analogously to the VAM terms, where the μ -tensor expansion is also almost converged after the 0th order. The quantitative analysis in Ref. [2] has shown that the 1st order still has a meaningful influence. However, because it shifts many progressions by a small amount and it does not influence the intensity particularly strongly, it is difficult to see in the spectrum. Nevertheless, Fig. 3.4 demonstrates that already the 0th order can be a very decent approximation. It shows that missing coupling terms do not lead to artifacts in the spectrum. This is in contrast to an insufficiently converged CI space and in some sense also different to the convergence behavior of J_{max} . Thus, the absence of higher order coupling terms is much more difficult to spot in the resulting spectra.

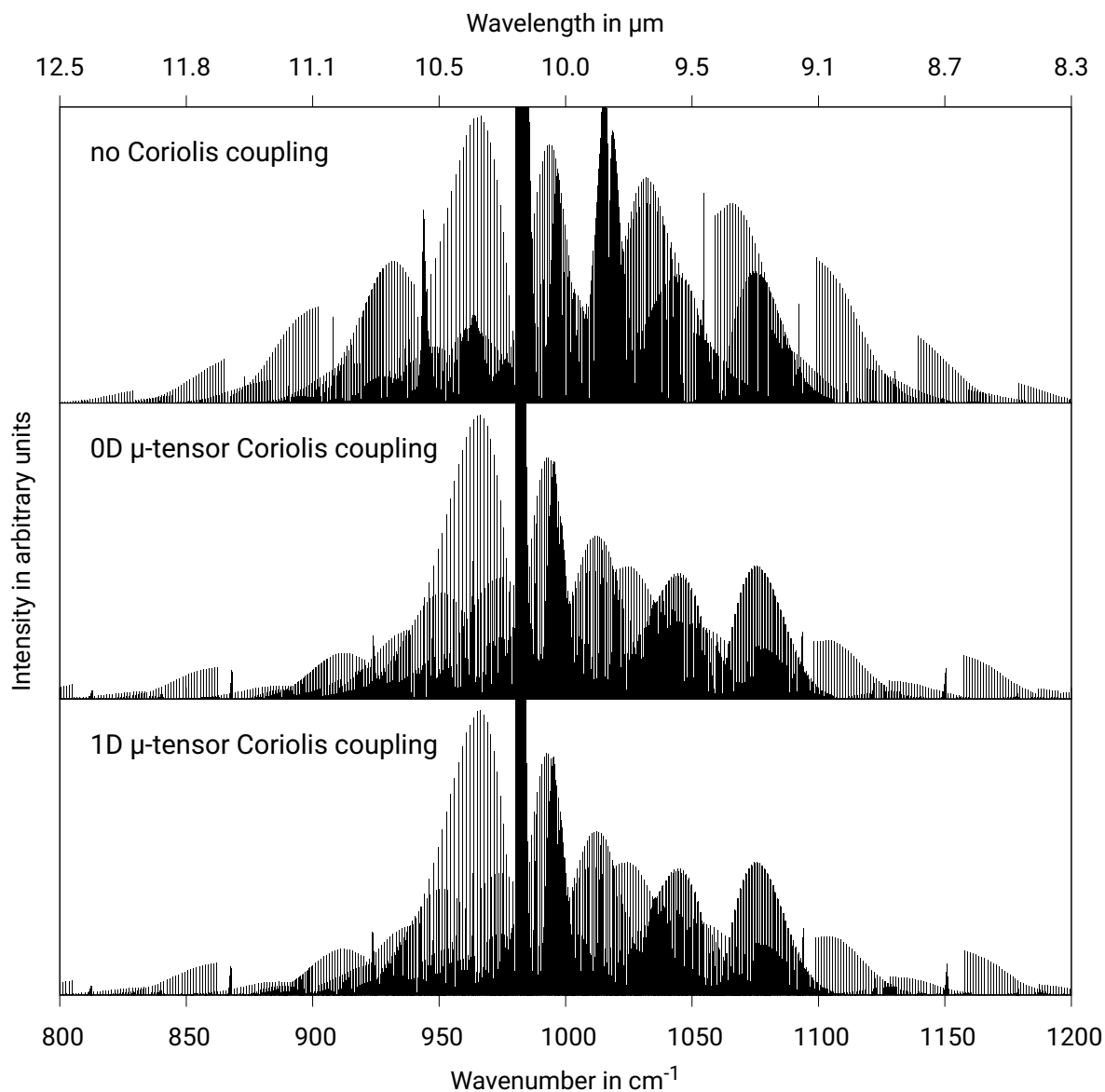


Figure 3.4: Influence of the μ -tensor expansion order of the Coriolis coupling term on the convergence behavior and the visual appearance of the rovibrational infrared spectrum. The example shows H_2CS in the strongly coupled region of the two quasi degenerate vibrational modes ν_4 and ν_6 at 989.4 cm^{-1} and 989.5 cm^{-1} , respectively. In addition, there is another fundamental band ν_3 at 1060.2 cm^{-1} . The vibrational basis set includes up to second overtones and threefold combination bands up to 5000 cm^{-1} , the μ -tensor was considered up to 2nd order for the rotational terms and 1st order for Coriolis coupling terms, the VCI space was set to its current default value $\text{levex}=5$ $\text{citype}=5$ and $\text{cimax}=15$ and $J_{\text{max}} = 45$.

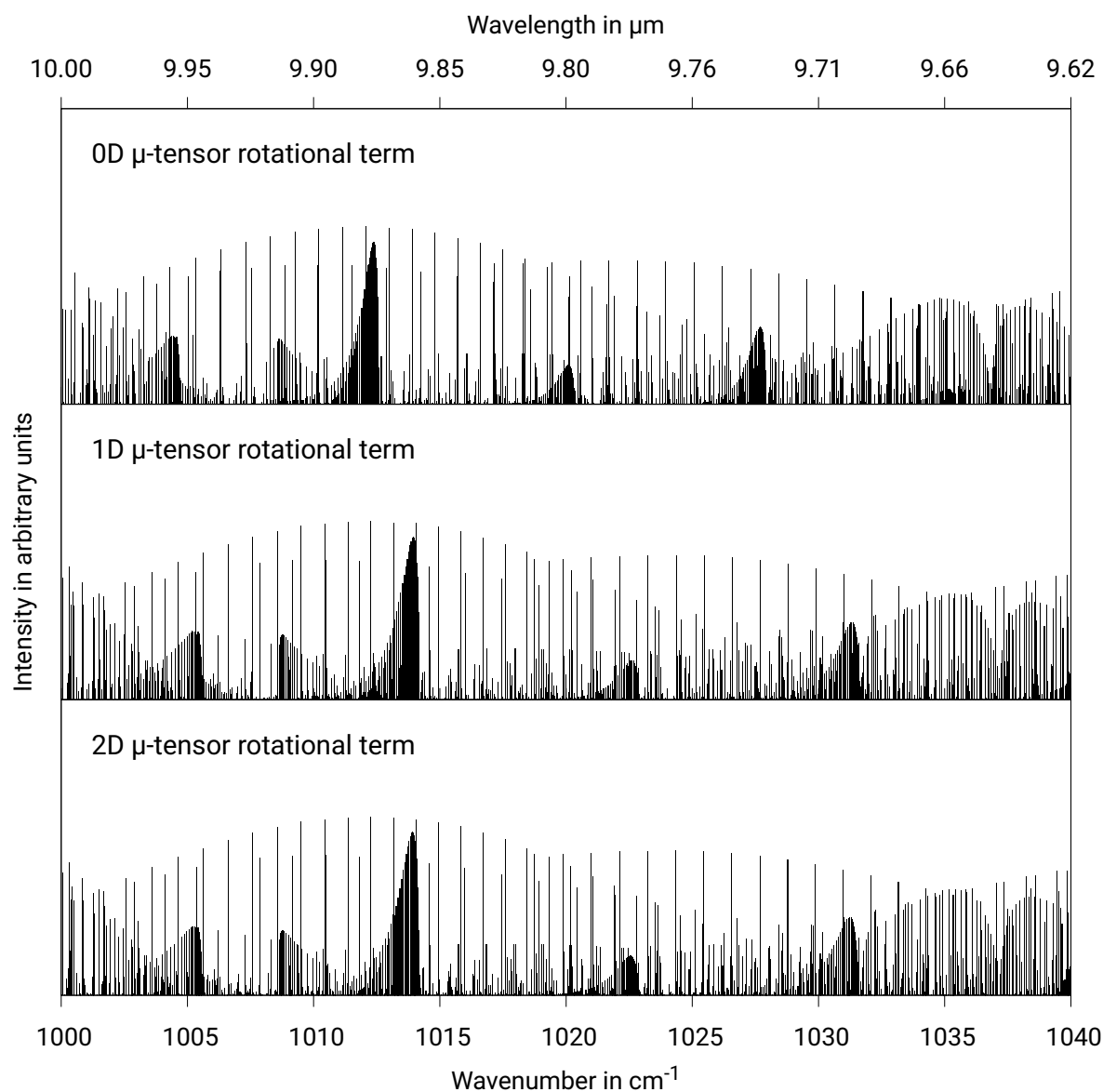


Figure 3.5: Influence of the μ -tensor expansion order of the rotational term on the convergence behavior and the visual appearance of the rovibrational infrared spectrum. The example shows H_2CS in a narrow spectral range of in the strongly coupled region of the quasi degenerate vibrational modes ν_4 and ν_6 at 989.4 cm^{-1} and 989.5 cm^{-1} , respectively. In addition to that there is another fundamental band ν_3 at 1060.2 cm^{-1} . The vibrational basis set includes up to second overtones and threefold combination bands up to 5000 cm^{-1} , the μ -tensor was considered up to 2nd order for the rotational terms and 1st order for Coriolis coupling terms, the VCI space was set to its current default value $1\text{evex}=5$ $\text{citype}=5$ and $\text{cimax}=15$.

3.1.5 ROTATIONAL TERM ORDER

In Ref. [2] it was found, that the rotational terms require a μ -tensor expansion that is one order higher, than for the Coriolis coupling terms. This means, for example, that a 1st order μ -tensor expansion in the Coriolis coupling terms results in an error that is equivalent to the error induced by 2nd order rotational terms. It should be noted that the region around 990 cm^{-1} is an unusual special case for Coriolis coupling and is not entirely representative. Furthermore, it was noted in the publication that a spectrum without 0th order rotational terms (similar to Fig. 3.4 for the Coriolis coupling terms) would not make sense, since this would be a pure vibrational spectrum. Consequently, Fig. 3.5 starts with the 0th order μ tensor. Similar to the comparison between different vibrational basis set sizes, the overall structure is already fairly similar to the reference calculation for the least computational demanding calculation. For this reason, a smaller spectral range was chosen again (40 cm^{-1}). A comparison between 0th and 1st order terms shows shifts in the order of 2 to 6 cm^{-1} for four bands. The strongest shift can be seen for a progression around 1035 cm^{-1} for 0th order, which moves to 1041 cm^{-1} for the 1st order. The changes induced by the 2nd order terms are not visible with this plot range. Note also that there are hardly any intensity shifts visible. Similar to the Coriolis coupling terms, the absence of higher order terms does not produce any artifacts in the spectrum, making it difficult to decide whether these terms are needed.

3.1.6 INFLUENCE OF NSSWS

So far, this section has mainly focused on the convergence behavior of different parameters, since this was the main topic of the second publication of this cumulative thesis. However, in this last subsection the influence of the degeneracy induced by the nuclear spins (NSSW) on the spectrum of H_2CS will be briefly discussed. Since H_2CS belongs to the C_{2v} point group, it has a total of four NSSWs, two of which are 1 and the other two are 3. In contrast, all other molecules discussed in this thesis belong to the point group C_s . Therefore, they formally have two NSSWs, but for symmetry reasons they have to be identical. Thus their influence on the spectra is only a global prefactor. For this reason, H_2CS is the only opportunity to discuss this effect.

Fig. 3.6 shows the strongly coupled region, that was discussed earlier. However, each transition is colored with respect to the assigned NSSW. This works as follows: The point group C_{2v} has four different irreps. A_1 and A_2 have a NSSW of 1 and B_1 and B_2 have a NSSW of 3. Rovibrational infrared transitions are only allowed between A_1 and A_2 as well as between B_1 and B_2 . For this reason, the NSSW of the initial state and final state are equal, and therefore the coloring of the transition also encodes the irreps of the corresponding rovibrational states (apart from parity). Except for the area around the two fundamental bands ν_4 and ν_6

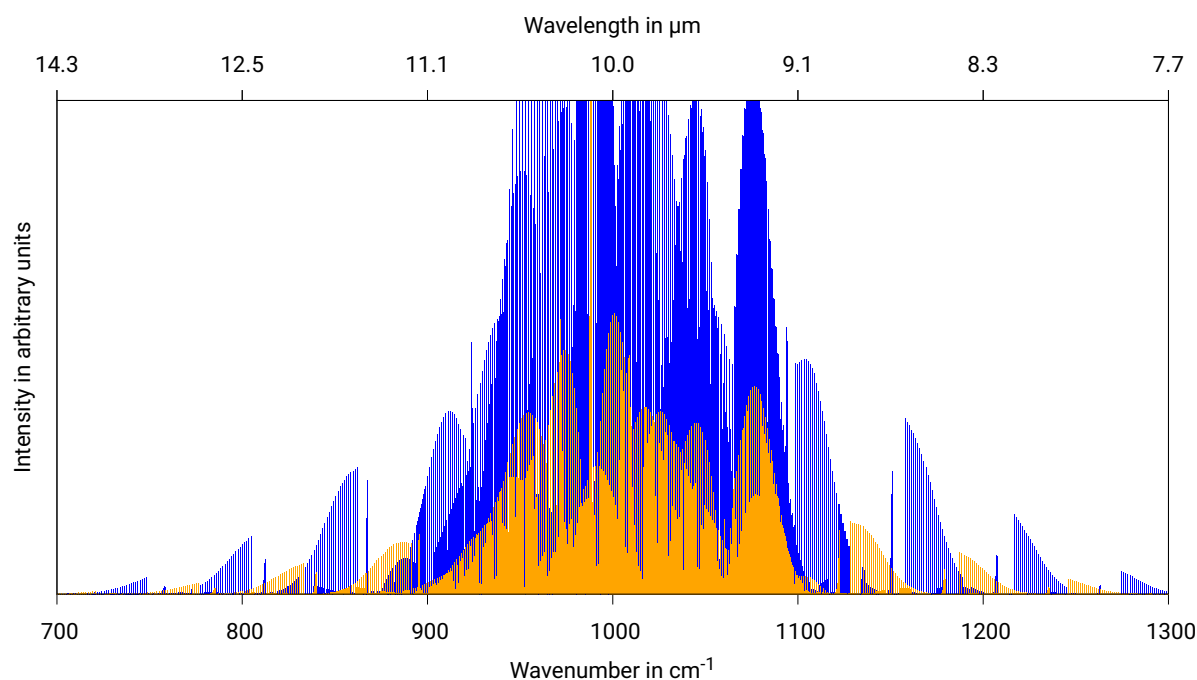


Figure 3.6: Influence of the NSSWs for the strongly coupled region of H_2CS . The vibrational basis set includes up to second overtones and threefold combination bands up to 5000 cm^{-1} , the μ -tensor was considered up to 2nd order for the rotational terms and 1st order for Coriolis coupling terms, $J_{\text{max}} = 45$, the VCI space was set to its current default value $\text{levex}=5$, $\text{citype}=5$ and $\text{cimax}=15$.

at 989.4 cm^{-1} and 989.5 cm^{-1} the effect of the NSSW can be seen very clearly. The intensity of the blue bands increases monotonically towards the middle of the figure. The same holds true for the orange progressions. However, due to the NSSWs the band intensities are alternating. The very complex spectra of asymmetric top molecules can be broken down into more intuitive patterns, by using a series of analyses like in this subsection this for the NSSWs.

3.2 KETENIMINE

In the first paper [1], which was written in the course of this thesis, ketenimine (CH_2CNH) was studied. It is a 6 atomic molecule with the point group C_s . It is a near-prolate asymmetric top ($\kappa = -0.9981$) with two NSSWs, both of which have a value of 24. (For more details see Ref. [1].) When this paper was published, the RVCi part of the *MOLPRO* program was relying on a number of approximations. For example, only the 0th order of μ -tensor for the rotational term and the Coriolis coupling term had been implemented. For the calculations performed in the course of this thesis, the expansion of the μ -tensor was increased to 2nd order for the rotational terms and 1st order for the Coriolis coupling terms. Due to the lack of optimization, it was also not yet possible to choose the size of the vibrational basis N_{vib} and the total angular momentum J to be high at the same time. For this reason, the com-

promise of $J_{\max} = 70$ and $N_{\text{vib}} = 27$ was used at that time. It has been shown that in such cases the convergence of J_{\max} is more important than the consideration of some more high vibrational states which themselves have no intensities but may be needed for couplings. Nevertheless, $N_{\text{vib}} = 58$ vibrational states could now be considered. The convergence of J_{\max} was also reconsidered, but it was found that $J_{\max} = 80$ does not add any significant rovibrational lines. Furthermore, due to the memory savings in the RVCi program and an optimization by Mathea in her PhD on the VAM terms, it is now possible to include the 1D terms on the diagonal of the VCI matrix. (The memory savings in RVCi are mainly indirect, since the calculations can now be executed on more CPU cores). However, the effects of the higher order VAM terms are hardly noticeable. Last but not least, there are a number of small changes, such as default values for thresholds within the VCI and RVCi, the number of basis functions in the VCI, adjustments due to a better understanding of converged VCI basis functions (see also Section 3.1) and improvements in the code.

Furthermore, at that time the vibrational transition moments were implemented only for the case that one of the two vibrational states is the ground state. This also means that the transition moments between two excited vibrational transitions were not yet implemented. On the one hand, this prevents the calculation of *hot bands*ⁱ. On the other hand, it also means that the full RVCi eigenvector for the initial state cannot be considered when evaluating the intensities. Instead, the eigenvector had to be restricted to the first $2J + 1$ elements belonging to the vibrational ground state. This approximation has been shown to work relatively well because, first, the initial rovibrational state always belongs to the vibrational ground state (as long as no hot bands are considered) and thus the most important part (with the largest coefficients) is included. On the other hand, the vibrational ground state is usually only weakly coupled with other vibrational states. Nevertheless, this limitation has now been removed, and due to the introduction of thresholds and parallelization, no additional computational time is required for the evaluation.

However, the major change compared to the earlier work concerns the quantum number assignment. The introduction of the MSRB as well as the use of the partial trace method (see Chapter 2) and the possibility that a set of quantum numbers ν and k can now be assigned more than once, has led to a significantly improved assignment. The previous limitation on the assignment, of these two bad quantum numbers resulted in two figures being shown for each spectrum. The lower figure shows the result for the uncoupled system (calculated by RCI), where the quantum numbers can be assigned unambiguously. Thus it was possible to color code the vibrational quantum number ν . The upper figure, on the other hand, shows the RVCi spectrum in a single color. It should be noted that virtually all other rovibrational

ⁱA hot band is a band centered on a transition between two excited vibrational states, i.e. neither is the overall ground state.

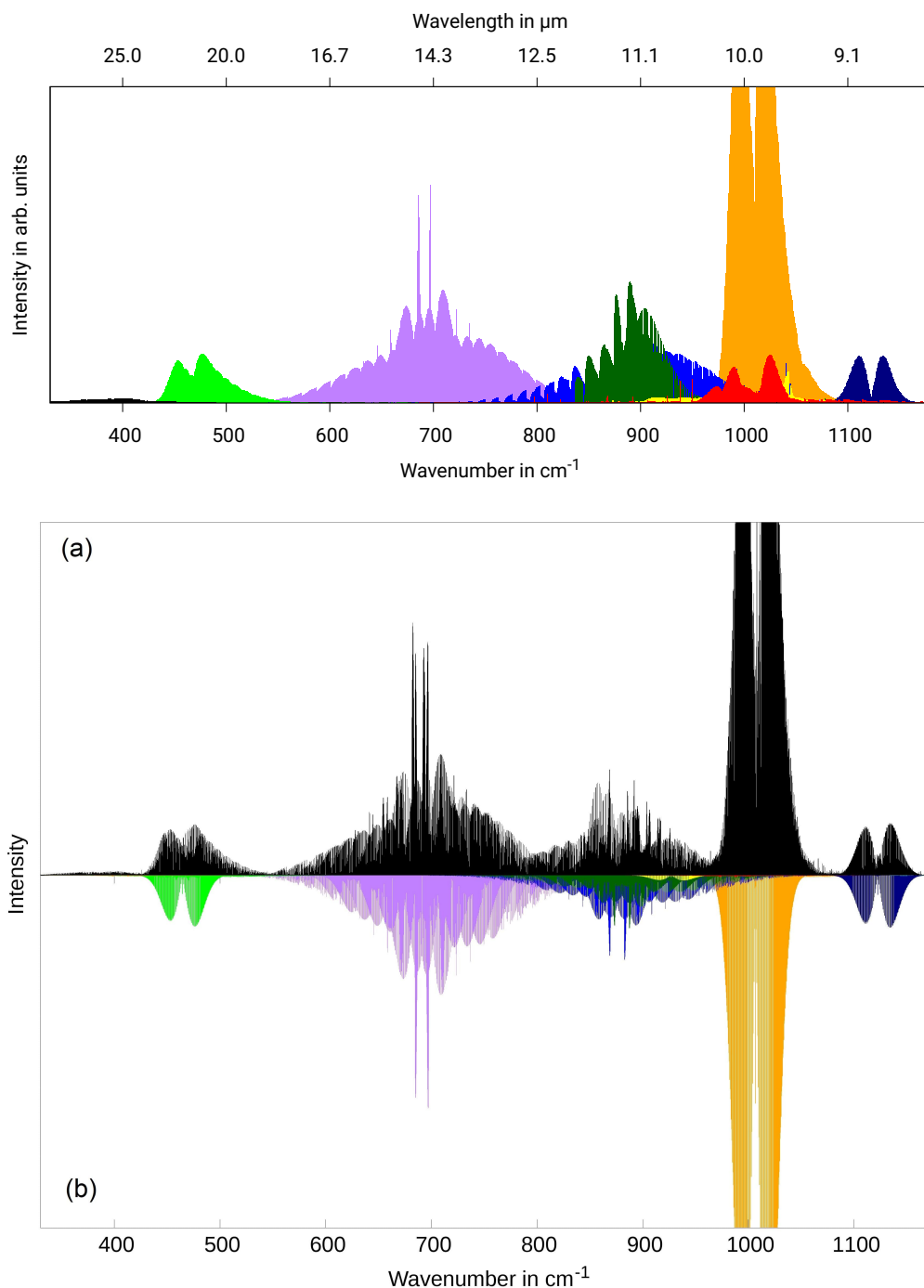


Figure 3.7: Overview of the low frequency infrared spectrum of ketenimine. The lower figure corresponds to the original Fig. 3 in [1] with a comparison between RVCI (a) and RCI (b) results. The upper figure provides most recent results of a calculation for this thesis, with 58 instead of 27 vibrational basis functions, new quantum number assignment, higher order coupling terms, etc (see text). Visible contributions are provided by the fundamental bands ν_8 (464 cm^{-1} , CCN in-plane bend, light green), ν_7 (691 cm^{-1} , CH_2 wagging, purple), ν_{11} (876 cm^{-1} , torsion, light blue), ν_6 (1007 cm^{-1} , CNH bend, orange), ν_5 (1123 cm^{-1} , CCN stretch, dark blue) as well as the combination band $\nu_8 + \nu_{12}$ (881 cm^{-1} dark green) and the overtone $2\nu_8$ (927 cm^{-1} yellow). The color transition between blue and green at 900 cm^{-1} is explained in the text.

theory groups worldwide restrict themselves to displaying the spectrum in *single color*, i.e. the quantum number ν is either not assigned at all or only the leading coefficient is considered. However, the previously mentioned improvements in the assignment in the context of this work make it possible to perform the color coding directly in the RVC I spectrum and still obtain consistent results in the vast majority of cases.

Fig. 3.7 shows a comparison between an original figure of Ref. [1] (bottom) and the result of the most recent calculation (top). First of all, the rough position of the vibrational bands has remained largely the same. Since this is determined by the VCI calculation and the majority of changes in the calculations are done for the RVC I calculations, this was to be expected. Moreover, the shape of the progressions are essentially the same as those from the RVC I figure, but the color coding corresponds to that of the RCI figure. However, upon closer inspection, some differences in the progressions can be identified. These are discussed in the enlarged Fig. 3.8 and 3.9 plots.

The low frequency spectrum in Fig. 3.8 shows that neither the additional vibrational states, nor the higher order coupling terms influenced this region significantly. Moreover, the quantum number assignment is very consistent, even in the challenging areas, like the strongest coupling region around 425 cm^{-1} to 450 cm^{-1} . An experienced spectroscopist can also see the different progressions for different quantum numbers k for the ν_8 mode. The only major differences between the two RVC I calculations are the small artifacts around 435 cm^{-1} in the old calculations. In contrast, Fig. 3.9 shows a variety of changes compared to the old calculations. The three most notable differences are as follows:

1. The fine structure of most modes are irregular/rugged in the older calculations. There are several reasons for this phenomenon. By far the largest reason is unstable lines [75, 125], that is rovibrational transitions related to (quasi-)degenerate rovibrational states belonging to the same quantum number J . For this reason, the eigenvectors of these states are not well defined and span a multidimensional subspace. Initially, an attempt was made to solve this problem by introducing a specific orientation by orthogonalizing and rotating the eigenvectors in a specific way. However, this did not lead to a proper stabilization of the unstable lines. For this reason a *perturbation algorithm* was introduced that creates a very small perturbation in the order of $1 \times 10^{-4}\text{ cm}^{-1}$. This is sufficient to lift the degeneracy numerically and thus prevent unstable lines. It should also be noted, that increasing the number of coupling terms and vibrational basis functions somewhat reduces the number of unstable lines. However, some of the unstable lines could never be resolved with additional coupling, but only with the perturbation algorithm. Other reasons for the irregular fine structure may be the aforementioned ground state transition moments approximation and an insufficient convergence of the

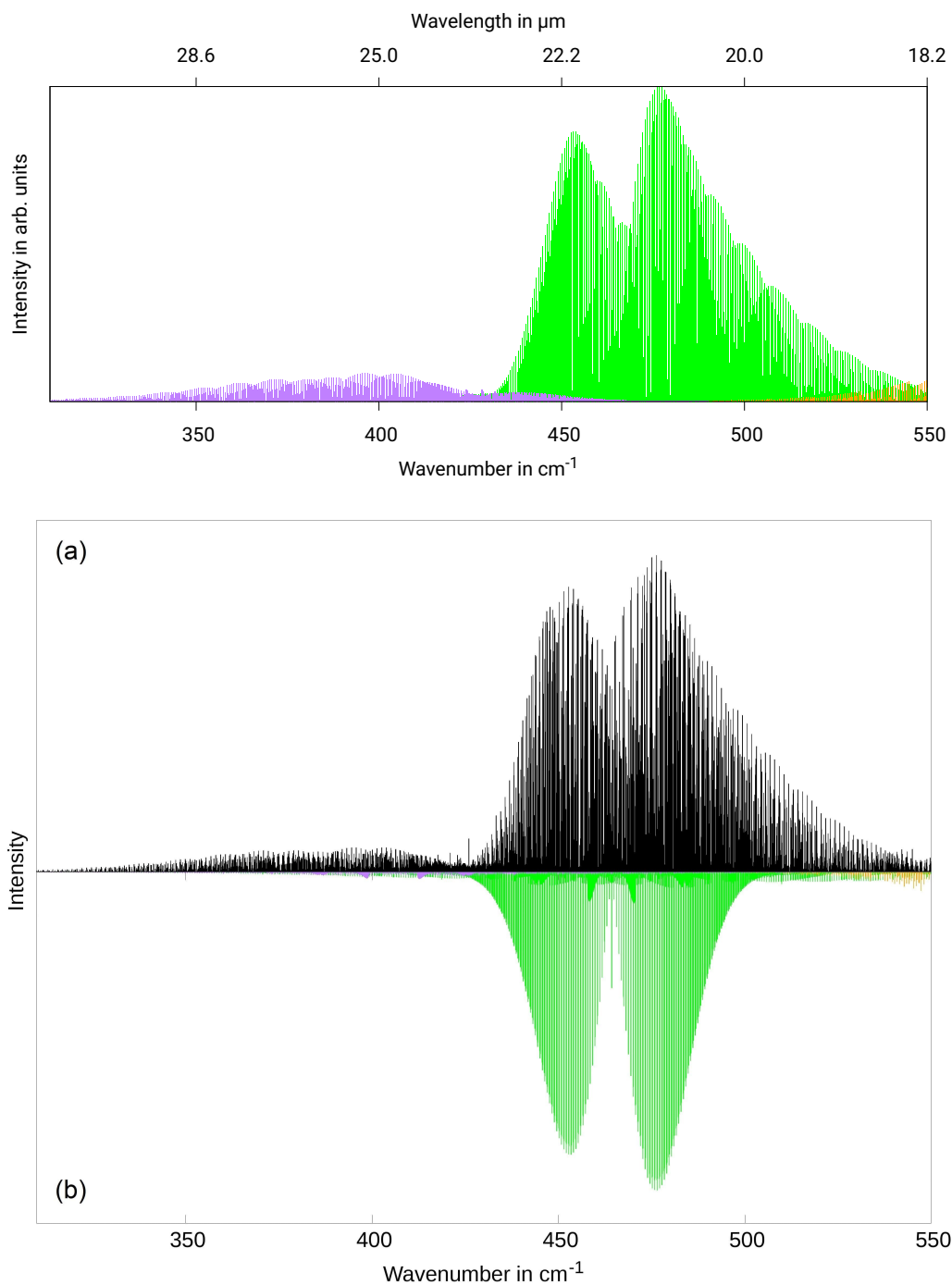


Figure 3.8: Low frequency infrared spectrum of ketenimine. The lower figure corresponds to the original Fig. 4 in [1] with a comparison between RVC1 (a) and RCI (b) results. The upper figure provides most recent results of a calculation for this thesis, with higher order coupling terms, a new quantum number assignment, 58 vibrational basis functions, etc (see text). The two lowest fundamental bands ν_{12} (406 cm^{-1} , CCN out-of-plane bend, VCI intensity 0.4 km/mol , purple) and ν_8 (464 cm^{-1} , CCN in-plane bend, VCI intensity 19.8 km/mol , light green) as well as small contributions of ν_7 (691 cm^{-1} , CH_2 wagging, orange).

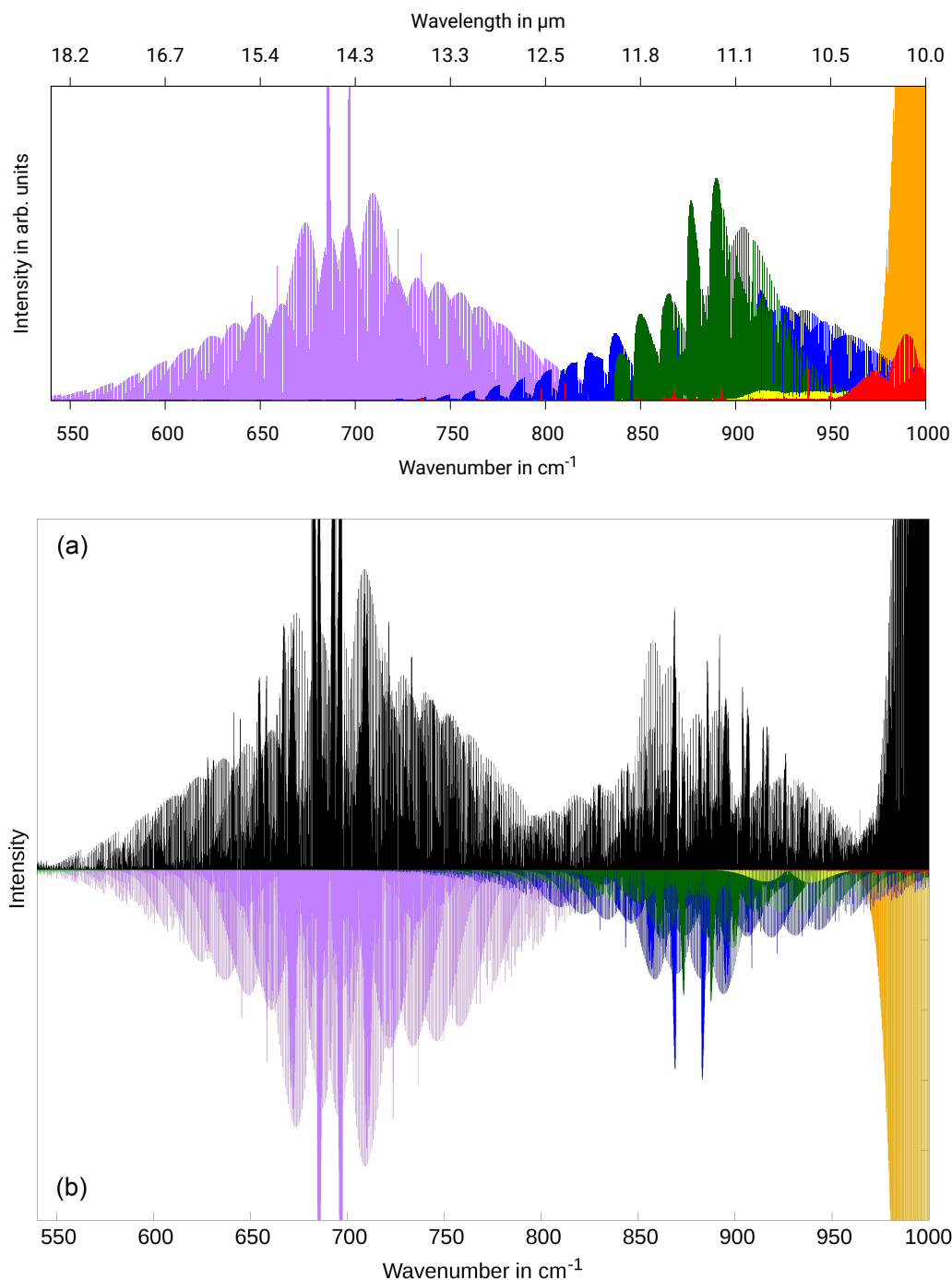


Figure 3.9: Infrared spectrum of ketenimine in a strongly coupled region. The lower figure corresponds to the original Fig. 5 in [1] with a comparison between RVC1 (a) and RCI (b) results. The upper figure provides most recent results of a calculation for this thesis, with higher order coupling terms, 58 instead of 27 vibrational basis functions, new quantum number assignment, etc (see text). Significant contributions come from the fundamental bands ν_7 (691 cm^{-1} , purple), ν_{11} (876 cm^{-1} , blue), ν_{10} (980 cm^{-1} , red, barely visible) and ν_6 (1007 cm^{-1} orange), the combination band $\nu_8 + \nu_{12}$ (880 cm^{-1} dark green) and the overtone $2\nu_8$ (927 cm^{-1} yellow). The color transition between blue and green at 900 cm^{-1} is explained in the text.

VCI wave functions. However, the latter would usually be significantly stronger (see also Section 3.1).

2. The overall structure of the green and blue bands $\nu_8 + \nu_{12}$ and ν_{11} changes significantly. In Ref. [1] it was already noted that this region is very demanding for several reasons. On the one hand, because the two modes are only separated by 4 cm^{-1} . On the other hand, because there are some additional vibrational bands, such as ν_{10} (three orders of magnitude less intensity than ν_6) and ν_{12}^2 (more than five orders of magnitude less intensity than ν_6). A large variation in the intensities are numerically especially demanding. Last but not least, the coupling between the bands $\nu_8 + \nu_{12}$ and ν_{11} requires a change of 3 modes in the vibrational quantum number and therefore it was discussed in Ref. [1] that the 1st and 2nd order rotational and Coriolis coupling terms could be needed. The strong coupling between these two bands causes an inconsistent assignment of the quantum number ν , which results in the color change between blue and green. Further analysis has now shown *a posteriori* that the 1st order coupling terms are sufficient, but the 0th order terms are not, and that no further vibrational states are needed (by comparing different recent calculations).
3. The four largest peaks for the purple ν_7 mode are degenerate to two peaks in the newer calculation. The origin of this problem is relatively difficult to explain, since additional coupling terms and vibrational basis functions should remove degeneracies, and not introduce additional ones. Moreover, the fact that there is an energetic degeneracy also means, that the origin of the phenomenon lies in the (ro-)vibrational energies (eigenvalues) and not in the eigenvectors or in the intensities. Thus, neither unstable lines nor missing transition moments can explain this issue.

A final insight of Fig. 3.9 concerns the assignment of the vibrational quantum numbers. There are some strongly coupled regions in the figure that show a consistent assignment of this quantum number. However, the blue ν_{11} and the green $\nu_8 + \nu_{10}$ bands clearly demonstrate the limitations of the current implementation. Compared to previous assignment methods, it is already a success that even in this region the coloring is consistent within each progression.

Four relatively strong vibrational bands can be found in the spectral region from 1950 cm^{-1} to 2150 cm^{-1} . Nonetheless, the previous study has shown that there is a surprisingly low amount of coupling. Considering the most recent results in Fig. 3.10, this is not due to the absence of higher order coupling terms, but reflects the physical reality. Within this spectral range, five additional vibrational bands are considered. All of them were excluded in the original publication, since their intensity nearly vanishes (lower than 0.04 km/mol in comparison to 203 km/mol for ν_3). In Fig. 3.10 some transitions are assigned to $\nu_{10} + \nu_6$ (blue), $\nu_{11} + \nu_5$ (yellow) and ν_7^3 (black). However, it is clear, that the assignment in this region is at least doubtful.

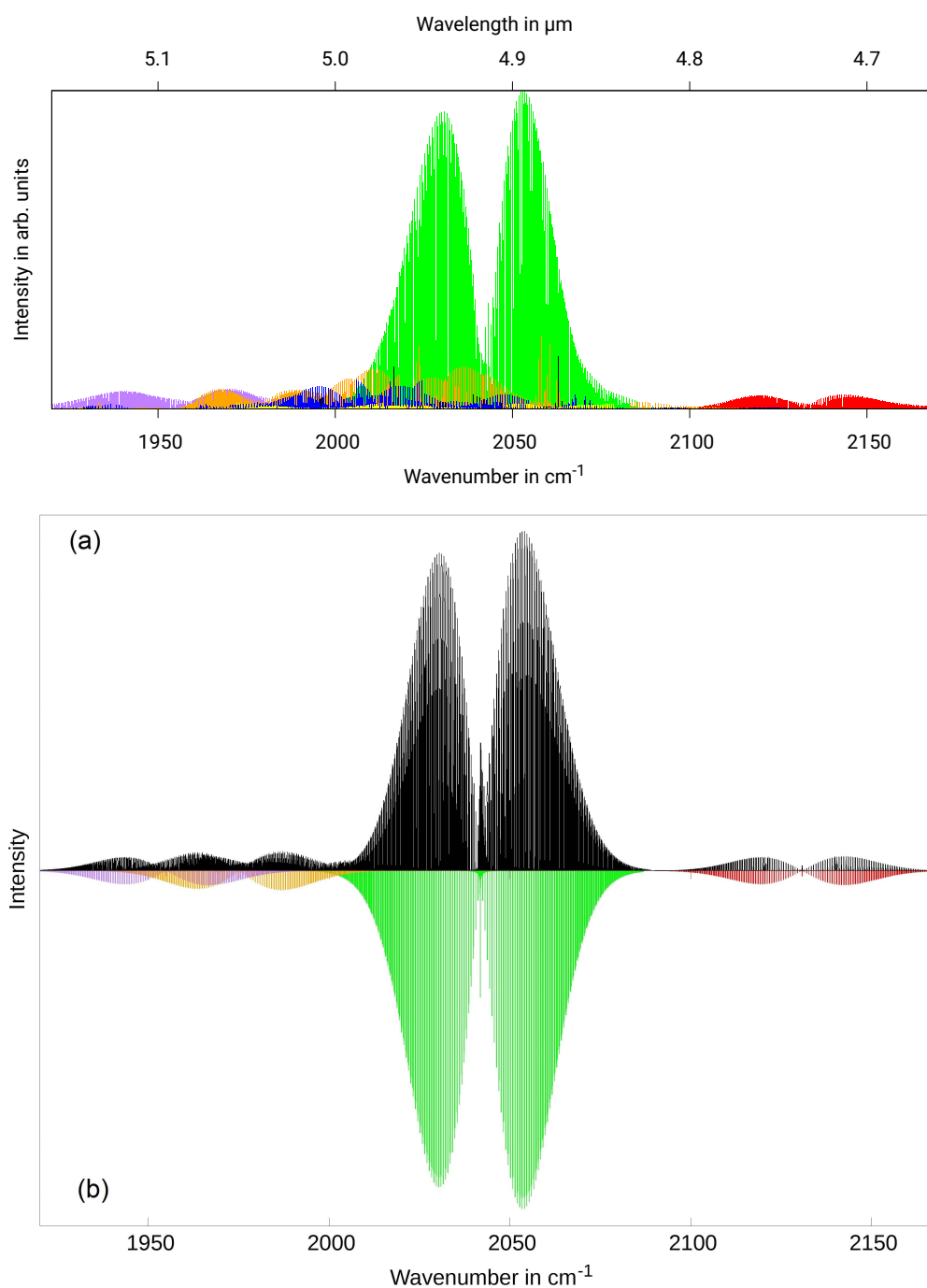


Figure 3.10: Rovibrational spectrum of ketenimine in the region of the strongest fundamental band ν_3 (2042 cm^{-1} , CCN stretch, green). The lower figure corresponds to the original Fig. 6 in [1] with a comparison between RVC1 (a) and RCI (b) results. The upper figure provides most recent results of a calculation for this thesis, new quantum number assignment, higher order coupling terms, etc (see text). In addition to the ν_3 mode, the overtones $2\nu_{10}$ (1955 cm^{-1} , purple) and $2\nu_6$ (1975 cm^{-1} , orange), as well as the combination band $\nu_5 + \nu_6$ (2131 cm^{-1} , red) provide visible contributions this spectral range. Additional bands only considered in the more recent calculation are $\nu_{10} + \nu_6$ (1988 cm^{-1} , bright-blue), $\nu_{11} + \nu_5$ (1999 cm^{-1} , yellow), $\nu_{10} + \nu_5$ (2102 cm^{-1} , dark-blue, not visible), $\nu_7 + \nu_4$ (2154 cm^{-1} , dark-green, not visible) and ν_7^3 (2012 cm^{-1} , black)

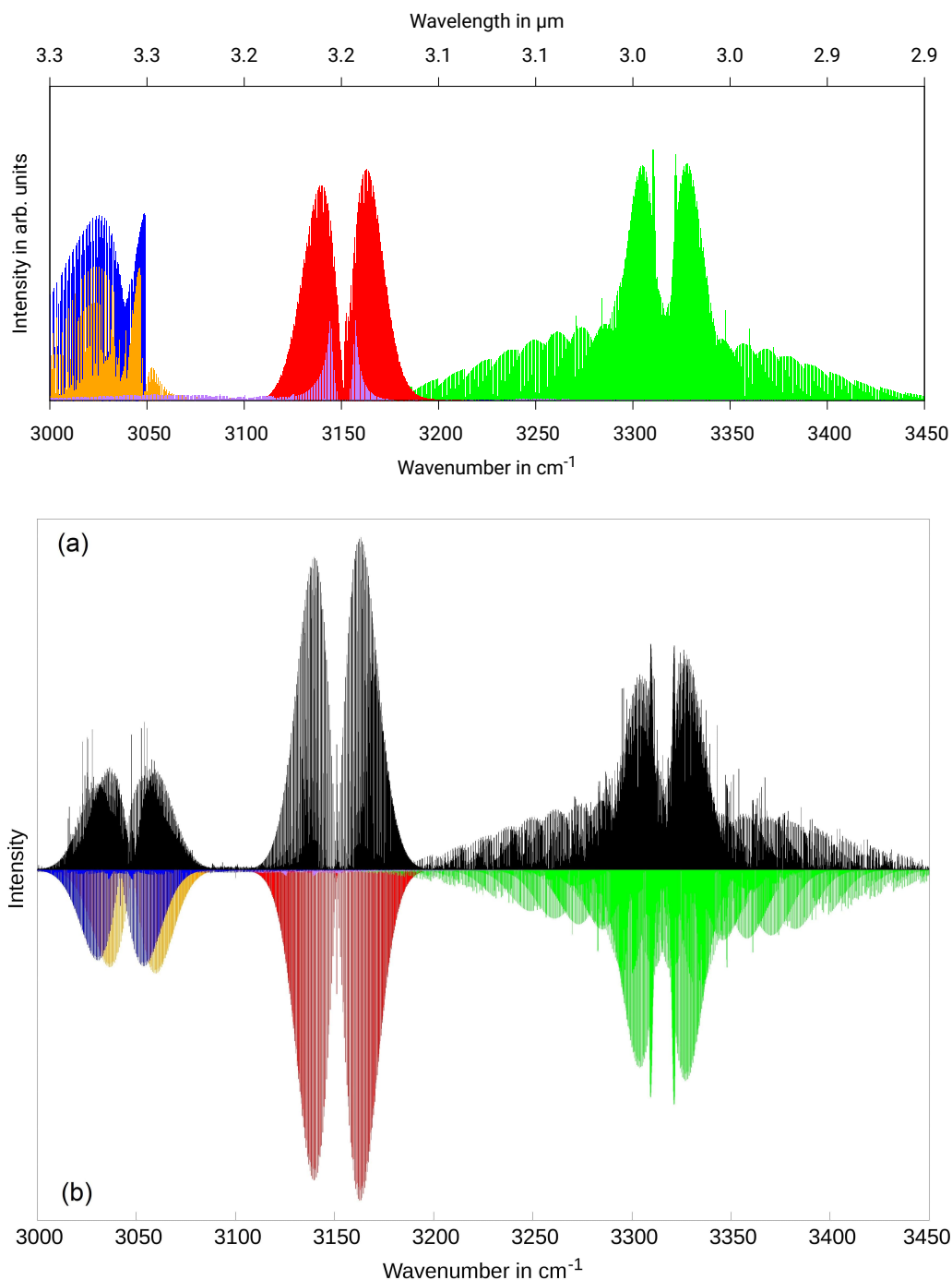


Figure 3.11: Rovibrational spectrum of ketenimine in the region of XH stretching fundamentals. The lower figure corresponds to the original Fig. 7 in [1] with a comparison between RVC1 (a) and RCI (b) results. The upper figure provides most recent results of a calculation for this thesis, new quantum number assignment, higher order coupling terms, etc (see text). Three fundamental bands ν_2 (3048 cm^{-1} , symmetric CH_2 stretch, orange), ν_9 (3133 cm^{-1} , anti-symmetric CH_2 stretch, purple, barely visible) and ν_1 (3315 cm^{-1} , NH stretch, light green) are shown, as well as the combination bands $\nu_3 + \nu_5$ (3042 cm^{-1} , blue) and $\nu_3 + \nu_6$ (3151 cm^{-1} , red). Comparison between RVC1 (a) and RCI (b) results.

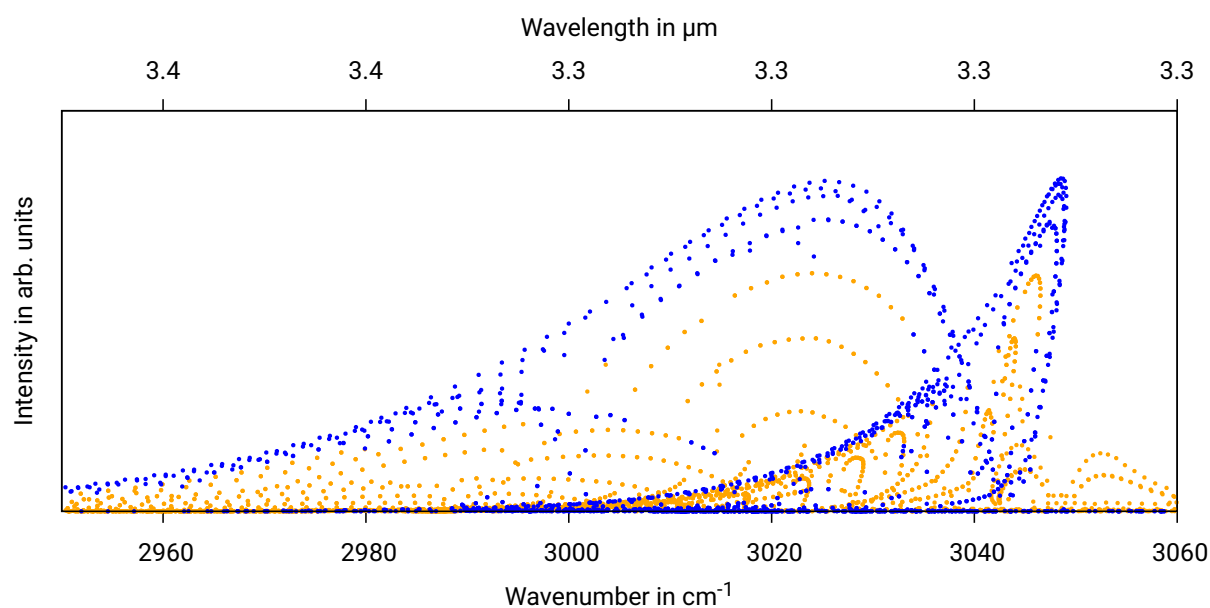


Figure 3.12: Close up of the high energy infrared spectrum of ketenimine in a dot plot, instead of the previous bar plots. In the region of XH stretching fundamentals. The fundamental band ν_2 (3048 cm^{-1} , orange) and the combination band $\nu_3 + \nu_5$ (3042 cm^{-1} , blue) are shown.

Therefore, an analysis for the details in this region is not provided. In summary, neglecting the higher order μ -tensor terms and additional vibrational modes yields a reasonable approximation for this region.

In Ref. [1], another region with several nearby vibrational bands, but only weak coupling, could be found between 3000 cm^{-1} and 3450 cm^{-1} . However, by considering higher order coupling terms, the band shapes for the two lowest vibrational transitions change drastically, in Fig. 3.11. A very similar band shape with a compression of the lines followed by a sudden end of the progression was also observed and analyzed in Ref. [3, 124]. Using a dot plot instead of a bar plot and enlarging the region of interest shows that the progression does not actually end (see Fig. 3.12). Instead, the R-branch turns around and has a decreasing frequency for an increasing quantum number J , which would be the expected behavior for the P-branch. In Ref. [3], this phenomenon was explained by the fact that the centrifugal distortion increases faster in the initial vibrational state than in the final vibrational state. As a result, the rovibrational energies associated with the lower vibrational state also increase faster than those associated with the upper vibrational state, leading to a decreasing frequency for larger J (see Ref. [1] for details). Besides this unusual effect, several more differences occur when comparing the original results of Ref. [1] and the more recent calculations in Fig. 3.11. For example, the intensity ratios are different, which is due to changes in the VCI calculations. Moreover, the older calculation shows a small number of transitions sticking out of the rest of the progressions (at 3050 cm^{-1} and 3360 cm^{-1}). This behavior vanishes in the more

recent calculations due to the additionally considered vibrational transition moments. The previously mentioned issue of an irregular fine structure, is again related to unstable lines and therefore resolved by the perturbation algorithm.

In conclusion, many of the previously necessary approximations did not influence the spectra drastically and yielded good results despite the early stage of implementation. For example, in the regions shown in Fig. 3.8, 3.10 and around 3100 to 3450 cm^{-1} , only minor changes appear. However, there is a number of improvements, which shows that the quality of the RVC I results could be significantly increased within the last three years. This can be seen for example in Fig. 3.11 between 3000 to 3100 cm^{-1} . Moreover, an assumption stated in Ref. [1] was confirmed, that is higher order μ -tensor terms are needed, when there are at least three vibrational *modes* that differ between two vibrational *states*. This happens for example in the coupling between $\nu_8 + \nu_{12}$ and ν_{11} . Another interesting finding, which could only be solved with the latest version of the RVC I implementation, was the turnaround progression between 3000 and 3100 cm^{-1} .

3.3 LINE BROADENING

In the previous sections, infrared rovibrational spectra were presented using bar plots without line broadening. To compare different theoretical spectra, it is common to neglect any line broadening, as this allows for a better analysis. However, to compare results with experimental groups, line broadening must be taken into account. There are many different broadening profiles to consider the different broadening effects with very different accuracy. These range from relatively simple Lorentz and Gaussian profiles to Voigt and beyond Voigt profiles [119, 126, 127]. Most of the more sophisticated methods are used for small molecules (2 – 4 atoms), such as N_2 , O_2 , H_2O [128], CO_2 [119], NH_3 , CH_4 [129] with low rovibrational state density. For this reason, different types of line broadening were investigated in the early stages of this PhD. However, only three different types of line broadening are now implemented in *MOLPRO*, as mentioned in Section 2.4. This is due to the fact, that larger molecules with a higher rovibrational state density are considered. Therefore, it should be sufficient to use a relatively simple broadening model. This assumption is discussed and verified in this section.

The environmental conditions considered in this work range from the ISM at $T = 10$ K and $p = 1 \times 10^{-13}$ Pa up to terrestrial conditions at $T = 300$ K and $p = 1 \times 10^5$ Pa. To show the influence of different types of line broadening, the terrestrial conditions are much more interesting. This is due to the extremely low pressure in the ISM. Therefore, there is virtually no pressure broadening (described by a Lorentz profile) and additionally the Voigt profile is almost identical to the Gaussian profile (describing temperature effects). In contrast,

for terrestrial conditions, the Voigt profile is dominated by pressure broadening, resulting in only small contributions from the Gaussian profile. However, the FWHM between pressure and Doppler broadening (responsible for temperature effects) is separated by only one order of magnitude for terrestrial conditions, in contrast to 10 orders of magnitude for the ISM.

The study of line broadening is based on the Ref. [3], i.e. propynal (CHCCHO) is used as a benchmark molecule. It is a 6 atomic molecule with point group C_s , with two identical NSSWs of $g_{ns} = 4$. Moreover, propynal is a near-prolate asymmetric top molecule ($\kappa = -0.990$). (See Ref. [3] for more details.)

Fig. 3.13 shows the lowest vibrational mode of propynal in a bar plot and with three different types of line broadening. A comparison of the Doppler broadening with the temperature broadening shows almost identical cross sections with respect to the macrostructure. As is typical for a broadened spectrum, there are nearly degenerate transitions that give rise to particularly strong single peaks that stand out from the progression. The only difference between Doppler and temperature broadening is that the pattern of these outlier peaks is slightly different. This result is rather surprising, since the Lorentz FWHM of $\Delta\bar{\nu}_L = 4.2 \times 10^{-4} \text{ cm}^{-1}$ is more than one order of magnitude larger than the Gaussian FWHM of $\Delta\bar{\nu}_G \approx 2.8 \times 10^{-5} \text{ cm}^{-1}$.

The wide spectral range and the fairly high rovibrational state density are the reasons why the differences between the two profile shapes and widths are barely visible. More precisely, the fact that the six atomic molecule propynal is relatively heavy (compared to H_2 , N_2 , H_2O , H_2S , CH_4 , NH_3 , etc) and it has a large moment of inertia tensor results in the high rovibrational state density. Since the difference between the profiles is only in the outer regions, but these regions are dominated by the next line (due to the high state density), the differences are not visible. Additionally, propynal is a near-prolate asymmetric top molecule. This results in a very regular and systematic spectrum in contrast to H_2O , H_2S for example. This essentially results in an envelope around the P- and R-branches. The only significant features are the quasi-degenerate lines mentioned above. This has important implications for the further development of the *MOLPRO* program:

- The series of rough approximations introduced in Section 2.4 is legitimate, since the influence of the exact line width is often negligible.
- For molecules with 6 – 10 atoms there is no need to consider very sophisticated broadening algorithms. This is in contrast to other theoretical rovibrational groups, which focus on 2 – 4 atomic molecules with highly accurate semi-empirical PES.
- Hence, the three implemented broadening types already allow for a higher accuracy and flexibility than is actually required for this type of molecules and calculations.

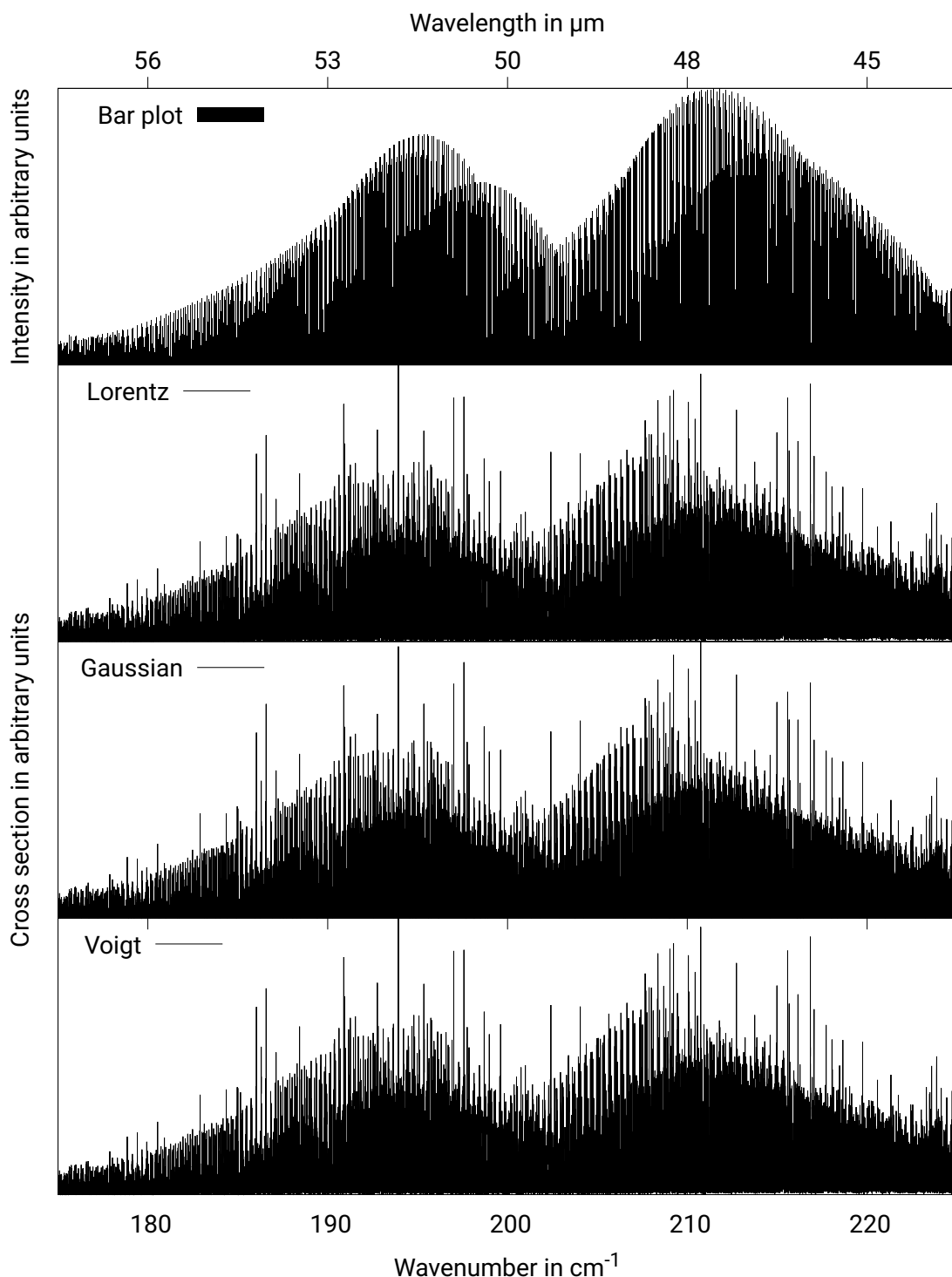


Figure 3.13: Comparison between different types of line broadening for the lowest vibrational band of propynal. The spectrum simulates a temperature of 300 K and a pressure of 1×10^5 Pa. The upper plot shows the spectrum without any broadening. Pure pressure broadening is considered using a Lorentz profile with a FWHM of $\Delta\bar{\nu}_L = 4.2 \times 10^{-4} \text{ cm}^{-1}$ and Doppler broadening is considered using a Gaussian profile with $\Delta\bar{\nu}_G \approx 2.8 \times 10^{-5} \text{ cm}^{-1}$ (depending on the exact line position) as was calculated in Section 2.4. To consider both effects together, a Voigt profile of width $\Delta\bar{\nu}_V = 4.3 \times 10^{-4} \text{ cm}^{-1}$ was used. The computational details for the line list are identical to [3].

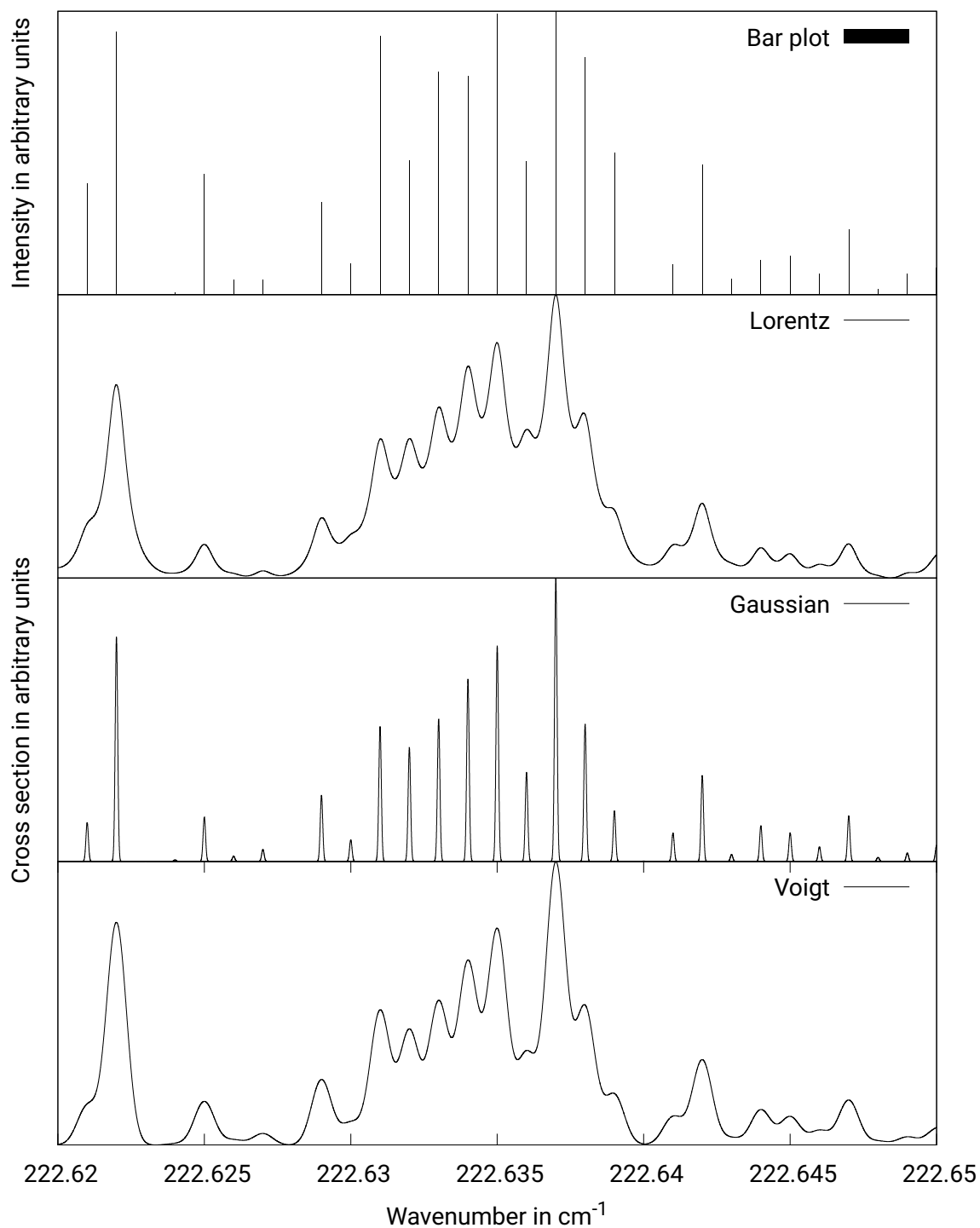


Figure 3.14: Comparison between different types of line broadening for a small number of rovibrational lines of propyne. The spectrum simulates a temperature of 300 K and a pressure of 1×10^5 Pa. The upper plot shows the spectrum without any broadening. Pure pressure broadening is considered using a Lorentz profile with a FWHM of $\Delta\bar{\nu}_L = 4.2 \times 10^{-4} \text{ cm}^{-1}$ and Doppler broadening is considered using a Gaussian profile with $\Delta\bar{\nu}_G \approx 2.8 \times 10^{-5} \text{ cm}^{-1}$ (depending on the exact line position) as was calculated in Section 2.4. To consider both effects together, a Voigt profile of width $\Delta\bar{\nu}_V = 4.3 \times 10^{-4} \text{ cm}^{-1}$ was used. The computational details for the line list are identical to [3].

Since Doppler and temperature broadening yield almost identical spectra, it is not surprising that the Voigt profile also yields the same result. As mentioned before, unlike the broadened spectra, the bar plot allows to see the microstructure consisting of many progressions. This is also the reason why line broadening is only used for comparisons with experiments and not for the spectroscopic analyses as for example in Ref. [1, 4] and in Section 3.2.

Fig. 3.14 shows a very small spectral range of only 0.03 cm^{-1} . It can be seen that the difference between the Lorentz and the Gaussian broadened spectra is indeed very significant. In addition, the Voigt profile yields a similar result to the pressure broadening. This is to be expected, since the convolution of the Lorentz function with the very sharp Gaussian peaks is similar to a convolution with a δ -distribution. Therefore, the profile should remain unchanged. The main conclusion from this figure is that the different types of broadening are correctly implemented and that they behave as expected. In conclusion, the spectral range shown in Fig. 3.14 is smaller than the expected accuracy of the rovibrational transition frequencies. Therefore, the accuracy of the applied broadening is higher than what can be achieved for the line positions.

3.4 RUNTIME OPTIMIZATIONS

Runtime optimizations are critical for quantum chemical calculations in general and for the simulation of rovibrational infrared spectra in particular. To tackle this challenge, quantum chemists employ various optimization techniques such as parallelization, which allows the workload to be distributed among multiple processor cores. Additionally, precalculations such as contractions or the calculation of specific integrals that appear multiple times can reduce the number of required calculations. Finally, sophisticated thresholds for the wave function coefficients can be set to minimize the computational effort required to achieve a desired level of accuracy. These optimizations enable more efficient and accurate simulations, allowing the study of larger molecules.

3.4.1 PARALLELIZATION

One of the most common optimization methods in modern programming is parallelization across multiple processor cores. Since on one hand the general idea is very clear and on the other hand the implementation details are extremely specialized, this will be discussed only briefly and the focus is on the resulting runtime savings. The most important points are that CPU parallelization is used (in contrast to GPU parallelization) and that there are parts in the code that will always run in serial and only for certain loops the parallelization will be used. If the specific loop passes are independent and there is a sufficiently high number of loop

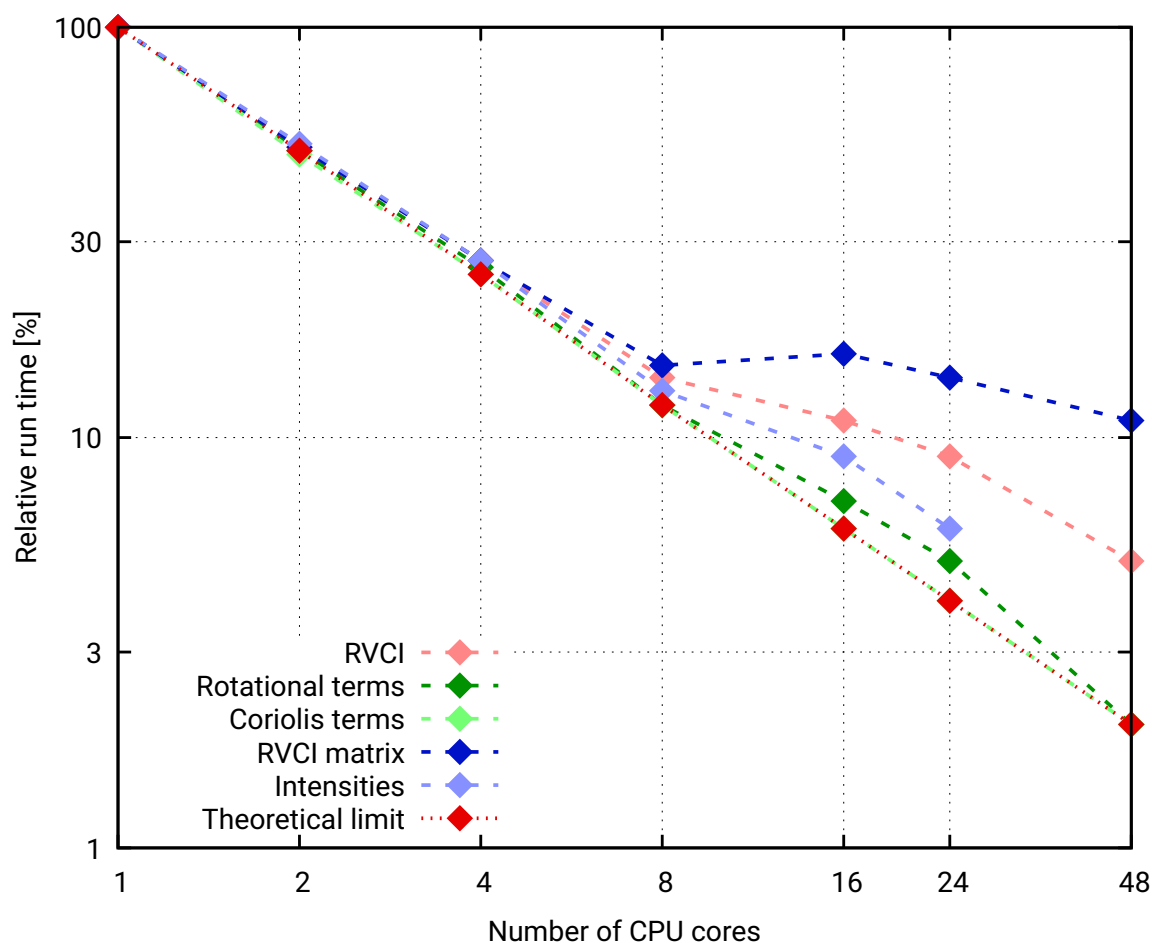


Figure 3.15: Relative runtime in % normalized to the time for one CPU core. In the theoretical limit, there is no overhead, i.e. the runtime scaling for n CPU cores corresponds to $1/n$. Benchmark calculation on H_2CS , with 45 vibrational basis functions, $J_{\max} = 45$, the μ -tensor was considered up to 2nd order for the rotational terms and 1st order for Coriolis coupling terms, the VCI space is restricted to $\text{levex}=5$, $\text{citype}=5$ and $\text{cimax}=15$. For the calculation on 48 CPU cores, an issue for the intensity (faint blue) runtime determination occurred. Since this makes that one data point unreliable, it was excluded.

passes (ideally much larger than the number of CPU cores), than the different passes can be distributed among the cores. The parallelization is implemented for,

- ... the precalculation of the vibrational integral $\langle \phi_{\text{vib}}^{i'} | \mu_{\alpha\beta} | \phi_{\text{vib}}^i \rangle$ of the rotational terms (see also (2.22)). The loops over the left and right vibrational basis functions are combined. Hence, if for example $n_{\text{vib}} = 45$ vibrational basis functions are considered, than $n_{\text{vib}}(n_{\text{vib}} + 1)/2 = 1035$ (for symmetry reasons only a triangle has to be calculated) tasks are distributed among the CPU cores. This results in a very high parallelization efficiency.
- ... the precalculation of the vibrational integral $\sum_{\alpha} \langle \phi_{\text{vib}}^{i'} | \pi_{\alpha} \mu_{\alpha\beta} | \phi_{\text{vib}}^i \rangle$ of the Coriolis coupling terms. Again, the loops over the left and right vibrational basis functions are combined, resulting in a very high parallelization efficiency.

- ... the build up and diagonalization of the RVCI matrices for the different quantum numbers J . Hence, for a large number of CPU cores (> 8) the parallelization efficiency is much lower, since there are only up to J_{\max} tasks to distribute. In the following example for H_2CS $J_{\max} = 45$ is lower than the maximum number of CPU cores, that was considered. However, for large molecules J_{\max} can easily increase up to 100. Further improvements are possible once the block-diagonal structure in the irreps is abused as well.
- ... the intensity calculations. Again, two loops over vibrational states are combined. In contrast to the precalculations, where the loops iterate over vibrational basis functions, in this case the iteration is the assigned initial and final vibrational state. Note that the number of initial vibrational states is 1, if hot bands are not considered. Therefore, a high parallelization efficiency is given, if there are at least some hot bands.
- ... the determination of the vibrational transition moments. The aforementioned loop combination was applied again. However, this part of the program usually takes less than 1 % of the total calculation time. For this reason, and because of the low accuracy of measuring short time intervals (< 5 s), they will not be analyzed in the further discussion.

For the benchmark calculations it was necessary to choose a small molecule with low memory demands. Otherwise the use of up to 48 CPU cores would not be feasible. For this reason, H_2CS with $n_{\text{vib}} = 45$ vibrational basis functions, $J_{\max} = 45$, 2nd order μ -tensor for the rotational terms and 1st order for Coriolis coupling terms was considered. A larger value for J_{\max} and n_{vib} would have been beneficial for the parallelization, but unrealistic and unnecessary for such a small molecule. Hence, this can be understood as a lower bound for the parallelization efficiency. In Fig. 3.15 the two types of precalculations (dark and bright green) nearly reach the maximum possible efficiency, with 158 s (rotational term) and 383 s (Coriolis term) for the single core calculations and 4.5 s and 10.1 s for the 48 core calculations. As mentioned before, the parallelization efficiency is the lowest for the build up and diagonalization of the RVCI matrices (especially for more than 8 CPU cores) and significantly better for the determination of the intensities (bright blue). A problem in the runtime tracking for the 48 core intensity calculation, is the reason that there is one data point missing. The pink curve in Fig. 3.15 shows the overall parallelization efficiency of the RVCI. The exact numbers show that a 48 core calculation requires about 5.3 % of the time for a single core calculation. In contrast, the theoretical limit would be $1/48 = 2.1$ %. This shows that the parallelization is already very efficient, even though the molecule is relatively small.

Table 3.1: Wall clock times of different parts in the RVC1 program with precalculations t_{precalc} and without precalculations t_{Initial}

Program part	t_{Initial} [s]	t_{precalc} [s]
MSRB determination:	9.8	9.2
Precalculation rotation terms:	—	158.1
Precalculation Coriolis terms:	—	382.6
RVC1 energies:	26915.4	3155.5
Vib. trans moments:	22.5	22.4
Infrared intensities:	4842.6	4857.1
RVC1-Total:	31842.7	8562.5

Note: Single core benchmark calculation for H_2CS with $n_{\text{vib}} = 45$ vibrational basis functions, $J_{\text{max}} = 45$, 2nd order μ -tensor for the rotational terms and 1st order for Coriolis coupling terms. Calculation was performed during implementation of the precalculation, hence calculation times can differ from most recent version of the code.

3.4.2 PRECALCULATIONS

The first runtime optimization introduced in the course of this PhD is related to precalculations of vibrational integrals for the RVC1 matrix. As mentioned before, the rotational term can be written as,

$$\frac{1}{2} \sum_{\alpha\beta \in \{x,y,z\}} \langle \phi'_{\text{vib}} | \mu_{\alpha\beta} | \phi''_{\text{vib}} \rangle \langle \phi'_{\text{rot}} | J_{\alpha} J_{\beta} | \phi''_{\text{rot}} \rangle \quad (3.1)$$

with a vibrational integral $\langle \phi'_{\text{vib}} | \mu_{\alpha\beta} | \phi''_{\text{vib}} \rangle$ and a rotational integral $\langle \phi'_{\text{rot}} | J_{\alpha} J_{\beta} | \phi''_{\text{rot}} \rangle$. In addition, the Coriolis coupling term is given by

$$\frac{1}{2} \sum_{\alpha\beta \in \{x,y,z\}} \langle \phi'_{\text{vib}} | \pi_{\alpha} \mu_{\alpha\beta} | \phi''_{\text{vib}} \rangle \langle \phi'_{\text{rot}} | J_{\beta} | \phi''_{\text{rot}} \rangle \quad (3.2)$$

plus a commuted term. There is also a vibrational integral $\langle \phi'_{\text{vib}} | \pi_{\alpha} \mu_{\alpha\beta} | \phi''_{\text{vib}} \rangle$ and a rotational integral $\langle \phi'_{\text{rot}} | J_{\beta} | \phi''_{\text{rot}} \rangle$ for this term. The trivial way to implement this would be to calculate the vibrational integrals for each of the J_{max} different RVC1 matrices. However, since these integrals are independent of J , they are the same for all RVC1 matrices. In Tab. 3.1, the runtime savings are very large. About 86% of the computational time or about a factor of 8 can be saved. The only disadvantage of this optimization is that two additional arrays have to be stored. However, they are much smaller than the RVC1 coefficient array and the intensity array. Therefore, this additional memory demand can be neglected.

Table 3.2: Wall clock times of different parts of the program with contraction $t_{\text{Contracted}}$ and without contraction t_{Initial}

Program part	t_{Initial} [s]	$t_{\text{Contracted}}$ [s]
Precalculation terms:	4.5	4.4
RVCI energies:	3200.1	3251.6
Infrared intensities:	6312.6	1616.9
RVCI-Total:	9614.5	4969.8

Note: Single core benchmark calculation for H_2CS ($n_{\text{vib}} = 25$ vibrational basis functions, $J_{\text{max}} = 70$, 0th order rotational term, 0th order Coriolis coupling term). Since the calculations are performed during implementation, the times can differ for most recent program version. 126 024 rovibrational states and 2 467 195 rovibrational transitions were calculated, with 118 739 transitions being significant enough for printout (relative intensity larger than 1×10^{-6}).

Table 3.3: Wall clock times of different parts of the program with contraction $t_{\text{Contracted}}$ and without contraction t_{Initial}

Program part	t_{Initial} [s]	$t_{\text{Contracted}}$ [s]
Precalculation terms:	56.5	56.9
RVCI energies:	683.5	735.7
Infrared intensities:	248570.6	6672.2
RVCI-Total:	249313.4	7467.4

Note: Single core benchmark calculation for ketenimine ($n_{\text{vib}} = 22$, $J_{\text{max}} = 50$, 0th order rotational terms, 0th order Coriolis coupling terms). 127 448 rovibrational states and 5 634 178 rovibrational transitions were calculated, with 459 017 transitions being significant.

3.4.3 CONTRACTION

Analyses within this PhD have shown that neither the rigid rotor basis (RRB) nor the Wang basis (WB) allow for an accurate quantum number assignment of k . For this reason the molecule specific rotational basis (MSRB) was invented in the course of this PhD. Since the latter is a linear combination of the RRB or the WB, an additional loop over the number of MSRB coefficients occurs in the intensity calculation. More precisely, both the initial and the final rovibrational state require this additional loop. Thus for a calculation with $J_{\text{max}} = 50$ this yields up to $(2J + 1)^2 = 10201$ times more iterations over the innermost routines of the intensity calculation and for $J_{\text{max}} = 70$ it gives $(2J + 1)^2 = 19881$ times more iterations.

However, it is possible to remove these additional loops. To do this, the MSRB coefficients need to be contracted with the RVCI coefficients. This effectively means that the RVCI coefficients are transformed from the MSRB to the RRB or WB. Since similar contraction methods are already used in *MOLPRO*, the technical details will not be discussed here. However, the amount of computational time saved will be quantified.

Two different benchmark calculations are provided, since the results are extremely sensitive to the considered molecule. Note that an older version of the code was used to calculate these timings, as there is no permanent keyword to switch between the uncontracted and the

contracted versions of the program. For H₂CS it can be seen in Tab. 3.2 that the calculation of the RVCIs and eigenvectors takes about 51 s or 1.6 % more due to the additional transformation at the end. However, the intensity calculation takes about 74 % less time. For the total RVCIs computation time, this results in a saving of only about 50 %. There are two reasons for this: First, due to the small number of rovibrational transitions compared to the number of rovibrational states, the energy calculations require an unusually large amount of time. Second, it was found that the influence of the MSRB is smaller for H₂CS compared to ketenimine or propynal. This means that the vectors of the MSRB transformation have large leading coefficients for H₂CS. As a result, many of the iterations in the two additional loops could be skipped. For ketenimine Tab. 3.3 shows that the energy and eigenvector calculation time increases by 7.6 %, but the intensities are determined 97 % faster. Since for ketenimine the intensity calculations dominate the total RVCIs computation time much more, the overall savings are also much higher for ketenimine.

3.4.4 RVCIs COEFFICIENT THRESHOLD

In quantum chemical calculations, it is a common phenomenon that time-consuming loops over a large number of eigenvector coefficients occur. In most cases, only a minority of the coefficients contribute to the majority of the final result. Therefore, it is common to skip the loop pass if the coefficient is smaller than a certain threshold. Common examples of this are during the calculation of Hamiltonian matrix elements or intensities. In both cases, it is usual that the coefficients occur in pairs, since both bra and ket contribute with a coefficient. In this case, it is not obvious how to best apply the threshold. In the course of this thesis, three different ways of applying the thresholds have been studied. This seems to be a rather small detail, but it turned out that there is a large potential for runtime savings. Moreover, many of the results can be generalized and used for different types of quantum chemical simulations.

Checking both coefficients individually with the same threshold will be called *both coefficients method (BCM)*. In the case of a small coefficient in the outer loop, this has the advantage, that the entire inner loop can be skipped. However, there are two *if* statements that need to be checked. If the skipping-ratio, i.e. the number of coefficients below the threshold divided by the number of all coefficients, is not small enough, it produces a lot of unnecessary overhead to check the *if* statements. Another disadvantage occurs when both individual coefficients are a bit too large to be skipped, but the product is small enough to be skipped. However, this is never checked with the BCM.

In contrast, the *product only method (POM)* applies the threshold to the product of the coefficients and not to the individual coefficients themselves. Since this method is more selective, it should be possible to choose a higher threshold, i.e. more calculations can be skipped. One of the main advantages is, that in total more cases will be skipped, since the product of two

Table 3.4: Comparison for the three different threshold methods.

Threshold	Both Coefficients			Product Only			Hybrid		
	t [s]	visual	n_{trans}	t [s]	visual	n_{trans}	t [s]	visual	n_{trans}
1×10^{-2}	1013	✗	50566	7158	✗	55544	1012	✗	55544
1×10^{-3}	1194	✗	19874	7225	✗	46820	1186	✗	46820
1×10^{-4}	1561	○	1842	7220	○	29034	1525	○	29034
1×10^{-5}	2140	✓	48	7197	✓	7073	2044	✓	7073
1×10^{-6}	2774	✓	0	7214	✓	850	2621	✓	850
1×10^{-7}	3399	✓	0	7276	✓	0	3184	✓	0
1×10^{-8}	3996	✓	0	7357	✓	0	3724	✓	0

Note: The total number of transitions is 86387.

coefficients will always be smaller than the individual coefficients. The other advantage is, that the threshold will be checked only once, hence there are potentially less *if* statements. However, a major disadvantage is that, unlike with the BCM, the inner loop cannot be skipped entirely. Therefore, in some cases it may actually require more *if* statement calls.

The *hybrid method (HM)* tries to combine the advantages of both previous methods. It uses both a threshold on the first coefficient and a threshold on the product. The former has the potential to skip the entire inner loop, as mentioned above. The only disadvantage of HM compared to POM is that there are two *if* statements instead of one in the POM. This should only come into play when the skipping-ratio is extremely small.

Since these benchmarks were performed at an earlier stage of the PhD, the reference calculation uses a less time consuming parameter set, than the previous ones. For this reason, H_2CS with $n_{\text{vib}} = 25$ vibrational basis functions, $J_{\text{max}} = 35$, 1st order μ -tensor for the rotational terms and 0st order for the Coriolis coupling terms was considered. To compare the results, two different methods are used to judge whether the influence of the thresholds is reasonably small. The first metric is the number of transitions that differ between the reference calculation without a threshold and the specific calculation with the threshold. This is denoted as n_{trans} in Tab. 3.4. Note that transitions are only printed, if their strength is at least 1×10^{-6} of the strongest line in the spectrum. Moreover, there are 86387 transitions printed in total and they are considered “different” if their change in intensity exceeds 1%. Thus, for a threshold of 1×10^{-4} using the BCM yields a total of 1842 changing lines, i.e. 2.1% of the lines are changed by the threshold. However, this metric is somewhat problematic, because it does not distinguish whether the 1% change in intensity is on a strong or a weak transition. This is solved by the second metric, which is done by visual inspection of the spectra. Although this may not seem very scientific and is not automated, it has the advantage of not being susceptible to numerical noise. In the end, the goal was to provide a binary label of whether the system had converged or not. However, it turned out that distinguishing between three different states

reflects the reality much better. In Tab. 3.4 the symbol ✓ denotes no changes in the spectrum, ✗ denotes significant changes and a o mark barely visible changes. In addition, Tab. 3.4 shows the computation time in seconds for the three different methods. Each method converges at about the same threshold, according to the visual inspection. This makes the analysis much easier, since the quality of the spectra at a given threshold can be assumed to be roughly the same for the different methods.

Tab. 3.4 shows that the BCM leads to a lower number of modified transitions than POM for equal thresholds. This is to be expected since the product of the coefficients is always smaller than the individual coefficient and therefore more loop passes are skipped. Moreover, the POM and HM yield the same results in terms of n_{trans} , which could also be expected for the same reason. The visual comparison shows that the large differences in n_{trans} between the BCM and POM are much less significant, than they appear from the raw numbers. The most important result, however, is the runtime advantage of BCM and HM over POM. While the POM saves about 5%, the other two methods can save up to 80% of computational time without losing too much accuracy. This is due to the fact that POM cannot completely skip the entire inner coefficient loop, while BCM and HM can. The other important finding is, that BCM is only slightly slower than the HM. This is despite the fact, that it leads to one order of magnitude lower n_{trans} in the interesting threshold range between 1×10^{-4} and 1×10^{-6} . In conclusion, although the topic discussed in this subsection may seem unimportant, it could be shown that there are significant runtime improvements possible by choosing the appropriate method. Since similar methods are used for the build up of the RVCI matrix and the VCI matrix, there is also a significant potential for generalization. Moreover, these results can be improved by introducing sparse coefficient arrays. In this case, the if statements are applied only once per coefficient, as opposed to many times in the intensity calculation.

4

Summary and Conclusion

A new implementation of rovibrational configuration interaction (RVCI) theory has been developed in this thesis for the determination of rovibrational energies and infrared intensities using configuration interaction theory. The approach is based on a multi-mode expansion of the multi-dimensional potential energy surface (PES) and dipole moment surface (DMS), incorporating vibrational self-consistent field (VSCF) theory and vibrational configuration interaction (VCI) theory. Unlike the previously developed rotational configuration interaction (RCI), the new approach accounts for the interaction between rotational and vibrational bands by using a direct product between vibrational and rotational basis functions. The rotational and Coriolis coupling terms are implemented including the higher order terms of the inverse effective moment of inertia tensor μ of the Watson Hamiltonian. In addition, a new rotational basis function called molecule specific rotational basis (MSRB) is introduced to improve the assignment of the quantum number k .

For the convergence of various series expansions for the RVCI theory H_2CS is used as a benchmark molecule. In contrast to Ref. [2], this work shows mainly qualitative differences in the spectra. Five different parameters are considered in terms of their convergence behavior, with some of them showing a very individual phenomenon in the spectrum if not sufficiently converged. The calculations obtained with smaller J_{max} show an artificial additional band head. Since this is always the case when J_{max} is not converged, it is relatively easy to detect in

most cases. The artifacts caused by an improper convergence of J_{\max} are significant and are therefore not a valid compromise to save computation time.

Larger molecules such as ketenimine and propynal depend critically on the convergence of the CI space. This applies not only to the VCI energies but also to the wave functions. A slightly too small CI space will only result in frequency and intensity shifts. In this case, the VCI wave functions are largely converged. In contrast, the effect of an insufficiently converged VCI wave function leads to extreme artifacts and there is almost no agreement with the correct spectrum. Consequently, the VCI energies are a weak indicator for the convergence of the corresponding wave functions. A better indicator is provided by the VCI intensities.

The size of the vibrational basis set is a crucial parameter in terms of quantitative changes, but the qualitative changes are much more subtle than for J_{\max} and for the CI space. The overall structure remains relatively unchanged regardless if only 4 or 45 excited vibrational bands are considered. A larger vibrational basis set leads to shifts for these bands, but an insufficient convergence does not lead to artifacts and is therefore difficult to detect. Usually the spectral separation between different vibrational bands is a good indicator for the strength of the coupling.

A characteristic feature of H_2CS is the particularly strong Coriolis coupling between two quasi-degenerate vibrational modes. The 0th order Coriolis coupling is very significant in this region. A comparison of the 0th order Coriolis coupling with the 1st order shows almost no difference in the macrostructure. In contrast to the Coriolis coupling terms, the rotational terms require a one order higher μ -tensor expansion. A comparison between the 0th and 1st order rotational terms shows shifts for progressions of at most 5 cm^{-1} . The changes induced by the 2nd order terms are not visible on a 40 cm^{-1} wide plot range. Moreover, it should be noted that there are hardly any intensity shifts visible. In addition, the absence of higher order coupling terms does not cause artifacts in the spectrum. This is in contrast to an insufficiently converged CI space or J_{\max} . Hence, a lack of higher order coupling terms is much more difficult to spot in the resulting spectra.

The first paper [1] written in the course of this thesis studied ketenimine (CH_2CNH). The calculation in that paper relied on a number of approximations, that could be removed over the last years. Most of these approximations did not drastically affect the spectra. Except for the regions at 800 to 950 cm^{-1} and 2900 to 3100 cm^{-1} there are only minor changes. However, the quality of the quantum number assignment, the consistency of the intensities and the consideration of coupling has improved significantly over the last three years. This can be seen for the ν_1 band and for the strong coupling between $\nu_8 + \nu_{12}$ and ν_{11} . The latter two bands also confirmed an assumption made in Ref. [1] that higher order μ -tensor terms are only needed when at least three vibrational *modes* differ between two vibrational *states*. The new calculations also revealed an interesting turnaround progression in this region.

The line broadening study is based on the Ref. [3] using propynal (CHCCHO) as a benchmark molecule. For small molecules (N_2 , H_2O , CH_4 , NH_3 , etc) different broadening profiles (for different broadening effects) have been invented, ranging from Lorentz and Gaussian profiles to Voigt and beyond Voigt profiles. Since the RVCI theory is specialized for larger molecules (6 – 10 atoms), it was assumed that the more sophisticated broadening profiles were not needed. However, Lorentz, Gaussian, and Voigt profiles have been implemented during this PhD project. Although the Lorentz FWHM is more than one order of magnitude larger than the Gaussian FWHM under terrestrial conditions, a comparison of the Doppler broadening with the temperature broadening shows almost identical cross sections for propynal. The reason for this is that the high mass (compared to N_2 , H_2O , CH_4 , NH_3 , etc) and the larger moment of inertia tensor lead to the high rovibrational state density. This confirms the assumption that for molecules with 6 – 10 atoms there is no need to consider sophisticated broadening algorithms.

Four different types of runtime optimizations have been implemented and analyzed in this thesis. The parallelization scales almost perfectly in the number of CPU cores for the two types of precalculations and intensity calculation. Only the RVCI matrix build up and diagonalization saturates at 8 CPU cores for small molecules. The precalculations of vibrational integrals save about 86% or a factor of 8 in total computation time. The contraction of the MSRB coefficients and the RVCI coefficients result in a total computational time reduction of 50% for H_2CS and 97% for ketenimine. Lastly, a comparison between different implementations of the RVCI coefficient thresholds showed that the most efficient way is to check both thresholds individually with up to 80% runtime savings.

5

Outlook

To achieve the goal of predicting infrared reference spectra for *6-12 atomic* biologically relevant gases at *room temperature* for a *broad spectral range*, with *MOLPRO*, no additional features are actually needed. Instead, the main problem lies in the memory requirements and the runtime efficiency of the program. Thus, the calculation of the three applications presented in this thesis was only achieved through compromises in one or more of the above aspects: in some cases, 4-atomic molecules were calculated (which is on the edge what other research groups can also calculate), or the spectral range had to be very small (see [3], 6 atoms but only 0 to 350 cm⁻¹). In addition, the focus was on low temperatures in the range from 10 to 200 K as found in the interstellar medium (ISM). These results are very valuable and useful for the ISM community and offer many further applications in the future. However, the current state of the program is still not quite performant enough to calculate larger molecules at higher temperatures, mainly due to computational efficiency. Therefore, at first various methods to improve the efficiency will be presented (see Section 5.1). Subsequently, a series of additional functionalities will be introduced to make the program more universally applicable (see Section 5.2). Last but not least, an outlook is given for a number of projects that were started as part of this PhD but were not originally planned and therefore have not yet come to a final conclusion (see Section 5.3).

5.1 RUNTIME AND MEMORY SAVINGS

The RVC matrix has a block-diagonal structure in the J quantum number, which is of course exploited. In addition, there is another block-diagonal structure in the rovibrational irreps. Exploiting this symmetry-based optimization requires the use of one of the two Wang bases mentioned before. This rotational basis was implemented by Erfort. In this thesis, an algorithm was implemented that swapped the rows and columns of the matrix to visualize this block diagonal structure for the matrix build up and diagonalization. However, this was only for testing purposes, to check if the Wang combinations and the MSRB are implemented correctly. Based on this, it is now possible to actually exploit the block diagonal structure with little effort. This would have several advantages: There are memory savings due to shorter eigenvectors. (For example, for C_2 or C_S symmetry by a factor of 2, for C_{2v} symmetry by a factor of 4, etc.) An equally important effect is the runtime savings: On the one hand, because fewer matrix elements have to be calculated, on the other hand, because the diagonalization is faster, and last but not least, because the vectors become shorter for the intensity calculations.

Another, and perhaps the most powerful way to save memory is to exploit sparsity in the array that saves the RVC eigenvector coefficients. This is allocated at full size prior to computing the RVC matrices and is one of the two most memory consuming arrays in RVC, along with the array storing the intensities and transition moments. The main reason why the memory optimization is so crucial is that the parallelization can no longer be used in a meaningful way due to the vast amount of memory required. For example, a calculation for a 6 atomic molecule, with a vibrational basis of about 100 states and $J_{\max} = 100$ requires in some cases 150 GB working memory. This only allows the computation to be done on 3-6 cores instead of 48 cores otherwise. This is mainly a technical problem. The exploitation of sparsity combined with parallelization and the static memory management of *MOLPRO* make this task challenging. Since the array that stores all eigenvectors is allocated prior to setting up the RVC matrices for different J values in parallel and diagonalizing them, the knowledge of how large the sparse eigenvector array has to be is missing during allocation. A possible solution could be to write the eigenvectors temporarily in a sparse way on the disk and to read them later again.

As mentioned before, there are two arrays which cause most of the total memory requirements. One of the two arrays stores the intensity and the transition moments. Since for asymmetric top molecules only the selection rule for J is valid but not the rule for k_a and k_c , there is an extremely high number of rovibrational transitions which are taken into account, but only a small part of them has meaningful intensity. For instance, during the calculations for DPNN, 1×10^8 transitions were initially considered, although ultimately only 4×10^5 transitions had a sufficiently high intensity of 0.1 % relative to the most intense rovibrational line

in the spectrum. Concerning the 6 atomic propynal, 1.7×10^8 transitions were first considered of which 1×10^7 had a relative intensity higher than 0.001 % (very conservatively chosen). Moreover, for each transition, both the temperature-independent rovibrational transition moment and the intensity for each desired temperature are stored. Thus, an array size of more than 1×10^9 entries is achieved easily. However, by using the program within this PhD, it has been shown that calculating and storing the transition moment without any intensities is perfectly adequate and is also common in the community. To determine the temperature dependent prefactor for the thermal occupation of the states and thus the intensities only the partition function for the corresponding temperature is required. Thus, the size of the array can be reduced to the number of transition moments. Furthermore, sparsity could be used for this array as well, since a large amount of considered transitions has no meaningful intensity. An easy solution for the abuse of sparsity is prevented by the fact that neither linked lists nor dynamic memory management can be used in *MOLPRO*. A possible workaround is a batch mode that occasionally prints the already calculated values and keeps only a part of the array in the memory. However, this will cause minor printout problems for parallel calculations of the program, since the transitions will be printed in an unsorted way. Alternatively, at first all sufficiently intensive transitions could be written on the disk, while the program is in parallel mode. After all transitions have been calculated, the parallel mode is terminated, the information is read again, sorted and printed in an ordered fashion.

While some successful attempts have been made for the rotational terms to save runtime, this has not yet been done for the Coriolis coupling terms. The 0D μ -tensor coupling terms are usually computed very quickly and probably do not need any optimization. As shown in Ref. [2], the 1D μ -tensor terms for a 4 atomic molecule can still be computed in ≈ 50 s, but the efficiency scales very poorly, so that even for such a small molecule the runtime for the 2D terms increase to ≈ 1600 s. In the previously mentioned publication, H_2CS was deliberately chosen as it is a relatively strongly coupled molecule. For states with high assignment confidence, the 2D terms, have shown average errors of only 0.2 cm^{-1} . However, on average over all states, the deviations are about 5.3 cm^{-1} . Therefore, it would be useful to introduce an intermediate level between 1D and 2D terms, where prescreening is used to identify the largest contributions of the 2D terms early on and only consider them in the calculation. Also, some runtime critical if-statements in the innermost loops in the code (due to Kronecker δ s in the equations) could be removed together with one of the loops by loop-unrolling. The number of nested if-statements increases strongly with order, which is why this could be especially important for the 2D terms. Another point for optimization is the threshold value used to decide whether the product of the coefficients of the two VCI wave functions (initial and final state) is large enough to calculate the Coriolis coupling term for this matrix entry. So far, this

threshold is independent of whether 0D, 1D or 2D terms are calculated. As at other places in the program code and e.g. with the rotational terms could be tightened for the higher orders.

A further small runtime optimization occurs in the intensity calculation when Wang combinations are used as the rotational basis. However, the integrals for the rotational part are implemented for symmetric top basis functions. That is, the integral $\langle J', k' | D | J'', k'' \rangle$ (with the DMS D) can be computed directly by an analytic expression. If a Wang combination $|J'', K'', \tau''\rangle \propto |J'', k''\rangle \pm |J'', -k''\rangle$ is used, the integral must be evaluated four times (two possibilities each for $\langle J', K', \tau' |$ and $|J'', K'', \tau''\rangle$). However, since there is a loop over the RVCI basis functions anyway, there is the possibility of a contraction of the two Wang coefficients with the RVCI coefficients. This could save up to a factor of four in runtime during the intensity calculation.

An additional method that could potentially save runtime in the calculation of RVCI energies concerns the rotational integrals. These are generally calculated analytically and are therefore already relatively efficient. However, the same rotational integrals are calculated very often (especially for large J quantum numbers). In principle, these values could be calculated once, stored in an array and then only read in. In contrast to the other methods presented here, it is very difficult to estimate how big the runtime benefit is, since in this case the computational effort must be weighed against the time required to read out an array.

5.2 ADDITIONAL FUNCTIONALITY

So far, there are some limitations in the implementation of RVCI. For example, only molecules that are non-linear and with an asymmetric top moment of inertia tensor can be computed. The modifications of algorithms for symmetric and spherical tops are mainly related to changes in the assignment and are thus fairly localized. In addition, there are effects on the selection rules, whereby this primarily results in runtime savings. In contrast, non-linear molecules require changes in the Watson Hamiltonian, in the consideration of non-Abelian point groups, in the assignment of quantum numbers, especially with respect to the l quantum number, and last but not least in the selection rules. Some of these changes are already partially implemented, but for the rovibrational code, most of it is still to come.

An essential feature of the *MOLPRO* program package is its ease of use compared to similar programs. It is crucial to set as many input parameters as possible automatically, without the need for the user to understand all parts of the program. Since the RVCI program is a very new part, it still requires relatively many user settings. So far the maximum total angular momentum J_{\max} has to be set manually. This could be determined automatically from the convergence behavior of the partition function. Also, the order of the μ tensor for the rotational and Coriolis coupling terms could possibly be set automatically by prescreening of

the corresponding integrals. However, non-converged VCI wave functions are a bigger problem for the subsequent RVC calculation. This leads to artifacts in the rotational vibration spectra, as discussed in Chapter 4. The fact, that the VCI wave functions are sometimes not converged is not surprising, since during the iterations of the VCI calculations so far there is only a convergence check for the energy eigenvalues, but not for the eigenvectors. However, this phenomenon can only be detected after the RVC calculation is finished. In principle there are different possible solutions, which shall not be discussed here. However, at the end some key aspects will be to have at least a monitoring of the convergence behavior of the eigenvectors and an algorithm that automatically determines whether a rovibrational progression contains artifacts.

The determination of the partition function is a relatively simple part of the program, which leads for the isotopically pure spectra that we consider only to a global prefactor. However, this prefactor becomes crucial when different isotopes or different molecules are represented in a single spectrum. Moreover, the partition function is also of interest apart from line lists and spectra, since it is an important thermodynamical quantity. As mentioned above, two methods for its calculation have been implemented so far. In the first case, the separation approximation or the rigid rotor approximation is used. Thereby, the VSCF modals can be used to efficiently approximate vibrational energies up to an arbitrary level. The same is true for the rotational energies using the RCI. Alternatively, the separation approximation can be dropped and the RVC energies can be used directly to calculate the partition function. Although this removes an approximation, it does not necessarily lead to a more accurate result, because the calculation of the RVC matrices for high J is very time-consuming and therefore the expansion has to be stopped earlier than with the RCI. Furthermore, the vibrational space spanned by the VCI wave functions is significantly smaller compared to using VSCF modals in the separation method. The solution here would be a hybrid method, which uses the RVC energies for low J values and vibrational frequencies and approximates the remaining part with the separation approximation.

A final additional feature that is critical to the computation of line lists are uncertainties or error estimates for the rovibrational energies and intensities. In well-known infrared (IR) databases such as HITRAN [127, 130] and Exomol [84], the uncertainties are given for either one or both quantities. This is of particular importance for the identification of molecules, since it is preferable to skip uncertain lines rather than plotting them incorrectly in the spectrum. For the determination of uncertainties for the energy and intensities there are in principle a number of possibilities, such as statistical approaches in which the calculations are run several times and then the mean and standard deviation are determined for each line position and strength. The use of learning algorithms is also conceivable. These can generalize e.g. for one spectrum from a small number of labeled lines to all lines. Alternatively, they could be

trained on a small number of molecules and then generalized to many molecules. Furthermore, uncertainties in the energies could be estimated using the residuals in the parameter fitting (PFIT).

5.3 MISCELLANEOUS

Last but not least, there are a number of projects that were started within the framework of this PhD, but were not originally planned and therefore have not yet come to a final conclusion. The most important of these projects are briefly outlined here.

As already mentioned before, the parameter fitting (PFIT) program already provides values for the rotational and all centrifugal distortion constants up to the sextic order. However, the implemented Gauss-Newton optimizer converges relatively unreliably and slowly. This could be addressed by a more sophisticated optimizer. Also, a proper algorithm to reduce the number of states that are fitted is needed. This is also done in the *SPFIT* used by experimenters to achieve better convergence. Currently, this task is solved by relying on the assignment threshold and an iterative residuum cutoff, which is considered an interim solution. Once the PFIT program provides reliable values, the fitted Hamiltonian could then be used to feed back information to the RVC program, to improve the quality of its results. For example, the quantum number assignment could be improved, estimates for the uncertainties in the RVC energies could be made, unstable lines could be identified, or unconverged VCI wave functions could be detected. Hence, the PFIT has the potential to accomplish much more tasks, than purely fitting the spectroscopic constants.

The presence of unstable lines has already been addressed in Chapter 3. An algorithm to solve the problem was also presented. However, this phenomenon is also described in the works of the groups of Tennyson [125] and Tyuterev [75]. Since neither group follows our approach, a comparison with their methods might be helpful and inspirational. So far, in *MOLPRO*, a random minimal perturbation (of about $1 \times 10^{-3} \text{ cm}^{-1}$) is applied to all rovibrational states to cancel the degeneracy. Although this has never caused problems before, it does not seem to be a great solution. If there were an algorithm that detected the unstable lines, this minimal perturbation could be applied much more selectively. For this reason, the search for such an algorithm seems to be a very desirable goal.

One topic where a lot has been achieved within this PhD is the assignment of the k and ν quantum numbers and for the irreps. The introduction of the MSRB, the use of the projection method instead of purely considering the leading coefficients, and an irrep assignment based on the irrep of the RVC basis functions instead of the detour via the bad k, ν quantum number of the RVC eigenvector has led to much more stable and consistent results. Nevertheless, there are of course cases where the assignment of the k, ν quantum number does

not work reliably. As mentioned above, the assignment of the irreps – and thus that of the NSSW prefactor – has been decoupled from the assignment of the k and J quantum numbers. This makes it necessary to find out whether there is really a practical benefit to improving the assignment of k and J , or whether this is a purely academic problem.

Abbreviations

AGB	asymptotic giant branch
BCM	both coefficients method
COM	complex organic molecules
DIM	direct imaging method
DMS	dipole moment surface
EM	exomoon
EP	exoplanet
EPA	exoplanet atmosphere
FWHM	full width at half maximum
HM	hybrid method
IR	infrared
ISM	interstellar medium
MSRB	molecule specific rotational basis
NSSW	nuclear spin statistical weights
PES	potential energy surface
PFIT	parameter fitting
POM	product only method

PS	polarisability surface
RCI	rotational configuration interaction
RRB	rigid rotor basis
RVCI	rovibrational configuration interaction
RVM	radial velocity method
SNR	signal-to-noise ratio
TM	transit method
VAM	vibrational angular momentum
VCI	vibrational configuration interaction
VSCF	vibrational self-consistent field
WB	Wang basis

List of Figures

1.1	Program Structure Overview	5
3.1	Convergence behavior of J_{\max}	49
3.2	Convergence behavior of the VCI space	51
3.3	Convergence behavior of the vibrational basis set size	53
3.4	Convergence behavior of μ -tensor expansion for Coriolis coupling term	55
3.5	Convergence behavior of μ -tensor expansion for rotational term	56
3.6	Influence of NSSWs for H ₂ CS	58
3.7	Ketenimine Overview Spectrum	60
3.8	Ketenimine Low Frequency Spectrum	62
3.9	Ketenimine Strongly Coupled Region Spectrum	63
3.10	Ketenimine Medium Frequency Spectrum	65
3.11	Ketenimine High Frequency Spectrum	66
3.12	Ketenimine Turnaround Progression	67
3.13	Propynal line broadening wide spectrum	70
3.14	Propynal line broadening wide spectrum	71
3.15	Parallelization	73

List of Tables

2.1	Transformation k to k_a and k_c quantum numbers	32
3.1	Wall clock times with and without precalculations	75
3.2	Wall clock times with and without contraction thioformaldehyde	76
3.3	Wall clock times with and without contraction ketenimine	76
3.4	Comparison threshold methods	78

Bibliography

- [1] M. Tschöpe, B. Schröder, S. Erfort, and G. Rauhut, *Frontiers Chem.* **8**, 623641 (2021), URL <https://www.frontiersin.org/articles/10.3389/fchem.2020.623641>.
- [2] M. Tschöpe and G. Rauhut, *J. Chem. Phys.* **157**, 234105 (2022), URL <https://doi.org/10.1063/5.0129828>.
- [3] M. Tschöpe and G. Rauhut, *Mon. Not. R. Astron. Soc.* **520**, 3345–3354 (2023), URL <https://doi.org/10.1093/mnras/stad251>.
- [4] M. Tschöpe and G. Rauhut, *Astrophys. J.* **949**, 1 (2023), URL <https://doi.org/10.3847/1538-4357/acc9ad>.
- [5] M. H. Hart, *An Explanation for the Absence of Extraterrestrials* (Cambridge University Press, 1995), pp. 1–8, URL <https://doi.org/10.1017/CB09780511564970.003>.
- [6] P. Ward and D. Brownlee, *Donald Brownlee*. New York: Copernicus (2000), URL <https://doi.org/10.1007/b97646>.
- [7] A. Sandberg, E. Drexler, and T. Ord, arXiv preprint arXiv:1806.02404 (2018), URL <https://doi.org/10.48550/arXiv.1806.02404>.
- [8] C. D. Dressing and D. Charbonneau, *Astrophys. J.* **767**, 95 (2013), URL <https://doi.org/10.48550/arXiv.1302.1647>.
- [9] A. Wandel, *Astrophys. J.* **941**, 184 (2022), URL <https://doi.org/10.3847/1538-4357/ac9e00>.
- [10] U. Peter, *9. Extraterrestrial Intelligent Life* (Springer Berlin Heidelberg, Berlin, Heidelberg, 2003), p. 205–227, URL https://doi.org/10.1007/978-3-540-43988-2_9.
- [11] D. A. Gurnett, *Trans. Am. Clin. Climatol.* **120**, 299 (2009), URL <https://pubmed.ncbi.nlm.nih.gov/19768185>.

- [12] Y. Oba, Y. Takano, Y. Furukawa, T. Koga, D. P. Glavin, J. P. Dworkin, and H. Naraoka, *Nat. Commun.* **13**, 2008 (2022), URL <https://doi.org/10.1038/s41467-022-29612-x>.
- [13] D. Qasim, H. L. McLain, J. C. Aponte, D. P. Glavin, J. P. Dworkin, and C. K. Materese, *ACS Earth Space Chem.* **7**, 156–167 (2023), URL <https://doi.org/10.1021/acsearthspacechem.2c00274>.
- [14] F. Roques, Q. Kral, J. Schneider, and P. Thébault, *The Extrasolar Planets Encyclopaedia*, <http://www.exoplanet.eu/> (2023), [Online; accessed 15-March-2023].
- [15] D. M. Kipping, *Mon. Notices Royal Astron. Soc.* **392**, 181 (2008), URL <https://doi.org/10.1111/j.1365-2966.2008.13999.x>.
- [16] D. M. Kipping, *Mon. Notices Royal Astron. Soc.* **396**, 1797 (2009), URL <https://doi.org/10.1111/j.1365-2966.2009.14869.x>.
- [17] L. Kreidberg, R. Luger, and M. Bedell, *Astrophys. J. Lett* **877**, L15 (2019), URL <https://dx.doi.org/10.3847/2041-8213/ab20c8>.
- [18] K. O. Todorov, Ph.D. thesis, Connecticut College (2008), URL <https://digitalcommons.conncoll.edu/cgi/viewcontent.cgi?article=1000&context=physicsph>.
- [19] K. Todorov, D. Deming, J. Harrington, K. B. Stevenson, W. C. Bowman, S. Nymeyer, J. J. Fortney, and G. A. Bakos, *Astrophys. J.* **708**, 498 (2009), URL <https://dx.doi.org/10.1088/0004-637X/708/1/498>.
- [20] J. T. Wright and B. S. Gaudi, arXiv preprint arXiv:1210.2471 (2012), URL <https://doi.org/10.48550/arXiv.1210.2471>.
- [21] *Methods of detecting exoplanets*, https://en.wikipedia.org/wiki/Methods_of_detecting_exoplanets (2023), [Online; accessed 16-March-2023].
- [22] H. J. Deeg and R. Alonso, in *Handbook of Exoplanets* (Springer International Publishing, 2018), pp. 633–657, URL https://doi.org/10.1007%2F978-3-319-55333-7_117.
- [23] H. A. Knutson, D. Dragomir, L. Kreidberg, E. M.-R. Kempton, P. R. McCullough, J. J. Fortney, J. L. Bean, M. Gillon, D. Homeier, and A. W. Howard, *Astrophys. J.* **794**, 155 (2014), URL <https://dx.doi.org/10.1088/0004-637X/794/2/155>.

- [24] L. Kreidberg, D. D. B. Koll, C. Morley, R. Hu, L. Schaefer, D. Deming, K. B. Stevenson, J. Dittmann, A. Vanderburg, D. Berardo, et al., *Nature* **573**, 87 (2019), URL <https://doi.org/10.1038/s41586-019-1497-4>.
- [25] M. R. Swain, R. Estrela, G. M. Roudier, C. Sotin, P. B. Rimmer, A. Valio, R. West, K. Pearson, N. Huber-Feely, and R. T. Zellem, *Astrophys. J. Lett.* **161**, 213 (2021), URL <https://dx.doi.org/10.3847/1538-3881/abe879>.
- [26] L. V. Mugnai, D. Modirrousta-Galian, B. Edwards, Q. Changeat, J. Bouwman, G. Morello, A. Al-Refaie, R. Baeyens, M. F. Bieger, D. Blain, et al., *Astrophys. J. Lett.* **161**, 284 (2021), URL <https://dx.doi.org/10.3847/1538-3881/abf3c3>.
- [27] J. E. Libby-Roberts, Z. K. Berta-Thompson, H. Diamond-Lowe, M. A. Gully-Santiago, J. M. Irwin, E. M.-R. Kempton, B. V. Rackham, D. Charbonneau, J.-M. Désert, J. A. Dittmann, et al., *Astrophys. J. Lett.* **164**, 59 (2022), URL <https://dx.doi.org/10.3847/1538-3881/ac75de>.
- [28] Z. K. Berta, D. Charbonneau, J.-M. Désert, E. M.-R. Kempton, P. R. McCullough, C. J. Burke, J. J. Fortney, J. Irwin, P. Nutzman, and D. Homeier, *Astrophys. J.* **747**, 35 (2012), URL <https://dx.doi.org/10.1088/0004-637X/747/1/35>.
- [29] Parviainen, H., Pallé, E., Chen, G., Nortmann, L., Murgas, F., Nowak, G., Aigrain, S., Booth, A., Abazorus, M., and Iro, N., *Astron. Astrophys.* **609**, A33 (2018), URL <https://doi.org/10.1051/0004-6361/201731113>.
- [30] Y. Kawashima and M. Ikoma, *Astrophys. J.* **877**, 109 (2019), URL <https://dx.doi.org/10.3847/1538-4357/ab1b1d>.
- [31] J. E. Owen and Y. Wu, *Astrophys. J.* **775**, 105 (2013), URL <https://doi.org/10.1088/0004-637X/775/2/F105>.
- [32] B. J. Fulton, E. A. Petigura, A. W. Howard, H. Isaacson, G. W. Marcy, P. A. Cargile, L. Hebb, L. M. Weiss, J. A. Johnson, T. D. Morton, et al., *Astrophys. J. Lett.* **154**, 109 (2017), URL <https://dx.doi.org/10.3847/1538-3881/aa80eb>.
- [33] D. Charbonneau, T. M. Brown, R. W. Noyes, and R. L. Gilliland, *Astrophys. J.* **568**, 377 (2002), URL <https://dx.doi.org/10.1086/338770>.
- [34] M. R. Swain, G. Vasisht, G. Tinetti, J. Bouwman, P. Chen, Y. Yung, D. Deming, and P. Deroo, *Astrophys. J.* **690**, L114 (2008), URL <https://dx.doi.org/10.1088/0004-637X/690/2/L114>.

- [35] M. R. Swain, G. Tinetti, G. Vasisht, P. Deroo, C. Griffith, J. Bouwman, P. Chen, Y. Yung, A. Burrows, L. R. Brown, et al., *Astrophys. J.* **704**, 1616 (2009), URL <https://dx.doi.org/10.1088/0004-637X/704/2/1616>.
- [36] K. Haynes, A. M. Mandell, N. Madhusudhan, D. Deming, and H. Knutson, *Astrophys. J.* **806**, 146 (2015), URL <https://dx.doi.org/10.1088/0004-637X/806/2/146>.
- [37] A. Tsiaras, M. Rocchetto, I. P. Waldmann, O. Venot, R. Varley, G. Morello, M. Damiano, G. Tinetti, E. J. Barton, S. N. Yurchenko, et al., *Astrophys. J.* **820**, 99 (2016), URL <https://dx.doi.org/10.3847/0004-637X/820/2/99>.
- [38] A. Tsiaras, I. P. Waldmann, G. Tinetti, J. Tennyson, and S. N. Yurchenko, *Nat. Astron.* **3**, 1086 (2019), URL <https://doi.org/10.1038/s41550-019-0878-9>.
- [39] S. Seager, M. Schrenk, and W. Bains, *Astrobiology* **12**, 61 (2012), URL <https://doi.org/10.1089/ast.2010.0489>.
- [40] S. J. Messenger, Ph.D. thesis, Massachusetts Institute of Technology (2013), URL <http://hdl.handle.net/1721.1/79156>.
- [41] S. Seager, W. Bains, and J. Petkowski, *Astrobiology* **16**, 465 (2016), URL <https://doi.org/10.1089/ast.2015.1404>.
- [42] W. Cash, *Nature* **442**, 51 (2006), URL <https://doi.org/10.1038/nature04930>.
- [43] W. Cash, *Astrophys. J.* **738**, 76 (2011), URL <https://dx.doi.org/10.1088/0004-637X/738/1/76>.
- [44] V. P. Bailey, M. Bottom, E. Cady, F. Cantalloube, J. De Boer, T. Groff, J. Krist, M. A. Millar-Blanchaer, A. Vigan, J. Chilcote, et al., in *Space Telescopes and Instrumentation 2018: Optical, Infrared, and Millimeter Wave* (SPIE, 2018), vol. 10698, pp. 1913–1925, URL <https://doi.org/10.1117/12.2313820>.
- [45] J. Krist, R. Effinger, B. Kern, M. Mandic, J. McGuire, D. Moody, P. Morrissey, I. Poberezhskiy, A. Riggs, N. Saini, et al., in *Space Telescopes and Instrumentation 2018: Optical, Infrared, and Millimeter Wave* (SPIE, 2018), vol. 10698, pp. 788–810, URL <http://dx.doi.org/10.1117/12.2310043>.
- [46] B. S. Gaudi, S. Seager, B. Mennesson, A. Kiessling, K. Warfield, G. Kuan, K. Cahoy, J. T. Clarke, S. Domagal-Goldman, L. Feinberg, et al., arXiv preprint arXiv:1809.09674 (2018), URL <https://doi.org/10.48550/arXiv.1809.09674>.

- [47] J. Wang, D. Mawet, R. Hu, G. Ruane, J.-R. Delorme, and N. Klimovic, *Baseline requirements for detecting biosignatures with the habex and luvor mission concepts* (2018), URL <https://doi.org/10.48550/arXiv.1806.04324>.
- [48] H. S. P. Müller, S. Thorwirth, D. A. Roth, and G. Winnewisser, *Astron. Astrophys.* **370**, L49 (2001), URL <https://doi.org/10.1051/0004-6361:20010367>.
- [49] H. S. P. Müller, F. Schlöder, J. Stutzki, and G. Winnewisser, *J. Mol. Struct.* **742**, 215 (2005), URL <https://doi.org/10.1016/j.molstruc.2005.01.027>.
- [50] C. P. Endres, S. Schlemmer, P. Schilke, J. Stutzki, and H. S. P. Müller, *J. Mol. Spectrosc.* **327**, 95 (2016), URL <https://doi.org/10.1016/j.jms.2016.03.005>.
- [51] J. A. Ball, C. A. Gottlieb, A. E. Lilley, and H. E. Radford, *Astrophys. J.* **162**, L203 (1970), URL https://ui.adsabs.harvard.edu/link_gateway/1970ApJ..162L.203B/doi:10.1086/180654.
- [52] L. J. Allamandola, A. G. G. M. Tielens, and J. R. Barker, *Astrophys. J. Suppl. Ser.* **71**, 733 (1989), URL <https://doi.org/10.1086/191396>.
- [53] J. Cami, J. Bernard-Salas, E. Peeters, and S. E. Malek, *Science* **329**, 1180 (2010), URL <http://dx.doi.org/10.1126/science.1192035>.
- [54] E. Herbst and E. F. van Dishoeck, *Annu. Rev. Astron. Astrophys.* **47**, 427 (2009), URL <https://doi.org/10.1146/annurev-astro-082708-101654>.
- [55] D. E. Woon, *Astrophys. J.* **571**, L177 (2002), URL <https://doi.org/10.1086/341227>.
- [56] P. Theule, F. Borget, F. Mispelaer, G. Danger, F. Duvernay, J. C. Guillemin, and T. Chiavassa, *Astron. Astrophys.* **534**, A64 (2011), URL <https://doi.org/10.1051/0004-6361/201117494>.
- [57] M. Ohishi, in *Astrobiology: From the Origins of Life to the Search for Extraterrestrial Intelligence*, edited by A. Yamagishi, T. Kakegawa, and T. Usui (Springer Singapore, Singapore, 2019), pp. 11–21, URL https://doi.org/10.1007/978-981-13-3639-3_2.
- [58] P. R. Bunker and P. Jensen, *Molecular Symmetry and Spectroscopy, 2nd Ed.* (NRC Research Press, 2006), URL <https://doi.org/10.1139/9780660196282>.
- [59] R. N. Zare, *Angular momentum: understanding spatial aspects in chemistry and physics* (Wiley & Sons, New York [i.a.], 1988), URL <https://doi.org/10.1007/BF00690083>.

- [60] G. Hose and H. S. Taylor, *Phys. Rev. Lett.* **51**, 947 (1983), URL <https://doi.org/10.1103/PhysRevLett.51.947>.
- [61] S. Carter, J. M. Bowman, and N. C. Handy, *Mol. Phys.* **110**, 775 (2012), URL <https://doi.org/10.1080/00268976.2012.669504>.
- [62] S. Carter, Y. Wang, and J. M. Bowman, *J. Phys. Chem. A* **121**, 1616 (2017), URL <https://doi.org/10.1021/acs.jpca.6b13013>.
- [63] S. Carter, A. R. Sharma, J. M. Bowman, P. Rosmus, and R. Tarroni, *J. Chem. Phys.* **131**, 224106 (2009), URL <https://doi.org/10.1063/1.3266577>.
- [64] X.-G. Wang and T. Carrington Jr., *Mol. Phys.* **111**, 2320 (2013), URL <https://doi.org/10.1080/00268976.2013.808387>.
- [65] J. Simmons, X.-G. Wang, and T. J. Carrington, *J. Phys. Chem. A* **123**, 10281 (2019), URL <https://doi.org/10.1021/acs.jpca.9b09045>.
- [66] J. Sarka, C. Petty, and B. Poirier, *J. Chem. Phys.* **151**, 174304 (2019), URL <https://doi.org/10.1063/1.5125145>.
- [67] J. Smydke, C. Fabri, J. Sarka, and A. G. Császár, *Phys. Chem. Chem. Phys.* **21**, 3453 (2019), URL <https://doi.org/10.1039/C8CP04672G>.
- [68] R. Tobias, T. Furtenbacher, J. Tennyson, and A. G. Császár, *Phys. Chem. Chem. Phys.* **21**, 3473 (2019), URL <https://doi.org/10.1039/C8CP05169K>.
- [69] D. Ferenc and E. Matyus, *Mol. Phys.* **117**, 1694 (2019), URL <https://doi.org/10.1080/00268976.2018.1547430>.
- [70] A. M. Santa Daria, G. Avila, and E. Matyus, *J. Chem. Phys.* **154**, 224302 (2021), URL <https://doi.org/10.1063/5.0054512>.
- [71] H. M. Pickett, *J. Mol. Spectrosc.* **148**, 371 (1991), URL [https://doi.org/10.1016/0022-2852\(91\)90393-0](https://doi.org/10.1016/0022-2852(91)90393-0).
- [72] H. Pickett, R. Poynter, E. Cohen, M. Delitsky, J. Pearson, and H. Müller, *J. Quant. Spectrosc. Rad. Trans.* **60**, 883 (1998), URL <https://linkinghub.elsevier.com/retrieve/pii/S0022407398000910>.
- [73] C. M. Western, *J Quant Spectrosc Radiat Transf* **186**, 221 (2017), satellite Remote Sensing and Spectroscopy: Joint ACE-Odin Meeting, 2015, URL <https://www.sciencedirect.com/science/article/pii/S0022407316300437>.

- [74] P. R. Franke, J. F. Stanton, and G. E. Douberly, *J. Phys. Chem* **125**, 1301 (2021), URL <https://doi.org/10.1021/acs.jpca.0c09526>.
- [75] A. V. Nikitin, M. Rey, and V. G. Tyuterev, *J. Quant. Spectrosc. Radiat. Transfer* **200**, 90 (2017), URL <https://doi.org/10.1016/j.jqsrt.2017.05.023>.
- [76] M. Rey, A. V. Nikitin, and V. G. Tyuterev, *Astrophys. J.* **847**, 105 (2017), URL <https://doi.org/10.3847/1538-4357/aa8909>.
- [77] V. G. Tyuterev, A. Barbe, D. Jacquemart, C. Janssen, S. N. Mikhailenko, and E. N. Starikova, *J. Chem. Phys.* **150**, 184303 (2019), URL <https://doi.org/10.1063/1.5089134>.
- [78] M. Rey, *J. Chem. Phys.* **156**, 224103 (2022), URL <https://doi.org/10.1063/5.0089097>.
- [79] S. N. Yurchenko, W. Thiel, and P. Jensen, *J. Mol. Spectrosc.* **245**, 126 (2007), URL <http://dx.doi.org/10.1016/j.jms.2007.07.009>.
- [80] A. Yachmenev, S. N. Yurchenko, T. Ribeyre, and W. Thiel, *J. Chem. Phys.* **135**, 074302 (2011), URL <https://doi.org/10.1063/1.3624570>.
- [81] A. Yachmenev, I. Polyak, and W. Thiel, *J. Chem. Phys.* **139**, 204308 (2013), URL <https://doi.org/10.1063/1.4832322>.
- [82] S. N. Yurchenko, D. S. Amundsen, J. Tennyson, and I. P. Waldmann, *Astron. Astrophys.* **605**, A65 (2017), URL <https://doi.org/10.1051/0004-6361/201731026>.
- [83] V. H. J. Clark, A. Owens, J. Tennyson, and S. N. Yurchenko, *J. Quant. Spectrosc. Radiat. Transfer* **246**, 106929 (2020), URL <https://doi.org/10.1016/j.jqsrt.2020.106929>.
- [84] J. Tennyson, S. N. Yurchenko, A. F. Al-Refaie, V. H. J. Clark, K. L. Chubb, E. K. Conway, A. Dewan, M. N. Gorman, C. Hill, A. E. Lynas-Gray, et al., *J. Quant. Spectrosc. Radiat. Transfer* **255**, 107228 (2020), URL <https://www.sciencedirect.com/science/article/pii/S002240732030491X>.
- [85] S. N. Yurchenko, R. J. Barber, A. Yachmenev, W. Thiel, P. Jensen, and J. Tennyson, *J. Phys. Chem. A* **113**, 11845–11855 (2009), URL <https://doi.org/10.1021/jp9029425>.
- [86] S. N. Yurchenko and J. Tennyson, *Mon. Not. R. Astron. Soc.* **440**, 1649 (2014), URL <http://dx.doi.org/10.1093/mnras/stu326>.

- [87] S. Erfort, M. Tschöpe, and G. Rauhut, *J. Chem. Phys.* **152**, 244104 (2020), URL <https://doi.org/10.1063/5.0011832>.
- [88] L. Landau and E. Lifshitz, *Quantum Mechanics* (Pergamon, 1977), 3rd edition ed., ISBN 978-0-08-020940-1, URL <https://doi.org/10.1016/B978-0-08-020940-1.50008-6>.
- [89] P. Jensen and P. R. Bunker, *Mol. Phys.* **97**, 821 (1999), URL <https://doi.org/10.1080/00268979909482882>.
- [90] J. K. G. Watson, *Mol. Phys.* **15**, 479 (1968), URL <https://doi.org/10.1080/00268976800101381>.
- [91] J. M. Bowman, T. C. Jr., and H. D. Meyer, *Mol. Phys.* **106**, 2145 (2008), URL <https://doi.org/10.1080/00268970802258609>.
- [92] B. Ziegler and G. Rauhut, *J. Chem. Phys.* **149**, 164110 (2018), URL <http://dx.doi.org/10.1063/1.5047912>.
- [93] B. Ziegler and G. Rauhut, *J. Phys. Chem. A* **123**, 3367 (2019), URL <https://doi.org/10.1021/acs.jpca.9b01604>.
- [94] B. Ziegler and G. Rauhut, *Mol. Phys.* **117**, 1741 (2019), URL <https://doi.org/10.1080/00268976.2018.1522004>.
- [95] B. Ziegler and G. Rauhut, *J. Chem. Phys.* **144**, 114114 (2016), URL <http://dx.doi.org/10.1063/1.4943985>.
- [96] B. Schröder and G. Rauhut, *Vibrational Dynamics of Molecules* (World Scientific, Singapore, 2022), pp. 1–40, URL <https://doi.org/10.1142/12305>.
- [97] O. Christiansen, *J. Chem. Phys.* **119**, 5773 (2003), URL <https://doi.org/10.1063/1.1601593>.
- [98] D. A. Clabo, W. D. Allen, R. B. Remington, Y. Yamaguchi, and H. F. Schaefer, *Chem. Phys.* **123**, 187 (1988), URL [https://doi.org/10.1016/0301-0104\(88\)87271-9](https://doi.org/10.1016/0301-0104(88)87271-9).
- [99] G. Rauhut, *J. Chem. Phys.* **121**, 9313 (2004), URL <https://doi.org/10.1063/1.1804174>.
- [100] K. M. Christoffel and J. M. Bowman, *Chem. Phys. Lett.* **85**, 220 (1982), URL <https://doi.org/10.1063/1.4865098>.

- [101] J. M. Bowman, K. Christoffel, and F. Tobin, *J. Phys. Chem.* **83**, 905 (1979), URL <https://doi.org/10.1021/j100471a005>.
- [102] S. Heislbetz and G. Rauhut, *J. Chem. Phys.* **132**, 124102 (2010), URL <https://doi.org/10.1063/1.3364861>.
- [103] F. Pfeiffer and G. Rauhut, *J. Chem. Phys.* **140**, 064110 (2014), URL <https://doi.org/10.1063/1.4865098>.
- [104] O. Christiansen, *J. Chem. Phys.* **120**, 2149 (2004), URL <https://doi.org/10.1063/1.1637579>.
- [105] V. Nagalakshmi, V. Lakshminarayana, G. Sumithra, and M. Durga Prasad, *Chem. Phys. Lett.* **217**, 279–282 (1994), URL <https://www.sciencedirect.com/science/article/pii/0009261493E1380Y>.
- [106] T. Petrenko and G. Rauhut, *J. Chem. Phys.* **146**, 124101 (2017), URL <https://doi.org/10.1063/1.4978581>.
- [107] M. Neff, Ph.D. thesis, University of Stuttgart (2013).
- [108] V. Špirko, P. Jensen, P. Bunker, and A. Čejchan, *J. Mol. Spectrosc.* **112**, 183 (1985), URL [https://doi.org/10.1016/0022-2852\(85\)90203-6](https://doi.org/10.1016/0022-2852(85)90203-6).
- [109] T. Mathea, Ph.D. thesis, University of Stuttgart (2022), URL <http://dx.doi.org/10.18419/opus-12159>.
- [110] M. Schneider, Master's thesis, University of Stuttgart (2020).
- [111] G. Placzek, *Handbuch der Radiologie*, vol. 6 (Akademische Verlagsgesellschaft, Leipzig, 1934).
- [112] V. I. Starikov and A. E. Protasevich, *Opt Spectrosc* **97**, 9 (2004), URL <https://doi.org/10.1134/1.1781275>.
- [113] D. A. Long, *The Raman Effect: A Unified Treatment of the Theory of Raman Scattering by Molecules* (John Wiley & Sons, Ltd, New York, 2002), ISBN 9780471490289, URL <http://dx.doi.org/10.1002/0470845767.ch3>.
- [114] A. H. Weber and S. Brodersen, eds., *Raman spectroscopy of gases and liquids*, Topics in current physics ; 11 (Springer, Berlin ; Heidelberg, 1979), URL <https://doi.org/10.1007/978-3-642-81279-8>.

- [115] S. Erfort, M. Tschöpe, and G. Rauhut, *J. Chem. Phys.* **156**, 124102 (2022), URL <https://doi.org/10.1063/5.0087359>.
- [116] M. Hiereth, *Methods of detecting exoplanets*, http://www.pci.tu-bs.de/aggericke/PC4e_osv/Spectroscopy050119/node7.html (2005), TU Braunschweig; Online; accessed 10-April-2023.
- [117] S. Thapa, L. Pant, B. Vamosi, M. Saaranen, and S. B. Bayram, *Time-Resolved Vibrational Spectroscopy to Measure Lifetime of the $E^3\pi_g(v = 3)$ state of Molecular Iodine* (2021), URL <https://doi.org/10.48550/arXiv.2109.02683>.
- [118] R. Thapa, Kansas City State University Press (2005), URL <http://hdl.handle.net/2097/133>.
- [119] L. Rutkowski, A. C. Johansson, A. Filipsson, P. Maslowski, and A. Foltynowicz, in *Fourier Transform Spectroscopy* (Optica Publishing Group, 2018), pp. FM4B-1, URL <https://doi.org/10.1364/FTS.2018.FM4B.1>.
- [120] N. Ngo, D. Lisak, H. Tran, and J.-M. Hartmann, *J Quant Spectrosc Radiat Transf* **129**, 89 (2013), URL <https://www.sciencedirect.com/science/article/pii/S0022407313002422>.
- [121] *Atomic radii of the elements (data page)*, [https://en.wikipedia.org/wiki/Atomic_radii_of_the_elements_\(data_page\)](https://en.wikipedia.org/wiki/Atomic_radii_of_the_elements_(data_page)) (2023), [Online; accessed 11-April-2023].
- [122] J. Luque, M. Calzada, and M. Saez, *J Quant Spectrosc Radiat Transf* **94**, 151 (2005), URL <https://www.sciencedirect.com/science/article/pii/S0022407304004017>.
- [123] H. Lefebvre-Brion and R. W. Field, *The spectra and dynamics of diatomic molecules: revised and enlarged edition* (Elsevier, 2004), URL <https://doi.org/10.1016/B978-0-12-441455-6.X5000-8>.
- [124] R. A. Ashby, *J. Chem. Educ.* **52**, 632 (1975), URL <https://doi.org/10.1021/ed052p632>.
- [125] L. Lodi and J. Tennyson, *J Quant Spectrosc Radiat Transf* **113**, 850-858 (2012), three Leaders in Spectroscopy, URL <https://www.sciencedirect.com/science/article/pii/S0022407312000878>.
- [126] A. C. Johansson, A. Filipsson, L. Rutkowski, P. Masłowski, and A. Foltynowicz, in *Conference on Lasers and Electro-Optics* (Optica Publishing Group, 2018), p. STu3P.6.

- [127] I. Gordon, L. Rothman, C. Hill, R. V. Kochanov, Y. Tan, P. Bernath, M. Birk, V. Boudon, A. Campargue, K. Chance, et al., *J. Quant. Spectrosc. Radiat. Transfer* **203**, 3–69 (2017), URL <https://www.sciencedirect.com/science/article/pii/S0022407317301073>.
- [128] J. Tennyson, P. F. Bernath, L. R. Brown, A. Campargue, A. G. Csaszar, L. Daumont, R. R. Gamache, J. T. Hodges, O. V. Naumenko, O. L. Polyansky, et al., *J. Quant. Spectrosc. Radiat. Transfer* **117**, 29–58 (2013), URL <https://doi.org/10.1016/j.jqsrt.2012.10.002>.
- [129] L. R. Brown, K. Sung, D. C. Benner, V. M. Devi, V. Boudon, T. Gabard, C. Wenger, A. Campargue, O. Leshchishina, S. Kassi, et al., *J. Quant. Spectrosc. Radiat. Transfer* **130**, 201–219 (2013), URL <https://doi.org/10.1016/j.jqsrt.2013.06.020>.
- [130] L. S. Rothman, *Nature Rev. Phys.* **3**, 302 (2021), URL <https://doi.org/10.1016/j.jqsrt.2010.01.027>.

Publication 1: High-Level Rovibrational
Calculations on Ketenimine



High-Level Rovibrational Calculations on Ketenimine

Martin Tschöpe[†], Benjamin Schröder[†], Sebastian Erfort[†] and Guntram Rauhut^{*}

Institute for Theoretical Chemistry, University of Stuttgart, Stuttgart, Germany

OPEN ACCESS

Edited by:

Majdi Hochlaf,
Université Paris Est Marne la Vallée,
France

Reviewed by:

David Lauvergnat,
Université Paris-Saclay, France
Nicola Tassinato,
Normal School of Pisa, Italy

*Correspondence:

Guntram Rauhut
rauhut@theochem.uni-stuttgart.de

†ORCID:

Martin Tschöpe
orcid.org/0000-0001-9888-4577
Benjamin Schröder
orcid.org/0000-0002-4016-2034
Sebastian Erfort
orcid.org/0000-0003-4196-639X

Specialty section:

This article was submitted to
Astrochemistry,
a section of the journal
Frontiers in Chemistry

Received: 30 October 2020

Accepted: 03 December 2020

Published: 06 January 2021

Citation:

Tschöpe M, Schröder B, Erfort S and
Rauhut G (2021) High-Level
Rovibrational Calculations on
Ketenimine. *Front. Chem.* 8:623641.
doi: 10.3389/fchem.2020.623641

From an astrochemical point of view ketenimine (CH₂CNH) is a complex organic molecule (COM) and therefore likely to be a building block for biologically relevant molecules. Since it has been detected in the star-forming region Sagittarius B2(N), it is of high relevance in this field. Although experimental data are available for certain bands, for some energy ranges such as above 1200 cm⁻¹ reliable data virtually do not exist. In addition, high-level *ab initio* calculations are neither reported for ketenimine nor for one of its deuterated isotopologues. In this paper, we provide for the first time data from accurate quantum chemical calculations and a thorough analysis of the full rovibrational spectrum. Based on high-level potential energy surfaces obtained from explicitly correlated coupled-cluster calculations including up to 4-mode coupling terms, the (ro)vibrational spectrum of ketenimine has been studied in detail by variational calculations relying on rovibrational configuration interaction (RVCI) theory. Strong Fermi resonances were found for all isotopologues. Rovibrational infrared intensities have been obtained from dipole moment surfaces determined from the distinguishable cluster approximation. A comparison of the spectra of the CH₂CNH molecule with experimental data validates our results, but also reveals new insight about the system, which shows very strong Coriolis coupling effects.

Keywords: ketenimine, *ab initio* calculations, Fermi resonances, rotational spectrum, VSCF/VCI theory, rovibrational calculations

1. INTRODUCTION

More than 200 molecules have been detected in the interstellar medium (ISM) or circumstellar shells (Müller et al., 2001, 2005; Endres et al., 2016; McGuire, 2018) presenting a chemical variety from rather stable to highly reactive species such as radicals, carbenes, and molecular ions. In a similar way, the size measured by the number of atoms varies substantially from simple diatomics (e.g., CO, CN, and OH; Weinreb et al., 1963; Jefferts et al., 1970; Wilson et al., 1970), to carbon-chain molecular species like cyanopolynes (HC_nN; Ohishi and Kaifu, 1998) and simple organic molecules like methanol (CH₃OH; Ball et al., 1970), up to still larger compounds like polycyclic aromatic hydrocarbons (PAHs; Allamandola et al., 1989) and fullerenes (C₆₀; Cami et al., 2010). Within the context of astrochemistry molecules with 6 or more atoms are usually referred to as complex molecules and when carbon is present also as complex *organic* molecules (COMs; Herbst and van Dishoeck, 2009). Such compounds are thought to be important building blocks for biologically relevant molecules (Woon, 2002; Theule et al., 2011; Ohishi, 2019) and accordingly, much attention has been paid to the study of formation pathways for COMs (Herbst and van Dishoeck, 2009; Öberg, 2016, and references therein).

Examples of such COMs are the class of imines ($R-C=NH$). They have been shown to be important intermediates for the hydrogenation of CN moieties (Theule et al., 2011; Krim et al., 2019). Recently, formation of imines has been reported for radiative-processing of ices. Vasconcelos et al. investigated the products from ion irradiation of N_2-CH_4 ice mixtures by *in-situ* Fourier transform infrared spectroscopy (FTIR) and, among others, methyleneimine was identified (Vasconcelos et al., 2020). In a similar fashion, Carvalho and Pilling (2020) detected ketenimine by FTIR spectroscopy upon irradiation of acetonitrile ice with X-rays (6–2000 eV). Ketenimine ($H_2C=C=NH$) is one of only 4 imines which have been conclusively identified to be present in the ISM (Godfrey et al., 1973; Kawaguchi et al., 1992; Lovas et al., 2006; Zaleski et al., 2013). Using the 100 m Green Bank Telescope Lovas and coworkers observed three rotational transitions of ketenimine toward the star-forming region Sagittarius B2(N) (Lovas et al., 2006). It is known that temperatures in Sagittarius B2(N) vary between 40 K in the envelope and 300 K in the hot dense core (Martín-Pintado et al., 1996). Therefore, it could be possible that not only the rotational spectrum of ketenimine can be detected with radio telescopes, but also the rovibrational spectrum due to IR spectroscopy. Since Sagittarius B2(N) is a star forming region, the question arises whether ketenimine can be found in protoplanetary disks or even exoplanet atmospheres. Considering the recent successes in this field (Charbonneau et al., 2002; Mandell et al., 2013; Gandhi et al., 2020) as well as the upcoming space telescopes James Webb Space Telescope (JWST) and Atmospheric Remote-sensing Infrared Exoplanet Large-survey (ARIEL) with high sensitivity in this spectral range this is a feasible aim.

Given its importance as the simplest member of a larger class of chemically interesting molecules (Alajarin et al., 2012), ketenimine has been subject to a number of experimental spectroscopic investigations which revealed a complex rovibrational spectrum. The first spectroscopic investigation of ketenimine was reported by Jacox and Milligan (1963). Infrared transitions of the transient species were tentatively assigned following the reaction of NH with acetylene in argon matrix. The assignment was later confirmed and extended by Jacox (1979) in an argon matrix-isolation study of the photoisomerization of acetonitrile.

A gas phase rotational spectrum of ketenimine was obtained by Rodler and coworkers using microwave spectroscopy (Rodler et al., 1984). Ground-state rotational parameters of $A_0 = 201443.69$, $B_0 = 9663.138$, and $C_0 = 9470.127$ MHz were determined from a fit to Watson's S-reduced rotational Hamiltonian (Watson, 1977) in the I' representation. The latter parameters show that ketenimine is a near-prolate asymmetric top (asymmetry parameter $\kappa = -0.998$). Measurements of Stark-splittings (Rodler et al., 1984) yielded the ground state dipole moments $^a\mu_0 = 0.431(1)$ D and $^c\mu_0 = 1.371(6)$ D. Rodler et al. later carried out a high-resolution analysis in the 4–7 GHz region for the main as well as the ND isotopologue revealing small splittings in the former case, due to the imino inversion (Rodler et al., 1986). The latest study of the vibrational ground state rotational spectrum of ketenimine was performed by Degli Esposti at submillimeter wavelength (Degli Esposti

et al., 2014). In total, 297 line frequencies were analyzed yielding spectroscopic parameters that allow for the accurate prediction of rotational transitions up to 1 THz.

The rovibrational spectrum of ketenimine has been studied by both, in low-resolution (August, 1986) as well as high-resolution (Ito et al., 1990; Ito and Nakanaga, 2010; Bane et al., 2011a,b,c). A gas phase spectrum of the $\tilde{\nu}_3 = 2044$ cm^{-1} CCN-stretching vibration has been obtained by Ito et al. (1990) using FTIR spectroscopy. Analysis of the spectrum revealed a complicated structure due to several Coriolis-type interactions, which could only be analyzed approximately due to missing information on the perturbing states. Almost 20 years later Ito and Nakanaga reported the observation of the CNH bending rovibrational spectrum around $\tilde{\nu}_6 = 1000$ cm^{-1} using FTIR spectroscopy. Again, strong Coriolis perturbations precluded a detailed analysis of the ν_6 state and only effective spectroscopic parameters for individual K_a sub-bands were obtained. The latter values allowed the ν_{10} (CH_2 rocking) and ν_{11} (torsion) vibrations to be identified as likely perturbers, based on their large contribution to the vibration-rotation interaction constant α_6^A .

In a series of articles Bane and coworkers presented a thorough experimental analysis of the low lying fundamental bands of ketenimine (Bane et al., 2011a,b,c). The observed bands encompass the out-of-plane and in-plane CCN bending vibrations around $\tilde{\nu}_{12} = 409$ and $\tilde{\nu}_8 = 466$ cm^{-1} (Bane et al., 2011c), respectively, the CH_2 wagging mode ($\tilde{\nu}_7 = 693$ cm^{-1} ; Bane et al., 2011b) and the CH_2 rocking mode ($\tilde{\nu}_{10} = 983$ cm^{-1}) as well as the strong CNH bending mode ν_6 (Bane et al., 2011a). Following the assignment of more than 6,000 rovibrational transitions and fitting of the spectrum, an intricate system of Coriolis-coupled states was revealed whereby all 5 observed states are coupled via Coriolis-coupling either directly (e.g., a -axis Coriolis coupled ν_{12} & ν_8) or indirectly. The analysis required the inclusion of unobserved “dark states” $2\nu_8$, $\nu_8 + \nu_{12}$, and $2\nu_{12}$ which are also expected to be strongly Coriolis-coupled amongst themselves. While the global fit to Watson's S-reduced Hamiltonian (I') reproduced the observed rovibrational transition frequencies, Bane et al. noted that the torsion fundamental ν_{11} around 880 cm^{-1} probably also adds to the complex rovibrational coupling but considered inclusion of this interaction intractable.

Theoretical work on the rotational and rovibrational spectroscopy of ketenimine is rather scarce and either based on limited *ab initio* methods (Kaneti and Nguyen, 1982; Brown et al., 1985) or has been done only in support of dedicated experimental investigations (Ito et al., 1990; Ito and Nakanaga, 2010; Bane et al., 2011c). In the latter case, the work of Bane and coworkers (Bane et al., 2011c) provided the previously most accurate predictions of the fundamental frequencies with a root-mean-squared deviation of 11 cm^{-1} . The results were obtained from B3LYP/cc-pVTZ harmonic frequencies which were uniformly scaled by a factor of 0.965. Given its possible importance in astrochemical reaction networks and the strong rovibrational couplings a more in-depth look at the rotational and rovibrational spectroscopy of ketenimine appears desirable.

Recently, some of us reported on the implementation of a new program for variational rovibrational calculations within the

MOLPRO package of *ab initio* programs (Erfort et al., 2020a). The approach combines the well established MOLPRO capabilities (Werner et al., 2020) of obtaining multidimensional potential energy and dipole moment surfaces, comprehensive symmetry information and the accurate determination of vibrational wave functions with efficient calculation of partition functions, rovibrational transition frequencies, and transition dipole matrix elements in an almost black-box manner. Within this study here, we report about high-level *ab initio* calculations based on anharmonic potential energy surfaces obtained from explicitly correlated coupled-cluster theory, which allows for a detailed analysis of the (ro)vibrational spectra of the title compound. Compared to previous work the rovibrational calculations have been extended by pure rotational spectra, which is a newly implemented feature in MOLPRO.

2. COMPUTATIONAL DETAILS

Geometries, harmonic frequencies and normal coordinates of ketenimine (X^1A') and its C_s symmetric isotopologues were computed at the level of frozen-core explicitly correlated coupled-cluster theory, CCSD(T)-F12b, in combination with a basis set of triple- ζ quality, i.e., cc-pVTZ-F12 (Adler et al., 2007). Hartree-Fock energies were corrected by addition of the complementary auxiliary basis set singles correction (CABS) (Knizia and Werner, 2008).

n -mode expansions of the potential energy surface (PES) and the dipole moment surface (DMS) being truncated after 4th order were used in all calculations (Ziegler and Rauhut, 2018). A multi-level scheme has been employed throughout (Pflüger et al., 2005; Yagi et al., 2007), in which the 1D and 2D terms of the PES were computed at the CCSD(T)-F12b/cc-pVTZ-F12 level, while the explicitly correlated distinguishable clusters approach, DCSD-F12b, in combination with a smaller cc-pVDZ-F12 basis was used for the 3D and 4D terms. The 1D and 2D terms of the DMS were computed at the conventional DCSD/cc-pVTZ-F12 level and the 3D and 4D terms at the DCSD/cc-pVDZ-F12 level (Kats and Manby, 2013; Kats et al., 2015). In total about 170,000 *ab initio* points were used for representing the surfaces. Efficient Kronecker product fitting was employed to transform this grid representation into an analytical one consisting of 10 local B-splines per dimension (Ziegler and Rauhut, 2016).

Vibrational self-consistent field theory (VSCF) has been used to determine one-mode wavefunctions (modals) based on the Watson Hamiltonian (Watson, 1968). Vibrational angular momentum terms (VAM) were not included within the variational determination of the modals, but were added *a posteriori* to the state energies (Neff et al., 2011). A mode-dependent basis of 20 distributed Gaussians has been used throughout for representing the modals. Subsequent state-specific configuration-selective vibrational configuration interaction calculations (VCI) were used for calculating accurate state energies (Neff and Rauhut, 2009). The correlation space contained single to 6-tuple excitations up to the 8th root per mode and a maximum sum of quantum numbers of 15. This resulted in about $4 \cdot 10^6$ Hartree products (configurations)

per irreducible representation. These calculations included VAM terms based on a constant μ -tensor. Eigenvalues were determined with our residuum based eigenvalue solver (RACE) (Petrenko and Rauhut, 2017).

Within the calculation of the rovibrational spectra we also use the Watson-operator (Watson, 1968)

$$H_{\text{Watson}} = \frac{1}{2} \sum_{\alpha\beta} J_{\alpha} \mu_{\alpha\beta} J_{\beta} - \frac{1}{2} \sum_{\alpha\beta} (J_{\alpha} \mu_{\alpha\beta} \pi_{\beta} + \pi_{\alpha} \mu_{\alpha\beta} J_{\beta}) + H_{\text{Vib}}, \quad (1)$$

where J_{α} denotes the total angular momentum operator, π_{α} the vibrational angular momentum operator and $\mu_{\alpha\beta}$ refers to an element of the inverse effective moment of inertia tensor. The summations over α and β run over the three molecule fixed Cartesian space coordinates. The first term in Equation (1) gives the kinetic energy of rotational motion and the second term couples rotation and vibration and is referred to as Coriolis term. All other terms of the Watson Hamiltonian are purely vibrational operators and are thus summarized in the term denoted H_{Vib} . Within rovibrational configuration interaction (RVCI) theory the rovibrational wave functions are expanded in terms of products of VCI wave functions and rotational basis functions (Erfort et al., 2020a,b). The latter can be either primitive symmetric top eigenfunctions or Wang combinations of symmetric top functions (Wang, 1929; Špirko et al., 1985).

In the following, we will distinguish between rotational configuration interaction (RCI) and rovibrational configuration interaction (RVCI). RCI is an approximation, in which no rovibrational interaction between different vibrational states is considered. This corresponds to neglecting the second term, see Equation (1), as well as all terms off-diagonal in the vibrational quantum numbers, arising from the 1D and higher order expansion of the μ -tensor (centrifugal distortion). Since every RCI-matrix is thus constructed for a single VCI wave function, the vibrational state identity can be trivially assigned for every rovibrational state. In contrast, within RVCI all rovibrational interactions are considered. As a consequence the only “good” quantum number is the angular momentum quantum number J and the parity of the rovibrational state. In this sense, RVCI yields the physically meaningful results. However, we found that a comparison of RVCI with the RCI results is helpful to understand and visualize both the effects of Coriolis interaction and intensity borrowing mechanisms in general. Again, it shall be noted that for comparison with experiments only RVCI results should be used.

The rovibrational intensities are calculated according to

$$I = \frac{2\pi^2}{3} \frac{N_A}{\epsilon_0 h^2 c^2} \frac{e^{-E''/k_B T} (1 - e^{-(E' - E'')/k_B T})}{Q(T)} (E' - E'') R^2. \quad (2)$$

In Equation (2), the first two prefactors contain only constants. The next factor corresponds to the thermal distribution function, with the temperature T , Boltzmann constant k_B , the energy of the lower state E'' and the upper state E' as well as the temperature dependent partition function $Q(T)$. For the latter, we use the separability approximation $Q = Q_{\text{vib}} Q_{\text{rot}}$ for several reasons.

First, we are investigating a relatively low temperature regime up to 300 K, where the partition function converges quickly with increasing excitation, such that errors in energies for high-lying states have little influence. Second, we have shown in our previous work (Erfort et al., 2020a), that for H₂CO and H₂CS the differences between experimental $Q(T)$ values and theoretically approximated $Q_{\text{vib}}Q_{\text{rot}}$ values for the partition function are lower than 2% up to 300 K. In addition to that, the partition function is the same global factor for every transition and since we are primarily interested in relative intensities rather than in absolute intensities, it is therefore not crucial for us. The last two factors in Equation (2) correspond to the frequency of the transition ($E' - E''$) and the squared transition moment R^2 . The calculation of the latter within RVCi has been outlined previously (Erfort et al., 2020a). For ketenimine all nuclear spin statistical weights show the values of 24.

Further approximations are used to limit the calculation times. First of all, we are not considering hot bands. Due to relatively low temperatures and absence of fundamentals with particularly low energies, these bands have fairly low intensities and are mainly hidden behind significantly more intense transitions arising from the vibrational ground state. This is supported by a comparison to the results of Bane and coworkers (Bane et al., 2011c). Moreover, the inverse effective moment of inertia tensor μ is expanded to the 0th order for the RVCi calculation. Within these computations all fundamental bands, seven combination bands ($\nu_3 + \nu_5$, $\nu_3 + \nu_6$, $\nu_5 + \nu_6$, $\nu_6 + \nu_{10}$, $\nu_7 + \nu_8$, $\nu_7 + \nu_{12}$, and $\nu_8 + \nu_{12}$) and seven overtones ($2\nu_6$, $2\nu_7$, $2\nu_8$, $2\nu_{10}$, $2\nu_{12}$, $3\nu_8$, and $3\nu_{12}$) were simultaneously considered, giving in total $N_{\text{vib}} = 27$ vibrational states (including the ground state). As a convergence check we performed a calculation with angular momentum quantum number of $J \leq 70$ and one with $J \leq 100$. The VCI calculations were performed in parallel using 9 cores, with a total computational time of 100 h. The required memory for the subsequent serial RVCi treatment is less than 40 GB. As an example, the RVCi matrix for $J = 70$, with $N_{\text{vib}} = 27$ vibrational states is of size $(2J + 1)N_{\text{vib}} = 3,807$. Although, this is relatively small in comparison to other rovibrational software, the results are nevertheless very accurate. A possible reason for this lies in the very accurate and compact vibrational basis, in the form of VCI wavefunctions. Computational timings on a single CPU core were about 83 min for RVCi energies and about 14 h for RVCi intensities for $J \leq 70$. For the same upper bound of J there were 3.81×10^7 transitions considered and about 1.41×10^6 of them where found to be significant. For $T = 300$ K the partition function is converged to $Q(T) = 2.05 \times 10^5$ at $J = 71$.

3. RESULTS AND DISCUSSION

3.1. Geometrical Parameters, Rotational Constants, and Dipole Moments

Geometrical parameters of the main ketenimine isotopologue as well as two deuterated variants have been calculated and are provided in Table 1. The parameters obtained from the Born-Oppenheimer equilibrium geometry are denoted r_e . The only experimental geometrical parameter available for comparison is a

mixed experimental-theoretical valence angle $\alpha(\text{C}_2\text{NH}_3)$ (Rodler et al., 1986). From a semi-rigid bender analysis of the $9_{1,8}-10_{0,10}$ ground state rotational transition, Rodler and coworkers determined a value of $115.4 \pm 0.6^\circ$ for $\alpha(\text{C}_2\text{NH}_3)$ which is in excellent agreement with our optimized value of 114.76° . To account for vibrational effects r_a and r_g parameters have been calculated. While the former correspond to parameters obtained from atomic positions averaged over the VCI ground state wavefunction, the latter are instantaneous inter-nuclear distances calculated from an expectation value of the bond lengths expanded in terms of the normal coordinates. As is typically observed (Czakó et al., 2009; Dinu et al., 2020), both sets of vibrationally averaged bond lengths differ substantially from each other with the largest absolute difference of 0.0169 \AA observed for $r(\text{NH}_3)$ in the main isotopologue. The CNH angle $\alpha(\text{C}_2\text{NH}_3)$ shows a slightly larger vibrational effect compared to other angles, in line with the inversion character of this coordinate. The barrier to planarity (C_{2v}) was computed to be 5249 cm^{-1} at the CCSD(T)-F12b/cc-pVTZ-F12 level and is thus too high for tunneling effects in the fundamental modes to be of any importance. The semi-rigid bender analysis (Rodler et al., 1986) yielded a barrier height of $4700 \pm 200 \text{ cm}^{-1}$ which compares well with the present theoretical result. The imaginary frequency characterizing the transition state amounts to $i908 \text{ cm}^{-1}$. Note that there is no stationary point on the potential energy surface for a planar structure of neutral ketenimine.

Calculated and experimental (Rodler et al., 1984, 1986) rotational parameters for ketenimine isotopologues are compared in Table 2. There, rotational parameters A, B, and C obtained from the equilibrium geometry are denoted by method r^e . Following the work of Czakó et al. (2009), vibrationally averaged rotational parameters are approximated from the expectation value of the μ -tensor (Watson, 1968) over VCI wavefunctions. An n -mode expansion of the μ -tensor up to 3D terms has been employed in these calculations. Since this approach does not account for Coriolis coupling contributions to the rotational parameters, these are added via a correction based on Vibrational second-order perturbation theory (VPT2) (Rauhut, 2015; Dinu et al., 2020). The final equation for the rotational parameters B_v^α ($\alpha = a, b, c$) within a vibrational state v is thus given by

$$B_v^\alpha \approx \frac{\langle \mu_{\alpha\alpha} \rangle_v}{2} + \sum_k \frac{2(B_e^\alpha)^2}{\omega_k} \sum_l (\zeta_{kl}^\alpha)^2 \frac{3\omega_k^2 + \omega_l^2}{\omega_k^2 - \omega_l^2} \left(\nu_k + \frac{1}{2} \right). \quad (3)$$

In Equation (3), $\langle \mu_{\alpha\alpha} \rangle_v$ is the expectation value of a diagonal μ -tensor element evaluated over the VCI wavefunction for state v . In the second term of Equation (3), constituting the VPT2 Coriolis correction, B_e^α is the equilibrium rotational constant with respect to rotation about an axis α , ω_k are harmonic vibrational frequencies and ζ_{kl}^α are Coriolis constants that describe the coupling of vibrations k and l via rotation about the α -axis. Results obtained from Equation (3) for the vibrational ground state are denoted either $\langle \mu_{\alpha\alpha} \rangle_0$ or $\langle \mu_{\alpha\alpha} \rangle_0 + \text{VPT2}$ in Table 2, depending on whether the Coriolis correction is included or not. Notice that in the evaluation of $\langle \mu_{\alpha\alpha} \rangle_v$ the μ -tensor has been expanded up to 3D terms.

TABLE 1 | Computed geometrical parameters of ketenimine and its deuterated isotopologues.

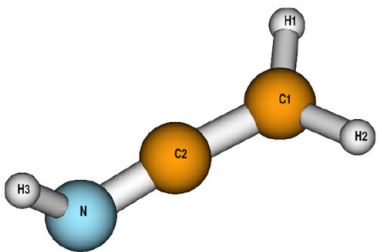
Coord.	r_e	$H_2C=C=NH$		$D_2C=C=ND$		$H_2C=C=ND$		
		r_a	r_g	r_a	r_g	r_a	r_g	
	$r(C_1H_1)$	1.0791	1.0829	1.0991	1.0823	1.0938	1.0818	1.0992
	$r(C_1C_2)$	1.3135	1.3175	1.3205	1.3172	1.3203	1.3173	1.3204
	$r(C_2N)$	1.2284	1.2302	1.2335	1.2302	1.2336	1.2303	1.2335
	$r(NH_3)$	1.0174	1.0202	1.0371	1.0196	1.0318	1.0211	1.0316
	$\alpha(C_2NH_3)$	114.76	115.07		114.95		115.02	
	$\alpha(C_1C_2N)$	174.05	174.10		174.08		174.10	
	$\alpha(H_1C_1C_2)$	119.88	119.73		119.78		119.75	

TABLE 2 | Computed and experimental rotational constants in GHz.

Isotopologue	Method	A	B	C
$H_2C=C=NH$	r^e	201.08792 (−0.18%)	9.65878 (−0.05%)	9.47482 (+0.05%)
	$\langle\mu_{\alpha\alpha}\rangle_0$	201.79883 (+0.18%)	9.62993 (−0.34%)	9.43904 (−0.33%)
	$\langle\mu_{\alpha\alpha}\rangle_0$ +VPT2	200.31173 (−0.56%)	9.62412 (−0.40%)	9.43309 (−0.39%)
	Exp. ^a	201.44527	9.66315	9.47015
$D_2C=C=ND$	r^e	103.66119	8.05874	7.78830
	$\langle\mu_{\alpha\alpha}\rangle_0$	104.74983	8.03709	7.75996
	$\langle\mu_{\alpha\alpha}\rangle_0$ +VPT2	103.35526	8.03232	7.75515
$H_2C=C=ND$	r^e	162.40310 (−0.51%)	9.03436 (+0.02%)	8.96746 (+0.06%)
	$\langle\mu_{\alpha\alpha}\rangle_0$	163.27301 (+0.02%)	9.00356 (−0.33%)	8.93460 (−0.31%)
	$\langle\mu_{\alpha\alpha}\rangle_0$ +VPT2	162.21271 (−0.63%)	8.99879 (−0.38%)	8.92979 (−0.36%)
	Exp. ^a	163.24242	9.03295	8.96219

^aValues determined from fits to Watson's *S*-reduced Hamiltonian (Rodler et al., 1984, 1986).

Where available, percentage deviations of calculated results with respect to experimental data is given in parentheses.

Inspection of **Table 2** shows rather large deviations of the Coriolis-corrected vibrationally averaged rotational parameters of -0.56 , -0.40 , and -0.39% with respect to experimental results (Rodler et al., 1984, 1986) for A_0 , B_0 , and C_0 , respectively. In contrast, the calculated equilibrium rotational parameters are in much better agreement with the experimental ground state rotational parameters, which is mainly due to error compensation. To confirm this, a geometry optimization at the all-electron CCSD(T)-F12b level of theory in conjunction with a cc-pCVTZ-F12 basis set (Hill et al., 2010) was carried out. This yields equilibrium rotational parameters (in GHz) for the main ketenimine isotopologue of 202.06657, 9.70127, and 9.51561 for A_e , B_e , and C_e , respectively. Adding the corrections due to vibrational averaging and Coriolis-coupling results in $A_0 = 201.29038$ GHz (-0.08%), $B_0 = 9.66661$ GHz ($+0.04\%$), and $C_0 = 9.46440$ GHz ($+0.04\%$), where deviations with respect to the experimental results of Rodler et al. (1984, 1986) are given in parentheses. The agreement of these corrected results with the experimental ones is excellent, but it is well-known that core correlation effects should not be considered without the inclusion of high-level coupled-cluster terms, e.g., CCSDT(Q), at the same time, because they often partly compensate each other (Ruden et al., 2004; Meier et al., 2011; Puzzarini et al., 2020). Moreover, rovibrational intensities as considered below

depend on several quantities and the impact of these additional corrections might be different for the individual quantities. Consequently, there is no unique answer, if the partial inclusion of these corrections will lead to better results. In any case, the inclusion of these high-level corrections is beyond the focus of this study and we neither did account for core correlation effects nor high-order coupled-cluster terms in the calculations presented below.

Experimental high-resolution spectroscopic investigations have revealed strong *a*-axis Coriolis coupling among the low lying vibrational states of ketenimine, especially for the pair of fundamentals ν_8 and ν_{12} (Bane et al., 2011a,b,c). This can also be shown by comparing rotation-vibration coupling constants α_i^{β} . From the rotational constants presented by Bane et al. (2011a) α_i^{β} can be approximated by $\alpha_i^{\beta} = B_0^{\beta} - B_i^{\beta}$. This yields 6185.3, -34.0 , and -13.4 MHz for α_{12}^A , α_{12}^B , and α_{12}^C , respectively, and -2845.0 , -8.1 , and -22.1 MHz for α_8^A , α_8^B , and α_8^C , respectively. These values should be compared to our theoretical VPT2 results of 444.5, -34.2 , and -14.7 MHz for α_{12}^A , α_{12}^B , and α_{12}^C , respectively, and 2497.5, -9.3 and -22.7 MHz for α_8^A , α_8^B and α_8^C , respectively. Following Papoušek and Aliev (1982), the latter values have been corrected for the *a*-axis Coriolis resonance between ν_{12} and ν_8 in order to be comparable with the results of Bane and coworkers.

TABLE 3 | Calculated dipole moments $\vec{\mu}$ (in D) of ketenimine and its deuterated isotopologues.

Isotopologue	$\vec{\mu}_e$			$\vec{\mu}_0$		
	${}^a\mu_e$	${}^c\mu_e$	$ \vec{\mu}_e $	${}^a\mu_0$	${}^c\mu_0$	$ \vec{\mu}_0 $
H ₂ C=C=NH ^a	0.5008	1.4056	1.4912	0.4587	1.3766	1.4510
H ₂ C=C=ND	0.4643	1.4170	1.4912	0.4314	1.4028	1.4676
D ₂ C=C=ND	0.4669	1.4162	1.4912	0.4394	1.3940	1.4616

^aExperimental results (Rodler et al., 1984): ${}^a\mu_0 = 0.434(1)$, ${}^c\mu_0 = 1.371(6)$, and $|\vec{\mu}_0| = 1.438(6)$ D.

To this end, the corresponding $(i, j) = (12, 8)$ or $(8, 12)$ term in the Coriolis contribution to α_i^β (cf. second term in Equation 3) is replaced according to

$$(\zeta_{ij}^\beta)^2 \frac{3\omega_i^2 + \omega_j^2}{\omega_i^2 - \omega_j^2} \rightarrow -(\zeta_{ij}^\beta)^2 \frac{B_e^\beta (\omega_i - \omega_j)^2}{\omega_i \omega_j (\omega_i + \omega_j)}$$

We have also investigated whether symmetry allowed off-diagonal contributions α_k^{AC} are important for ketenimine, following the work of Aliev and Watson (1985), but found their contribution to effective $\tilde{\alpha}_{12}^\beta$ and $\tilde{\alpha}_8^\beta$ after diagonalization of the respective $B_i^{\alpha\beta}$ matrices negligible.

While the B and C components are in excellent agreement between experiment and theory, the A components show large differences. Moreover, the differences between experiment and theory for ν_{12} and ν_8 are almost identical but of opposite sign (-5740.8 MHz for ν_{12} and 5342.5 MHz for ν_8). For comparison, not accounting for Coriolis resonance yields unphysical VPT2 values of -59021.2 and 61996.7 MHz for α_8^A and α_{12}^A , respectively. Such effects are unambiguous indications of strong Coriolis coupling. The preceding discussion clearly shows that a simple treatment of the rotational problem and the rovibrational couplings in ketenimine, based on e.g., Equation (3) or VPT2, has to proceed with caution. A variational treatment employing the exact rovibrational Hamiltonian automatically includes all interactions necessary for a correct description of the internal dynamics.

Calculated dipole moments of ketenimine and its isotopologues are listed in **Table 3**. Our DMS yields equilibrium dipole moments for the main ketenimine isotopologue of ${}^a\mu_e = 0.5008$ D and ${}^c\mu_e = 1.4056$ D, where superscripts a and c refer to the principal axis components of the dipole vector $\vec{\mu}_e$. Symmetric H/D substitution results in a rotation of the a - and c -axis around the b -axis. As a consequence, the components ${}^a\mu_e$ and ${}^c\mu_e$ of the dipole vector differ among the ketenimine isotopologues but the total dipole moment of $|\vec{\mu}_e| = 1.4912$ D is unchanged. The situation is different for the ground state dipole moments $\vec{\mu}_0$ due to variations of vibrational averaging effects. Overall, vibrational averaging results in a lowering of both a - and c -axis components. The non-deuterated isotopologue shows slightly larger effects due to vibrational averaging, especially for the c -axis component. Rodler et al. (1984) determined the dipole vector components of

the main isotopologue and from Stark shifts of the $2_{02} \leftarrow 1_{01}$ and $2_{11} \leftarrow 1_{10}$ rotational transitions. While the resulting ${}^c\mu_0 = 1.371(6)$ D is in excellent agreement with our calculated value of 1.3766 D, a somewhat larger difference is observed between the experimental ${}^a\mu_0 = 0.431(1)$ D and calculated 0.4587 D. This difference is in part due to a geometric effect. Using the optimized ae-CCSD(T)-F12b/CVTZ-F12 geometry, equilibrium dipole moments of ${}^a\mu_e = 0.4854$ D (-0.0154 D) and ${}^c\mu_e = 1.4029$ D (-0.0027 D) were obtained from DCSD/VTZ-F12 calculations, where values in parentheses correspond to the difference with respect to the values quoted in **Table 3**. Adding the vibrational averaging correction yields an approximate ${}^a\mu_0 \approx 0.4433$ D, closer to the experimental result. Again, the influence of high-order coupled-cluster terms would be required to further reduce the remaining error.

3.2. Vibrational Spectrum

The purely vibrational transitions of ketenimine and its isotopologues are listed in **Table 4**. Clearly, for the deuterated species the majority of experimental assignments is missing and a comparison of the different experimental results for H₂CCNH shows that these results bear an uncertainty of several wavenumbers.

Concerning the assignments for the non-deuterated ketenimine, a huge difference of more than 80 cm⁻¹ between the computed and experimental values of Bane et al. (2011c) can be seen for mode ν_4 . An analysis showed that this mode shows a strong Fermi resonance with the overtone of ν_7 and our calculated value of 1350.9 cm⁻¹ for $2\nu_7$ agrees nicely with the experimental value of 1355 cm⁻¹. As our calculations clearly assign the transition at 1435.9 cm⁻¹ to the fundamental mode, we believe that the experimental value of 1355 cm⁻¹ belongs to the $2\nu_7$ overtone, which is the lower state of this Fermi pair. The reason for this misassignment might be that the infrared intensity of the overtone is much stronger than that for the fundamental. A closer look at this particular resonance reveals a peculiar feature. While the band intensity at the VSCF level amounts to 3.42 km/mol for ν_4 and 4.47 km/mol for $2\nu_7$, almost all intensity is transferred to the overtone within the VCI calculations. This can be understood by comparison to a VPT2 based analysis that accounts for the Fermi resonance (Vázquez and Stanton, 2007). Then, the intensities of the Fermi dyad in question are predominantly determined by the mixed a -axis transition dipole moments $\langle {}^a\mu \rangle_\nu$. The latter are obtained from the eigenvector components C_ω^ν of the Fermi resonance matrix and the (deperturbed; dp) transition dipole moments $\langle {}^a\mu \rangle_\omega^{\text{dp}}$ evaluated over harmonic basis functions $|\omega\rangle$ according to:

$$\begin{aligned} \langle {}^a\mu \rangle_{\nu_4} &= C_{\omega_4}^{\nu_4} \cdot \langle {}^a\mu \rangle_{\omega_4}^{\text{dp}} + C_{2\omega_7}^{\nu_4} \cdot \langle {}^a\mu \rangle_{2\omega_7}^{\text{dp}} \\ &= 0.78 \cdot 0.033 \text{ D} + 0.62 \cdot -0.044 \text{ D} \approx 0.002 \text{ D} \end{aligned}$$

and

$$\begin{aligned} \langle {}^a\mu \rangle_{2\nu_7} &= C_{\omega_4}^{2\nu_7} \cdot \langle {}^a\mu \rangle_{\omega_4}^{\text{dp}} + C_{2\omega_7}^{2\nu_7} \cdot \langle {}^a\mu \rangle_{2\omega_7}^{\text{dp}} \\ &= -0.62 \cdot 0.033 \text{ D} + 0.78 \cdot -0.044 \text{ D} \approx -0.055 \text{ D} \end{aligned}$$

TABLE 4 | Comparison of calculated VCI fundamental frequencies of H₂C=C=NH and its deuterated isotopologues with experimental data.

#	Sym.	H ₂ C=C=NH							D ₂ C=C=ND				H ₂ C=C=ND				
		Harm.	VCI	Int.	Exp. ^a	Exp. ^b	Exp. ^c	Exp. ^d	Harm.	VCI	Int.	Exp. ^d	Harm.	VCI	Int. ^a	Exp. ^d	
ν_1	A'	3492.7	3315.4	10.9		3321.8			2563.0	2464.4	17.1		3177.1	3046.7	29.7		
ν_2		3177.0	3048.0	2.6					2325.3	2250.1	40.7	2246	2562.9	2467.4	20.1		
ν_3		2084.4	2041.8	281.9		2037	2043.6	2040	2044.1	1997.7	150.2	1998	2067.2	2027.7	287.0	2028	
ν_4		1440.3	1435.9	0.1		1355			1231.5	1207.2	0.7		1440.2	1424.7	3.4		
ν_5		1140.1	1122.5	16.9		1127		1124	944.4	921.7	23.3	921	1136.0	1120.4	11.7	1120	
ν_6		1045.1	1006.7	200.2	1000.2	1004	1000.2	1000	824.5	804.1	77.0	800	829.9	807.7	74.1	817	
ν_7		705.5	691.1	77.2	692.9			690	555.3	549.6	39.8		705.2	679.5	53.4	693	
ν_8		463.3	464.3	19.8	466.5				417.6	415.5	27.0		427.9	426.5	24.0		
ν_9	A''	3276.2	3132.5	0.2					2441.0	2359.3	0.0		3276.4	3131.4	0.2		
ν_{10}		1000.3	980.7	0.6	983.1				842.2	831.0	0.0		1000.4	979.2	0.1		
ν_{11}		904.6	876.0	29.6		872		872	666.2	653.7	27.9	648	752.2	731.4	19.1		
ν_{12}		405.8	405.7	0.4	409.0				351.4	349.4	0.2		400.8	399.4	0.2		

Frequencies are given in cm⁻¹ and infrared intensities in km/mol.

^aExperimental gas phase values taken from Bane et al. (2011c,c,a).

^bExperimental values taken from the compilation in Bane et al. (2011c).

^cExperimental values taken from Ito et al. (1990) and Ito and Nakanaga (2010).

^dExperimental Ar matrix values taken from Jacox and Milligan (1963) and Jacox (1979).

where the corresponding values have been inserted. As can be seen from above equations, the efficient intensity stealing results from a compensation of the signs of the eigenvectors and the deperturbed transition dipole moments. The analysis and composition of all observed resonances of the fundamental modes of all isotopologues based on VCI calculations is summarized in **Table 5**. For all other fundamental modes of the non-deuterated molecule the agreement of the VCI calculations with the experimental results is excellent and the maximum deviation is no larger than 6.2 cm⁻¹, which is within the error bar of potential energy surfaces obtained from explicitly correlated coupled-cluster theory (Rauhut et al., 2009). In order to reduce this remaining error even further one would need to incorporate a number of corrections within the electronic structure calculations as for example high-order coupled-cluster terms, core-correlation effects, relativistic contributions, etc. (Ruden et al., 2004; Meier et al., 2011).

The results for the fully deuterated isotopologue, i.e., D₂CCND are of the same quality as for H₂CCNH and thus the VCI results most likely provide reliable predictions for all fundamentals. Most remarkably for this isotopologue are the very strong intensities for ν_3 and its resonance partners (cf. **Table 5**). The results for H₂CCND look more inconsistent than for the other two isotopologues. While modes ν_3 and ν_5 are in excellent agreement with the experimental results, the VCI results for ν_6 and ν_7 deviate by 9.3 and 13.5 cm⁻¹ from the experimental reference data, respectively. According to our VCI calculation, ν_6 shows a weak Fermi resonance with the overtone of ν_{12} (due to its weak character it has not been listed in **Table 5**). As such coupling pairs are sensitive with respect to environmental effects as arising from the argon matrix, the deviation of 9.3 cm⁻¹ may be explained this way. However, we consider this rather unlikely, but suspect difficulties in pinpointing the transition energies in the experiment, because Jacox reports

that overlapping parent molecule absorptions and unassigned contributions of other products such as the partially deuterated methyl cyanides complicate the assignment of other absorptions to the partially deuterated ketenimines (Jacox, 1979). Note that for all isotopologues, ν_4 shows strong Fermi resonances, but with different partners and in all cases the intensity of the overtone is stronger than for the fundamental.

3.3. Rotational Spectrum

In **Figure 1**, our computed RVCi rotational spectrum of ketenimine (**Figure 1A**) is compared with a simulated experimental spectrum (**Figure 1B**) for a temperature of $T = 50$ K. The latter spectrum has been calculated with the SPCAT program (Pickett, 1991) using the spectroscopic parameters of Degli Esposti et al. (2014) determined from the submillimeter wave spectrum, while intensities are based on the experimentally determined dipole moments in the vibrational ground state (Rodler et al., 1984). Intensities are given relative to the strongest line at $T = 50$ K, which corresponds to the 5_{2,3} → 6_{3,3} transition in both cases. Excellent agreement between the RVCi and the experimental spectrum is observed. Only very subtle frequency differences appear upon close inspection, which occur mainly due to the difference of about 0.3 GHz in the employed A rotational constants (compare **Table 2**). The overall shape of the spectrum, which is dominated by ^cR₁₀ branch progressions and the sharp ^cQ branches, is nicely reproduced by the RVCi spectrum.

We have studied the temperature dependence of the ground state rotational spectrum in the range 20 to 300 K and results are depicted in **Figure 2**. With increasing temperature the intensity of the rotational transitions decrease by about a factor of 2 and the rather sharp ^cQ₁₀ branches below 600 GHz broaden significantly. While for $T = 20$ K the ^cR₁₀ transitions originating in $K_a = 1$ states are the strongest up to 2 THz, with each

TABLE 5 | Resonances of the fundamental modes of ketenimine and its isotopologues.

Molecule	Mode	Freq.	Int.	Composition				
H ₂ CCNH	ν_4	1435.9	0.1	4 ¹	(55.8%)	7 ²	(35.2%)	
		1350.9	8.4	7 ²	(53.3%)	4 ¹	(36.1%)	
	ν_{11}	876.0	29.6	11 ¹	(59.6%)	8 ¹ 12 ¹	(36.7%)	
		880.5	18.6	8 ¹ 12 ¹	(57.1%)	11 ¹	(39.0%)	
D ₂ CCND	ν_4	1207.2	0.7	4 ¹	(69.9%)	6 ¹ 12 ¹	(21.4%)	
		1220.6	1.9	6 ¹ 12 ¹	(60.3%)	4 ¹	(25.6%)	
	ν_3	1997.7	150.2	3 ¹	(49.1%)	4 ¹ 6 ¹	(24.8%)	
		2019.2	40.1	4 ¹ 6 ¹	(52.3%)	6 ² 8 ¹	(16.7%)	3 ¹ (13.3%)
		2001.0	136.6	6 ² 8 ¹	(41.2%)	3 ¹	(42.0%)	
	ν_1	2464.4	17.1	1 ¹	(65.0%)	6 ¹ 10 ²	(27.5%)	
2467.0		12.0	6 ¹ 10 ²	(55.2%)	1 ¹	(37.2%)		
H ₂ CCND	ν_5	1120.4	11.7	5 ¹	(50.9%)	7 ¹ 8 ¹	(27.8%)	11 ¹ 12 ¹ (16.8%)
		1108.1	8.1	7 ¹ 8 ¹	(64.4%)	5 ¹	(28.9%)	
		1133.6	4.8	11 ¹ 12 ¹	(77.1%)	5 ¹	(15.8%)	
	ν_4	1424.7	3.4	4 ¹	(52.7%)	7 ²	(28.5%)	
		1345.3	12.9	7 ²	(57.8%)	4 ¹	(31.6%)	

Frequencies are given in cm^{-1} and infrared intensities in km/mol .

^{1,2}The superscripts denote the excitation levels of the individual modes.

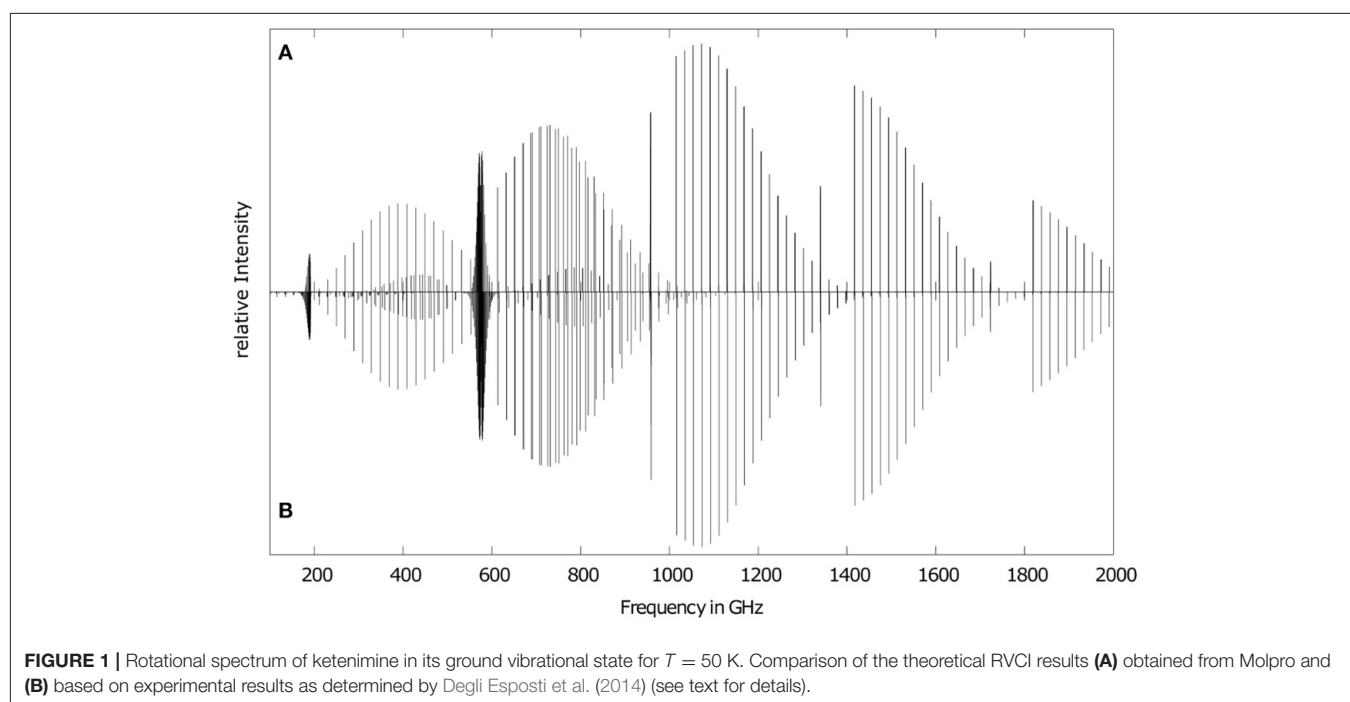


FIGURE 1 | Rotational spectrum of ketenimine in its ground vibrational state for $T = 50$ K. Comparison of the theoretical RVC1 results (A) obtained from Molpro and (B) based on experimental results as determined by Degli Esposti et al. (2014) (see text for details).

increase in temperature the maximum shifts by one unit in K_a . Furthermore, the effect of asymmetry splitting in $K_a = 1$ states are clearly visible. All these observations originate in the Boltzmann distribution function resulting in a higher partition function and a shift in the thermal distribution toward higher K_a and J . The former is responsible for the emergence of higher energy branches and the latter for the shifts in the maximum for individual J -progressions, highlighting the importance of an accurate determination of the partition function.

3.4. Rovibrational Spectrum

It is known that the rovibrational spectrum of ketenimine shows many strongly coupled rovibrational bands in the energy regime between 300 and 1200 cm^{-1} (Bane et al., 2011a,b,c). For this reason, we want to give a broad overview over this area with **Figure 3**. The figure shows the 5 fundamental bands ν_5 , ν_6 , ν_7 , ν_8 , ν_{11} , as well as the overtone $2\nu_8$ and the combination band $\nu_{12} + \nu_8$. The comparison between RVC1 and RCI spectra allows for a better understanding of the coupling and resonance

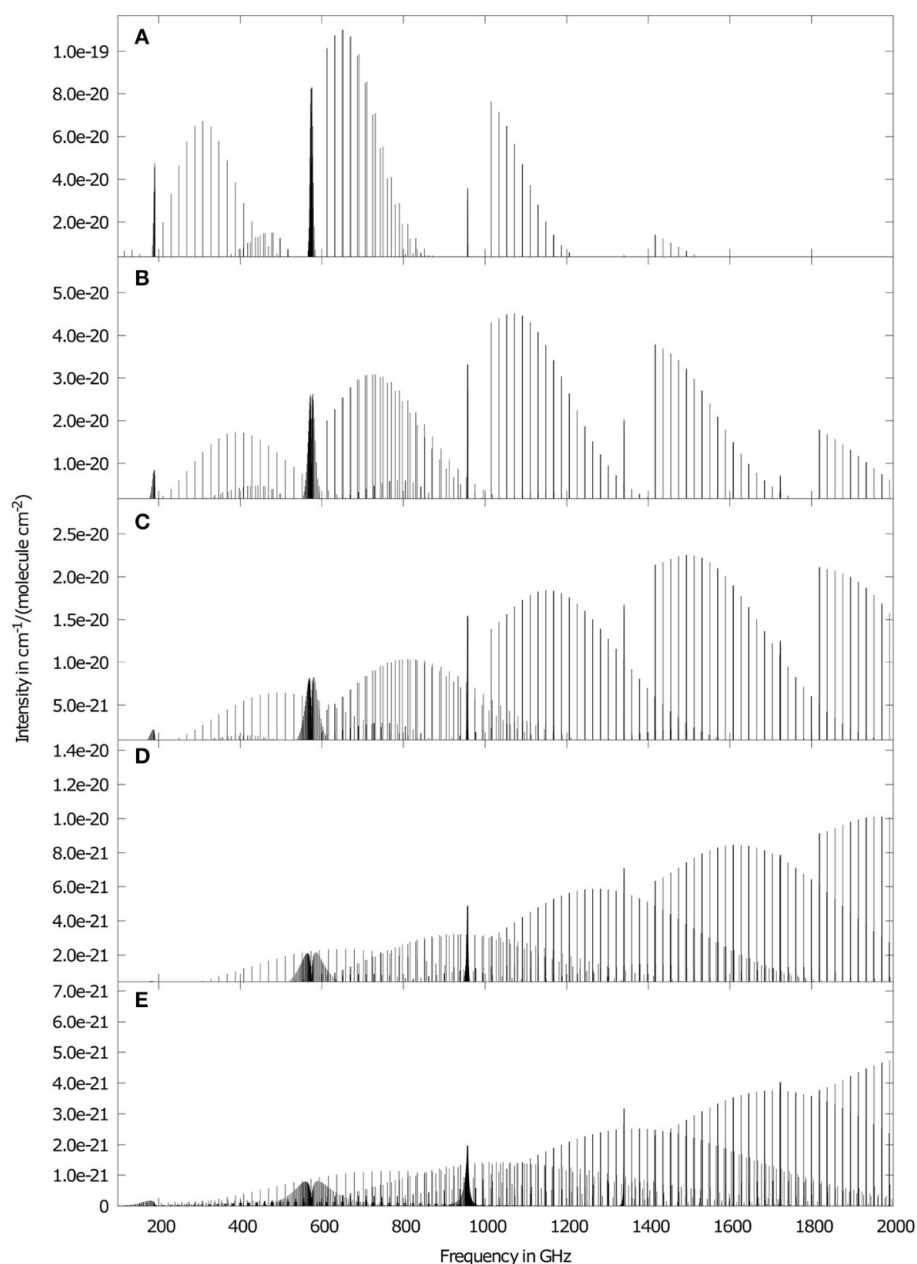


FIGURE 2 | Ground state rotational RVC1 spectrum of ketenimine for different temperatures, **(A)** 20 K, **(B)** 50 K, **(C)** 100 K, **(D)** 200 K, **(E)** 300 K. Temperatures are considered only in the occupation numbers and not in line broadening. For the sake of clarity, the intensity axis of adjacent sub-figures are downscaled by a factor of two for increasing temperatures.

effects. Two examples for these couplings can be seen around 400 and 900 cm^{-1} . Therefore these areas are displayed in separate **Figures 4** and **5** and will be discussed below. For the following figures, we did not use any line broadening, since no direct comparison with experimental results is depicted.

A good example for the strong Coriolis-coupling in this system can be seen in **Figure 4** between ν_8 and ν_{12} . The bottom subplot (**Figure 4B**) shows the results of the RCI calculation, where Coriolis-coupling is not considered. ν_{12} has about two

orders of magnitude less intensity than ν_8 , in line with the band intensities obtained from VCI (cf. **Table 4**). The in-plane CCN bending vibration ν_8 clearly shows an A-type spectrum, whereas the out-of-plane CCN bend ν_{12} shows the expected B-type intensity pattern. Inclusion of Coriolis-coupling in the upper subplot (**Figure 4A**) results in ν_{12} gaining about one order of magnitude in intensity by intensity borrowing in the RVC1 calculation. The missing intensity in the stronger band is hard to see, since the relative difference is smaller. Furthermore, ν_{12}

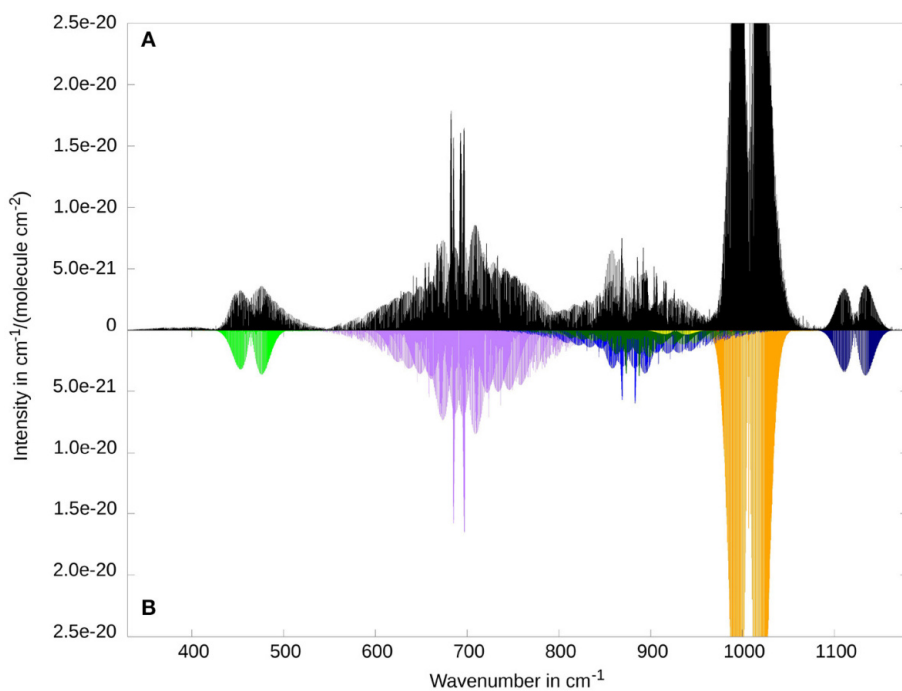


FIGURE 3 | Overview of the low frequency range of the rovibrational spectrum of ketenimine. Comparison between RVC1 (A) and RCI (B) results. Visible contributions are provided by the fundamental bands ν_8 (at 464.4 cm^{-1} , CCN in-plane bend, in light green), ν_7 (at 691.2 cm^{-1} , CH_2 wagging, in purple), ν_{11} (at 876.2 cm^{-1} , torsion, in light blue), ν_6 (at 1007.1 cm^{-1} , CNH bend, in orange), ν_5 (at 1122.5 cm^{-1} , CCN stretch, in dark blue) as well as the combination band $\nu_8 + \nu_{12}$ (at 880.7 cm^{-1} in dark green), and the overtone $2\nu_8$ (at 927.3 cm^{-1} in yellow).

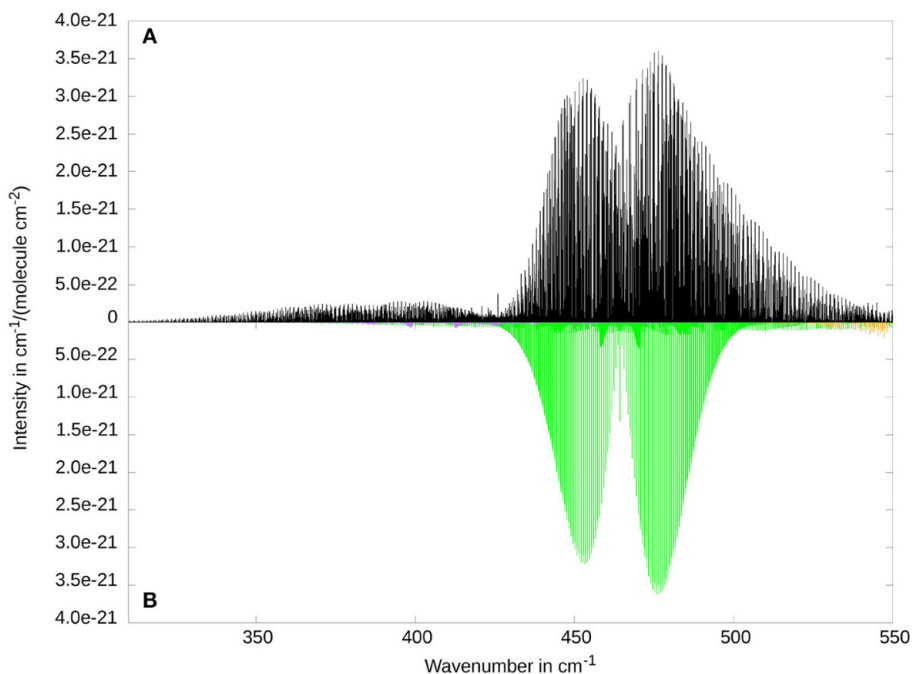


FIGURE 4 | The two lowest fundamental bands ν_{12} (at 405.7 cm^{-1} , CCN out-of-plane bend, VCI intensity 0.4 km/mol , in purple) and ν_8 (at 464.4 cm^{-1} , CCN in-plane bend, VCI intensity 19.8 km/mol , in light green) as well as small contributions of ν_7 (at 691.2 cm^{-1} , CH_2 wagging, in orange). Comparison between RVC1 (A) and RCI (B).

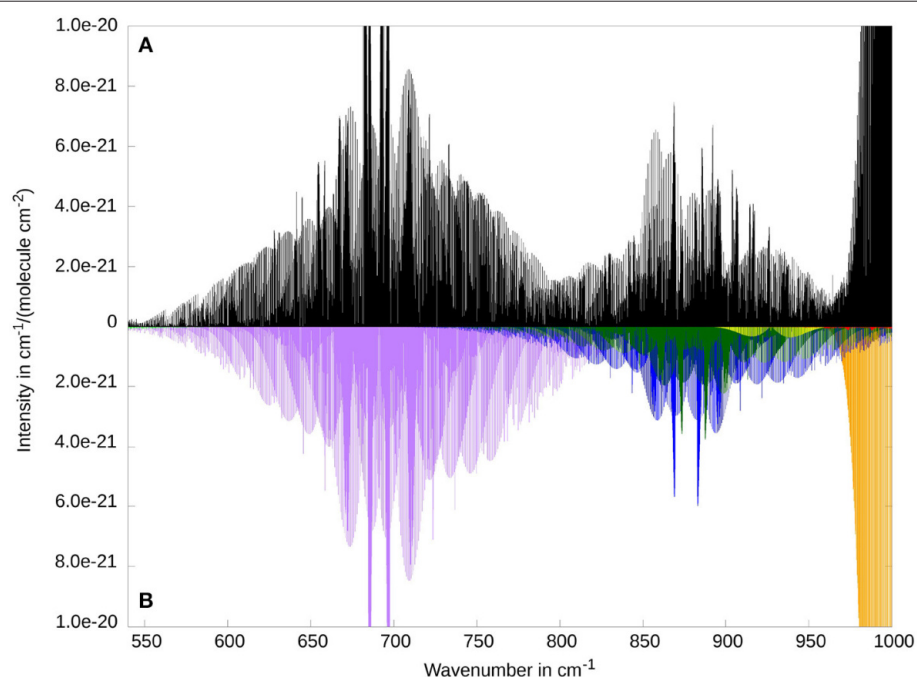


FIGURE 5 | Rovibrational spectrum of ketenimine of the fundamental bands ν_7 (at 691.2 cm^{-1} , in purple), ν_{11} (at 876.2 cm^{-1} , in light blue), ν_{10} (at 980.7 cm^{-1} , in red, barely visible) and ν_8 (at 1007.1 cm^{-1} in orange) and the combination band $\nu_8 + \nu_{12}$ (at 880.7 cm^{-1} in dark green), and the overtone $2\nu_8$ (at 927.3 cm^{-1} in yellow). Comparison between RVC1 (A) and RCI (B) results.

can neither be assigned to an *A*-type nor a *B*-type band structure, due to the lifting of the typical selection rules via Coriolis-coupling. For the ν_8 fundamental, the overall shape of an *A*-type transition is retained. Both bands show a rather asymmetric structure, with a supposed band center of the ν_{12} mode shifted by about 20 cm^{-1} to lower energies and visible transitions well below 350 cm^{-1} . This is in contrast to ν_8 , where both branches gain intensity toward higher energies, with an overlapping region at about 470 cm^{-1} . The high energy tails of the *R*-branch (around 530 cm^{-1}) could also be influenced by the ν_7 mode (orange in **Figure 4**). However, we expect that effect to be small, since the VCI energies of the two modes ν_7 and ν_8 are separated by more than 200 cm^{-1} .

A comparison with the experimental and simulated spectra of Bane and coworkers (Figures 2A and B in Bane et al., 2011c) shows in general good agreement for ν_{12} (**Figure 4** as well as in **Supplementary Figure 1**). This holds for both the number of progressions and their distribution over the spectral range from 330 to 410 cm^{-1} . However, there seems to be a sudden drop in intensity at 410 cm^{-1} that can not be found in our calculated results. The slight shift of our RVC1-spectrum by about 4 cm^{-1} compared to experiment can be explained by our error in the VCI energy of 3.3 cm^{-1} (cf. **Table 4**). Comparing the spectra of Bane et al. for ν_8 (Figures 2C and D in Bane et al., 2011c) with ours (compare also in **Supplementary Figure 2**) shows somewhat larger deviations. While the *A*-type *P* and *R* branch structure is still recognizable in **Figure 4**, the spectra of Bane et al. show a broader distribution of the K_a sub-bands leading to the *A*-type band shape being partially obscured. It

should be mentioned that there are isolated peaks protruding both bands (see Bane et al., 2011c). Tests have shown (see **Supplementary Figures 1–4**) that such prominent peaks as well as the above discussed differences in the intensity patterns originate from line broadening. Since we do not use any broadening, those protruding peaks cannot be expected in our spectrum, but of course must appear in the experimental spectra.

In contrast to the previously considered modes, the CH_2 wagging mode ν_7 does not change its macroscopic shape due to Coriolis coupling. As can be seen in **Figure 5**, the general form of ν_7 corresponds to a *C*-type transition of a near-prolate asymmetric top molecule. The main difference due to RVC1 (in the top panel) is the splitting of the central *Q*-branches. In comparison with the work of Bane et al. (Figure 2B in Bane et al., 2011b), there are two small deviations besides the overall good agreement (compare also in **Supplementary Figure 3**). First, there is a small shift for the two high peaks in the middle of the mode. Second, the experiment seems to show a sudden drop in intensity between the middle (650 and 730 cm^{-1}) and the outer parts of the progression (above 730 and 650 cm^{-1}). As mentioned before, the distributed peaks shown in the paper of Bane et al. (2011b), are caused by a Gauss broadening of the experimental results and are therefore not to be expected in our spectra. The possible coupling of ν_7 with higher energy modes (above 750 cm^{-1} in **Figure 5**) is not shown in the simulated spectrum of Bane et al. (2011b).

Another example of extensive rovibrational coupling occurs between 780 and 970 cm^{-1} (see **Figure 5**). The reason for

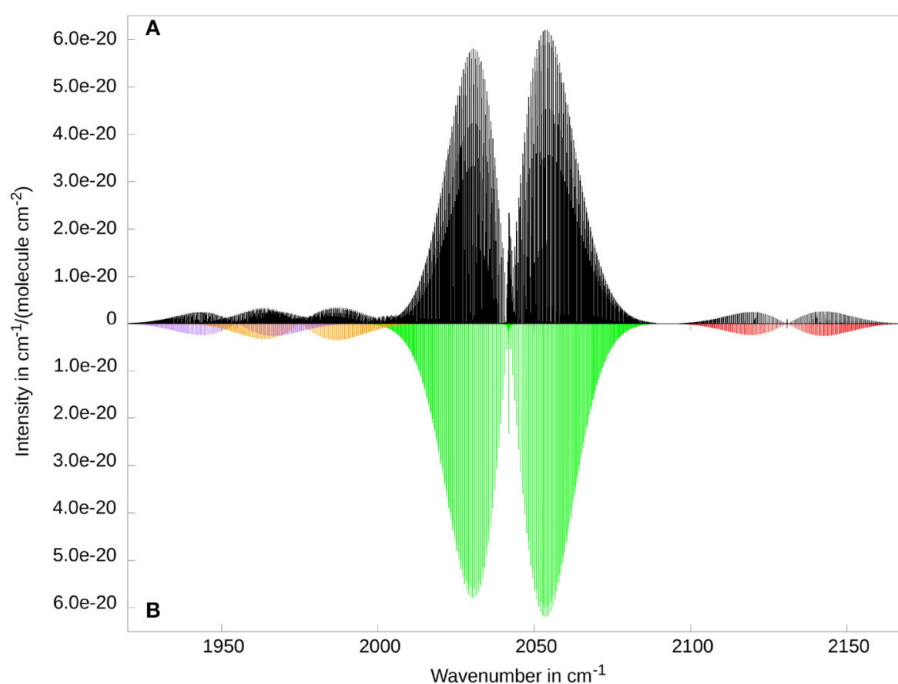


FIGURE 6 | Rovibrational spectrum of ketenimine in the region of the strongest fundamental band ν_3 (at 2041.8 cm^{-1} , CCN stretch, in green). Additionally, the overtones $2\nu_{10}$ (at 1955.0 cm^{-1} , in purple), and $2\nu_6$ (at 1975.1 cm^{-1} , in orange), as well as the combination band $\nu_5 + \nu_6$ (at 2130.8 cm^{-1} , in red) provide visible contributions in this spectral range. Comparison between RVC1 (**A**) and RCI (**B**) results.

this is the close proximity of three vibrational bands: one fundamental band (ν_{11} at 876.2 cm^{-1} , torsion, A'' symmetry), one combination band ($\nu_8 + \nu_{12}$ at 880.7 cm^{-1} , A'' symmetry) and one overtone ($2\nu_8$ at 927.3 cm^{-1} , A' symmetry) within 50 cm^{-1} . Additionally, there is a further “dark state” involved, corresponding to the overtone of the out-of-plane CCN bending mode ($2\nu_8$ at 809.6 cm^{-1} , A' symmetry). While the overtones $2\nu_{12}$ and $2\nu_8$ are strongly coupled to the combination band $\nu_8 + \nu_{12}$ via a -axis Coriolis-coupling ($\zeta_{8,12}^a = -0.802$), similar to the correspondingly coupled fundamentals, the ν_{11} fundamental has been shown to be in Fermi resonance with the combination band (cf. **Table 5**). The resulting rovibrational coupling leads to an almost complete loss of discernible band structure when comparing the RCI (bottom panel) and the RVC1 spectrum (top panel). As a consequence, experimental assignment and interpretation of this spectral region will be highly difficult without reliable estimates of spectroscopic parameters obtained from theory.

Figure 6 reveals only very weak Coriolis coupling between ν_3 and $2\nu_6$, respectively $2\nu_{10}$. One reason for this is that the largest non-vanishing ζ constants for $\zeta_{3,6}^\alpha$ and $\zeta_{3,10}^\alpha$ correspond to b and c direction, respectively. Hence the rotational constants along the b and c direction have to be considered. Since they are a factor of 20 smaller than the A rotational constant, the coupling is significantly weaker. In addition to that, Coriolis coupling between a fundamental band and the overtone of another band requires at least the first order in the μ -tensor expansion. Therefore, it is possible that in experiments a somewhat stronger

coupling occurs, even though it is unlikely due to the small rotational constants. The only experimental results for this mode have been presented by Ito et al. (1990). While a direct comparison of spectra is ambiguous, due to relatively low resolution and a contamination of the experimental probe, Ito et al. do note signs of Coriolis perturbations in the fitted effective spectroscopic parameters of the ν_3 band.

Figure 7 shows the XH stretching fundamental region between 3000 and 3500 cm^{-1} . The corresponding fundamental bands are the symmetric (ν_2) and antisymmetric (ν_9) CH_2 stretch vibrations and the NH stretching mode (ν_1), in energetically ascending order. Additionally, the $\nu_3 + \nu_5$ and the $\nu_3 + \nu_6$ combination bands provide a significant contribution to the spectrum. All bands show the expected shapes of A -type (ν_2 , $\nu_3 + \nu_5$, and $\nu_3 + \nu_6$), B -type (ν_1), and C -type (ν_9) transitions. So far there were no experimental results published for any of these bands. The comparison between RCI (bottom) and RVC1 results (top) gives no indications for substantial Coriolis coupling among the fundamental bands. This is supported by taking the corresponding Coriolis coupling constants into account, where the largest (absolute) value is found for $\zeta_{2,9}^c \approx 0.05$. Due to the restriction to a constant μ -tensor, no direct Coriolis coupling between fundamentals ν_i and combination bands $\nu_j + \nu_k$ is included in the RVC1-matrix. While a strong interaction between ν_2 and $\nu_3 + \nu_5$ is unlikely because of very small ζ -constants ($|\zeta_{2j}^b| \approx 0.003$), such a coupling might be relevant for the ν_9 fundamental due to the close by $\nu_3 + \nu_6$ combination band and the substantial intensity difference. However, experimental

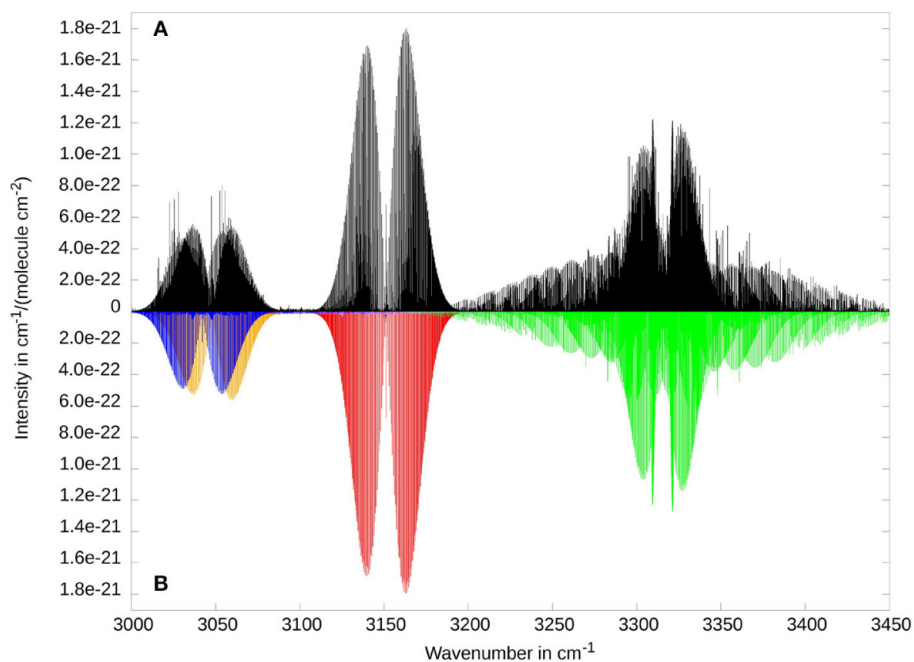


FIGURE 7 | Rovibrational spectrum of ketenimine in the region of XH stretching fundamentals. Three fundamental bands ν_2 (at 3048.0 cm^{-1} , symmetric CH_2 stretch, in orange), ν_3 (at 3132.5 cm^{-1} , anti-symmetric CH_2 stretch, in purple, barely visible) and ν_1 (at 3315.4 cm^{-1} , NH stretch, in light green) are shown, as well as the combination bands $\nu_3 + \nu_5$ (at 3042.0 cm^{-1} , in blue) and $\nu_3 + \nu_6$ (at 3151.1 cm^{-1} in red). Comparison between RVCi (**A**) and RCI (**B**) results.

observation of ν_9 will be complicated by the fact that ν_9 rovibrational transitions will most likely be hidden in between the stronger $\nu_3 + \nu_6$ band. Overall the rovibrational transitions in this spectral region have rather low intensity compared to other spectral regions. The VCI band intensity of the strongest vibrational transition ν_1 (10.9 km/mol) is already a factor of about 20 lower than the two strongest fundamental bands (cf. **Table 4**).

3.5. Summary and Conclusions

The vibrational, rotational and rovibrational spectra of ketenimine have been studied by high-level *ab initio* methods for the first time. Based on a new series of almost black-box algorithms being implemented in the MOLPRO package of quantum chemical programs, it was possible to simulate and analyze the complex rovibrational features of this near-prolate asymmetric top molecule. Note, that the input information for these calculations comprises just the molecular structure and the call of the requested modules, which act in a highly optimized—with respect to memory requirements and CPU time—and automated manner. Agreement with available experimental data, i.e., ground state rotational constants, vibrational band origins, dipole moments or the rotational spectrum as a whole, was found to be excellent or at least very good. Beside the reliable reproduction of experimental reference data, many predictions could be provided, which we consider a trustworthy guidance for new experimental studies or astrochemical observations. The occurrence of several Fermi resonances even for fairly low lying transitions requested accurate potential energy and dipole

surfaces, which has been accomplished by explicitly correlated coupled-cluster theory and the rather new distinguishable clusters approximation. A proper description of these resonances was found to be important for the subsequent rovibrational calculations. For example, the strong Fermi resonance of mode ν_{11} with the combination band $\nu_8 + \nu_{12}$ has significant impact on the spectrum, but was not discussed in the experimental work (Bane et al., 2011a). This example demonstrates the benefits, that can arise from combined experimental and theoretical studies to provide reliable reference data for astrophysical studies. Covering a wide spectral range and identifying signature areas within the spectrum are challenging goals in the future. Currently, work is in progress to include coupling terms originating from higher-order μ -tensor terms and hot bands.

DATA AVAILABILITY STATEMENT

The original contributions generated for the study are included in the article/**Supplementary Material**, further inquiries can be directed to the corresponding author/s.

AUTHOR CONTRIBUTIONS

MT performed all RVCi calculations, generated all figures, and wrote parts of the text. GR supervised the project, performed the VCI calculations, and wrote parts of the text. SE wrote large parts of the program being used for producing the data. BS performed VCI and RCI calculations, analyzed the spectra, and wrote parts

of the text. All authors contributed to the article and approved the submitted version.

ACKNOWLEDGMENTS

We are very grateful to Dr. Luca Bizzocchi and Prof. Luca Dore for supporting us with their experimental results, allowing for a direct comparison of our theoretical results with experimental reference data. Financial support by the

Studienstiftung des deutschen Volkes and the Deutsche Forschungsgemeinschaft (Project No. Ra 656/23-1) is kindly acknowledged.

SUPPLEMENTARY MATERIAL

The Supplementary Material for this article can be found online at: <https://www.frontiersin.org/articles/10.3389/fchem.2020.623641/full#supplementary-material>

REFERENCES

- Adler, T. B., Knizia, G., and Werner, H.-J. (2007). A simple and efficient CCSD(T)-F12 approximation. *J. Chem. Phys.* 127:221106. doi: 10.1063/1.2817618
- Alajarin, M., Marin-Luna, M., and Vidal, A. (2012). Recent highlights in ketenimine chemistry. *Eur. J. Org. Chem.* 2012, 5637–5653. doi: 10.1002/ejoc.201200383
- Aliev, M. R., and Watson, J. K. G. (1985). “Chapter 1 - Higher-order effects in the vibration-rotation spectra of semirigid molecules,” in *Molecular Spectroscopy: Modern Research, Vol. 3*, ed K. N. Rao (Orlando, FL: Academic Press), 1–67. doi: 10.1016/B978-0-12-580643-5.50006-3
- Allamandola, L. J., Tielens, A. G. G. M., and Barker, J. R. (1989). Interstellar polycyclic aromatic hydrocarbons: the infrared emission bands, the excitation/emission mechanism, and the astrophysical implications. *Astrophys. J. Suppl. Ser.* 71:733. doi: 10.1086/191396
- August, J. (1986). Spectroscopic studies of nitriles, enimes and ynamines of importance in interstellar chemistry. Ph.D. thesis. Sussex University.
- Ball, J. A., Gottlieb, C. A., Lilley, A. E., and Radford, H. E. (1970). Detection of methyl alcohol in sagittarius. *Astrophys. J.* 162:L203. doi: 10.1086/180654
- Bane, M. K., Robertson, E. G., Thompson, C. D., Appadoo, D. R. T., and McNaughton, D. (2011a). High-resolution Fourier-transform infrared spectroscopy of the ν_6 and Coriolis perturbation allowed ν_10 modes of ketenimine. *J. Chem. Phys.* 135:224306. doi: 10.1063/1.3664624
- Bane, M. K., Robertson, E. G., Thompson, C. D., Medcraft, C., Appadoo, D. R. T., and McNaughton, D. (2011b). High-resolution Fourier-transform infrared spectroscopy of the Coriolis coupled ground state and ν_7 mode of ketenimine. *J. Chem. Phys.* 134:234306. doi: 10.1063/1.3597775
- Bane, M. K., Thompson, C. D., Robertson, E. G., Appadoo, D. R. T., and McNaughton, D. (2011c). High-resolution FTIR spectroscopy of the ν_8 and Coriolis perturbation allowed ν_12 bands of ketenimine. *Phys. Chem. Chem. Phys.* 13, 6793–6798. doi: 10.1039/C0CP01816C
- Brown, R., Rice, E., and Rodler, M. (1985). *Ab initio* studies of the structures and force fields of ketenimine and related molecules. *Chem. Phys.* 99, 347–356. doi: 10.1016/0301-0104(85)80175-0
- Cami, J., Bernard-Salas, J., Peeters, E., and Malek, S. E. (2010). Detection of C_60 and C_70 in a Young Planetary Nebula. *Science* 329, 1180–1182. doi: 10.1126/science.1192035
- Carvalho, G. A., and Pilling, S. (2020). Photolysis of CH_3CN Ices by soft X-rays: implications for the chemistry of astrophysical ices at the surroundings of X-ray sources. *J. Phys. Chem. A* 124, 8574–8584. doi: 10.1021/acs.jpca.0c06229
- Charbonneau, D., Brown, T. M., Noyes, R. W., and Gilliland, R. L. (2002). Detection of an extrasolar planet atmosphere. *Astrophys. J.* 568:377. doi: 10.1086/338770
- Czakó, G., Mátyus, E., and Császár, A. G. (2009). Bridging theory with experiment: a benchmark study of thermally averaged structural and effective spectroscopic parameters of the water molecule. *J. Phys. Chem. A* 113, 11665–11678. doi: 10.1021/jp902690k
- Degli Esposti, C., Dore, L., and Bizzocchi, L. (2014). Accurate rest-frequencies of ketenimine (CH_2CNH) at submillimetre wavelength. *Astron. Astrophys.* 565:A66. doi: 10.1051/0004-6361/201423589
- Dinu, D. F., Ziegler, B., Podewitz, M., Liedl, K. R., Loerting, T., Grothe, H., et al. (2020). The interplay of VSCF/VCI calculations and matrix-isolation IR spectroscopy—Mid infrared spectrum of CH_3CH_2F and CD_3CD_2F . *J. Mol. Spectrosc.* 367:111224. doi: 10.1016/j.jms.2019.111224
- Endres, C. P., Schlemmer, S., Schilke, P., Stutzki, J., and Müller, H. S. P. (2016). The cologne database for molecular spectroscopy, CDMS, in the virtual atomic and molecular data centre, VAMDC. *J. Mol. Spectrosc.* 327, 95–104. doi: 10.1016/j.jms.2016.03.005
- Erfort, S., Tschöpe, M., and Rauhut, G. (2020a). Toward a fully automated calculation of rovibrational infrared intensities for semi-rigid polyatomic molecules. *J. Chem. Phys.* 152:244104. doi: 10.1063/5.0011832
- Erfort, S., Tschöpe, M., Rauhut, G., Zeng, X., and Tew, D. P. (2020b). *Ab initio* calculation of rovibrational states for non-degenerate double-well potentials: cis-trans isomerization of HOPO. *J. Chem. Phys.* 152:174306. doi: 10.1063/5.0005497
- Gandhi, S., Brogi, M., Yurchenko, S. N., Tennyson, J., Coles, P. A., Webb, R. K., et al. (2020). Molecular cross-sections for high-resolution spectroscopy of super-Earths, warm Neptunes, and hot Jupiters. *Mon. Not. R. Astron. Soc.* 495, 224–237. doi: 10.1093/mnras/staa981
- Godfrey, P. D., Brown, R. D., Robinson, B. J., and Sinclair, M. W. (1973). Discovery of Interstellar Methanimine (Formaldimine). *Astrophys. Lett.* 13:119.
- Herbst, E., and van Dishoeck, E. F. (2009). Complex organic interstellar molecules. *Annu. Rev. Astron. Astrophys.* 47, 427–480. doi: 10.1146/annurev-astro-082708-101654
- Hill, J. G., Mazumder, S., and Peterson, K. A. (2010). Correlation consistent basis sets for molecular core-valence effects with explicitly correlated wave functions: the atoms B-Ne and Al-Ar. *J. Chem. Phys.* 132:054108. doi: 10.1063/1.3308483
- Ito, F., and Nakanaga, T. (2010). Observation of the high-resolution spectrum of the N-H bending vibration of ketenimine CH_2CNH . *J. Mol. Spectrosc.* 264, 100–104. doi: 10.1016/j.jms.2010.09.012
- Ito, F., Nakanaga, T., Sugawara, K.-i., Takeo, H., Sugie, M., Matsumura, C., et al. (1990). Observation of the High-Resolution Infrared Spectrum of the ν_4 Band of Ketenimine, CH_2CNH . *J. Mol. Spectrosc.* 140, 177–184. doi: 10.1016/0022-2852(90)90016-J
- Jacox, M. E. (1979). Matrix isolation study of the interaction of excited argon atoms with methyl cyanide, vibrational and electronic spectra of ketenimine. *Chem. Phys.* 43, 157–172. doi: 10.1016/0301-0104(79)85184-8
- Jacox, M. E., and Milligan, D. E. (1963). Infrared study of the reactions of CH_2 and NH with C_2H_2 and C_2H_4 in solid argon. *J. Am. Chem. Soc.* 85, 278–282. doi: 10.1021/ja00886a006
- Jefferts, K. B., Penzias, A. A., and Wilson, R. W. (1970). Observation of the CN radical in the orion nebula and W51. *Astrophys. J.* 161:L87. doi: 10.1086/180576
- Kaneti, J., and Nguyen, M. T. (1982). Theoretical study of ketenimine: geometry, electronic properties, force constants and barriers to inversion and rotation. *J. Mol. Struct.* 87, 205–210. doi: 10.1016/0166-1280(82)80054-7
- Kats, D., Kreplin, D., Werner, H.-J., and Manby, F. R. (2015). Accurate thermochemistry from explicitly correlated distinguishable cluster approximation. *J. Chem. Phys.* 142:064111. doi: 10.1063/1.4907591
- Kats, D., and Manby, F. R. (2013). The distinguishable cluster approximation. *J. Chem. Phys.* 139:021102. doi: 10.1063/1.4813481
- Kawaguchi, K., Takano, S., Ohishi, M., Ishikawa, S.-I., Miyazawa, K., Kaifu, N., et al. (1992). Detection of HNCCC in TMC-1. *Astrophys. J.* 396:L49. doi: 10.1086/186514
- Knizia, G., and Werner, H.-J. (2008). Explicitly correlated RMP2 for high-spin open-shell reference states. *J. Chem. Phys.* 128:154103. doi: 10.1063/1.2889388

- Krim, L., Guillemin, J., and Woon, D. (2019). Formation of methyl ketenimine ($\text{CH}_3\text{CH}=\text{C}=\text{NH}$) and ethylcyanide ($\text{CH}_3\text{CH}_2\text{C}\equiv\text{N}$) isomers through successive hydrogenations of acrylonitrile ($\text{CH}_2=\text{CH}-\text{C}\equiv\text{N}$) under interstellar conditions: the role of $\text{CH}_3\text{C}^*\text{H}-\text{C}\equiv\text{N}$ radical in the activation of the cyano group chemistry. *MNRAS* 485, 5210–5220. doi: 10.1093/mnras/stz698
- Lovas, F., Hollis, J., Remijan, A., and Jewell, P. (2006). Detection of ketenimine (CH_2CNH) is Sagittarius B2(N) hot cores. *Astrophys. J.* 645, L137–L140. doi: 10.1086/506324
- Mandell, A. M., Haynes, K., Sinukoff, E., Madhusudhan, N., Burrows, A., and Deming, D. (2013). Exoplanet transit spectroscopy using wfc3: Wasp-12 b, wasp-17 b, and wasp-19 b. *Astrophys. J.* 779:128. doi: 10.1088/0004-637X/779/2/128
- Martín-Pintado, J., de Vicente, P., Wilson, T. L., and Gaume, R. (1996). “A hot ring in the Sgr B2 molecular cloud,” in *Science With Large Millimetre Arrays*, ed P. A. Shaver (Berlin; Heidelberg: Springer Berlin Heidelberg), 210–213. doi: 10.1007/978-3-540-69999-6_30
- McGuire, B. A. (2018). 2018 census of interstellar, circumstellar, extragalactic, protoplanetary disk, and exoplanetary molecules. *Astrophys. J. Suppl. Ser.* 239:17. doi: 10.3847/1538-4365/aae5d2
- Meier, P., Neff, M., and Rauhut, G. (2011). Accurate vibrational frequencies of borane and its isotopologues. *J. Chem. Theory Comput.* 7, 148–152. doi: 10.1021/ct1004752
- Müller, H. S. P., Schlöder, F., Stutzki, J., and Winnewisser, G. (2005). The cologne database for molecular spectroscopy, CDMS: a useful tool for astronomers and spectroscopists. *J. Mol. Struct.* 742, 215–227. doi: 10.1016/j.molstruc.2005.01.027
- Müller, H. S. P., Thorwirth, S., Roth, D. A., and Winnewisser, G. (2001). The cologne database for molecular spectroscopy, CDMS. *Astron. Astrophys.* 370, L49–L52. doi: 10.1051/0004-6361:20010367
- Neff, M., Hrenar, T., Oschetzki, D., and Rauhut, G. (2011). Convergence of vibrational angular momentum terms within the Watson Hamiltonian. *J. Chem. Phys.* 134:064105. doi: 10.1063/1.3551513
- Neff, M., and Rauhut, G. (2009). Toward large scale vibrational configuration interaction calculations. *J. Chem. Phys.* 131:124129. doi: 10.1063/1.3243862
- Öberg, K. I. (2016). Photochemistry and astrochemistry: photochemical pathways to interstellar complex organic molecules. *Chem. Rev.* 116, 9631–9663. doi: 10.1021/acs.chemrev.5b00694
- Ohishi, M. (2019). “Prebiotic complex organic molecules in space,” in *Astrobiology: From the Origins of Life to the Search for Extraterrestrial Intelligence*, eds A. Yamagishi, T. Kakegawa, and T. Usui (Singapore: Springer Singapore), 11–21. doi: 10.1007/978-981-13-3639-3_2
- Ohishi, M., and Kaifu, N. (1998). Chemical and physical evolution of dark clouds - Molecular spectral line survey toward TMC-1. *Faraday Discuss.* 109, 205–216. doi: 10.1039/a801058g
- Papoušek, D., and Aliev, M. R. (1982). *Molecular Vibrational-rotational Spectra: Theory and Applications of High Resolution Infrared, Microwave and Raman Spectroscopy of Polyatomic Molecules*. Elsevier Science Ltd.
- Petrenko, T., and Rauhut, G. (2017). A new efficient method for the calculation of interior eigenpairs and its application to vibrational structure problems. *J. Chem. Phys.* 146:124101. doi: 10.1063/1.4978581
- Pflüger, K., Paulus, M., Jagiella, S., Burkert, T., and Rauhut, G. (2005). Multi-level vibrational SCF calculations and FTIR measurements on Furazan. *Theor. Chem. Acc.* 114, 327–332. doi: 10.1007/s00214-005-0678-4
- Pickett, H. M. (1991). The fitting and prediction of vibration-rotation spectra with spin interactions. *J. Mol. Spectrosc.* 148, 371–377. doi: 10.1016/0022-2852(91)90393-O
- Puzzarini, C., Salta, Z., Tassinato, N., Lupi, J., Cavallotti, C., and Barone, V. (2020). A twist on the reaction of the CN radical with methylamine in the interstellar medium: new hints from a state-of-the-art quantum-chemical study. *MNRAS* 496, 4298–4310. doi: 10.1093/mnras/staa1652
- Rauhut, G. (2015). Anharmonic Franck-Condon factors for the $\tilde{X}^2B_1 \leftarrow \tilde{X}^1A_1$ photoionization of ketene. *J. Phys. Chem. A* 119, 10264–10271. doi: 10.1021/acs.jpca.5b06922
- Rauhut, G., Knizia, G., and Werner, H.-J. (2009). Accurate calculation of vibrational frequencies using explicitly correlated coupled-cluster theory. *J. Chem. Phys.* 130:054105. doi: 10.1063/1.3070236
- Rodler, M., Brown, R. D., Godfrey, P. D., and Kleinbömer, B. (1986). The rotation-inversion spectrum of ketenimine, $\text{H}_2\text{C}=\text{C}=\text{NH}$. *J. Mol. Spectrosc.* 118, 267–276. doi: 10.1016/0022-2852(86)90240-7
- Rodler, M., Brown, R. D., Godfrey, P. D., and Tack, L. M. (1984). Generation, microwave spectrum and dipole moment of ketenimine. *Chem. Phys. Lett.* 110, 447–451. doi: 10.1016/0009-2614(84)87068-2
- Ruden, T. A., Helgaker, T., Jørgensen, P., and Olsen, J. (2004). Coupled-cluster connected quadruples and quintuples corrections to the harmonic vibrational frequencies and equilibrium bond distances of HF, N₂, F₂, and CO. *J. Chem. Phys.* 121, 5874–5884. doi: 10.1063/1.1780155
- Špirko, V., Jensen, P., Bunker, P., and Čejchan, A. (1985). The development of a new Morse-oscillator based rotation-vibration Hamiltonian for H_3^+ . *J. Mol. Spectrosc.* 112, 183–202. doi: 10.1016/0022-2852(85)90203-6
- Theule, P., Borget, F., Mispelaer, F., Danger, G., Duvernay, F., Guillemin, J. C., et al. (2011). Hydrogenation of solid hydrogen cyanide HCN and methanimine CH_2NH at low temperature. *Astron. Astrophys.* 534:A64. doi: 10.1051/0004-6361/201117494
- Vasconcelos, F., Pilling, S., Agnihotri, A., Rothard, H., and Boduch, P. (2020). Methylenimine and cyanomethanimine synthesis from ion irradiation of N₂-CH₄ ice: implication on the formation of prebiotic molecules in outer solar system bodies. *Icarus* 351:113944. doi: 10.1016/j.icarus.2020.113944
- Vázquez, J., and Stanton, J. F. (2007). Treatment of Fermi resonance effects on transition moments in vibrational perturbation theory. *Mol. Phys.* 105, 101–109. doi: 10.1080/00268970601135784
- Wang, S. C. (1929). On the asymmetrical top in quantum mechanics. *Phys. Rev.* 34, 243–252. doi: 10.1103/PhysRev.34.243
- Watson, J. K. G. (1968). Simplification of the molecular vibration-rotation Hamiltonian. *Mol. Phys.* 15, 479–490. doi: 10.1080/00268976800101381
- Watson, J. K. G. (1977). “Aspects of quartic and sextic centrifugal effects on rotational energy levels,” in *Vibrational Spectra and Structure*, Vol. 6, ed J. R. Durig (Amsterdam: Elsevier), 1–89.
- Weinreb, S., Barrett, A. H., Meeks, M. L., and Henry, J. C. (1963). Radio observations of OH in the interstellar medium. *Nature* 200, 829–831. doi: 10.1038/200829a0
- Werner, H.-J., Knowles, P., Manby, F., Black, J., Doll, K., Heßelmann, A., et al. (2020). The Molpro quantum chemistry package. *J. Chem. Phys.* 152:144107. doi: 10.1063/5.0005081
- Wilson, R. W., Jefferts, K. B., and Penzias, A. A. (1970). Carbon monoxide in the orion nebula. *Astrophys. J.* 161:L43. doi: 10.1086/180567
- Woon, D. E. (2002). Pathways to glycine and other amino acids in ultraviolet-irradiated astrophysical ices determined via quantum chemical modeling. *Astrophys. J.* 571, L177–L180. doi: 10.1086/341227
- Yagi, K., Hirata, S., and Hirao, K. (2007). Multiresolution potential energy surfaces for vibrational state calculations. *Theor. Chem. Acc.* 118, 681–691. doi: 10.1007/s00214-007-0363-x
- Zaleski, D. P., Seifert, N. A., Steber, A. L., Muckle, M. T., Loomis, R. A., Corby, J. F., et al. (2013). Detection of E-cyanomethanimine toward sagittarius B2(N) in the green bank telescope PRIMOS survey. *Astrophys. J. Lett.* 765:L10. doi: 10.1088/2041-8205/765/1/L10
- Ziegler, B., and Rauhut, G. (2016). Efficient generation of sum-of-products representations of high-dimensional potential energy surfaces based on multimode expansions. *J. Chem. Phys.* 144:114114. doi: 10.1063/1.4943985
- Ziegler, B., and Rauhut, G. (2018). Rigorous use of symmetry within the construction of multidimensional potential energy surfaces. *J. Chem. Phys.* 149:164110. doi: 10.1063/1.5047912

Conflict of Interest: The authors declare that the research was conducted in the absence of any commercial or financial relationships that could be construed as a potential conflict of interest.

Copyright © 2021 Tschöpe, Schröder, Erfort and Rauhut. This is an open-access article distributed under the terms of the Creative Commons Attribution License (CC BY). The use, distribution or reproduction in other forums is permitted, provided the original author(s) and the copyright owner(s) are credited and that the original publication in this journal is cited, in accordance with accepted academic practice. No use, distribution or reproduction is permitted which does not comply with these terms.

Publication 2: Convergence of series expansions
in rovibrational configuration interaction
(RVCI) calculations

Convergence of series expansions in rovibrational configuration interaction (RVCI) calculations

Cite as: J. Chem. Phys. 157, 234105 (2022); doi: 10.1063/5.0129828

Submitted: 7 October 2022 • Accepted: 23 November 2022 •

Published Online: 15 December 2022



View Online



Export Citation



CrossMark

Martin Tschöpe^{a)}  and Guntram Rauhut^{b)} 

AFFILIATIONS

Institute for Theoretical Chemistry, University of Stuttgart, Pfaffenwaldring 55, 70569 Stuttgart, Germany

^{a)}tschoepe@theochem.uni-stuttgart.de

^{b)}Author to whom correspondence should be addressed: rauhut@theochem.uni-stuttgart.de

ABSTRACT

Rotational and rovibrational spectra are a key in astrophysical studies, atmospheric science, pollution monitoring, and other fields of active research. The *ab initio* calculation of such spectra is fairly sensitive with respect to a multitude of parameters and all of them must be carefully monitored in order to yield reliable results. Besides the most obvious ones, i.e., the quality of the multidimensional potential energy surface and the vibrational wavefunctions, it is the representation of the μ -tensor within the Watson Hamiltonian, which has a significant impact on the desired line lists or simulated spectra. Within this work, we studied the dependence of high-resolution rovibrational spectra with respect to the truncation order of the μ -tensor within the rotational contribution and the Coriolis coupling operator of the Watson operator. Moreover, the dependence of the infrared intensities of the rovibrational transitions on an n -mode expansion of the dipole moment surface has been investigated as well. Benchmark calculations are provided for thioformaldehyde, which has already served as a test molecule in other studies and whose rovibrational spectrum was found to be fairly sensitive. All calculations rely on rovibrational configuration interaction theory and the discussed high-order terms of the μ -tensor are a newly implemented feature, whose theoretical basics are briefly discussed.

Published under an exclusive license by AIP Publishing. <https://doi.org/10.1063/5.0129828>

I. INTRODUCTION

The identification of molecules in the interstellar medium (ISM) is a grand challenge in astrophysics and is mainly based on rotational and rovibrational infrared (IR) spectroscopy. Reference spectra for these molecules can either be measured in the lab or obtained from simulations.^{1–3} While the former approach may struggle with the extreme conditions needed to trap these systems, the latter suffers from limited accuracy with respect to experimental measurements. Yurchenko and Tennyson *et al.*,^{4–7} Tyuterev, Nikitin, and Rey,^{8–10} Bowman and Carter *et al.*,^{11,12} Carrington and co-workers,^{13,14} Császár *et al.*,^{15,16} Mátyus *et al.*,^{17,18} and other groups¹⁹ have studied the rovibrational spectra of many molecules based on highly accurate (and refined) potential energy surfaces using variational approaches with impressive agreement with respect to experimental reference data as available in popular databases.^{2,3,20,21} Within this context, different strategies relying on different Hamiltonians and coordinates have been followed up. The latter range from polyspherical,²² different internal to normal coordinates, while grid-based and analytical finite basis approaches

are used for determining the desired eigenpairs. Particular effort has been put into techniques that efficiently extract Hamiltonians from the potentials and refine these by experimental data in order to increase the final accuracy.²³ It is the occurrence of large amplitude motions, which often require sophisticated techniques and Hamiltonians, while the Watson Hamiltonian is restricted to semi-rigid molecules. A comparison by Cassam-Chenai *et al.*²⁴ of effective Hamiltonians either being based on generalized perturbation theory or on contact transformation techniques showed that the difference between the results of the investigated methods decreases as the orders of the expanded Hamiltonians increase. Consequently, our work here has a related focus. In contrast to the approaches of the groups mentioned above,^{4–19} which try to avoid any limitations, rovibrational spectra are also frequently simulated on the basis of model Hamiltonians with parameters obtained from fits to experimental transitions or from vibrational perturbation theory (VPT).^{25,26} As our interest is in the investigation of semi-rigid organic molecules in the interstellar medium (at low temperatures), we employ the Watson Hamiltonian²⁷ within the framework of configuration interaction theory.

In general, the *ab initio* calculation of rovibrational line lists or the simulation of high-resolution infrared spectra of molecules in the gas phase is a non-trivial task^{28–39} as many quantities need to be monitored and controlled in order to yield reliable results. In many approaches for the description of nuclear motions, this problem arises mainly from truncated series expansions of terms arising in the Hamiltonian. In the following, we will exclusively focus on the Watson Hamiltonian²⁷ and the specific terms within it. The most obvious expansion, which is not bound to rovibrational calculations, concerns the representation of the potential energy surface (PES). This issue has repeatedly been discussed in the literature^{40,41} and, thus, we take an n -mode expansion of the PES being truncated after the four-mode coupling terms for granted, which guarantees a certain level of accuracy.^{42–44} We will not discuss this topic in any detail, but, instead, we examined the convergence of the line intensities with respect to the expansion order of the dipole moment surface (DMS). However, our emphasis is on the expansion of the μ -tensor, the inverse of an effective moment of inertia tensor,²⁷ and, thus, on all three quantities depending on it, i.e., we focus on the convergence of state energies and rovibrational infrared intensities in dependence of the μ -tensor expansion for the (a) vibrational angular momentum (VAM) terms, (b) purely rotational contributions, and (c) the Coriolis coupling terms. About a decade ago, we have studied the dependence of purely vibrational transitions on a μ -tensor expansion of the VAM terms for rigid molecules and within the context of tunneling splittings as arising from double minimum potentials.⁴⁵ The effect of neglecting Coriolis and related coupling terms has been studied for different internal coordinates by Sarka *et al.*⁴⁶ Moreover, the dependence of the final results of a rovibrational study on the size of the vibrational basis will be studied.

As a result of this benchmark study, we will provide a set of recommendations in order to guide accurate rovibrational configuration interaction (RVCI) calculations. RVCI theory or its counterpart for non-rotating molecules, i.e., vibrational configuration interaction (VCI) theory,^{47–50} are appealing approaches for studying (ro)vibrational spectra as they are, in principle, unlimited in accuracy and can account for all sorts of resonances, e.g., Fermi⁵¹ or Darling Dennison resonances.⁵² This study is based on a fairly new implementation of RVCI theory within a development version of the MOLPRO suite of *ab initio* programs,⁵³ which can deal with any molecule belonging to an Abelian point group. We will briefly recall the basic principles of this particular implementation, which are necessary to understand the discussion of the benchmark calculations. We have restricted this study to calculations on thioformaldehyde (H₂CS, C_{2v}), as this molecule has been used as a benchmark molecule by several authors.^{4,5,54–57} Due to two quasi-degenerate vibrational modes, which, however, belong to different irreducible representations (irreps), the calculated spectrum was found to be extremely sensitive with respect to the Coriolis coupling. This and its limited size qualify this system for the investigations of this study.

II. THEORY

A. Rovibrational energies

As mentioned above, our implementation of RVCI theory relies on the Watson Hamiltonian²⁷ making use of potential energy surfaces V spanned by normal coordinates q_i , i.e.,

$$H = \frac{1}{2} \sum_{\alpha\beta} (J_\alpha - \pi_\alpha) \mu_{\alpha\beta} (J_\beta - \pi_\beta) - \frac{1}{2} \sum_i \frac{\partial^2}{\partial q_i^2} - \frac{1}{8} \sum_\alpha \mu_{\alpha\alpha} + V(\vec{q}), \quad (1)$$

with $\alpha, \beta \in \{x, y, z\}$, and J_α denoting a Cartesian component of the angular momentum operator. The VAM operator π_α is given as

$$\pi_\alpha = -i \sum_{jk} \zeta_{jk}^\alpha q_j \frac{\partial}{\partial q_k}, \quad (2)$$

with ζ_{jk}^α denoting the antisymmetric Coriolis ζ -constants. The μ -tensor is represented by an n -mode expansion and can be written as

$$\mu_{\alpha\beta} = \mu_{\alpha\beta}^{(0)} + \sum_i \mu_{\alpha\beta}^{(1)}(q_i) + \sum_{i<j} \mu_{\alpha\beta}^{(2)}(q_i, q_j) + \dots, \quad (3)$$

with

$$\mu_{\alpha\beta}^{(0)} = \frac{\delta_{\alpha\beta}}{I_{\alpha\beta}^{(0)}} = (I_{\alpha\alpha}^{(0)})^{-1}, \quad (4)$$

where $I_{\alpha\beta}$ is an element of the moment of inertia tensor and the superscript (0) denotes its value at the reference geometry. At positions given by elongations along the normal coordinates, the μ -tensor reads

$$\mu_{\alpha\beta} = I_{\alpha\beta}^{\prime-1} \quad \text{with} \quad I_{\alpha\beta}'(\vec{q}) = I_{\alpha\beta}(\vec{q}) - \sum_{ijk} \zeta_{ik}^\alpha \zeta_{jk}^\beta q_i q_j. \quad (5)$$

With Eqs. (4) and (5), the first and second order terms of the n -mode expansion of the μ -tensor can be written as

$$\mu_{\alpha\beta}^{(1)}(q_i) = I_{\alpha\beta}^{\prime-1}(q_i) - \mu_{\alpha\beta}^{(0)}, \quad (6)$$

$$\mu_{\alpha\beta}^{(2)}(q_i, q_j) = I_{\alpha\beta}^{\prime-1}(q_i, q_j) - \sum_{k \in \{ij\}} \mu_{\alpha\beta}^{(1)}(q_k) - \mu_{\alpha\beta}^{(0)}. \quad (7)$$

The evaluation of the individual terms of the μ -tensor essentially takes no time since only the displaced geometry needs to be evaluated and no *ab initio* electronic structure calculations are required. Likewise, the transformation of the grid representation of the tensor to an analytical form using Kronecker product fitting is very fast.⁴¹ With that and assuming monomials as basis functions, the respective terms of the μ -tensor expansion can be written as

$$\mu_{\alpha\beta}^{(1)}(q_i) = \sum_r d_{\alpha\beta}^{i,r} q_i^r, \quad (8)$$

$$\mu_{\alpha\beta}^{(2)}(q_i, q_j) = \sum_{rs} d_{\alpha\beta}^{ij,rs} q_i^r q_j^s, \quad (9)$$

with $d_{\alpha\beta}^{i,r}$ and $d_{\alpha\beta}^{ij,rs}$ denoting the respective coefficients. Using these relations, any integrals arising from the μ -tensor can be evaluated the same way as for the potential energy surface.

In the first step, we determine purely vibrational wavefunctions Φ_v ,

$$|\Phi_v\rangle = \sum_I c_I |\phi_v^I\rangle, \quad (10)$$

by solving the Schrödinger equation for non-rotating molecules using configuration-selective VCI theory. For details, see Refs. 58–60.

Switching now to RVCi theory, the Watson operator can be written as

$$H = \underbrace{\frac{1}{2} \sum_{\alpha\beta} \mu_{\alpha\beta} J_{\alpha} J_{\beta}}_{H_{\text{rot}}} - \underbrace{\frac{1}{2} \sum_{\alpha\beta} (J_{\alpha} \mu_{\alpha\beta} \pi_{\beta} + \pi_{\alpha} \mu_{\alpha\beta} J_{\beta})}_{H_{\text{rv}}} + H_{\text{vib}}, \quad (11)$$

where H_{vib} denotes the purely vibrational part of the Watson Hamiltonian, which was used for determining Φ_v . H_{rot} is the rotational contribution and H_{rv} is the well-known Coriolis coupling operator. Due to the n -mode expansion, the latter term cannot be simplified, because the VAM operator does not commute with respect to the individual μ -tensor terms. Using the ansatz

$$|\Psi_{\text{rovib.}}\rangle = \sum_{rv} c_{rv} |\Phi_r\rangle |\Phi_v\rangle \quad (12)$$

for the rovibrational wavefunction, the corresponding rovibrational Hamiltonian matrices need to be set up. For the rotational basis functions, we use a linear combination of Wang combinations⁶¹ being termed molecule specific rotational basis (MSRB). To obtain the MSRB wave functions, the pure rotational problem is solved [denoted rotational configuration interaction (RCI)]. Hence, for every value of J , a matrix of size $(2J + 1)$ describing the vibrational ground state needs to be determined and diagonalized. The resulting eigenvectors serve as rotational basis functions for the subsequent RVCi calculations. For details, see Ref. 56.

It is important to note that within the VCI approach, a very large number of Hartree products (configurations) are screened to determine the vibrational wavefunctions Φ_v in a compact form, while only a very limited number of these vibrational state functions need to be used in the rovibrational calculations.^{62–64} The number of these functions to be included is a matter of this investigation. Formally, for two rovibrational basis functions, distinguished by ' and ', the arising matrix elements for the rotational and Coriolis coupling terms can be written as

$$\langle v' | \mu_{\alpha\beta} | v'' \rangle \langle Jk' m' | J_{\alpha} J_{\beta} | Jk'' m'' \rangle \quad (13)$$

and

$$\langle v' | \mu_{\alpha\beta} \pi_{\beta} | v'' \rangle \langle Jk' m' | J_{\alpha} | Jk'' m'' \rangle. \quad (14)$$

While the integrals for $\langle v' | \mu_{\alpha\beta} | v'' \rangle$ are straightforward to evaluate [see Eqs. (8) and (9)], the vibrational contribution to the Coriolis coupling terms [cf. Eq. (14)] is more intricate and explicit expressions are provided in the Appendix. Since the vibrational integrals in (13) and (14) are independent of J , they do not have to be recalculated for the different RVCi matrices, but can be precalculated.

It is the truncation of the expansion of the μ -tensor within these integrals and the importance of the individual orders, which is the subject of this study here. The rotational contributions in Eqs. (13) and (14) can be solved analytically, as has repeatedly been shown in the literature once rigid rotor functions or their linear combinations have been employed.⁶⁵

As a multitude of RVCi matrices has to be evaluated, these can be distributed among the available processors, and thus, very efficient parallelization schemes can be exploited.

B. Intensities

Rovibrational infrared line intensities can be computed according to

$$I = \frac{2\pi^2 N_A}{3\epsilon_0 h^2 c^2} \frac{e^{-E''/kT} (1 - e^{-(E' - E'')/kT})}{Q(T)} (E' - E'') R. \quad (15)$$

The prefactor contains only natural constants, a temperature-dependent factor with the thermal occupancies of the initial and final states with energies E'' and E' , respectively, the rovibrational partition function $Q(T)$, the energy difference $(E' - E'')$ of the transition, and the square of the transition moment, R .

A separability approximation for the partition function has been used within our calculations, i.e.,

$$Q = Q_{\text{vib}} Q_{\text{rot}}, \quad (16)$$

which was found to work very well for thioformaldehyde.⁵⁶ Within the calculation of the vibrational partition function, state energies were simply approximated by the sum of modal energies. The rotational partition function requires the calculation of nuclear spin statistical weights, g_{ns} , in order to account for degeneracies. These were obtained from the Landau–Lifshitz formula corrected by Jonas.^{66,67} The computationally most demanding and sensitive contribution is the square of the transition moment, R , which in case of a rigid rotor basis is given by

$$R = g_{\text{ns}} (2J'' + 1) (2J' + 1) \left| \sum_{\sigma=-1}^1 (-1)^{\sigma} \sum_{v''v'} \langle v'' | \mu_m^{(1,\sigma)} | v' \rangle \times \sum_{k''k'} (-1)^{k''} (C_{v''jk''}^{\prime\prime})^* C_{v'jk'}^{\prime} \begin{pmatrix} J'' & 1 & J' \\ k'' & \sigma & -k' \end{pmatrix} \right|^2. \quad (17)$$

The $(2J + 1)$ prefactors arise from the energetic degeneracy with respect to the m quantum number and the Wigner 3- j symbols from the transformation of the dipole moment from the molecule-fixed to the space-fixed coordinate system. The coefficients C_{vjk} are obtained by the diagonalization of the RVCi matrices. The vibrational dipole moment integrals in spherical tensor form $\mu_m^{(1,\sigma)}$ are obtained by the Cartesian components and can easily be precomputed. As the dipole moment is also expanded in terms of an n -mode expansion, the transition moment depends on the corresponding expansion order, which has been investigated in this work.

C. Computational details

The equilibrium geometry of H_2CS , the harmonic frequencies, and the corresponding normal coordinates have been determined by explicitly correlated coupled-cluster theory including single and double excitations and a perturbative treatment of the triple excitations, CCSD(T)-F12a.⁶⁸ An orbital basis set of triple- ζ quality, i.e., cc-pVTZ-F12, as provided by Peterson *et al.*,⁶⁹ has been used in these calculations. Corresponding JKFIT and OPTRI auxiliary basis sets have been employed throughout this work.⁷⁰ The exponent for the Slater-type frozen geminals was chosen to be 1.0.⁷¹

The 3C(FIX) ansatz was used within the initial MP2-F12 calculations and the complementary auxiliary basis set (CABS) singles correction was added to the total energies.^{68,72}

The multidimensional PES was represented by an n -mode expansion being truncated after the four-mode coupling terms.⁷³ A multi-level scheme⁷⁴ has been used to reduce the computational effort, i.e., the 1D and 2D contributions have been determined at the same level of electronic structure theory as the harmonic frequencies, while a smaller basis set of double- ζ quality has been used for the 3D and 4D terms. Conventional coupled-cluster theory, i.e. coupled-cluster with single, double and perturbative triple excitations [CCSD(T)] in combination with aug-cc-pVQZ (1D and 2D) and aug-cc-pVTZ (3D and 4D) basis sets has been employed to compute the corresponding dipole moment surface. The symmetry has been exploited twofold, within the electronic single point calculations and the individual terms of the n -mode expansion.⁴² The grid representations of the surfaces were transformed to an analytical sum-of-products representation of nine monomials per mode using Kronecker product fitting.⁴¹

Vibrational wavefunctions have been determined in a variational manner from state-specific configuration-selective vibrational configuration interaction theory (VCI).^{58–60} A symmetry-adapted basis of Hartree products (configurations) has been generated from ground-state based vibrational self-consistent field (VSCF) one-mode wavefunctions (modals), i.e., linear combinations of mode-specific distributed Gaussians. A constant μ -tensor has been used within the VSCF iterations. The correlation space within the VCI calculations has been restricted by up to quintuple excitations, a maximal sum of vibrational quantum numbers of 15, and a maximal excitation per mode up to the sixth root. A residuum based eigenvalue solver (RACE) has been used to determine the eigenenergies of predefined states. VAM terms were accounted for with zeroth order terms of the μ -tensor.⁴⁵ For details of our VCI program, see Refs. 58–60.

In the RVCI calculations, the total angular momentum operator J has been set to a maximum value of $J_{\max} = 45$ for the calculation of the rovibrational states. As mentioned before, the partition function relies on separability approximation $Q = Q_{\text{vib}} Q_{\text{rot}}$. Considering sums of modal energies up to $\approx 10\,593\text{ cm}^{-1}$ yields $Q_{\text{vib}} \approx 1.025$. Furthermore, the required rotational energies converged at $J_{\max} = 54$ and yields $Q_{\text{rot}} \approx 5951.992$. In total, this results in a partition function of $Q \approx 6100.290$. Note that, in contrast to our previous work published in Ref. 56, this value differs by $\approx 0.1\%$, due to a change in convergence thresholds. For the calculation of the partition function and the intensities, the temperature has been set to $T = 300\text{ K}$. During the calculation of the rotational terms, the expansion of the μ -tensor has been varied between zeroth and third order. Contrarily, within the Coriolis coupling terms, the maximal expansion order of the μ -tensor was 2. The number of vibrational basis functions (VCI states) was varied between 16 and 67, whereas the number of rotational basis functions has always been set to $2J + 1$, which is the maximum number of rotational basis functions that can be considered. As mentioned before, the rotational basis functions (MSRB) are a linear combination of Wang combinations. For the calculation of intensities, all rovibrational states are considered, which fulfill the selection rule $\Delta J \in \{0, \pm 1\}$ and which show a thermal population of the lower state of at least 0.1%. However, hot bands have not been considered as the lowest vibrational mode is at $\nu_i \approx 990\text{ cm}^{-1}$.

All calculations have been performed with the MOLPRO program package.⁵³

III. BENCHMARK CALCULATIONS

The goal of the benchmark calculations is the determination of the impact of different simulation parameters and to set the level of accuracy in perspective to the required computation time. All calculations refer to the rovibrational infrared spectrum of thioformaldehyde. In the following, the influence of a number of parameters on this spectrum shall be studied, namely, (1) the order of the inverse effective moment of inertia tensor μ for the rotational terms, (2) the μ -tensor order for the Coriolis Coupling terms, (3) the multi-mode expansion order of the dipole moment surface (DMS), and (4) the size of the vibrational basis set. Besides these parameters, many others may be studied, like the accuracy of the electronic structure theory, the expansion order of the potential energy surface, or the expansion order of the μ -tensor in the VAM terms. However, most of them have been investigated before.^{45,60}

All test calculations presented below are compared to reference calculations, in which every parameter is set to its largest level (see above), i.e., the rotational terms include third order μ -tensor contributions and Coriolis coupling includes up to second order terms of the μ -tensor expansion. For the DMS, the n -mode expansion was truncated after fourth order and the number of vibrational basis functions was set to 67 (see below).

A. Rotational and Coriolis coupling terms

In the first step, the influence of the rotational and the Coriolis coupling terms shall be studied. For the rotational terms, the μ -tensor expansion is varied in the range between zeroth order and third order. In contrast to that, the Coriolis coupling studies do not start with zeroth order, but with completely neglecting Coriolis coupling. This is reasonable as one already yields a rovibrational spectrum without considering these terms—due to the considered rotational term.

Rovibrational states from different calculations are compared by searching for matching sets of assigned quantum numbers. A complete set of quantum numbers consists of the vibrational quantum number ν , the total angular momentum quantum number J , and the z -component of the angular momentum k , respectively, k_a and k_c for asymmetric top molecules. While J is a good quantum number, this does not hold for ν and k . Hence, the validity of comparing different rovibrational calculations depends crucially on the quantum number assignment. To account for this effect, two different metrics are used in this comparison. The first is the mean absolute deviation (MAD) of all states, while the second only considers the subset of states that have an assignment confidence $A > 0.5$ in both calculations. This is done in a two-step process. At first, the final rovibrational wave functions are projected on the different vibrational basis functions and the rotational basis functions. The maximum value yields the confidence for the assignment of the vibrational quantum number, A_ν , and the assignment confidence for the rotational quantum number, A_r . The minimum of these two values corresponds to A . For being able to assign local quantum numbers to these states, a value of 0.5 is required.⁷⁵ By using these two metrics, it is possible to separate the effects of wrongly

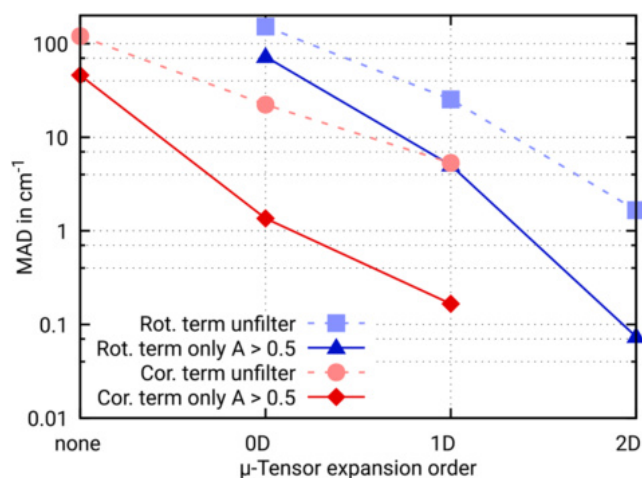


FIG. 1. Mean absolute deviation (MAD) of the state energies for different orders of the μ -tensor expansion. Red lines show the impact of the Coriolis coupling terms and blue lines show the dependence on the rotational terms. The results of the statistics, in which only states with a quantum number assignment confidence $A > 0.5$ are considered, are displayed in dark colors and solid lines, while the statistics for all states is presented in faint colors and dashed lines. The other benchmark parameters are set to their highest values, i.e., the number of vibrational basis functions is $N_{\text{vib}} = 67$, while the dimension of the DMS is irrelevant as intensities are not considered.

assigned states from actual shifts in the state energies up to a certain extent. It should be noted that there is also a correlation between the assignment confidence A and the coupling strength. This means that purely focusing on the statistics of the subset of filtered states would systematically undervalue the strongly coupled states.

The impact of these terms on the accuracy of the calculation is shown in Fig. 1. Clearly, all four lines show a nearly linear decline in this logarithmic plot, which has to be expected for a converging expansion. Furthermore, the subset that fulfills the condition $A > 0.5$ has a consistently lower MAD than the full set of compared states. By increasing the μ -tensor expansion order, this deviation also increases significantly from a factor of about 2.5 for the lowest order, up to a factor of about 25 for the highest order. The exact numbers for the MADs can be seen in Tables I and II. In general, the rotational terms require a μ -tensor order, which is about one order higher than the corresponding Coriolis coupling terms for a comparable accuracy.

TABLE I. Calculation times t for the evaluation of the rotational terms, mean absolute deviation (MAD) of all calculated states $\Delta E_{\text{all}}^{\text{MAD}}$, as well as the MAD $\Delta E_{\text{filter}}^{\text{MAD}}$ for the subset with quantum number assignment confidence $A > 0.5$. The Coriolis coupling term uses a μ -tensor expansion up to second order. The number of vibrational basis functions (VCI states) is set to $N_{\text{vib}} = 67$.

μ -tensor	t (s)	$\Delta E_{\text{all}}^{\text{MAD}}$ (cm^{-1})	$\Delta E_{\text{filter}}^{\text{MAD}}$ (cm^{-1})
0D	10.9	152.25	72.64
1D	21.1	25.37	5.04
2D	22.2	1.66	0.07
3D	29.0	... ^a	... ^a

^aReference calculation.

TABLE II. Calculation times t for the evaluation of the Coriolis coupling terms, mean absolute deviation (MAD) of all calculated states $\Delta E_{\text{all}}^{\text{MAD}}$, as well as the MAD $\Delta E_{\text{filter}}^{\text{MAD}}$ for the subset with quantum number assignment confidence larger than 0.5. The rotational term uses μ -tensor terms up to third order and the number of vibrational basis functions (VCI states) is set to $N_{\text{vib}} = 67$.

μ -tensor	t (s)	$\Delta E_{\text{all}}^{\text{MAD}}$ (cm^{-1})	$\Delta E_{\text{filter}}^{\text{MAD}}$ (cm^{-1})
None	0.0	120.50	46.07
0D	4.2	22.27	1.36
1D	48.2	5.31	0.17
2D	1617.2	... ^a	... ^a

^aReference calculation.

In addition to the MADs, the aforementioned tables also contain the central processing unit (CPU) times.

It should be noted that the times presented in Tables I and II are not the CPU times for a complete RVCI calculation, but only for the corresponding precalculations described in Sec. II A. For the rotational terms, there is only a moderate increase in CPU time due to efficient prescreening of the VCI wavefunction coefficients as well as contraction of integrals. In contrast to this, Coriolis coupling terms show a near exponential increase in computation time. One reason for this is the intrinsically higher complexity of these terms due to the additional π_{α} operator [cf. Eq. (2)], which results in a larger number of different cases that have to be considered. Another reason is that the Coriolis coupling terms have not yet been fully optimized with respect to the CPU time in our implementation so far. Since computation times for the precalculations depend crucially on the number of selected VCI configurations, the determined trends can only be generalized to molecules with a roughly similar number of configurations (Hartree products). For H_2CS , the most viable strategy is to set the μ -tensor order of the rotational terms to its maximum and to choose the μ -tensor order for Coriolis coupling depending on the desired accuracy and available computational resources. This will be discussed in more detail, in Sec. III D.

B. Vibrational basis size

A crucial parameter in configuration interaction methods is the number and proper selection of basis functions. Our implementation of RVCI relies on a direct product of vibrational and rotational basis functions. While the latter has an upper limit of meaningful basis functions that depends on J and is equal to $(2J + 1)$, the number of the former, i.e., VCI wavefunctions, is, in principle, unlimited and, therefore, the subject of study in this section.

In Sec. III A, two types of metrics have been used to evaluate the accuracy of the different expansion orders of the μ -tensor. These are the MAD of all calculated states and the subset of states with a quantum number assignment confidence of $A > 0.5$. Since the quality of the assignment is very poor for a rather small set of vibrational basis functions, the unfiltered metric becomes meaningless. For this reason, the MAD for the filtered subset $\Delta E_{\text{filter}}^{\text{MAD}}$ serves as the main metric in this section. Furthermore, the median for the same subset of filtered states is used as it is less sensitive to any outliers.

An almost linear trend with a small negative slope for the MAD (red line) is shown in the logarithmically scaled Fig. 2. One reason for the slow convergence can be seen by comparing the median

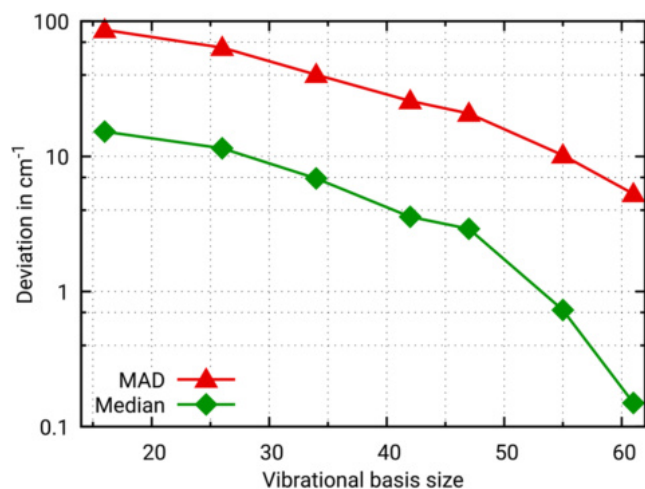


FIG. 2. Deviation of RVCI state energies from the reference calculation for different vibrational basis set sizes. The red line describes mean absolute deviation (MAD) and the green line describes the median. States where the quantum number assignment confidence A is lower than 0.5 are not shown, because for small numbers of vibrational states, inconsistent assignments of the states make the statistics meaningless. The other benchmark parameters are set to its highest values; i.e., the μ -tensor order for the rotational term is set to 3 and for Coriolis coupling, the μ -tensor order is 2. The dimension of the DMS is again not relevant as intensities are not considered.

and MAD in Fig. 2. The median, $\Delta E_{\text{filter}}^{\text{Median}}$, which roughly shows a quadratic behavior, is consistently a factor of about 7 lower than $\Delta E_{\text{filter}}^{\text{MAD}}$, except for the last two basis set sizes, where the deviation increases to roughly a factor of 50. Hence, there is a number of outliers that dominate the overall results in the statistics.

In comparison to the results of Sec. III A, where an accuracy of $\Delta E_{\text{filter}}^{\text{MAD}} \leq 5 \text{ cm}^{-1}$ could be reached with low computational effort, only the second largest vibrational basis set can meet this level of accuracy. The corresponding CPU times are listed in Table III. Note that this table shows the *total* CPU times of both, the VCI and RVCI calculations, instead of the run time for the precalculations only. This is due to the fact that the size of the vibrational basis influences all time demanding steps within VCI and RVCI theory, while the selected μ -tensor order almost exclusively influences the precalculation times. In summary, it can clearly be seen that achieving convergence in the vibrational basis size is much more demanding with respect to the CPU time than achieving convergence for the coupling terms. For this reason, it is particularly difficult and likewise important to find a good tradeoff between accuracy and computation times. This, for example, is in contrast to the less critical choice of the truncation of the μ -tensor expansion in the rotational terms with regard to the CPU time. Besides this, we found it to be important that all VCI wavefunctions being used in the RVCI calculations need to be tightly converged with respect to the correlation space in the underlying VCI calculations, which is not necessarily the case for high lying overtones or combination bands. As a consequence, modals with large quantum numbers should be employed in the generation of the Hartree products, i.e., the basis of the VCI wavefunctions, which render these calculations expensive.

TABLE III. Total VCI and RVCI computation times t for different vibrational basis set sizes, mean absolute deviation (MAD), $\Delta E_{\text{filter}}^{\text{MAD}}$, and median, $\Delta E_{\text{filter}}^{\text{Median}}$, for all calculated states, with quantum number assignment confidence larger than 0.5. The rotational term employs a μ -tensor expansion up to third order and the Coriolis coupling operator contains up to second order μ -tensor contributions.

No. vib. states	t (s)	$\Delta E_{\text{filter}}^{\text{MAD}}$ (cm^{-1})	$\Delta E_{\text{filter}}^{\text{Median}}$ (cm^{-1})
16	171.1	86.2	15.2
26	416.8	63.7	11.5
34	747.8	40.2	6.9
42	1111.2	25.7	3.6
47	1818.9	20.7	2.9
55	2263.6	10.2	0.7
61	3000.2	5.3	0.1
67	4189.0	... ^a	... ^a

^aReference calculation.

C. Dipole moment surface expansion

Secs. III A and III B focused on parameters influencing the RVCI energies directly and the intensities, which depend on the transition energies [cf. Eq. (15)], indirectly. In contrast to that, this section studies the impact of the expansion order of the dipole moment surface (DMS) on the resulting intensities. The metrics used here, which are directly related to the metrics for the transition energies, are the relative MAD for intensity changes, $\Delta I_{\text{all}}^{\text{MAD}}$, in the full set of *relevant transitions* and $\Delta I_{\text{filter}}^{\text{MAD}}$, which is defined analogously for the subset of transitions, in which both states of the transition have an assignment confidence larger than $A > 0.5$. The term *relevant transition* is used as the total number of possible transitions has been reduced to those, which show sufficient intensity. For example, when $J_{\text{max}} = 45$ and 67 vibrational states are considered, there are about $1.47 \cdot 10^7$ transitions fulfilling the selection rule $\Delta J \in \{-1, 0, +1\}$ and the condition $\nu_i \leq 7000 \text{ cm}^{-1}$. A check for the thermal occupation of at least 0.1% for the lower rovibrational states reduces this to $6.6 \cdot 10^6$ transitions. Considering only transitions, which have an intensity ratio of at least 10^{-7} , relative to the strongest line in the spectrum and filtering transitions with unambiguously assigned states leads to the final number of 44 768 transitions. Including the filter for an assignment confidence of $A > 0.5$ reduces the number of transitions only slightly to 39 866. For this reason, the difference between the two metrics must be expected to be small.

Similar to the μ -tensor expansion (cf. Fig. 1), Fig. 3 shows a fast convergence in dependence on the order of the DMS. The resulting error, $\Delta I_{\text{all}}^{\text{MAD}}$, is reduced by more than two orders of magnitude when the order of the surface is increased by 2. The exact numbers are given in Table IV. Comparing the two different metrics, i.e., $\Delta I_{\text{all}}^{\text{MAD}}$ and $\Delta I_{\text{filter}}^{\text{MAD}}$, shows no significant difference. There are two reasons for this behavior: (1) As the DMS has no impact on state energies, the assignment of any states is entirely independent from it. Consequently, any misassigned states do not affect the relative consideration of the spectrum with respect to different expansion orders of the DMS. (2) Furthermore, as mentioned before, the set of transitions with sufficient intensity and without ambiguously assigned states leads to a set of states with most of them showing a large assignment confidence ($\sim 89\%$). Hence the differences of the two

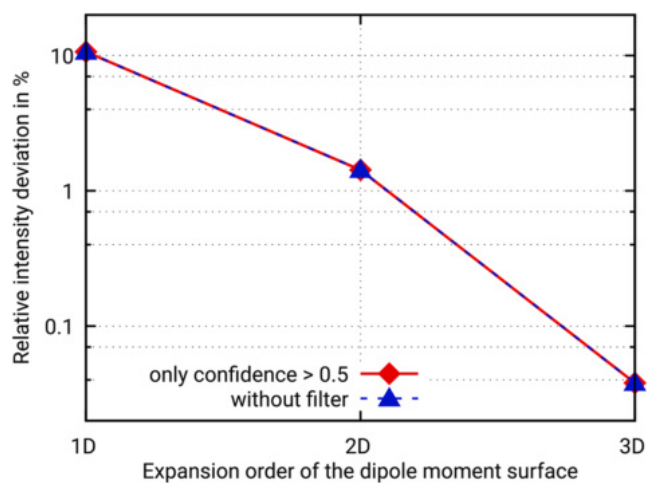


FIG. 3. Relative MAD of the intensities for different orders of multimode expansion for the DMS. The results of a statistics, where only states with quantum number assignment confidence $A > 0.5$ are considered, are displayed in a solid red line and dots, while the statistics for all states is presented in a blue and dashed line. The other benchmark parameters are set to its highest values; i.e., 3D μ -tensor for rotational terms and 2D μ -tensor for Coriolis coupling, and the number of vibrational basis functions is $N_{\text{vib}} = 67$.

lines in Fig. 3 are hardly visible and, thus, only one metric is provided in Table IV.

In contrast to the previous tables, Table IV does not compare the computation time for the different orders of the expansion. This is due to negligible CPU times of about 6 s for this part of the code and, thus, for H_2CS , the calculation of the vibrational transition moments requires almost no time in comparison to other parts. Consequently, for this molecule, the calculation essentially is independent of the order of the DMS expansion. The most prominent reasons for that are a very effective prescreening on the products of the VCI wave function coefficients and the low number of configurations in the VCI wave functions as obtained from our configuration-selective implementation of VCI theory.

D. Influence on spectra

The previous studies revealed the influence of the different approximations on the different metrics. In this section, the impact

TABLE IV. Mean absolute deviation (MAD) of the percentage change in intensities for all calculated states, $\Delta I_{\text{all}}^{\text{MAD}}$, for different expansion orders of the dipole moment surface. The number of vibrational basis functions is set to $N_{\text{vib}} = 67$. The rotational term uses third order μ -tensor and the Coriolis coupling term uses a second order μ -tensor expansion.

DMS order	$\Delta I_{\text{all}}^{\text{MAD}}$ (%)
1D	10.66
2D	1.43
3D	0.04
4D	... ^a

^aReference calculation.

shall be demonstrated by a visual comparison of the respective spectra and scatter plots. Moreover, we do not focus on the variation of a single parameter, but rather three different levels of accuracy are introduced.

Since there are two parameters that were found to be not critical with respect to the overall computation time, i.e., the μ -tensor expansion order for the rotational terms and the expansion order of the dipole moment surface, they will be set to the reference values, i.e., 2 and 3. In contrast to that, the expansion order of the μ -tensor within the Coriolis coupling terms is set to 0 for the low accuracy calculation, 1 for the medium accuracy, and 2 for the high accuracy. In addition to that, for low accuracy, the vibrational basis corresponds to all VCI states, which have a frequency lower than or equal to 4200 cm^{-1} and have a sum of vibrational quantum numbers not exceeding 3. This corresponds to the 42 vibrational states in Table III. For the medium accuracy, the frequency threshold was set to 5700 cm^{-1} , which corresponds to 61 VCI states. The results with high accuracy were achieved by using a frequency threshold of 7000 cm^{-1} resulting in 67 vibrational modes.

The results of the three calculations are shown in Fig. 4 for a small region of about 3.5 cm^{-1} . It shows a progression belonging to a strong coupling region involving the three fundamental bands ν_4 , ν_6 , and ν_3 . The differences between the three simulations in that plot are visible in terms of a shift in the whole progression. In addition to that the spacing within the lines of the progression has changed.

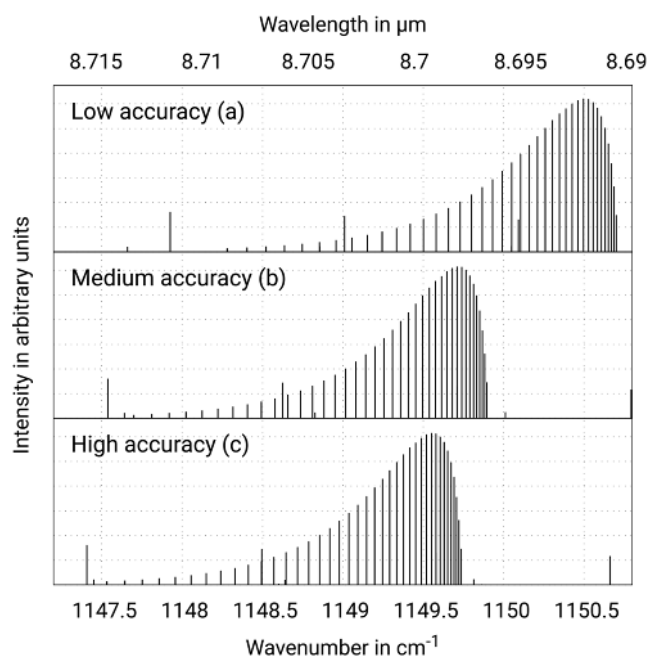


FIG. 4. Narrow section of the rovibrational spectrum of H_2CS in dependence on different levels of accuracy. The selected area covers a part of the tail of the strongly coupling region, between three fundamental bands [ν_4 at 989.4 cm^{-1} with B_1 symmetry, $\nu_6(B_2)$ at 989.5 cm^{-1} and $\nu_3(A_1)$ at 1060.2 cm^{-1}]. Low accuracy calculation (a) employs $N_{\text{vib}} = 42$ vibrational basis functions and zeroth order μ -tensor expansion for Coriolis coupling. Medium accuracy (b) uses $N_{\text{vib}} = 61$ with first order μ -tensor in Coriolis coupling and for high accuracy, (c) $N_{\text{vib}} = 67$ is employed with second order μ -tensor in Coriolis coupling.

The reason for that is a change in the centrifugal distortion, which could be expected as the impact of the Coriolis coupling terms has changed.

Another way to investigate the influence of different levels of accuracy is by analyzing scatter plots. For this reason, all transitions of two different calculations are compared pairwise when all quantum numbers match and the resulting plot is shown in Fig. 5. The red dots show the difference between the calculations with low and high accuracy and the blue dots show the same for the calculations with medium and high accuracy. The figure reveals several aspects: (1) the deviations in the transition frequencies are about two orders of magnitude smaller than the deviation in the intensities. However, both errors decrease substantially when increasing the accuracy of the calculation, i.e., considerations of the blue points instead of the red ones in Fig. 5. (2) In the majority of compared transitions the lack of accuracy leads to an underestimation of the frequency, but rarely to an overestimation. For the intensity on the other hand, there is no such general systematic effect. (3) Moreover, there are no data points in blue for which the error for both the intensity and frequency is high. Although the figure shows only the most interesting section of the whole dataset, this statement also holds true for the latter. As a result of that, it is unlikely that there are many transitions belonging to states, for which the assignment differs between the calculation with medium and high accuracy, i.e., misassignments in one of the calculations. In contrast to that, the comparison between calculations with low and high accuracy shows data points

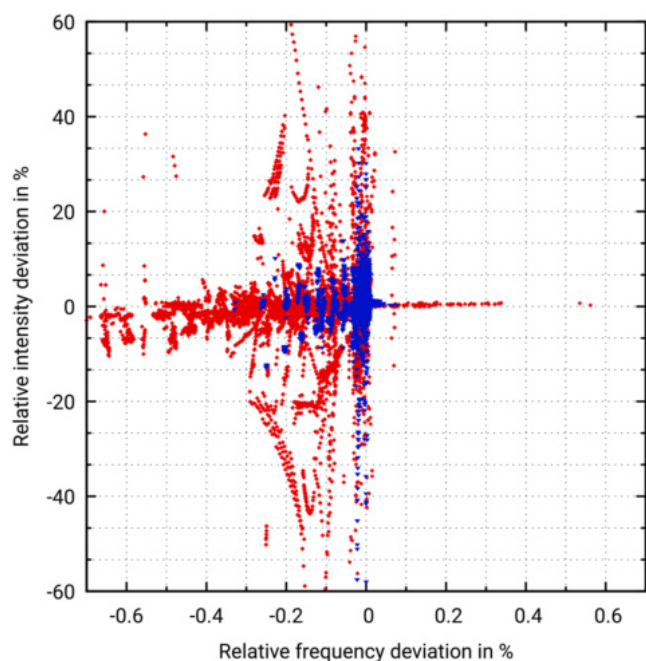


FIG. 5. Scatter plot for the relative deviations in frequencies and intensities for different levels of accuracy. All rovibrational transitions of H_2CS with $J \leq 45$ originating in the vibrational ground state and ending either in the vibrational ground state or in one of the fundamental bands are considered. Red dots denote the differences between the calculations with low accuracy and high accuracy (reference) and blue dots denote the differences between the calculations with medium accuracy and high accuracy.

with $\approx 35\%$ error in intensity and $\approx 0.5\%$ error in frequency. A comparison of the energies of all three computational levels with experimental data in terms of state lists is provided in Table IV.

The computation time for the calculation with lowest accuracy amounts to $t = 738$ s, which is about 33% less in comparison to the calculation in Table III with a vibrational basis set size of 42, which is due to the additional reduction in the order of the μ -tensor expansion. For the medium and high accuracy calculations, the computation time increases to $t = 1946$ s and $t = 4189$ s, respectively.

IV. SUMMARY AND CONCLUSIONS

The dependence of rovibrational transitions and their corresponding intensities on the truncation orders of n -mode expansions of the μ -tensor and dipole moment surfaces (DMS) has been studied by benchmark calculations for thioformaldehyde. The explicit consideration of high order terms, i.e., 2D, of the μ -tensor in the purely rotational contributions to the Watson Hamiltonian was found to be important in order to yield accurate results. However, these terms do not constitute a computational bottleneck and, thus, there are essentially no reasons to exclude these terms from standard calculations. Likewise conclusions hold true for the expansion terms of the DMS within the calculation of rovibrational intensities. However, it is an efficient prescreening, which is responsible for the efficiency in these calculations. The inclusion of high-order Coriolis coupling terms is much more demanding, and improved implementations are needed to limit the computational effort. Work in that direction is currently in progress. 2D Coriolis coupling terms may still be important for accurate calculations, but it needs to be kept in mind that thioformaldehyde is a sensitive molecule with respect to Coriolis coupling and, thus, it might be that for many molecules the inclusion of 1D terms is sufficient. This needs to be verified by calculations for other systems. The most crucial factor appears to be a proper number of vibrational basis functions (VCI wavefunctions) to be included in the RVCI calculations. Apparently, an inclusion of the fundamental VCI transitions is not sufficient and a number of overtones and combination bands need to be considered as well, but these can be controlled by energetically upper limits and the excitation patterns within the combination bands. Algorithms, which predict important VCI states to be included, would be very beneficial as general rules may fail for challenging molecules. Moreover, while a good visual appearance of an overall spectrum can be achieved with rather limited effort, the accurate calculation of line positions leads to a fast increase in the CPU time demands. In general, relative deviations with respect to intensities were found to be larger than for energies. With this, the findings of this study can be used as an initial guess of input parameters for RVCI calculations, which need to be optimized in dependence on the molecule to be studied and the available computational resources.

ACKNOWLEDGMENTS

The authors are thankful to the Deutsche Forschungsgemeinschaft (DFG) (Project No. Ra 656/23-3) and the Studienstiftung des deutschen Volkes for financial support. Moreover, the authors are grateful for helpful discussions with Dr. Benjamin Schröder, Sebastian Erfort, and Claudia Franke.

AUTHOR DECLARATIONS

Conflict of Interest

The authors have no conflicts to disclose.

Author Contributions

Martin Tschöpe: Conceptualization (supporting); Data curation (lead); Formal analysis (lead); Investigation (lead); Methodology (lead); Software (lead); Validation (lead); Visualization (lead); Writing – original draft (supporting); Writing – review & editing (lead). **Guntram Rauhut:** Conceptualization (lead); Funding acquisition (lead); Methodology (supporting); Project administration (lead); Resources (lead); Supervision (lead); Writing – original draft (lead); Writing – review & editing (supporting).

DATA AVAILABILITY

The data that support the findings of this study are openly available in Zenodo at <https://www.doi.org/10.5281/zenodo.7151868>.

APPENDIX: CORIOLIS INTEGRALS

The Hartree product (configuration) of a vibrational wavefunction according to Eq. (10) is given by

$$\phi_v^I = \prod_{i=1}^{3N-6} \phi_i^I(q_i), \quad (\text{A1})$$

with $\phi_i^I(q_i)$ denoting the one-mode wavefunctions (modals) and the set of normal mode indices $M \in \{1, \dots, i, \dots, 3N-6\}$. Using the n -mode representation of the μ -tensor with the individual terms expressed as shown in Eqs. (8) and (9), the Coriolis integrals $\langle \phi_v^I | \pi_\alpha \mu_{\alpha\beta} + \mu_{\alpha\beta} \pi_\beta | \phi_v^I \rangle$ can be evaluated by the terms of different order. The antisymmetry of the ζ -constants, i.e., $\zeta_{ij}^\alpha = -\zeta_{ji}^\alpha$ and $\zeta_{ii}^\alpha = 0$, and the symmetry of the μ -tensor reduce the number of contributing integrals to just some very few, which will be presented in the following. For brevity, the sums over α and β , as well as prefactors, e.g., the Coriolis ζ -constants, are neglected.

1. Zeroth order integrals

As $\mu_{\alpha\beta}^{(0)}$ is just a constant, the terms $(\pi_\alpha \mu_{\alpha\beta}^{(0)} + \mu_{\alpha\beta}^{(0)} \pi_\beta)$ of the Coriolis coupling operator are identical and yield the integral

$$I_{cc}^{(0)} = 2 \left\langle \phi_v^I \left| q_i \frac{\partial}{\partial q_j} \right| \phi_v^I \right\rangle. \quad (\text{A2})$$

Using the abbreviations,

$$Q_{ia}^I = \langle \phi_i^I | q_i^a | \phi_i^I \rangle, \quad (\text{A3})$$

$$\Delta_{ia}^I = \left\langle \phi_i^I \left| q_i^a \frac{\partial}{\partial q_i} \right| \phi_i^I \right\rangle, \quad (\text{A4})$$

$$\delta_{i\dots j}^I = \left\langle \prod_{k \in M \setminus \{i, \dots, j\}} \phi_k^I \left| \prod_{k \in M \setminus \{i, \dots, j\}} \phi_k^I \right. \right\rangle, \quad (\text{A5})$$

with δ_{ij}^I denoting a mode-reduced Kronecker- δ of two Hartree products, and the zeroth order term can be computed as

$$I_{cc}^{(0)} = 2 Q_{i1}^I \Delta_{j0}^I \delta_{ij}^I. \quad (\text{A6})$$

2. First order integrals

The two contributions of the first order term of the Coriolis coupling operator, i.e.,

$$\sum_k \langle \phi_v^I | \pi_\alpha \mu_{\alpha\beta}^{(1)}(q_k) + \mu_{\alpha\beta}^{(1)}(q_k) \pi_\beta | \phi_v^I \rangle, \quad (\text{A7})$$

do not necessarily commute and three different cases for $I_{cc}^{(1)}$ must be distinguished,

$$k = i \neq j : 2 \sum_r d_{\alpha\beta}^{i,r} Q_{i(r+1)}^I \Delta_{j0}^I \delta_{ij}^I, \quad (\text{A8})$$

$$k \neq i \neq j = k : \sum_r d_{\alpha\beta}^{j,r} Q_{i1}^I (2\Delta_{jr}^I + r Q_{j(r-1)}^I) \delta_{ij}^I, \quad (\text{A9})$$

$$k \neq i \neq j \neq k : 2 \sum_r d_{\alpha\beta}^{k,r} Q_{i1}^I \Delta_{j0}^I Q_{kr}^I \delta_{ijk}^I. \quad (\text{A10})$$

Within the conditions, the indices i and j refer to the VAM-operator π_α and the index k to the μ -tensor expansion. The variable $d_{\alpha\beta}^{i,r}$ is already defined in Eq. (8).

3. Second order integrals

A likewise expression can be derived for $I_{cc}^{(2)}$, which refers to

$$\sum_{kl} \langle \phi_v^I | \pi_\alpha \mu_{\alpha\beta}^{(2)}(q_k, q_l) + \mu_{\alpha\beta}^{(2)}(q_k, q_l) \pi_\beta | \phi_v^I \rangle. \quad (\text{A11})$$

As $\mu_{\alpha\beta}^{(2)}(q_k, q_l)$ denotes a difference, cf. Eq. (7), the diagonal coefficients $d_{\alpha\beta}^{k,k,r}$ must be zero and, thus, always $k \neq l$. The four different cases, which need to be distinguished, are

$$\frac{k \ l}{i \neq \neq \ j \neq \neq} : 2 \sum_{rs} d_{\alpha\beta}^{kl,rs} Q_{i1}^I \Delta_{j0}^I Q_{kr}^I Q_{ls}^I \delta_{ijkl}^I, \quad (\text{A12})$$

$$\frac{k \ l}{i = \neq \ j \neq \neq} : 2 \sum_{rs} d_{\alpha\beta}^{jl,rs} Q_{i(r+1)}^I \Delta_{j0}^I Q_{rs}^I \delta_{ijl}^I, \quad (\text{A13})$$

$$\frac{k \ l}{i \neq \neq \ j = \neq} : \sum_{rs} d_{\alpha\beta}^{il,rs} Q_{i1}^I (2\Delta_{jr}^I + r Q_{j(r-1)}^I) Q_{ls}^I \delta_{ijl}^I, \quad (\text{A14})$$

$$\frac{k \ l}{i = \neq \ j \neq =} : \sum_{rs} d_{\alpha\beta}^{ij,rs} Q_{i(r+1)}^I (2\Delta_{js}^I + s Q_{j(s-1)}^I) \delta_{ij}^I. \quad (\text{A15})$$

It shall be noted here that the condition for arising integrals can be generalized to any further high-order Coriolis coupling terms, but in all these cases, just four integrals do not vanish, which refer to the four cases of the 2D contributions.

REFERENCES

- ¹H. S. P. Müller, F. Schlöder, J. Stutzki, and G. Winnewisser, "The cologne database for molecular spectroscopy, CDMS: A useful tool for astronomers and spectroscopists," *J. Mol. Struct.* **742**, 215–227 (2005).
- ²J. Tennyson, S. N. Yurchenko, A. F. Al-Refaie, V. H. J. Clark, K. L. Chubb, E. K. Conway, A. Dewan, M. N. Gorman, C. Hill, A. E. Lynas-Gray, T. Mellor, L. K. McKemmish, A. Owens, O. L. Polyansky, M. Semenov, W. Somogyi, G. Tinetti, A. Upadhyay, I. Waldmann, Y. Wang, S. Wright, and O. P. Yurchenko, "The 2020 release of the ExoMol database: Molecular line lists for exoplanet and other hot atmospheres," *J. Quant. Spectrosc. Radiat. Transfer* **255**, 107228 (2020).
- ³I. E. Gordon, L. S. Rothman, C. Hill, R. V. Kochanov, Y. Tan, P. F. Bernath, M. Birk, V. Boudon, A. Campargue, K. V. Chance, B. J. Drouin, J.-M. Flaud, R. R. Gamache, J. T. Hodges, D. Jacquemart, V. I. Perevalov, A. Perrin, K. P. Shine, M.-A. H. Smith, J. Tennyson, G. C. Toon, H. Tran, V. G. Tyuterev, A. Barbe, A. G. Császár, V. M. Devi, T. Furtenbacher, J. J. Harrison, J.-M. Hartmann, A. Jolly, T. J. Johnson, T. Karman, I. Kleiner, A. A. Kyuberis, J. Loos, O. M. Lyulin, S. T. Massie, S. N. Mikhailenko, N. Moazzen-Ahmadi, H. S. P. Müller, O. V. Naumenko, A. V. Nikitin, O. L. Polyansky, M. Rey, M. Rotger, S. W. Sharpe, K. Sung, E. Starikova, S. A. Tashkun, J. V. Auwera, G. Wagner, J. Wilzewski, P. Wcislo, S. Yu, and E. J. Zak, "The HITRAN-2016 molecular spectroscopic database," *J. Quant. Spectrosc. Radiat. Transfer* **203**, 3–69 (2017).
- ⁴A. Yachmenev, S. N. Yurchenko, T. Ribeyre, and W. Thiel, "High-level *ab initio* potential energy surfaces and vibrational energies of H₂CS," *J. Chem. Phys.* **135**, 074302 (2011).
- ⁵A. Yachmenev, I. Polyak, and W. Thiel, "Theoretical rotation-vibration spectrum of thioformaldehyde," *J. Chem. Phys.* **139**, 204308 (2013).
- ⁶S. N. Yurchenko, D. S. Amundsen, J. Tennyson, and I. P. Waldmann, "A hybrid line list for CH₄ and hot methane continuum," *Astron. Astrophys.* **605**, A95 (2017).
- ⁷V. H. J. Clark, A. Owens, J. Tennyson, and S. N. Yurchenko, "The high-temperature rotation-vibration spectrum and rotational clustering of silylene (SiH₂)," *J. Quant. Spectrosc. Radiat. Transfer* **246**, 106929 (2020).
- ⁸V. G. Tyuterev, A. Barbe, D. Jacquemart, C. Janssen, S. N. Mikhailenko, and E. N. Starikova, "Ab initio predictions and laboratory validation for consistent ozone intensities in the MW, 10 and 5 μm ranges," *J. Chem. Phys.* **150**, 184303 (2019).
- ⁹A. V. Nikitin, M. Rey, and V. G. Tyuterev, "Accurate line intensities of methane from first-principles calculations," *J. Quant. Spectrosc. Radiat. Transfer* **200**, 90–99 (2017).
- ¹⁰M. Rey, A. V. Nikitin, and V. G. Tyuterev, "Accurate theoretical methane line lists in the infrared up to 3000 K and quasi-continuum absorption/emission modeling for astrophysical applications," *Astrophys. J.* **847**, 105 (2017).
- ¹¹S. Carter, Y. Wang, and J. M. Bowman, "The rovibrational spectra of trans- and cis-HOCO, calculated by MULTIMODE with *ab initio* potential energy and dipole moment surfaces," *J. Phys. Chem. A* **121**, 1616–1626 (2017).
- ¹²S. Carter, J. M. Bowman, and N. C. Handy, "Multimode calculations of rovibrational energies of C₂H₄ and C₂D₄," *Mol. Phys.* **110**, 775–781 (2012).
- ¹³J. Simmons, X.-G. Wang, and T. Carrington, "Computational study of the rovibrational spectra of CH₂D⁺ and CHD₂⁺," *J. Phys. Chem. A* **123**, 10281–10289 (2019).
- ¹⁴X.-G. Wang and T. Carrington, Jr., "Computing rovibrational levels of polyatomic molecules with polyspherical coordinates and a contracted basis built with a K-independent vibrational primitive basis," *Mol. Phys.* **111**, 2320–2333 (2013).
- ¹⁵J. Smydke, C. Fabri, J. Sarka, and A. G. Császár, "Rovibrational quantum dynamics of the vinyl radical and its deuterated isotopologues," *Phys. Chem. Chem. Phys.* **21**, 3453–3472 (2019).
- ¹⁶R. Tóbiás, T. Furtenbacher, J. Tennyson, and A. G. Császár, "Accurate empirical rovibrational energies and transitions of H₂¹⁶O," *Phys. Chem. Chem. Phys.* **21**, 3473–3495 (2019).
- ¹⁷A. M. Santa Daria, G. Avila, and E. Matyus, "Performance of a black-box-type rovibrational method in comparison with a tailor-made approach: Case study for the methane–water dimer," *J. Chem. Phys.* **154**, 224302 (2021).
- ¹⁸D. Ferenc and E. Mátyus, "Bound and unbound rovibrational states of the methane-argon dimer," *Mol. Phys.* **117**, 1694–1707 (2019).
- ¹⁹J. Sarka, C. Petty, and B. Poirier, "Exact bound rovibrational spectra of the neon tetramer," *J. Chem. Phys.* **151**, 174304 (2019).
- ²⁰L. S. Rothman, "History of the HITRAN database," *Nat. Rev. Phys.* **3**, 302–304 (2021).
- ²¹M. Rey, A. V. Nikitin, Y. L. Babikov, and V. G. Tyuterev, "TheoReTs – An information system for theoretical spectra based on variational predictions from molecular potential energy and dipole moment surfaces," *J. Mol. Spectrosc.* **327**, 138–158 (2016).
- ²²X. Chappuisat and C. Jung, "Vector parametrization of the N-body problem in quantum-mechanics: Polyspherical coordinates," *Phys. Rev. A* **45**, 6217–6235 (1992).
- ²³M. Rey, "Novel methodology for systematically constructing global effective models from *ab initio*-based surfaces: A new insight into high-resolution molecular spectra analysis," *J. Chem. Phys.* **156**, 224103 (2022).
- ²⁴P. Cassam-Chenaï, Y. Bouret, M. Rey, S. A. Tashkun, A. V. Nikitin, and V. G. Tyuterev, "Ab initio effective rotational Hamiltonians: A comparative study," *Int. J. Quantum Chem.* **112**, 2201–2220 (2012).
- ²⁵H. S. P. Müller *et al.*, "Rotational spectroscopy of isotopic oxirane, *c*-C₂H₄O," *J. Mol. Spectrosc.* **384**, 111584 (2022).
- ²⁶G. Batra, P. Pinacho, A. L. Steber, V. M. Rivilla, J. Martín-Pintado, I. Jiménez-Serra, and M. Schnell, "The missing conformer: A comprehensive rotational spectroscopy study and astronomical search of two conformers of methyl cyanoacetate," *Front. Astron. Space Sci.* **9**, 977488 (2022).
- ²⁷J. K. G. Watson, "Simplification of the molecular vibration-rotation Hamiltonian," *Mol. Phys.* **15**, 479–490 (1968).
- ²⁸Y. Tan, F. M. Skinner, S. Samuels, R. J. Hargreaves, R. Hashemi, and I. E. Gordon, "H₂, He, and CO₂ pressure-induced parameters for the HITRAN database. II. Line lists of CO₂, N₂O, CO, SO₂, OH, OCS, H₂CO, HCN, PH₃, H₂S, and GeH₄," *Astrophys. J., Suppl. Ser.* **262**, 40 (2022).
- ²⁹J. Tennyson, P. F. Bernath, L. R. Brown, A. Campargue, A. G. Császár, L. Daumont, R. R. Gamache, J. T. Hodges, O. V. Naumenko, O. L. Polyansky, L. S. Rothman, A. C. Vandaele, N. F. Zobov, A. R. Al Derzi, C. Fábri, A. Z. Fazliev, T. Furtenbacher, I. E. Gordon, L. Lodi, and I. I. Mizus, "IUPAC critical evaluation of the rotational–vibrational spectra of water vapor, Part III: Energy levels and transition wavenumbers for H₂¹⁶O," *J. Quant. Spectrosc. Radiat. Transfer* **117**, 29–58 (2013).
- ³⁰L. R. Brown, K. Sung, D. C. Benner, V. M. Devi, V. Boudon, T. Gabard, C. Wenger, A. Campargue, O. Leshchishina, S. Kass, D. Mondelain, L. Wang, L. Daumont, L. Régalia, M. Rey, X. Thomas, V. G. Tyuterev, O. M. Lyulin, A. V. Nikitin, H. M. Niederer, S. Albert, S. Bauerecker, M. Quack, J. J. O'Brien, I. E. Gordon, L. S. Rothman, H. Sasada, A. Coustenis, M. A. H. Smith, T. Carrington, Jr., X.-G. Wang, A. W. Mantz, and P. T. Spickler, "Methane line parameters in the HITRAN2012 database," *J. Quant. Spectrosc. Radiat. Transfer* **130**, 201–219 (2013).
- ³¹M. Rey, A. V. Nikitin, and V. G. Tyuterev, "Theoretical hot methane line lists up to 2000 K for astrophysical applications," *Astrophys. J.* **789**, 2 (2014).
- ³²M. Rey, A. V. Nikitin, and V. G. Tyuterev, "Complete nuclear motion Hamiltonian in the irreducible normal mode tensor operator formalism for the methane molecule," *J. Chem. Phys.* **136**, 244106 (2012).
- ³³M. Rey, I. S. Chizhmakova, A. V. Nikitin, and V. G. Tyuterev, "Towards a complete elucidation of the ro-vibrational band structure in the SF₆ infrared spectrum from full quantum-mechanical calculations," *Phys. Chem. Chem. Phys.* **23**, 12115–12126 (2021).
- ³⁴G. Avila and E. Mátyus, "Toward breaking the curse of dimensionality in (ro)vibrational computations of molecular systems with multiple large-amplitude motions," *J. Chem. Phys.* **150**, 174107 (2019).
- ³⁵K. A. Peterson and C. Puzzarini, "Systematically convergent basis sets for transition metals. II. Pseudopotential-based correlation consistent basis sets for the group 11 (Cu, Ag, Au) and 12 (Zn, Cd, Hg) elements," *Theor. Chem. Acc.* **114**, 283–296 (2005).

- ³⁶C. Puzzarini, J. Bloino, N. Tassinato, and V. Barone, "Accuracy and interpretability: The devil and the holy grail. New routes across old boundaries in computational spectroscopy," *Chem. Rev.* **119**, 8131–8191 (2019).
- ³⁷X. Huang, D. W. Schwenke, and T. J. Lee, "Rovibrational spectra of ammonia. I. Unprecedented accuracy of a potential energy surface used with nonadiabatic corrections," *J. Chem. Phys.* **134**, 044320 (2011).
- ³⁸X. Huang, D. W. Schwenke, and T. J. Lee, "Rovibrational spectra of ammonia. II. Detailed analysis, comparison, and prediction of spectroscopic assignments for $^{14}\text{NH}_3$, $^{15}\text{NH}_3$, and $^{14}\text{ND}_3$," *J. Chem. Phys.* **134**, 044321 (2011).
- ³⁹X. Huang, D. W. Schwenke, and T. J. Lee, "Empirical infrared line lists for five SO_2 isotopologues: $^{32/33/34/36}\text{S}^{16}\text{O}_2$ and $^{32}\text{S}^{18}\text{O}_2$," *J. Mol. Spectrosc.* **311**, 19–24 (2015).
- ⁴⁰G. Rauhut, "Efficient calculation of potential energy surfaces for the generation of vibrational wave functions," *J. Chem. Phys.* **121**, 9313–9322 (2004).
- ⁴¹B. Ziegler and G. Rauhut, "Efficient generation of sum-of-products representations of high-dimensional potential energy surfaces based on multimode expansions," *J. Chem. Phys.* **144**, 114114 (2016).
- ⁴²B. Ziegler and G. Rauhut, "Rigorous use of symmetry within the construction of multidimensional potential energy surfaces," *J. Chem. Phys.* **149**, 164110 (2018).
- ⁴³B. Ziegler and G. Rauhut, "Accurate vibrational configuration interaction calculations on diborane and its isotopologues," *J. Phys. Chem. A* **123**, 3367–3373 (2019).
- ⁴⁴B. Ziegler and G. Rauhut, "Vibrational analysis of nitrosamine, a molecule with an almost constant potential along the inversion coordinate," *Mol. Phys.* **117**, 1741–1745 (2019).
- ⁴⁵M. Neff, T. Hrenar, D. Oschetzki, and G. Rauhut, "Convergence of vibrational angular momentum terms within the Watson Hamiltonian," *J. Chem. Phys.* **134**, 064105 (2011).
- ⁴⁶J. Sarka, B. Poirier, V. Szalay, and A. G. Császár, "On neglecting Coriolis and related couplings in first-principles rovibrational spectroscopy: Considerations of symmetry, accuracy, and simplicity," *Sci. Rep.* **10**, 4872 (2020).
- ⁴⁷K. M. Christoffel and J. M. Bowman, "Investigations of self-consistent field, SCF CI and virtual state configuration-interaction vibrational energies for a model 3-mode system," *Chem. Phys. Lett.* **85**, 220–224 (1982).
- ⁴⁸J. M. Bowman, K. Christoffel, and F. Tobin, "Application of SCF-CI theory to vibrational motion in polyatomic molecules," *J. Phys. Chem.* **83**, 905–912 (1979).
- ⁴⁹M. Neff and G. Rauhut, "Toward large scale vibrational configuration interaction calculations," *J. Chem. Phys.* **131**, 124129 (2009).
- ⁵⁰F. Pfeiffer and G. Rauhut, "Multi-reference vibration correlation methods," *J. Chem. Phys.* **140**, 064110 (2014).
- ⁵¹E. Fermi, "Über den Ramaneffekt des Kohlendioxids," *Z. Phys.* **71**, 250–259 (1931).
- ⁵²B. T. Darling and D. M. Dennison, "The water vapor molecule," *Phys. Rev.* **57**, 128–139 (1940).
- ⁵³H.-J. Werner, P. J. Knowles, F. R. Manby, J. A. Black, K. Doll, A. Heßelmann, D. Kats, A. Köhn, T. Korona, D. A. Kreplin, Q. Ma, T. F. Miller, A. Mitrushchenkov, K. A. Peterson, I. Polyak, G. Rauhut, and M. Sibaev, "The Molpro quantum chemistry package," *J. Chem. Phys.* **152**, 144107 (2020).
- ⁵⁴S. Carter, A. R. Sharma, J. M. Bowman, P. Rosmus, and R. Tarroni, "Calculations of rovibrational energies and dipole transition intensities for polyatomic molecules using multimode," *J. Chem. Phys.* **131**, 224106 (2009).
- ⁵⁵H.-D. Meyer, F. L. Quéré, C. Léonard, and F. Gatti, "Calculation and selective population of vibrational levels with the multiconfiguration time-dependent Hartree (MCTDH) algorithm," *Chem. Phys.* **329**, 179–192 (2006).
- ⁵⁶S. Erfort, M. Tschöpe, and G. Rauhut, "Toward a fully automated calculation of rovibrational infrared intensities for semi-rigid polyatomic molecules," *J. Chem. Phys.* **152**, 244104 (2020).
- ⁵⁷T. Mellor and S. N. Yurchenko, "A theoretical ro-vibrational line list of H_2CS using a new approach to construct the exact kinetic energy operator," in 2021 International Symposium on Molecular Spectroscopy (Virtual), June 21–25, 2021.
- ⁵⁸T. Mathea and G. Rauhut, "Advances in vibrational configuration interaction theory - part 1: Efficient calculation of vibrational angular momentum terms," *J. Comput. Chem.* **42**, 2321–2333 (2021).
- ⁵⁹T. Mathea, T. Petrenko, and G. Rauhut, "Advances in vibrational configuration interaction theory - part 2: Fast screening of the correlation space," *J. Comput. Chem.* **43**, 6–18 (2022).
- ⁶⁰B. Schröder and G. Rauhut, "Vibrational configuration interaction theory," in *Vibrational Dynamics of Molecules*, edited by J. M. Bowman (World Scientific, Singapore, 2022), pp. 1–40.
- ⁶¹V. Špirko, P. Jensen, P. Bunker, and A. Čejchan, "The development of a new Morse-oscillator based rotation-vibration Hamiltonian for H_3^+ ," *J. Mol. Spectrosc.* **112**, 183–202 (1985).
- ⁶²M. Tschöpe, B. Schröder, S. Erfort, and G. Rauhut, "High-level rovibrational calculations on ketenimine," *Front. Chem.* **8**, 623641 (2021).
- ⁶³S. Erfort, M. Tschöpe, G. Rauhut, X. Zeng, and D. P. Tew, "Ab initio calculation of rovibrational states for non-degenerate double-well potentials: cis-trans isomerization of HOPO," *J. Chem. Phys.* **152**, 174306 (2020).
- ⁶⁴S. Erfort, M. Tschöpe, and G. Rauhut, "Efficient and automated quantum chemical calculation of rovibrational nonresonant Raman spectra," *J. Chem. Phys.* **156**, 124102 (2022).
- ⁶⁵R. J. Whitehead and N. C. Handy, "Variational calculation of vibration-rotation energy levels for triatomic molecules," *J. Mol. Spectrosc.* **55**, 356–373 (1975).
- ⁶⁶P. R. Bunker and P. Jensen, *Molecular Symmetry and Spectroscopy*, 2nd ed. (NRC Research Press, 2006).
- ⁶⁷D. M. Jonas, "Spin statistics: An error in Landau and Lifschitz' quantum mechanics," *J. Chem. Phys.* **90**, 5563–5565 (1989).
- ⁶⁸T. B. Adler, G. Knizia, and H.-J. Werner, "A simple and efficient CCSD(T)-F12 approximation," *J. Chem. Phys.* **127**, 221106 (2007).
- ⁶⁹K. A. Peterson, T. B. Adler, and H.-J. Werner, "Systematically convergent basis sets for explicitly correlated wavefunctions: The atoms H, He, B–Ne, and Al–Ar," *J. Chem. Phys.* **128**, 084102 (2008).
- ⁷⁰K. E. Yousaf and K. A. Peterson, "Optimized auxiliary basis sets for explicitly correlated methods," *J. Chem. Phys.* **129**, 184108 (2009).
- ⁷¹A. J. May and F. R. Manby, "An explicitly correlated 2nd order Møller-Plesset theory using a frozen Gaussian geminal," *J. Chem. Phys.* **121**, 4479 (2004).
- ⁷²G. Knizia and H.-J. Werner, "Explicitly correlated RMP2 for high-spin open-shell reference states," *J. Chem. Phys.* **128**, 154103 (2008).
- ⁷³J. M. Bowman, T. Carrington, Jr., and H.-D. Meyer, "Variational quantum approaches for computing vibrational energies of polyatomic molecules," *Mol. Phys.* **106**, 2145–2182 (2008).
- ⁷⁴K. Pflüger, M. Paulus, S. Jagiella, T. Burkert, and G. Rauhut, "Multi-level vibrational SCF calculations and FTIR measurements on furazan," *Theor. Chem. Acc.* **114**, 327–332 (2005).
- ⁷⁵G. Hose and H. S. Taylor, "Quantum Kolmogorov-Arnol'd-Moser-like theorem: Fundamentals of localization in quantum theory," *Phys. Rev. Lett.* **51**, 947 (1983).

Publication 3: A theoretical study of propynal under interstellar conditions and beyond, covering low-frequency infrared spectra, spectroscopic constants, and hot bands

A theoretical study of propynal under interstellar conditions and beyond, covering low-frequency infrared spectra, spectroscopic constants, and hot bands

Martin Tschöpe¹ and Guntram Rauhut^{1*}

Institute for Theoretical Chemistry, University of Stuttgart, Pfaffenwaldring 55, D-70569 Stuttgart, Germany

Accepted 2023 January 20. Received 2023 January 19; in original form 2022 December 16

ABSTRACT

From an astrochemical point of view, propynal is a complex organic molecule. Moreover, it is a potential candidate for the formation of prebiotic propanal and propenal. Therefore, this molecule is of particular interest for astrochemical investigations. As it has been detected in the interstellar medium, it is of high relevance in this field of research. Although experimental data are available for the vibrational fundamental bands and rotational constants, experimental data for vibrational overtones and combination bands are scarce and fairly old. Additionally, high-level *ab initio* calculations are also not reported. In this work, we provide accurate quantum chemical calculations as well as a detailed analysis of vibrational and rovibrational properties for this molecule. The low-frequency spectrum up to 350 cm^{-1} has been studied for temperatures between 10 and 300 K. For the same temperature range, partition functions are provided. Furthermore, the impact of hot bands up to room temperature has been investigated. A comparison of our results with experimental data is provided for the rotational constants, geometrical parameters, and a rovibrational spectrum. The underlying potential energy surface within these calculations is based on explicitly correlated coupled-cluster theory and includes up to four-mode coupling terms within an n -mode expansion. The vibrational and rovibrational calculations rely on vibrational and rovibrational configuration interaction theories, respectively.

Key words: molecular data – line: identification – infrared: general – radiation mechanism: general – ISM: general – ISM: lines and bands.

1 INTRODUCTION

The first molecule detected in the interstellar medium (ISM) was methylidyne (CH) in 1937 (Dunham 1937; Swings & Rosenfeld 1937; McKellar 1940). Since then more than 200 molecular species have been detected in the interstellar and circumstellar media (Müller et al. 2001, 2005; Endres et al. 2016; McGuire 2018). One important subset of these is molecules with more than five atoms that contain at least one carbon atom. They are usually referred to as *complex organic molecules* (Herbst & van Dishoeck 2009) and they are thought to be important building blocks for biologically relevant molecules (Woon 2002; Theule et al. 2011; Ohishi 2019). Propynal falls into this class. Furthermore, as propynal is a potential candidate for the formation of prebiotic propenal (CH_2CHCHO) and propanal ($\text{CH}_3\text{CH}_2\text{CHO}$), it is of particular interest for astrochemical investigations (Irvine et al. 1988; Turner 1991; Hollis et al. 2004). The first detection of propynal in the ISM was by Irvine et al. (1988) and was followed by many more investigations in space (Turner 1991; Ohishi & Kaifu 1998; Hollis et al. 2004).

Independent from astrochemical investigations, over the last decades, propynal has been studied by several groups, mostly by experimental methods. In an early work, Brand & Watson (1960) determined all vibrational fundamental bands and some additional ones of propynal and its singly deuterated isotopologues by means of

gas-phase infrared spectroscopy. These studies were refined by the same group (Brand, Callomon & Watson 1963) using near-ultraviolet spectroscopy (see also Howe & Goldstein 1958) with a focus on the band at 382 nm.

A study of 15 different propynal isotopologues beyond deuteration has been performed by Costain & Morton (1959). Roughly at the same time, King & Moule (1961) employed gas-phase infrared spectroscopy in the region between 380 and 4000 cm^{-1} as well as Raman spectroscopy to measure the frequencies of the pure vibrational transitions. To reach an even higher accuracy, the subsequent works used either double resonance laser measurements (Takami & Shimoda 1976; Jones 1980) or direct current (DC) glow discharges (Jaman et al. 2011). While the previously mentioned publications focused more on gas-phase spectroscopy at room temperature, there are recent measurements of frequencies of the vibrational fundamental bands in amorphous propynal at $T = 10\text{ K}$ and in the crystal phase at $T = 125\text{ K}$ by Hudson & Gerakines (2018). In addition to that, the results of a simulation based on a potential energy surface (PES) obtained by density functional theory (DFT) for the aforementioned frequencies have been published by Margulès et al. (2020). However, it should be mentioned that this work mainly focuses on propynethial, which is the sulphur analogue of propynal.

The first experimental determination of rotational constants was performed by Howe & Goldstein (1955) and later on refined by Winnewisser (1973). The latter determined all quadratic and quartic spectroscopic constants, but only two of the seven sextic parameters. Three decades later, McKellar et al. (2008) did not only

* E-mail: rauhut@theochem.uni-stuttgart.de

determine the rotational and centrifugal distortion constants with much higher accuracy, they also calculated these constants for four different excited vibrational modes. The most recent publications on the spectroscopic constants of propynal are by Barros et al. (2015) using coherent synchrotron radiation Fourier transform spectrometry and by Jabri et al. (2020) determining also some octic centrifugal constants and investigating more excited vibrational bands.

Within these studies, there are only three spectra that have been published for the undeuterated propynal. The first one is by King & Moule (1961) for a very broad spectral range of 400–3600 cm⁻¹. Nearly five decades later, McKellar et al. (2008) presented a high-resolution spectrum for 215 K at 580–730 cm⁻¹. The most recently published spectrum of propynal was again by McKellar (2010), in a review article about high-resolution infrared spectroscopy with synchrotron sources. The section about propynal was based on earlier work of Robertson et al. (2009), showing a high-resolution spectrum at 80–410 cm⁻¹ measured at the Australian synchrotron, which has been used as reference spectrum within this work.

As mentioned earlier, the majority of these studies are based on laboratory experiment. The number of theoretical investigations and in particular ab initio calculations is very limited. Over the last decades, a multitude of different approaches for the simulation of vibrational and rovibrational spectra have been developed by the community (Rauhut 2004; Yachmenev et al. 2011; Carter, Bowman & Handy 2012; Wang & Carrington 2013; Yachmenev, Polyak & Thiel 2013; Carter, Wang & Bowman 2017; Nikitin, Rey & Tyuterev 2017; Rey, Nikitin & Tyuterev 2017; Yurchenko et al. 2017; Ferenc & Matyus 2019; Sarka, Petty & Poirier 2019; Simmons, Wang & Carrington 2019; Smydke et al. 2019; Tobias et al. 2019; Tyuterev et al. 2019; Clark et al. 2020; Santa Daria, Avila & Matyus 2021; Tschöpe et al. 2021). One of these approaches relies on the Watson Hamiltonian (Watson 1968) and subsequent vibrational configuration interaction (VCI; Bowman, Christoffel & Tobin 1979; Christoffel & Bowman 1982; Neff & Rauhut 2009; Pfeiffer & Rauhut 2014; Schröder & Rauhut 2022) and rovibrational configuration interaction (RVCI; Erfort et al. 2020a; Erfort, Tschöpe & Rauhut 2020b, 2022) calculations. It allows for the efficient determination of rovibrational spectra for semirigid molecules, by using high-level PESs described in normal coordinates (Ziegler & Rauhut 2016, 2018, 2019). Limitations for this approach occur for floppy molecules and vibrational modes with large deflections, because the underlying expansions converge slower, which makes the calculations less efficient. This approach, which is not bound to a model Hamiltonian, appears to be very suitable for our investigations for several reasons: (1) propynal is a semirigid system, (2) we focus on low temperatures, and (3) we are studying the spectra up to 350 cm⁻¹.

In this study, we use a high-level multidimensional PES as well as VCI and RVCI calculations to determine the (ro)vibrational spectrum of propynal. We present data for the geometrical parameters and values for the partition functions between 10 and 300 K. Furthermore, we provide spectra considering pressure broadening, infrared stick spectra, and vibrational line lists. In addition to that we discuss the influence of hot bands on the simulated spectra for different temperatures and compare our rotational constants with experimental results.

2 THEORY

2.1 Rovibrational energies

Our implementation of RVCI theory is based on the Watson Hamiltonian (Watson 1968),

MNRAS **520**, 3345–3354 (2023)

$$H = \underbrace{\frac{1}{2} \sum_{\alpha\beta} \mu_{\alpha\beta} J_{\alpha} J_{\beta}}_{H_{\text{rot}}} - \underbrace{\frac{1}{2} \sum_{\alpha\beta} (J_{\alpha} \mu_{\alpha\beta} \pi_{\beta} + \pi_{\alpha} \mu_{\alpha\beta} J_{\beta})}_{H_{\text{rv}}} + H_{\text{vib}} \quad (1)$$

$$H_{\text{vib}} = \frac{1}{2} \sum_{\alpha\beta} \pi_{\alpha} \mu_{\alpha\beta} \pi_{\beta} - \frac{1}{2} \sum_i \frac{\partial^2}{\partial q_i^2} - \frac{1}{8} \sum_{\alpha} \mu_{\alpha\alpha} + V(\vec{q}), \quad (2)$$

which relies on the Born–Oppenheimer PES V expanded in terms of normal coordinates q_i . Moreover, it depends on the Cartesian components of the angular momentum operator, J_{α} , and the vibrational angular momentum (VAM) operator

$$\pi_{\alpha} = -i \sum_{jk} \zeta_{jk}^{\alpha} q_j \frac{\partial}{\partial q_k} \quad (3)$$

with ζ_{jk}^{α} denoting an element of the antisymmetric Coriolis ζ -constant tensor. $\alpha, \beta \in \{x, y, z\}$ denote Cartesian components. The Watson Hamiltonian can be split into the rotational term H_{rot} , the Coriolis coupling term H_{rv} , and the pure vibrational term H_{vib} . The latter two depend on the inverse of the effective moment of inertia tensor μ (Watson 1968). We are using an n -mode expansion (Bowman, Carrington & Meyer 2008) and an analytical sum-of-products representation by means of polynomials to describe the potential V and the μ -tensor.

The rovibrational calculations rely on a two-step process. At first, VCI theory is used to solve the Schrödinger equation for the non-rotating molecule with respect to H_{vib} . This yields the vibrational energies and wavefunctions

$$|\Phi_v\rangle = \sum_I c_I |\phi_v^I\rangle. \quad (4)$$

Within the VCI approach, a large number of Hartree products $|\phi_v^I\rangle$ (configurations) are screened to determine the vibrational wavefunctions $|\Phi_v\rangle$ in a compact form (Mathea & Rauhut 2021; Mathea, Petrenko & Rauhut 2022).

In the second step, RVCI theory is used with a direct product of the VCI wavefunctions and pure rotational basis functions $|\Phi_r\rangle$ to solve the Schrödinger equation for the Watson operator of rotating molecules (equation 1) and to determine the rovibrational state energies and wavefunctions

$$|\Psi_{\text{rovib.}}\rangle = \sum_{rv} c_{rv} |\Phi_r\rangle |\Phi_v\rangle. \quad (5)$$

For $|\Phi_r\rangle$, we are using a molecule-specific rotational basis (MSRB), which is a linear combination of Wang combinations. It is determined by solving the Schrödinger equation of the pure rotational part of the Watson Hamiltonian H_{rot} and was introduced by Erfort et al. (2020b). The diagonalization of the resulting RVCI matrix yields the desired wavefunctions.

2.2 Intensities

The rovibrational infrared line intensities, given by

$$I = \frac{2\pi^2 N_A}{3\epsilon_0 h^2 c^2} \frac{e^{-E''/kT} (1 - e^{-(E' - E'')/kT})}{Q(T)} (E' - E'') R, \quad (6)$$

depend on some mathematical and physical constants in the prefactor as well as the thermal occupation of the specific rovibrational state, the energy difference $(E' - E'')$ between the two concerned states, and the square of the transition moment R . For the determination of the partition function

$$Q = \sum_{rv} g_{rv} e^{-E_{rv}/k_B T}, \quad (7)$$

all calculated rovibrational state energies E_{rv} and the corresponding degeneracies g_{rv} are used. This is in contrast to previous work, where we approximated the partition function by a separability approach. The degeneracies $g_{rv} = g_{ns}(2J + 1)$ depend on the nuclear spin statistical weights (NSSWs). For propynal, both irreducible representations A' and A'' yield the same value for the NSSWs of $g_{ns} = 4$.

3 COMPUTATIONAL DETAILS

The equilibrium geometry, the harmonic frequencies, and hence the normal coordinates of propynal have been calculated by explicitly correlated coupled-cluster theory including single and double excitations and a perturbative treatment of the triple excitations, CCSD(T)-F12b. For the calculation of the line lists and spectra, the frozen core approximation has been used within the calculation of the PES. This approximation relies on error compensation with respect to neglected contributions to the electronic energy, as for example high-order coupled-cluster terms, relativistic effects, diagonal Born–Oppenheimer corrections, and core-correlation contributions. This usually leads to vibrational frequencies that match nicely with experimental results as can be seen in our results below. In contrast to that, all electron (ae) correlation calculations have been used to determine the rotational constants, since previous work has shown (Schneider & Rauhut 2023) that this improves the quality significantly. The orbital basis set used in these calculations has triple- ζ quality, i.e. cc-pVTZ-F12 (Peterson, Adler & Werner 2008) in case of the frozen core approximation, and cc-pcVTZ-F12 for the ae calculations. Within the latter coupled-cluster calculations, different exponents γ were used for the Slater geminal functions referring to core–core, core–valence, and valence–valence orbital pairs, i.e. 0.8, 1.7, and 2.2, as recommended by May & Manby (2004), while for the frozen core calculations a constant γ of 1.0 has been chosen. The complementary auxiliary basis set correction has been used to improve the Hartree–Fock energies.

An n -mode expansion truncated after the four-mode coupling terms was used to represent the multidimensional PES (Bowman et al. 2008). The level of electronic structure theory used to determine the 1D and 2D subsurfaces was the same as for the calculation of the harmonic frequencies, while for the calculation of the 3D and 4D subsurfaces the distinguishable clusters approximation, DCSD, was applied in combination with a double- ζ basis set. Such so-called multilevel schemes are described by Pflüger et al. (2005). The dipole moment surface was calculated by the corresponding conventional methods without explicit correlation. Run time savings due to symmetry were exploited for both, the electronic single point calculations and the different terms of the n -mode expansion (Ziegler & Rauhut 2018). A transformation of the grid representations of the surfaces to an analytical sum-of-products representation was applied to save computational time within the subsequent VCI calculations. Kronecker product fitting with nine monomials per mode was used for this purpose (Ziegler & Rauhut 2016).

To determine vibrational wavefunctions, a state-specific configuration selective implementation of VCI theory has been used (Mathea & Rauhut 2021; Mathea et al. 2022; Schröder & Rauhut 2022). The basis functions for that are provided by means of Hartree products generated from one-mode wavefunctions (modals), which have been obtained from self-consistent field calculations for the vibrational ground state (GS). The correlation space was limited to a maximum of six different modes excited at the same time, the maximal sum of vibrational quantum numbers was set to 20, and a maximum excitation per mode up to the eighth root has been used. This resulted

Table 1. Partition functions for propynal at different temperatures.

T (K)	Q
9.375	506
18.750	1433
37.500	4054
75.000	11 792
150.000	40 812
225.000	97 783
300.000	195 486

in about 2×10^7 configurations per irreducible representation. Diagonal elements of the VCI matrix included up to 1D terms of the μ -tensor expansion within the VAM terms, while the off-diagonal terms were limited to a constant μ -tensor. To determine the energy eigenvalues of predefined states, a residuum-based eigenvalue solver has been used (Petrenko & Rauhut 2017).

The maximum value for the quantum number of the total angular momentum operator J was set to 95 within the RVC calculations. Since the main focus of this paper is to study propynal under conditions similar to the ISM, we have chosen a temperature range from 10 to 300 K. The upper temperature bound was chosen to provide a reference spectrum for lab experiments. As mentioned earlier, the partition function was calculated based on RVC state energies without using the separability approximation. The resulting partition functions for different temperatures are shown in Table 1. For the calculations of the integrals arising from the rotational operator within the Watson Hamiltonian the order of the μ -tensor was set to 2. In contrast to that, a first-order μ -tensor has been used for the Coriolis coupling integrals. These choices were based on our previous findings (Tschöpe & Rauhut 2022) and a similar analysis for propynal that was performed in the course of this study.

As mentioned earlier, the rovibrational basis functions are direct products of VCI wavefunctions for the vibrational subspace and MSRB functions for the rotational subspace. The selection of VCI wavefunctions was limited by a maximum transition frequency of 1500 cm^{-1} and a maximum sum of vibrational quantum numbers of 3. This yields $N_{\text{vib}} = 49$ vibrational modes, which include the modes $\nu_5 - \nu_{12}$ in Table 2 and all transitions listed in Table 3. The number of MSRB functions was set to $N_{\text{rot}} = 2J + 1$, which is the maximum number of rotational basis functions that can be considered. For this reason, the size of the largest matrix that had to be considered is $N = (2J + 1)N_{\text{vib}} = 9359$. The wall clock time for the combined VCI and RVC calculations was ≈ 4.3 d on four central processing unit cores.

The rovibrational intensity calculations considered ≈ 171 million transitions. The printout was filtered to ≈ 10.4 million transitions, which have an intensity of at least 10^{-6} relative to the strongest transition in the spectrum for $T = 300$ K. In contrast to previous work, we also considered hot bands in the spectrum if the thermal occupation of the lower vibrational mode is high. For $T = 300$ K, this was fulfilled by the four modes ν_9 , ν_{12} , $2\nu_9$, and $\nu_9 + \nu_{12}$.

4 RESULTS

4.1 Geometrical parameters

Geometrical parameters of propynal are provided in Table 4. The parameters denoted as \mathbf{r}_e are obtained from the Born–Oppenheimer equilibrium geometry. Vibrationally averaged geometrical parameters are given as \mathbf{r}_a and \mathbf{r}_g . The former can be obtained by averaging the atomic positions over the VCI GS wavefunction. The latter are

Table 2. Fundamental bands of propynal. Comparison between VCI results of this work and other theoretical and experimental data. Frequencies ν_i are given in cm^{-1} and infrared intensities I are given in km mol^{-1} .

Mode	Irrep	ν_i								I^i This work	Description
		This work ^a	This work ^b	Theory ^c	Exp. ^d	Exp. ^e	Exp. ^f	Exp. ^g	Exp. ^h		
ν_1	A'	3330.8	3319.0	3332.1	3326.0	3335	–	3234	3212	36.5	H ₂ –C stretch
ν_2	A'	2862.9	2859.0	2769.1	2858.2	2869	–	2889	2914	42.1	H ₁ –C stretch
ν_3	A'	2121.1	2110.6	2159.7	2106.0	2125	–	2099	2092	52.1	C≡C stretch
ν_4	A'	1707.6	1701.9	1721.4	1696.9	1692	–	1666	1644	141.8	C=O stretch
ν_5	A'	1390.9	1386.9	1432.5	1389.0	1398	–	1387	1394	9.0	H ₁ –C=O rock
ν_6	A'	944.4	939.8	940.8	943.7	950	–	952	959	95.3	C–C stretch
ν_7	A'	659.8	650.9	675.4	650.0	691	651.3143	713	732	40.1	C≡C–H ₂ in-plane wag
ν_8	A'	615.9	611.0	630.7	613.7	615	614.0146	624	631	3.0	C–C=O in-plane bend
ν_9	A'	206.4	202.7	216.2	205.3	–	–	–	–	5.1	C–C≡C in-plane bend
ν_{10}	A''	985.2	980.9	988.2	981.2	990	–	989	1006	0.1	H ₁ –C=O out-plane wag
ν_{11}	A''	699.1	692.6	757.8	692.7	669	692.7707	756	771	32.4	C≡C–H ₂ out-plane wag
ν_{12}	A''	260.0	255.9	279.1	260.6	–	–	–	–	9.3	C–C≡C out-plane bend
MAD ^j	–	5.2	2.9	30.3	Ref. ^d	13	–	32	46	–	–
MAX ^j	–	15.1	7.0	89.1	Ref. ^d	41	–	92	114	–	–

^a RVCi calculation based on ae PESs.^b RVCi calculation based on frozen core PESs.^c Calculated anharmonic frequencies values taken from Margulès et al. (2020).^d Experimental gas phase values taken from Brand et al. (1963). Used as reference for the calculation of MAD and MAX.^e Experimental gas phase values taken from King & Moule (1961).^f High-resolution (0.003 cm^{-1}) experimental gas phase values taken from McKellar et al. (2008).^g Experimental amorphous phase at $T = 10 \text{ K}$, values taken from Hudson & Gerakines (2018).^h Experimental crystalline phase at $T = 115 \text{ K}$, values taken from Hudson & Gerakines (2018).ⁱ Infrared intensities obtained by VCI calculations based on a frozen core PES.^j Mean absolute deviation (MAD) and maximum absolute deviation (MAX).

instantaneous inter-nuclear distances calculated from an expectation value of the bond lengths expanded in terms of the normal coordinates. Similar to other studies (Czakó, Mátyus & Császár 2009; Dinu et al. 2020), the two sets of vibrationally averaged bond lengths differ significantly from each other. The largest absolute difference can be found for $r(\text{C}_3\text{H}_2)$ of 0.0265 \AA . By utilizing different isotopologues, the geometrical parameters can also be determined experimentally from GS rotational constants, as it was performed by Costain & Morton (1959). The molecular structures obtained by substitution (\mathbf{r}_s) agree well with our vibrationally averaged parameters \mathbf{r}_a although these values cannot be compared directly.

4.2 Vibrational transitions

A list of the purely vibrational transitions of propynal is given in Table 2 for the fundamental bands and in Table 3 for overtones and combination bands. There is only one theoretical and four experimental data sets for a comparison of the fundamental bands. For all other vibrational transitions, there are no theoretical data and just a very limited number of assigned experimental lines. In Table 2, it can be seen that our calculations based on the frozen core approximation yield a mean absolute deviation (MAD) of 2.9 cm^{-1} to the apparently most precise complete gas-phase experiments of Brand et al. (1963). This error bar is in the usual range of such calculations (see, for example, the work of Schröder & Rauhut 2022). In contrast to that, the ae calculation has a significant larger MAD of 5.1 cm^{-1} . This is due to the lifting of the aforementioned error compensation with other approximations, mainly the high-order coupled-cluster terms. It is evident that the latter calculation overestimates the vibrational frequencies for all fundamentals. By comparing the frequencies for the single transitions instead of the MAD in Table 2, it can be seen that in the majority of cases the

deviation between our two calculations is smaller than 6 cm^{-1} . The results for the high-resolution gas-phase spectrum of McKellar et al. (2008) show excellent agreement for the modes ν_7 and ν_{11} when compared with our frozen core simulation. However, the ν_8 mode matches better with the ae result.

Some of the combination bands and overtones, e.g. ν_9^3 , $\nu_9 + 2\nu_{12}$, and $2\nu_9 + \nu_{12}$, showed a slow convergence with respect to the size of the VCI configuration space. For that reason, it was necessary to increase the maximum excitation per mode up to the eighth root.

Among the vibrational modes under investigation there are only a small number of noticeable resonances. First of all, the ν_2 mode at 2859 cm^{-1} shows a Fermi resonance with $2\nu_5$. This resonance is stronger for the ae calculation, since the higher frequency of ν_5 and its overtone $2\nu_5$ decreases the energetic separation between two resonating vibrational modes. Neither an overtone nor a combination band arising from two different modes as listed in Table 3 shows any significant resonances. However, there are two couples of threefold combination bands that resonate fairly significantly. Within the A' symmetry subspace, $\nu_9 + \nu_{11} + \nu_{12}$ at 1157 cm^{-1} resonates with $\nu_7 + 2\nu_{10}$ at 1167 cm^{-1} . At a similar energy but in the A'' symmetry subspace, it is $2\nu_9 + \nu_{11}$ at 1100 cm^{-1} and $\nu_7 + \nu_9 + \nu_{12}$ at 1115 cm^{-1} .

The comparison of our VCI results with the listed gas-phase transitions reveals very good agreement, although the experimental studies are about 60 yr old. However, we do not agree with the assignment of King & Moule (1961) for the modes ν_7 and ν_{11} at 691 and 669 cm^{-1} , respectively. Instead, we support the reversed assignment, as it was introduced by Brand et al. (1963). The deviation between the two experimental groups is based on an MAD of 13 cm^{-1} , about a factor of 4 larger than the deviation between our results and those of Brand et al. (1963). It should be mentioned that this statistics is dominated by the misassignment, since the largest

Table 3. Overtones and combination bands employed within RVCI calculations. Frequencies ν_i are given in cm^{-1} and infrared intensities I are given in km mol^{-1} .

Mode	Irrep	ν_i			I
		This work	Exp. ^a	Exp. ^b	This work
$2\nu_{11}$	A'	1381.6	1298	1275	4.5
$2\nu_7$	A'	1291.2	–	1340	8.5
$2\nu_8$	A'	1220.7	–	–	0.1
$2\nu_{12}$	A'	512.1	–	–	0.2
$2\nu_9$	A'	408.6	–	–	0.1
$3\nu_9$	A'	618.9	–	–	0.1
$3\nu_{12}$	A''	769.9	–	–	0.0
$\nu_7 + \nu_8 + \nu_9$	A'	1468.1	–	–	0.0
$\nu_6 + 2\nu_{12}$	A'	1457.0	–	–	0.0
$\nu_9 + \nu_{10} + \nu_{12}$	A'	1442.8	–	–	0.0
$2\nu_8 + \nu_9$	A'	1424.8	–	–	0.0
$\nu_6 + 2\nu_9$	A'	1350.9	–	–	0.0
$\nu_7 + \nu_8$	A'	1263.2	–	–	0.5
$\nu_{10} + \nu_{12}$	A'	1236.0	–	–	0.2
$\nu_7 + 2\nu_{12}$	A'	1167.7	–	–	0.0
$\nu_9 + \nu_{11} + \nu_{12}$	A'	1157.2	–	–	0.1
$\nu_6 + \nu_9$	A'	1143.6	1153	–	0.3
$\nu_8 + 2\nu_{12}$	A'	1127.1	–	–	0.0
$\nu_7 + 2\nu_9$	A'	1061.1	–	–	0.0
$\nu_8 + 2\nu_9$	A'	1021.1	–	–	0.0
$\nu_{11} + \nu_{12}$	A'	952.6	–	–	4.0
$\nu_7 + \nu_9$	A'	854.1	–	–	0.3
$\nu_8 + \nu_9$	A'	814.3	818	815	1.7
$\nu_9 + 2\nu_{12}$	A'	721.4	–	–	0.1
$2\nu_8 + \nu_{12}$	A''	1479.9	–	–	0.0
$\nu_6 + \nu_9 + \nu_{12}$	A''	1405.8	–	–	0.0
$2\nu_9 + \nu_{10}$	A''	1390.2	–	–	0.0
$\nu_7 + \nu_{11}$	A''	1358.7	1330	–	0.0
$\nu_8 + \nu_{11}$	A''	1303.6	–	–	0.0
$\nu_{11} + 2\nu_{12}$	A''	1214.0	–	–	0.0
$\nu_6 + \nu_{12}$	A''	1198.2	1210	–	0.2
$\nu_9 + \nu_{10}$	A''	1183.8	–	–	0.0
$\nu_7 + \nu_9 + \nu_{12}$	A''	1115.1	–	–	0.0
$2\nu_9 + \nu_{11}$	A''	1100.0	–	–	0.0
$\nu_8 + \nu_9 + \nu_{12}$	A''	1075.8	–	–	0.0
$\nu_7 + \nu_{12}$	A''	908.0	–	–	0.0
$\nu_9 + \nu_{11}$	A''	894.1	–	–	0.0
$\nu_8 + \nu_{12}$	A''	868.7	–	–	0.0
$2\nu_9 + \nu_{12}$	A''	670.1	–	–	0.2
$\nu_9 + \nu_{12}$	A''	461.6	–	–	0.0

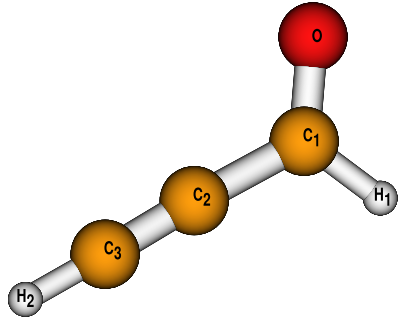
^a Experimental gas phase values taken from Brand & Watson (1960).

^b Experimental gas phase values taken from King & Moule (1961).

two errors between the two experiments of 41 and 24 cm^{-1} originate from that. The MAD is reduced to 8.6 cm^{-1} , if these two data points are removed from the statistics. As must be expected, the results of Hudson & Gerakines (2018) show large environmental effects of the solid-state phase and therefore a larger deviation than the other experiments. Furthermore, our results match significantly better with the experiments than the results obtained from DFT calculations, which have an MAD of ≈ 30 . This is mostly due to the use of more sophisticated electronic structure methods for the determination of the PES.

The majority of the non-fundamental bands displayed in Table 3 have neither experimental nor theoretical reference data for comparison. However, there are a few assigned transitions that can be compared. The only mode, which is in very good agreement with both experiments, is $\nu_8 + \nu_9$. There are two modes with a deviation of about 10 cm^{-1} , namely $\nu_6 + \nu_{12}$ and $\nu_6 + \nu_9$. Although the error

Table 4. Computed geometrical parameters of propynal. Bond lengths are given in Å and angles are given in degree. The PES was calculated with explicitly correlated coupled-cluster methods CCSD(T)-F12b, using a cc-pVTZ-F12 basis set and frozen core approximation.



Coord.	r_e	r_a	r_g	r_s^a
$r(\text{C}_1\text{C}_2)$	1.4538	1.4579	1.4611	1.4444
$r(\text{C}_1\text{O})$	1.2098	1.2123	1.2145	1.2144
$r(\text{C}_1\text{H}_1)$	1.1000	1.1073	1.1227	1.1057
$r(\text{C}_2\text{C}_3)$	1.2091	1.2089	1.2159	1.2091
$r(\text{C}_3\text{H}_2)$	1.0640	1.0554	1.0819	1.0552
$\alpha(\text{OC}_1\text{C}_2)$	123.32	123.35	–	123.90
$\alpha(\text{HC}_1\text{C}_2)$	115.07	114.84	–	113.92

^a Exp. values from Costain & Morton (1959).

is slightly larger than for the fundamental bands, the assignment of these transitions is safe. This does not hold true for the other experimentally determined vibrational modes in Table 3. First, the fact that mode $\nu_7 + \nu_{11}$ is assigned to the transition at 1330 cm^{-1} would result in a surprisingly large error. Secondly, the strength of the line was labelled as *medium* in the original literature, while our results reveal negligible intensity. Consequently, the origin of this peak remains unclear, as there are no other vibrational modes with A'' symmetry and noticeable intensity in that area. In addition to that, the assignment of the overtone $2\nu_{11}$ that is mistaken for $2\nu_7$ in some of the references is difficult. This results from the aforementioned misassignment of the fundamental bands in King & Moule (1961). In contrast to that, Brand & Watson (1960) did not assign $2\nu_7$, but misassigned $2\nu_{11}$ as well. However, they noted that the overtone is about 24 cm^{-1} lower than expected based on the fundamental band ν_7 and in addition to that, they corrected the frequency of that fundamental band by 31 cm^{-1} in Brand et al. (1963).

4.3 Rovibrational spectrum

An overview of the rovibrational spectrum of propynal in the range up to 350 cm^{-1} for a temperature of 100 K is given in Fig. 1. A clear separation between the vibrational GS in black and the two lowest excited vibrational states ν_9 (green) and ν_{12} (blue) can be seen. Since the next higher vibrational modes are the corresponding overtones $2\nu_9$ and $2\nu_{12}$, there is a distinct spectral separation towards higher energies. For that reason, the chosen spectral range appears to be very suitable for an individual investigation, especially for a study that focuses on low temperatures below 300 K. As the two vibrational fundamental bands belong to different irreducible representations, namely A' and A'', they do not resonate directly, but interact only via rovibrational coupling.

A more detailed analysis of the vibrational GS as well as a study of the temperature dependence of its spectrum can be found in Fig. 2 showing intensities in a stick spectrum and in the supplement material for the absorption cross-sections considering temperature

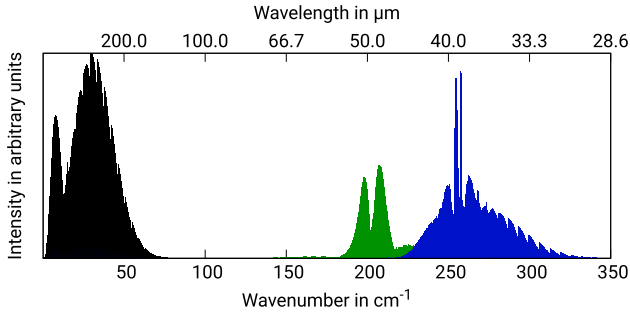


Figure 1. Overview of the rovibrational infrared stick spectrum of propynal at a temperature of 100 K. The vibrational GS and the modes ν_9 and ν_{12} are plotted in black, green, and blue, respectively. The maximum total angular momentum quantum number is set to $J = 95$. For the sake of simplicity, hot bands are not shown.

broadening. In addition to transitions from the vibrational GS to the vibrational GS that are shown in black, the figure also displays hot band transitions. The latter includes lines with initial and final vibrational quantum numbers corresponding to the modes ν_9 , ν_{12} , $2\nu_9$, and $\nu_9 + \nu_{12}$. The effect of hot bands starts to become noticeable at about 100 K. Below that temperature, ignoring hot bands is a decent approximation. For $T = 100$ K, only the two hot bands of modes ν_9 and ν_{12} need to be considered. In contrast to that for $T = 300$ K, all four vibrational modes contribute noticeably with the strongest reaching about one-third of the intensity of the GS. The shapes of the progressions for the different vibrational modes involved are very similar.

For low temperatures, the progressions of the two vibrational modes ν_9 and ν_{12} are spatially separated as can be seen in Fig. 3, in analogy to the GS spectrum. A noticeable contribution of hot bands can be found at a temperature of 100 K. Both bands show a slightly asymmetric structure, due to intensity borrowing by the P-branch of ν_{12} towards the R-branch of ν_9 . The high-energy tails at 300 cm^{-1} of the R-branch of ν_{12} could be influenced by the $2\nu_9$ mode at 408.6 cm^{-1} , which is the next higher vibrational mode. However, as the VCI frequencies of the two modes are separated by more than 100 cm^{-1} , we expect that effect to be small.

For higher temperatures especially, it can be seen that the band centre for the transitions from the vibrational GS to ν_9 (green) is offset in comparison to transitions from 9^1 to 9^2 (red). The reason for that is the significant shift in frequency of the cold band vibrational transition $\nu_{0 \rightarrow 9^1} = 202.7 \text{ cm}^{-1}$ in comparison to the frequency of the corresponding hot band $\nu_{9^1 \rightarrow 9^2} = 205.9 \text{ cm}^{-1}$. In contrast to that, this effect is much less prominent for the ν_{12} mode (blue) at $\nu_{0 \rightarrow 12^1} = 255.9$ and its corresponding hot band at $\nu_{12^1 \rightarrow 12^2} = 256.2$ (orange). It should be noted that even at higher temperatures, e.g. $T = 300$ K, all other hot bands (black) do not contribute significantly.

An interesting feature in Fig. 3 for $T = 300$ K is the sudden drop in intensity for some of the $9^1 \rightarrow 9^2$ transitions. This is especially prominent at 223 cm^{-1} and also at 245 cm^{-1} . Although such a pattern can be found in simulations, when the maximum value of the total angular momentum J_{max} is not sufficiently high, this is not the origin in this particular case. First of all, simulations have shown that this pattern is independent of J_{max} . Secondly, by analysing the different progressions in the line lists, it can be seen that the progressions do not stop at this frequency. This is further investigated in Fig. 4 by only plotting this one particular hot band $9^1 \rightarrow 9^2$ and highlighting different progressions with different colours. It can be seen that the rovibrational frequencies increase up to 223 cm^{-1} and $J \approx 57$. Hence, the rovibrational energies for the states belonging to

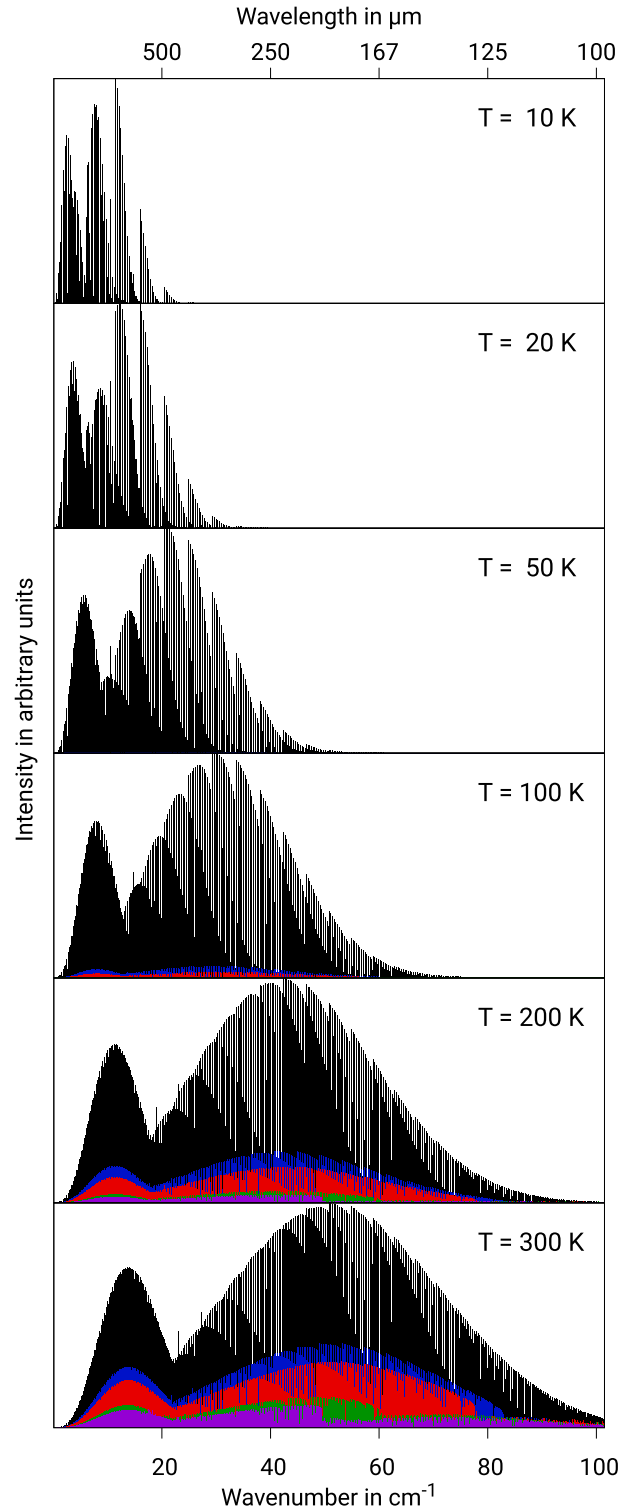


Figure 2. Vibrational GS stick spectrum of propynal for different temperatures. For all transitions, the vibrational quantum numbers of the initial and final states are equal; e.g. transitions from the vibrational GS to the vibrational GS are drawn in black. Hot bands for different vibrational modes are given in different colours. Transitions of the vibrational state 9^1 are coloured blue, and transitions within 12^1 , 9^2 , and $9^1 + 12^1$ are coloured red, green, and purple, respectively. The maximum total angular momentum was set to $J = 95$.

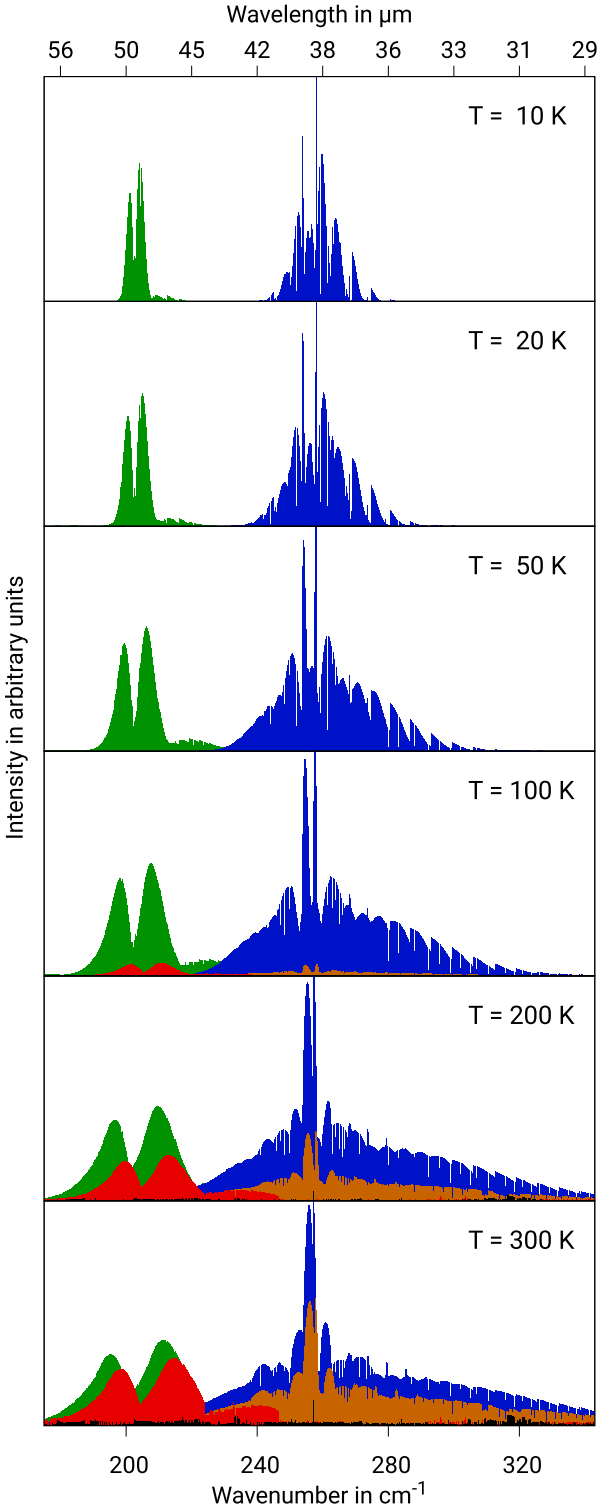


Figure 3. Stick spectrum of propynal for the lowest excited vibrational bands for different temperatures. Transitions from vibrational GS to 9^1 and 12^1 are given in green and blue, respectively. Hot bands from 9^1 to 9^2 are given in red and transitions from 12^1 to 12^2 are coloured orange. All other hot band combinations are given in black and not significant even for $T = 300$ K. The maximum total angular momentum was set to $J = 95$.

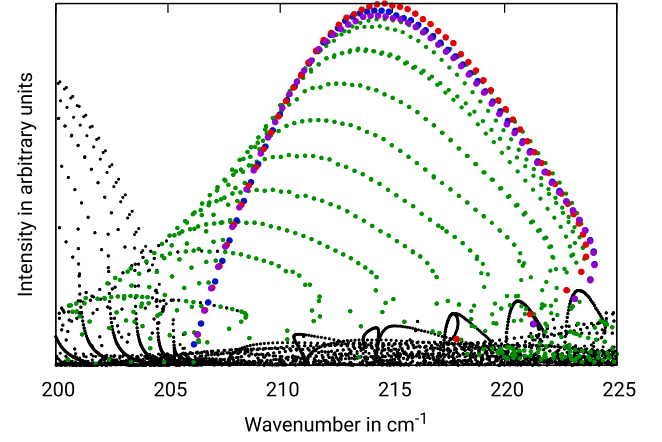


Figure 4. Progressions of propynal at $T = 300$ K for the hot band transition from 9^1 to 9^2 . Black dots mark transitions fulfilling $\Delta J = J' - J'' \in \{0, -1\}$. Hence, the remaining possible transitions are $\Delta J = 1$ and are marked by a dot in one of the other colours. Highlighted in blue is the progression fulfilling $K'_a = K''_a = 0$ and $\Delta K_c = 1$. Both the red and purple dots show progressions with $K'_a = K''_a = 1$ and either $\Delta K_c = -1$ or $\Delta K_c = 0$. The maximum total angular momentum was set to $J = 95$.

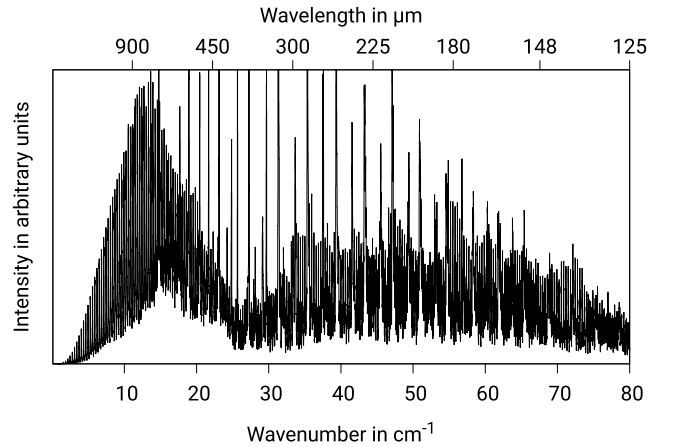


Figure 5. Infrared spectrum of the vibrational GS for propynal at $T = 300$ K. A Lorentz broadening profile for atmospheric pressure conditions was used. All calculated hot bands are included and the maximum total angular momentum was set to $J = 95$.

ν_9 increase faster than for $2\nu_9$ up to this value of J . After that, the frequencies decrease again, which shows that the rovibrational state energies belonging to the ν_9 mode increase slower than for $2\nu_9$.

Although this study has its focus on producing reference spectra relevant for the ISM, we also intend to provide a comparison for laboratory experiments at room temperature. For the two spectral regions discussed earlier, this can be seen in Figs 5 and 6. These spectra consider a pressure broadening via a Lorentz profile for a pressure of $p = 1$ bar, which is in contrast to the previously discussed stick spectra. Choosing a pure pressure broadening over a Voigt profile is a suitable approximation for a spectrum on the Earth, since the more accurate Voigt profile would be dominated by the Lorentz profile for $T = 300$ K and $p = 1$ bar.

The spectra for the two previously mentioned regions of Figs 2 and 3 shall be discussed first. After that, a comparison with an experimental spectrum is provided. In Fig. 5, it can be seen that the narrow branch on the lhs between 3 and 25 cm^{-1} is significantly more intense than the wider branch between 25 and 80 cm^{-1} . This is

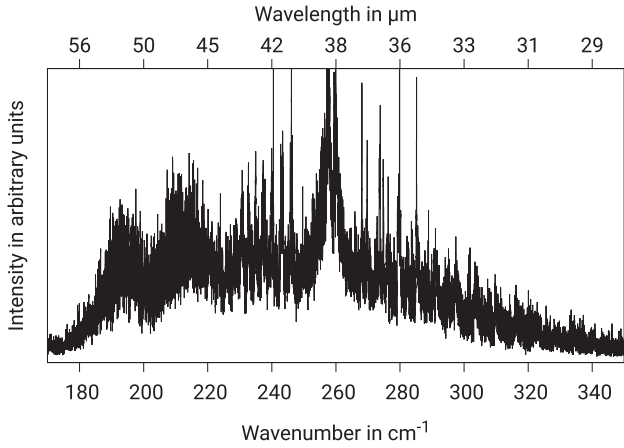


Figure 6. Infrared spectrum of propynal for the lowest excited vibrational states at $T = 300$ K. A Lorentz broadening profile for atmospheric pressure conditions was used. All calculated hot bands are included and the maximum total angular momentum was set to $J = 95$.

in contrast to the stick spectrum for $T = 300$ cm $^{-1}$ in Fig. 2. It can be explained by the much higher line density in that region. A similar effect can be found at around 233 cm $^{-1}$ in Fig. 6, where a plateau can be observed. In contrast to that, based on Fig. 3 a significant drop in intensity could be expected at that point. This is due to the already decreased intensity of the R-branch of the mode ν_9 and the hot band $2\nu_9$ and the still fairly low intensity of the P-branch of ν_{12} and the hot band $2\nu_{12}$. The overall very noisy structure of the spectrum originates in the fact that we did not include an additional broadening for a limited spectral resolution of the detector. By neglecting this effect, one yields a spectrum as it could be measured with infinite spectral resolution.

A comparison between the measured high-resolution infrared spectrum provided by McKellar (2010)¹ based on Robertson et al. (2009) and our computed results is shown in Fig. 7. The low pressure of 66.6 Pa in the experiments leads to a small Lorentz broadening and therefore a very fine structure, which is difficult to analyse for such a wide spectral range. However, the tail of the pure rotational spectrum on the left-hand side of the figure is clearly visible in both cases. This area appears to have more intensity in the experimental spectrum in comparison to the simulated one. This could be due to the fact that other experimental conditions besides the pressure, in particular the temperature, are not known to us. This limits a direct comparison and our ability to reproduce the experimental spectrum more precisely. Note that not only the intensity of the transitions depends on the temperature, but also the line broadening. Despite this limitation, the agreement between experiment and simulation is decent. Modes ν_9 and ν_{12} are clearly visible and distinguishable in the spectral region 180–330 cm $^{-1}$, although some of the details are less prominent in comparison to Fig. 6 that uses a different broadening. An obvious difference between the two spectra in Fig. 7 is the fine and extremely strong lines, which are due to water impurities in the experimental spectrum, as mentioned in McKellar (2010).

¹Reprinted from J. Mol. Spectrosc., 262, A. R. W. McKellar, High-resolution infrared spectroscopy with synchrotron sources, 1, 2010, with permission from Elsevier.

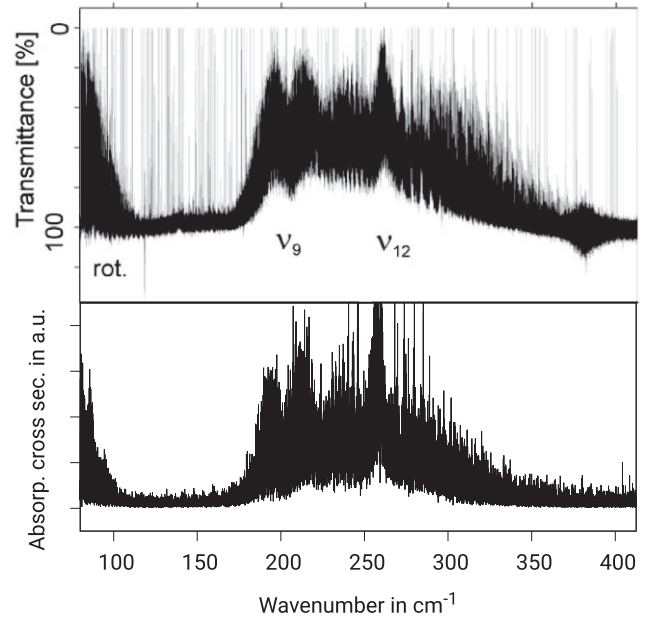


Figure 7. Comparison between an experimental¹ (upper figure) and our computed infrared spectrum (lower figure) of propynal for the lowest excited vibrational states at $T = 300$ K. A Lorentz broadening profile was used. All calculated hot bands are included and the maximum total angular momentum was set to $J = 95$.

4.4 Spectroscopic constants

Apart from comparing line lists and the visual appearance of spectra, spectroscopic constants are another way to investigate the rovibrational characteristics of molecules. By using a model Hamiltonian, they allow us to condense large line lists into a small set of well-defined molecule specific constants. We used our recent implementation in MOLPRO (Dinu et al. 2022) for determining rotational and centrifugal distortion constants. The so-called PFIT (parameter fitting) program relies on a non-linear least-squares fit exploiting a Gauss–Newton algorithm with an initial guess obtained from second-order vibrational perturbation theory (VPT2). For propynal, the majority of publications favour the A-reduced Hamiltonian over its alternative, the S-reduced Hamiltonian. Furthermore, we chose the I' orientation for this near-prolate asymmetric top molecule. We follow that choice and present our results for the PFIT method based on line lists obtained by RVC1 calculations as well as results obtained by VPT2 calculations and a comparison with the results of different experimental groups in Table 5. We like to emphasize here that the force constants as needed in VPT2 theory are retrieved from the polynomial fit of the PES rather than by calculating a true quartic force field. To produce the RVC1 line list, we used a PES relying on *ae* calculations, which is in contrast to the previous sections where the frozen core approximation was used.

In general, our computed rotational constants B and C in Table 5 match very well with experimental results. A key reason for this is the *ae* treatment, which decreases the relative error for those two constants by more than one order of magnitude in comparison to a frozen core calculation (Schneider & Rauhut 2023). In contrast to that, it decreases the agreement of the A constant slightly. This underlines the importance of high-quality electronic structure methods for the generation of the PES. For the B constant, the PFIT yields results much closer to the experiments than the VPT2

Table 5. Comparison of spectroscopic constants in MHz for the vibrational GS of propynal using Watson’s A -reduced Hamiltonian in the I' representation (1σ uncertainty in parenthesis). Values obtained by PFIT or VPT2 calculations are given for all sextic constants. Numerical sensitive values with respect to the input parameters are marked with squared brackets.

Parameter	This work, PFIT ^a	This work, VPT2 ^b	Exp. ^c	Exp. ^d	Exp. ^e
A	68 330.330(1)	68 247.00	68 035.308(25)	68 035.263(39)	68 035.299(43)
B	4826.2323(1)	4823.95	4826.288 05(97)	4826.293(6)	4826.3014(73)
C	4501.1928(1)	4498.57	4499.526 95(95)	4499.51(6)	4499.5107(69)
$10^3 \Delta_J$	1.919 69(7)	1.8758	1.9179(11)	1.913(4)	1.917(12)
$10^1 \Delta_{JK}$	−1.563 03(2)	−1.4821	−1.481 19(19)	−1.480 44(39)	−1.481 02(47)
Δ_K	8.3284(1)	8.7473	9.0033(57)	8.9926(87)	8.99124(97)
$10^4 \delta_J$	3.5178(7)	3.384	3.3742(15)	3.4564(12)	3.458(14)
$10^2 \delta_K$	3.189(4)	2.553	3.396(26)	3.47(28)	3.90(32)
$10^9 \Phi_J$	7.66(5)	6.43	7.54(21)	–	–
$10^7 \Phi_{JK}$	−1.0(2)	−4.1	−8.348(82)	−7.11(48)	−7.41(59)
$10^5 \Phi_{KJ}$	−2.08(1)	−0.827	−0.824(11)	−0.8264(12)	−0.831(13)
$10^3 \Phi_K$	1.786(3)	2.36	3.19(15)	2.36(6)	–
$10^9 \phi_J$	[1.51(4)]	[2.27]	–	–	–
$10^8 \phi_{JK}$	[6.2(28)]	[18.0]	–	–	–
$10^5 \phi_K$	[9.29(41)]	[10.36]	–	–	–

^a Theoretical results of RVC1 and PFIT calculations obtained by MOLPRO.

^b Theoretical results of VPT2 calculations based on a multidimensional ae PES.

^c Experimental coherent synchrotron radiation Fourier transform spectrometry values taken from Barros et al. (2015).

^d Experimental gas phase values taken from McKellar et al. (2008).

^e Experimental gas phase values taken from Winnewisser (1973).

calculation. This is in contrast to the A constant. However, for the C constant both theoretical methods produce a fairly similar deviation. A similar result can be found for the quartic constants. For three parameters, the VPT2 method yields better results and for two constants the PFIT based on RVC1 line list is closer to the experiment.

The different sets of experimental reference data were obtained from different numbers of fitting parameters for the sextic constants. Since the fitting processes for the individual constants are not independent, a change in the number of parameters influences the other constants as well. However, for the quadratic constants A , B , and C this effect can be neglected without introducing substantial errors as they are several orders of magnitudes larger than the sextic constants. Even for the quartic constants, this effect is rather small. However, for the sextic constants the different numbers of fitting parameters can be one reason for the deviation between the experiments. Since we decided to fit all parameters in our simulation, the results are again not completely comparable. Although the uncertainties for these values are higher – thus they are marked by squared brackets – we found it important to provide at least crude estimates for the last three sextic constants.

By comparing the results of our two theoretical methods for the sextic constants, it can be seen that the deviation is larger than for the other constants. This is not surprising, since the absolute values of these parameters are much smaller and therefore they require a much higher accuracy for the state energies or transition frequencies. However, for the majority of cases a good agreement between one of our theoretical methods and at least one of the experiments can be found: (a) The Φ_K constants obtained by the VPT2 calculations and the measurements of McKellar et al. (2008) match nicely. (b) The results of the PFIT method for the Φ_J constants are in good agreement with Barros et al. (2015). (c) The Φ_{KJ} constant obtained by the VPT2 method agrees with all experimental values. However, without any prior information and only one of the theoretical methods, it is hardly possible to predict reliable results for the sextic constants.

5 CONCLUSIONS

The rotational, vibrational, and rovibrational spectra of propynal have been studied by high-level *ab initio* methods for the first time. A multidimensional PES based on explicitly correlated coupled-cluster calculations and being represented by an n -mode expansion up to fourth order has been used within all calculations. VCI and RVC1 theories have been used for the determination of rovibrational frequencies and intensities. The simulations rely on our previously published implementations in the MOLPRO package.

Within this work, we were able to confirm previous experimental findings for the geometrical parameters. Moreover, we provided theoretical values for the transition frequencies of all vibrational fundamental bands. This allowed us to resolve a conflict in the assignment of the fundamentals ν_7 and ν_{11} in previous publications. 40 additional vibrational transition frequencies were determined, the majority of which are documented in literature for the first time. These calculations made it possible to confirm a Fermi resonance between ν_2 and $2\nu_5$. We also provided partition function values in a temperature range from interstellar conditions up to room temperature. Moreover, the low-frequency spectrum up to 350 cm^{-1} has been analysed, which allowed us to study the temperature-dependent effect of hot bands for propynal. A comparison with an experimental infrared spectrum is provided for the spectral range of $80\text{--}410 \text{ cm}^{-1}$ including the vibrational modes ν_9 and ν_{12} . Our spectroscopic constants are in good agreement with the previously known experimental measurements for the quadratic, quartic, and a few of the sextic parameters. However, it remains challenging to achieve the experimental accuracy for this particular rovibrational quantity.

ACKNOWLEDGEMENTS

We thank the Deutsche Forschungsgemeinschaft (DFG) (project Ra 656/23-3) and the Studienstiftung des Deutschen Volkes for financial support. The authors acknowledge support by the state of Baden–Württemberg through bwHPC and the DFG through grant no. INST 40/575-1 FUGG (JUSTUS 2 cluster).

DATA AVAILABILITY

The data that support the findings of this study, i.e. PESs and line lists, are available online on the Zenodo data base (<https://www.doi.org/10.5281/zenodo.7440037>).

REFERENCES

- Barros J., Appadoo D., McNaughton D., Robertson E., Medcraft C., Plathe R., Roy P., Manceron L., 2015, *J. Mol. Spectrosc.*, 307, 44
- Bowman J. M., Christoffel K., Tobin F., 1979, *J. Phys. Chem.*, 83, 905
- Bowman J. M., Carrington T., Jr, Meyer H. D., 2008, *Mol. Phys.*, 106, 2145
- Brand J. C. D., Watson J. K. G., 1960, *Trans. Faraday Soc.*, 56, 1582
- Brand J. C. D., Callomon J. H., Watson J. K. G., 1963, *Discuss. Faraday Soc.*, 35, 175
- Carter S., Bowman J. M., Handy N. C., 2012, *Mol. Phys.*, 110, 775
- Carter S., Wang Y., Bowman J. M., 2017, *J. Phys. Chem. A*, 121, 1616
- Christoffel K. M., Bowman J. M., 1982, *Chem. Phys. Lett.*, 85, 220
- Clark V. H. J., Owens A., Tennyson J., Yurchenko S. N., 2020, *J. Quant. Spectrosc. Radiat. Transfer*, 246, 106929
- Costain C. C., Morton J. R., 1959, *J. Chem. Phys.*, 31, 389
- Czakó G., Mátys E., Császár A. G., 2009, *J. Phys. Chem. A*, 113, 11665
- Dinu D. F., Ziegler B., Podewitz M., Liedl K. R., Loerting T., Grothe H., Rauhut G., 2020, *J. Mol. Spectrosc.*, 367, 111224
- Dinu D. F., Tschöpe M., Schröder B., Liedl K. R., Rauhut G., 2022, *J. Chem. Phys.*, 157, 154107
- Dunham T., Jr, 1937, *Publ. Astron. Soc. Pac.*, 49, 26
- Endres C. P., Schlemmer S., Schilke P., Stutzki J., Müller H. S. P., 2016, *J. Mol. Spectrosc.*, 327, 95
- Erfort S., Tschöpe M., Rauhut G., Zeng X., Tew D. P., 2020a, *J. Chem. Phys.*, 152, 174306
- Erfort S., Tschöpe M., Rauhut G., 2020b, *J. Chem. Phys.*, 152, 244104
- Erfort S., Tschöpe M., Rauhut G., 2022, *J. Chem. Phys.*, 156, 124102
- Ferenc D., Matyus E., 2019, *Mol. Phys.*, 117, 1694
- Herbst E., van Dishoeck E. F., 2009, *ARA&A*, 47, 427
- Hollis J., Jewell P., Lovas F., Remijan A., Møllendal H., 2004, *ApJ*, 610, L21
- Howe J. A., Goldstein J. H., 1955, *J. Chem. Phys.*, 23, 1223
- Howe J. A., Goldstein J. H., 1958, *J. Am. Chem. Soc.*, 80, 4846
- Hudson R. L., Gerakines P. A., 2018, *MNRAS*, 482, 4009
- Irvine W. M. et al., 1988, *ApJ*, 335, L89
- Jabri A., Kolesniková L., Alonso E., León I., Mata S., Alonso J., 2020, *J. Mol. Spectrosc.*, 372, 111333
- Jaman A., Bhattacharya R., Mandal D., Das A. K., 2011, *J. At. Mol. Phys.*, 2011, 439019
- Jones H., 1980, *J. Mol. Spectrosc.*, 81, 21
- King G., Moule D., 1961, *Spectrochim. Acta A*, 17, 286
- McGuire B. A., 2018, *ApJ*, 239, 17
- McKellar A., 1940, *PASP*, 52, 187
- McKellar A. R. W., 2010, *J. Mol. Spectrosc.*, 262, 1
- McKellar A. R. W., Watson J. K. G., Chu L.-K., Lee Y.-P., 2008, *J. Mol. Spectrosc.*, 252, 230
- Margulès L., McGuire B. A., Evans C. J., Motiyenko R. A., Remijan A., Guillemin J. C., Wong A., McNaughton D., 2020, *A&A*, 642, A206
- Mathea T., Rauhut G., 2021, *J. Comp. Chem.*, 42, 2321
- Mathea T., Petrenko T., Rauhut G., 2022, *J. Comp. Chem.*, 43, 6
- May A. J., Manby F. R., 2004, *J. Chem. Phys.*, 121, 4479
- Müller H. S. P., Thorwirth S., Roth D. A., Winniewisser G., 2001, *A&A*, 370, L49
- Müller H. S. P., Schlöder F., Stutzki J., Winniewisser G., 2005, *J. Mol. Struct.*, 742, 215
- Neff M., Rauhut G., 2009, *J. Chem. Phys.*, 131, 124129
- Nikitin A. V., Rey M., Tyuterev V. G., 2017, *J. Quant. Spectrosc. Radiat. Transfer*, 200, 90
- Ohishi M., 2019, in Yamagishi A., Kakegawa T., Usui T., eds, *Astrobiology: From the Origins of Life to the Search for Extraterrestrial Intelligence*. Springer, Singapore, p. 11
- Ohishi M., Kaifu N., 1998, *Discuss. Faraday Soc.*, 109, 205
- Peterson K. A., Adler T. B., Werner H.-J., 2008, *J. Chem. Phys.*, 128, 084102
- Petrenko T., Rauhut G., 2017, *J. Chem. Phys.*, 146, 124101
- Pfeiffer F., Rauhut G., 2014, *J. Chem. Phys.*, 140, 064110
- Pflüger K., Paulus M., Jagiella S., Burkert T., Rauhut G., 2005, *Theor. Chem. Acc.*, 114, 327
- Rauhut G., 2004, *J. Chem. Phys.*, 121, 9313
- Rey M., Nikitin A. V., Tyuterev V. G., 2017, *ApJ*, 847, 105
- Robertson E., Appadoo D., Thompson C., McNaughton D., Metha G., 2009, *Fifth Int. Conf. Adv. Vib. Spectrosc.*
- Santa Daria A. M., Avila G., Matyus E., 2021, *J. Chem. Phys.*, 154, 224302
- Sarka J., Petty C., Poirier B., 2019, *J. Chem. Phys.*, 151, 174304
- Schneider M., Rauhut G., 2023, *J. Comput. Chem.*, 44, 298
- Schröder B., Rauhut G., 2022, in Bowman J. M., ed., *Vibrational Dynamics of Molecules*. World Scientific, Singapore, p. 1
- Simmons J., Wang X.-G., Carrington T. J., 2019, *J. Phys. Chem. A*, 123, 10281
- Smydke J., Fabri C., Sarka J., Császár A. G., 2019, *Phys. Chem. Chem. Phys.*, 21, 3453
- Swings P., Rosenfeld L., 1937, *ApJ*, 86, 483
- Takami M., Shimoda K., 1976, *J. Mol. Spectrosc.*, 59, 35
- Theule P., Borget F., Mispelaer F., Danger G., Duvernay F., Guillemin J. C., Chiavassa T., 2011, *A&A*, 534, A64
- Tobias R., Furtenbacher T., Tennyson J., Császár A. G., 2019, *Phys. Chem. Chem. Phys.*, 21, 3473
- Tschöpe M., Rauhut G., 2022, *J. Chem. Phys.*, 157, 234105
- Tschöpe M., Schröder B., Erfort S., Rauhut G., 2021, *Frontiers Chem.*, 8, 623641
- Turner B., 1991, *ApJ*, 76, 617
- Tyuterev V. G., Barbe A., Jacquemart D., Janssen C., Mikhailenko S. N., Starikova E. N., 2019, *J. Chem. Phys.*, 150, 184303
- Wang X.-G., Carrington T., Jr, 2013, *Mol. Phys.*, 111, 2320
- Watson J. K. G., 1968, *Mol. Phys.*, 15, 479
- Winniewisser G., 1973, *J. Mol. Spectrosc.*, 46, 16
- Woon D. E., 2002, *ApJ*, 571, L177
- Yachmenev A., Yurchenko S. N., Ribeyre T., Thiel W., 2011, *J. Chem. Phys.*, 135, 074302
- Yachmenev A., Polyak I., Thiel W., 2013, *J. Chem. Phys.*, 139, 204308
- Yurchenko S. N., Amundsen D. S., Tennyson J., Waldmann I. P., 2017, *A&A*, 605, A65
- Ziegler B., Rauhut G., 2016, *J. Chem. Phys.*, 144, 114114
- Ziegler B., Rauhut G., 2018, *J. Chem. Phys.*, 149, 164110
- Ziegler B., Rauhut G., 2019, *J. Phys. Chem. A*, 123, 3367

SUPPORTING INFORMATION

Supplementary data are available at *MNRAS* online.

Please note: Oxford University Press is not responsible for the content or functionality of any supporting materials supplied by the authors. Any queries (other than missing material) should be directed to the corresponding author for the article.

This paper has been typeset from a $\text{\TeX}/\text{\LaTeX}$ file prepared by the author.

Publication 4: Spectroscopic characterization of
diazophosphane - a candidate for astrophysical
observations



Spectroscopic Characterization of Diazophosphane—A Candidate for Astrophysical Observations

Martin Tschöpe¹ and Guntram Rauhut¹

Institute for Theoretical Chemistry, University of Stuttgart, Pfaffenwaldring 55, Stuttgart, D-70569, Germany

Received 2023 February 16; revised 2023 March 30; accepted 2023 March 30; published 2023 May 18

Abstract

Quite recently, diazophosphane, $\text{HP-N}\equiv\text{N}$, was synthesized for the first time. This was accomplished by a reaction of PH_3 with N_2 under UV irradiation at 193 nm. As these two molecules have been observed in different astrophysical environments, as for example, in the circumstellar medium and, in particular, in the AGB star envelope IRC+10216, the question arises whether HPN_2 can be found as well. So far there is only the aforementioned experimental work, but neither rotational nor rovibrational data are available. Hence, the lack of accurate line lists, etc. to identify diazophosphane is the subject of this work, including a detailed analysis of the rotational, vibrational, and rovibrational properties for this molecule. Our calculations rely on multidimensional potential energy surfaces obtained from explicitly correlated coupled-cluster theory. The (ro)vibrational calculations are based on related configuration interaction theories avoiding the need for any model Hamiltonians. The rotational spectrum is studied between $T = 10$ and 300 K. In contrast, the partition functions for HPN_2 and DPN_2 are given and compared for temperatures up to 800 K. In addition, more than 70 vibrational transitions are calculated and analyzed with respect to resonances. All these vibrational states are considered within the subsequent rovibrational calculations. This allows for a detailed investigation of the infrared spectrum up to 2700 cm^{-1} including rovibrational couplings and hot bands. The results of this study serve as a reference and allow, for the first time, for the identification of diazophosphane, for example, in one of the astrophysical environments mentioned above.

Unified Astronomy Thesaurus concepts: Computational methods (1965); Spectral line identification (2073); Asymptotic giant branch stars (2100); Molecular data (2259); Molecular spectroscopic constants (2260); Infrared spectroscopy (2285)

1. Introduction


Since the first molecule was detected in the interstellar medium in 1937 (Dunham 1937; Swings & Rosenfeld 1937; McKellar 1940) more than 200 molecular species have been observed in the circumstellar or interstellar media (Müller et al. 2001, 2005; Endres et al. 2016; McGuire 2018). Two of these molecules are molecular nitrogen (N_2) and phosphane (PH_3). It was only in 2004, when Knauth et al. (2004) identified N_2 in the surroundings of HD 124314. Four years later, PH_3 was discovered simultaneously and independently by Agúndez et al. (2008) and Tenenbaum & Ziurys (2008).

Quite recently, Lu et al. (2022) were able to synthesize diazophosphane, $\text{HP-N}\equiv\text{N}$, for the first time. Moreover they analyzed its vibrational fundamental bands at 10 K. They obtained this species from the reaction of PH_3 with N_2 upon irradiation with UV-light at 193 nm. Since both molecules and the UV radiation are present in the circumstellar medium and can even be found in the envelope of the same AGB star IRC+10216 (Cherchneff 2012; Agúndez et al. 2014), the question arises whether HPN_2 can be found under similar conditions as well. To solve this question, highly accurate rotational, vibrational, and rovibrational spectra are of particular importance.

Although there are some studies about HPN_2 in the solid state (Ghellab et al. 2019) or as a crystalline powder (Schnick & Lücke 1992; Jacobs et al. 1997), these works refer to the

isomeric form of $\text{P} = \text{N}(\text{NH})$. In contrast to that, we focus on the isomer $\text{HP-N}\equiv\text{N}$, which was so far only synthesized by Lu et al. (2022), as mentioned before. These authors also provide experimental frequencies for four of the six fundamental vibrational modes as well as one overtone. Additionally, they provide theoretical results for all fundamental bands and the same overtone. Other than that, no simulations of HPN_2 exist. For this reason, the demand for line lists, microwave and infrared spectra, geometrical parameters, partition functions, etc. is largely unsatisfied. This issue will be tackled within this work.

During recent decades, various approaches avoiding the need for model Hamiltonians have been developed to investigate rotational, vibrational, and rovibrational spectra by the groups of Yachmenev et al. (2011) (Yachmenev et al. 2013; Yurchenko et al. 2017; Clark et al. 2020), Nikitin et al. (2017) (Rey et al. 2017; Tyuterev et al. 2019), Carter et al. (2012) (Carter et al. 2017), Rauhut (2004) (Tschöpe et al. 2021), Smydke et al. (2019) (Ferenc & Matyus 2019; Tobias et al. 2019; Santa Daria et al. 2021), and many more (Wang & Carrington 2013; Sarka et al. 2019; Simmons et al. 2019). Some of these are based on the seminal work of Watson (1968), introducing the respective Hamiltonian. Subsequently, vibrational configuration interaction (VCI) theory (Bowman et al. 1979; Christoffel & Bowman 1982; Neff & Rauhut 2009; Pfeiffer & Rauhut 2014; Schröder & Rauhut 2022) was introduced for nonrotating molecules and after that rovibrational configuration interaction (RVCI) theory (Erfort et al. 2020a, 2020b, 2022) for the simulation of rotating molecules. These approaches rely on high-level potential energy surfaces

 Original content from this work may be used under the terms of the [Creative Commons Attribution 4.0 licence](https://creativecommons.org/licenses/by/4.0/). Any further distribution of this work must maintain attribution to the author(s) and the title of the work, journal citation and DOI.

(PESs) (Ziegler & Rauhut 2016, 2018, 2019) for the efficient calculation of rovibrational line lists and spectra for semirigid molecules. The two main limitations for these methods are, that they lose much of their efficiency for vibrational modes with large deflections, i.e., for floppy molecules. Hence this method is very suitable for our application, since HPN₂ is a semirigid system.

In this work, we use high-level multidimensional PESs, VCI, and RVCI calculations, as implemented in the MOLPRO (Werner et al. 2020) package of ab initio programs, to determine the rovibrational spectrum of diazophosphane. Moreover, geometrical parameters as well as values for the partition functions at temperatures between 10 and 800 K will be presented. In addition, microwave and infrared spectra, vibrational line lists, and spectroscopic constants will be provided accompanied by a discussion about the influence of hot bands on the simulated spectra at different temperatures. These calculations were carried out for both HPN₂ and its deuterated isotopologue, DPN₂.

2. Theory

2.1. Rovibrational Energies

The implementation of VCI theory used in this work is based on the Watson Hamiltonian for nonrotating molecules H_{vib} , while the implementation of RVCI theory is based on the Watson Hamiltonian for rotating molecules:

$$H = \underbrace{\frac{1}{2} \sum_{\alpha\beta} \pi_{\alpha} \mu_{\alpha\beta} \pi_{\beta} - \frac{1}{2} \sum_i \frac{\partial^2}{\partial q_i^2} - \frac{1}{8} \sum_{\alpha} \mu_{\alpha\alpha}}_{H_{\text{vib}}} + V(\mathbf{q}) + \underbrace{\frac{1}{2} \sum_{\alpha\beta} \mu_{\alpha\beta} J_{\alpha} J_{\beta}}_{H_{\text{rot}}} - \underbrace{\frac{1}{2} \sum_{\alpha\beta} (J_{\alpha} \mu_{\alpha\beta} \pi_{\beta} + \pi_{\alpha} \mu_{\alpha\beta} J_{\beta})}_{H_{\text{rv}}} \quad (1)$$

The use of the Born–Oppenheimer approximation yields the PES, V , depending on the normal coordinates q_i . Equation (1) also depends on the Cartesian components of the angular momentum operator, J_{α} , and the vibrational angular momentum (VAM) operator

$$\pi_{\alpha} = -i \sum_{jk} \zeta_{jk}^{\alpha} q_j \frac{\partial}{\partial q_k}. \quad (2)$$

Thereby ζ_{jk}^{α} corresponds to an element of the antisymmetric Coriolis ζ -constant tensor, with Cartesian elements $\alpha, \beta \in \{x, y, z\}$. For the following discussion, it is favorable to split the Watson Hamiltonian in the following three parts: the pure vibrational term H_{vib} , the rotational term H_{rot} , and the Coriolis-coupling term H_{rv} . The inverse of the effective moment of inertia tensor is denoted by μ , see Watson (1968). Both, μ and the potential V , rely on an n -mode expansion (Bowman et al. 2008) and an analytic sum-of-products representation being obtained from efficient Kronecker product fitting (Ziegler & Rauhut 2016). In order to obtain rovibrational energies and intensities, a two-step process is used. First, the Schrödinger equation for the Hamiltonian of a nonrotating molecule H_{vib} is solved by VCI theory, yielding pure vibrational energies and the corresponding wave functions:

$$|\Phi_v\rangle = \sum_I c_I |\phi_v^I\rangle. \quad (3)$$

To determine the vibrational wave functions $|\Phi_v\rangle$ in a compact form, an initially large number of Hartree products $|\phi_v^I\rangle$ (configurations) is screened within a configuration-selective VCI approach (Mathea & Rauhut 2021; Mathea et al. 2022).

Second, the Schrödinger equation for the Hamiltonian of rotating molecules (see Equation (1)) is solved by RVCI theory. The basis functions are provided by a direct product of the VCI wave functions and pure rotational basis functions $|\Phi_r\rangle$. This yields rovibrational wave functions of the form:

$$|\Psi_{rv}\rangle = \sum_{rv} c_{rv} |\Phi_r\rangle |\Phi_v\rangle. \quad (4)$$

Within this work, molecule-specific rotational basis (MSRB) functions for $|\Phi_r\rangle$ have been employed, as they allow for a particular robust quantum number assignment. The MSRB is a linear combination of Wang combinations (Špirko et al. 1985) and is determined by solving the rotational Schrödinger equation for the vibrational ground state (Erfort et al. 2020a).

2.2. Infrared Intensities

Rovibrational infrared line intensities can be obtained by

$$I = \frac{2\pi^2 N_A}{3\epsilon_0 h^2 c^2} \frac{e^{-E''/kT} (1 - e^{-(E' - E'')/kT})}{Q(T)} (E' - E'') R. \quad (5)$$

They depend on a prefactor consisting of natural and physical constants, the square of the transition moment R and a temperature-dependent prefactor, describing the thermal occupation of the rovibrational states involved in the transition. The energies of the initial and final states are given by E'' and E' , respectively. The rovibrational partition function $Q(T)$ depends on the temperature and can be computed by

$$Q(T) = \sum_{rv} g_{rv} e^{-E_{rv}/k_B T}, \quad (6)$$

where the summation considers all rovibrational states rv . E_{rv} denotes the corresponding energies and g_{rv} the corresponding degeneracies. The latter is a product of the nuclear spin statistical weight (NSSW) g_{ns} and the degeneracy factor $2J + 1$ originating in the absence of electric and magnetic fields. Since diazophosphane shows C_s symmetry, the two NSSWs are identical, with a value of 36 for HPN₂ and 54 for DPN₂.

2.3. Computational Details

To determine the equilibrium geometry, the harmonic frequencies as well as the corresponding normal coordinates for diazophosphane, explicitly correlated coupled-cluster theory including single and double excitations, and a perturbative treatment of the triple excitations, CCSD(T)-F12b has been used (Adler et al. 2007). Two PESs have been calculated for each of the isotopologues. The first PES uses the frozen core (fc) approximation, which relies on error compensation with respect to neglected contributions to the electronic energy, as for example, relativistic effects, diagonal Born–Oppenheimer corrections, high-order coupled-cluster terms, and core-correlation contributions. This error compensation usually leads to nicely matching vibrational frequencies in comparison to experimental results. For this reason, this approximation is often used to calculate rovibrational line lists, spectra, and partition functions. The second PES was obtained by all-electron (ae) correlation calculations, which

explicitly account for core–core and core–valence interactions, since the work of Schneider & Rauhut (2022) has shown, that at least for the determination of spectroscopic constants this approach leads to slightly better results. In most of our analyses, we compare the results obtained from these two different PESs to narrow the range where experimental values could be expected.

While in the work of Lu et al. (2022), an orbital basis set of triple- ζ quality, i.e., cc-pVTZ-F12 (Peterson et al. 2008) was used, slightly larger orbital bases of quadruple- ζ quality, i.e., cc-pVQZ-F12 and cc-pcVQZ-F12, have been employed here. The all-electron explicitly correlated coupled-cluster calculations require an adjustment of the different γ exponents for the Slater geminal functions as recommended by May & Manby (2004). Consequently, the core–core, core–valence, and valence–valence orbital pair values were set to 0.8, 1.7, and 2.2, respectively. In contrast to that, a common exponent of $\gamma = 1.0$ was used within the frozen core calculations. Moreover, the complementary auxiliary basis set correction was added to the total energies (Adler et al. 2007; Knizia & Werner 2008).

All multidimensional PESs were represented by an n -mode expansion truncated after the four-mode coupling terms (Bowman et al. 2008). A multilevel scheme, as introduced by Pflüger et al. (2005), has been used throughout the calculations. More precisely, the 1D and 2D surfaces have been calculated at the same level of accuracy that was used for the determination of the equilibrium geometry and harmonic frequencies. In contrast, for the 3D and 4D contributions, a smaller basis set of triple- ζ quality has been used. A likewise multilevel scheme, but being based on calculations using the distinguishable clusters (DCSD) approximation (Kats & Manby 2013), has been used for determining the dipole moment surface (DMS). Runtime savings due to symmetry have been exploited twofold: within the electronic single point calculations and for the terms of the n -mode expansion (Ziegler & Rauhut 2018). The grid representations of the multidimensional surfaces have been transformed by Kronecker product fitting to an analytical sum-of-products representation based on nine monomials per mode.

Vibrational wave functions have been obtained from state-specific configuration-selective VCI theory (Mathea & Rauhut 2021; Mathea et al. 2022; Schröder & Rauhut 2022). The basis set used in these calculations is symmetry adapted and relies on Hartree products (configurations) being generated from one-mode wave functions (modals), which have been determined from ground-state based vibrational self-consistent field (VSCF) theory. A set of 18 mode-specific distributed Gaussians and a constant μ -tensor has been used within the VSCF calculations. The correlation space within the VCI calculations has been restricted twofold: The maximum number of vibrational quantum numbers was set to 15 and a maximum excitation per mode up to the sixth root was used. Moreover, the maximum number of simultaneously excited modes was chosen to be six, so there is no restriction in this respect. All these values do not refer to the ground state, but are relative to the leading configuration of the vibrational state of interest. This resulted in about 3×10^4 configurations per irreducible representation and thus we consider the final VCI results to be close to the full VCI limit. A μ -tensor expansion up to first order was used for the diagonal elements of the VCI matrix. In contrast, all other matrix elements are limited to a constant μ -tensor. A residuum based eigenvalue

solver (RACE) has been employed for the determination of the eigenenergies of predefined states (Petrenko & Rauhut 2017).

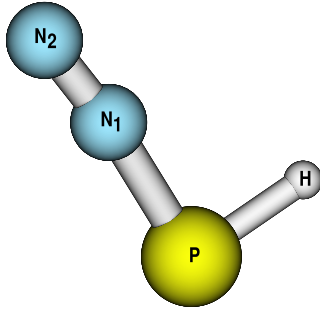
The RVCIs calculations use a maximum angular momentum number of $J_{\max} = 75$ for the calculations of the line list and $J_{\max} = 100$ for the determination of the partition function. A temperature range of 10–300 K has been chosen for the rovibrational spectra, while the partition functions are provided for temperatures up to 800 K. This covers the experimental conditions of Lu et al. (2022; 10 K), terrestrial conditions for further lab experiments and some astrophysical areas, for example the outer regions of the circumstellar medium. The latter have been determined from a sum of RVCIs state energies, i.e., no separability approximation has been used. For the evaluation of the rotational integrals originating from the Watson Hamiltonian, a second-order μ -tensor is used, while a first order μ -tensor is used for the Coriolis-coupling contributions. Based on a similar convergence analysis as shown in our previous work (Tschöpe & Rauhut 2022) these truncations of the n -mode expansions appear to be justified.

The rovibrational basis functions are provided by a direct product of VCI wave functions and molecule-specific rotational basis (MSRB) functions (see Equation (4)), as explained in detail by Erfort et al. (2020a). The basis set size for the vibrational subspace was limited by two criteria: the maximum vibrational transition frequency was chosen to be smaller than 5000 cm^{-1} and the maximum sum of vibrational quantum numbers was set to be less than 4. This yields $N_{\text{vib}} = 73$ vibrational states for HPN₂ and $N_{\text{vib}} = 80$ states for DPN₂. Since the maximum size of the rotational basis set is given by $2J_{\max} + 1 = 151$ for the calculation of rovibrational spectra, the largest matrix is of size $N_{\text{rovib}} = 12,080$. For HPN₂, the resulting wall clock time for the combined VCI and RVCIs calculations was ≈ 33 hr on six CPU (central processing units) cores. While the VCI calculations contributed less than 1% and the calculation of the RVCIs energies and wave functions about 15%, most of the time is spent for the calculation of the RVCIs intensities. For DPN₂, longer calculation times by about 50% were needed due to the larger number of vibrational basis functions, which increases the CPU time in two ways: by a larger number of rovibrational transitions and larger RVCIs wave function vectors. Within the RVCIs calculations, ≈ 50 million transitions for HPN₂ and ≈ 100 million transitions for DPN₂ have been considered. The printout was filtered to $\approx 161,000$ and $\approx 404,000$ transitions for HPN₂ and DPN₂, respectively. The main selection criterion was an intensity of at least 10^{-4} relative to the strongest transition in the spectrum for $T = 300 \text{ K}$.

3. Results and Discussion

3.1. Geometrical Parameters

Calculated geometrical parameters are presented in Figure 1. Parameters obtained by Born–Oppenheimer equilibrium geometries are denoted r_e . Since the equilibrium geometry is not affected by deuteration, this column is not explicitly given for DPN₂. In addition, two different types of vibrationally averaged geometrical parameters, r_a and r_g , are provided. Averaging the atomic positions over the VCI ground-state wave function yields the former. The latter uses the expectation value of the bond lengths expressed in normal coordinates to calculate instantaneous internuclear distances. It is well known (Czakó et al. 2009; Dinu et al. 2020; Tschöpe et al. 2021;



Coord.	fc						ae		
	HPN ₂			DPN ₂			HPN ₂		
	r _e	r _a	r _g	r _a	r _g	r _e	r _a	r _g	
r(N ₂ N ₁)	1.126	1.125	1.130	1.125	1.130	1.123	1.123	1.128	
r(N ₁ P)	1.698	1.706	1.708	1.706	1.708	1.692	1.700	1.702	
r(PH)	1.415	1.428	1.436	1.424	1.429	1.412	1.425	1.432	
α(N ₂ N ₁ P)	173.8	173.8		173.9		173.8	173.9		
α(N ₁ PH ₁)	88.8	89.0		88.9		88.8	89.0		

Figure 1. Computed Geometrical Parameters of Diazophosphane Bond lengths are given in Å and angles are given in degrees. Comparison between explicitly correlated coupled-cluster surfaces CCSD(T)-F12b based on the frozen core (fc) approximation with a cc-pVQZ-F12 basis set and all-electron (ae) correlation calculations with a cc-pcVQZ-F12 basis set. For DPN₂, equilibrium geometries are not explicitly given since they are identical for both isotopologues.

Tschöpe & Rauhut (2023) that these two approaches can yield significantly different results. Compared to these previous works, this effect is smaller for diazophosphane than for other molecules. This is not surprising, as the largest differences were observed for CH bond lengths (Tschöpe et al. 2021; Tschöpe & Rauhut 2023), which are not present in diazophosphane. However, the largest absolute difference between r_a and r_g was again found for the bond involving hydrogen, i.e., $\Delta r(\text{PH}) = 0.008$ Å. Comparing the results for HPN₂ and DPN₂ shows, on the one hand, that obviously the bond length $r(\text{PH})$ and $r(\text{PD})$, respectively, changes the most, but also that the angle involving water $\alpha(\text{N}_1\text{PH}_1)$ changes only marginally. Figure 1 also provides a comparison between calculations based on a PES relying on the frozen core approximation (fc) and another PES relying on all-electron (ae) correlation calculations. The difference between fc and ae calculations varies between 0.002 and 0.006 Å, with an expected and systematic trend toward smaller bond lengths for the ae calculations.

3.2. Partition Function

As mentioned before, the partition function has been determined by direct summation. A temperature range between 10 and 800 K has been chosen in order to consider a variety of astrophysical areas, the experimental conditions of Lu et al. (2022), and terrestrial conditions for further lab experiments. The results for both isotopologues of diazophosphane can be found in Table 1 and in Figure 2. The double logarithmic plot shows the same near-linear behavior as previously observed for other molecules (Martin et al. 1992; Harris et al. 1998; Vidler & Tennyson 2000). Up to a temperature of ≈ 300 K, the trend is almost exactly linear. However, at 300 K, a small increase in the slope arises. As discussed by Amyay et al. (2011), this effect can be caused by an increased state density, e.g., due to thermal occupation of excited vibrational bands, while a not properly converged summation would lead to a decreasing slope. The partition function for DPN₂ is about a factor of 2.1 larger than for HPN₂. The fact that the NSSWs of DPN₂ are 1.5 times larger than for HPN₂, explains some part of this effect. Moreover, due to the higher mass of DPN₂ the state energies decrease and thus show higher occupations for a fixed temperature, as can be seen from Equation (6).

3.3. Vibrational Transitions

Within our RVCi calculations, we considered 73 vibrational states for HPN₂ and 80 for DPN₂. The results for the

Table 1
Partition Functions for HPN₂ and DPN₂ for Different Temperatures

T (K)	Q	
	HPN ₂	DPN ₂
5	7.34×10^2	1.53×10^3
10	2.05×10^3	4.37×10^3
20	5.83×10^3	1.24×10^4
35	1.35×10^4	2.87×10^4
50	2.31×10^4	4.90×10^4
75	4.25×10^4	9.03×10^4
100	6.59×10^4	1.40×10^5
150	1.27×10^5	2.72×10^5
200	2.15×10^5	4.64×10^5
300	5.15×10^5	1.14×10^6
500	1.97×10^6	4.38×10^6
800	7.26×10^6	1.60×10^7

Note. RVCi calculations are based on a PES using the frozen core approximation because it yields vibrational frequencies closer to potential experimental results.

fundamental bands and overtones for both isotopologues are shown in Table 2. Results for combination bands are given in the supplementary material. As has been explained before, we provide a comparison between calculations based on a PES relying on the frozen core (fc) approximation and an all-electron (ae) correlation PES. As expected and previously observed for other molecules, the deviations between fc and ae results are smaller for fundamental bands than for overtones. Moreover, the relative deviations in the intensities are relatively small in most cases, except for $2\nu_2$, for which the all-electron calculation yields an approximately 50% higher intensity. Comparing our simulated results with the experimental results of Lu et al. (2022) shows a slightly better agreement with the frozen core calculation frequencies. However, the standard deviation is fairly high due to outliers and the small sample size of only five transitions. Moreover, it should be considered that Lu et al. (2022) used matrix spectroscopy, whereas our simulations refer to the gas phase.

Comparing the frequencies of the fundamental bands of HPN₂ and DPN₂ shows the expected strong deuteration effects for the H–P stretching and bending modes. Note that ν_1 is the H–P stretching mode for HPN₂ and ν_2 is the N≡N stretching mode. This is reversed for DPN₂, which can easily be seen by considering the intensities. Moreover, the H–P bending mode, ν_3 , is shifted by about 220 cm^{-1} and loses about 50% of its

Table 2
Vibrational Fundamental Bands and Overtones of Diazophosphane

Band	Irrep	HPN ₂				DPN ₂			
		ν		Ref. 1	I		ν	I	
		fc	ae		fc	ae			fc
ν_1	A'	2315.2	2320.0	2322.1	35.7	37.2	2030.3	467.4	
ν_2	A'	2030.0	2036.5	2022.7	469.9	471.3	1682.7	18.0	
ν_3	A'	934.3	938.9	935.2	16.2	16.4	712.4	8.2	
ν_4	A'	576.9	580.5	574.4	24.8	24.5	575.7	25.0	
ν_5	A''	440.8	443.7	n.o.	1.9	1.9	433.8	1.9	
ν_6	A'	354.0	356.5	n.o.	2.3	2.3	333.2	2.2	
$2\nu_1$	A'	4545.6	4555.1	n.o.	0.1	0.1	4029.6	3.1	
$2\nu_2$	A'	4030.8	4042.6	4045.4	2.2	3.2	3322.5	0.1	
$2\nu_3$	A'	1866.2	1874.6	n.o.	0.2	0.2	1424.4	0.1	
$2\nu_4$	A'	1135.6	1142.7	n.o.	0.0	0.0	1133.7	0.0	
$2\nu_5$	A'	880.3	886.0	n.o.	1.1	1.1	866.5	1.1	
$2\nu_6$	A'	705.7	710.7	n.o.	1.3	1.3	665.8	1.1	
$3\nu_3$	A'	2794.2	2806.1	n.o.	0.0	0.0	2134.9	0.0	
$3\nu_4$	A'	1675.6	1686.4	n.o.	0.2	0.2	1673.2	0.1	
$3\nu_5$	A''	1321.4	1329.9	n.o.	0.0	0.0	1299.7	0.0	
$3\nu_6$	A'	1061.5	1069.0	n.o.	0.0	0.0	1002.8	0.0	

Note. Comparison between VCI results of HPN₂ for the PES using the frozen core (fc) approximation and the all-electron (ae) correlation calculation. Frequencies ν are given in cm^{-1} and infrared intensities I are given in km mol^{-1} . Irreducible representations (irrep) are provided for each state.

References. (1) Experimental matrix spectroscopy by Lu et al. (2022).

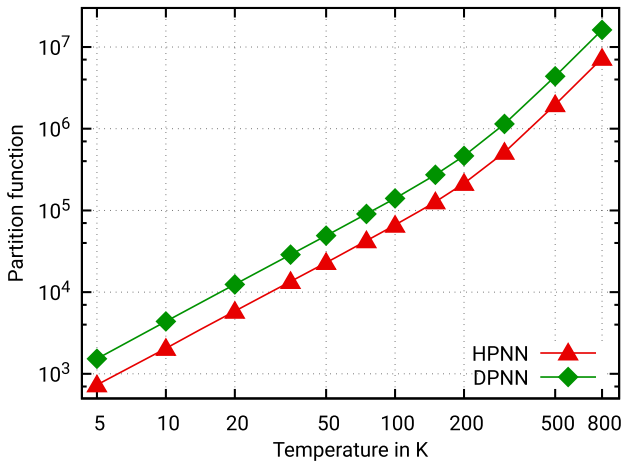


Figure 2. The partition function of diazophosphane for different temperatures.

intensity. All of these findings are in good agreement with the analysis in Lu et al. (2022).

Since resonances are intrinsically accounted for in VCI theory, an analysis of resonating states is straightforward and is provided in our calculations once a configuration contributes more than 10% to the state of interest. Among the considered vibrational bands, there are only a small number of meaningful resonances. Neither the fundamental bands nor the overtones for HPN₂ and DPN₂ show any Fermi (Fermi 1931) or Darling–Dennison (Darling & Dennison 1940) resonances. The only coupling for an overtone of HPN₂ can be found for $2\nu_2$ and $\nu_2 + 2\nu_4 + 2\nu_5$ at about 4030 cm^{-1} . Moreover, the combination band $\nu_3 + \nu_5$ shows a strong resonance with $\nu_4 + \nu_5 + \nu_6$ at 1375 cm^{-1} (see the supplementary material). However, since neither of the two bands involved has a noticeable intensity, experimental confirmation of the latter resonance is not possible.

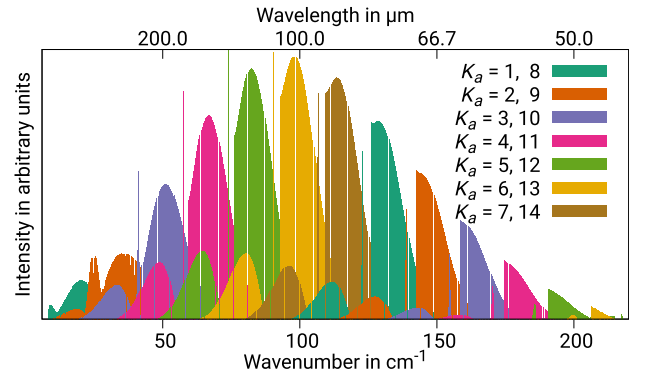


Figure 3. Vibrational ground-state stick spectrum of diazophosphane for 300 K. The color of the transitions are defined by the K_a quantum number of the upper state. For the sake of clarity, hot bands are not shown. The maximum total angular momentum was set to $J = 75$.

3.4. Rotational Spectrum

The pure rotational spectrum at a temperature of 300 K for diazophosphane is provided by Figure 3. Hot bands are not shown in this figure for two reasons: First, it allows for a better analysis of the spectrum. Second, they will be discussed in detail later on. The color coding in Figure 3 visualizes the assigned K_a quantum number of the initial rovibrational state. The first progressions between 5 and 25 cm^{-1} shown in dark green correspond to $K_a = 1$, the orange progressions denote $K_a = 2$, and so on. The color pattern repeats after the seventh color, hence the dark green progressions at 125 and 150 cm^{-1} correspond to $K_a = 8$. The fact that each progression is given in a single color shows that the assignment of the quantum number K_a is consistent for the vibrational ground state. Moreover, for each K_a value, the coloring allows us to identify the thin but dense Q-branch in the center, the strong R-branch

at the rhs, and the much weaker P-branch at the lhs. However, it should be noted that, for $K_a = 1$ and $K_a > 11$, only two branches are clearly visible.

A study of the temperature-dependent effect of the spectrum including hot bands is shown in Figure 4. The previously discussed Figure 3 corresponds to the black transitions of the bottom panel in Figure 4. In addition, this figure shows three different hot bands ($4^1 \rightarrow 4^1$, $5^1 \rightarrow 5^1$, $6^1 \rightarrow 6^1$) all given in red.

Up to a temperature of 100 K, ignoring hot bands is a decent approximation. At 200 K, the contribution of hot bands is about one order of magnitude smaller than for the ground-state transitions and is almost entirely driven by the $6^1 \rightarrow 6^1$ transitions. Moreover, even in cases where hot bands contribute more strongly to the overall appearance of the rotational spectrum, i.e., at 300 K, this does not lead to a shift in intensities toward higher or lower frequencies. This is in contrast to other molecules (Tschöpe & Rauhut 2023) and other parts of the diazophosphane spectrum (see Section 3.6).

3.5. Rovibrational Spectrum

An overview of the rovibrational infrared spectrum of diazophosphane for a temperature of 300 K and spectral range up to 2700 cm^{-1} is provided in Figure 5. In contrast to Figure 3, here the color coding refers to the vibrational states involved. More precisely, for the transitions in orange, both the initial and final vibrational quantum numbers correspond to the vibrational ground state. The dark green lines denote vibrational fundamental bands (e.g., ν_6). First overtones (e.g., $2\nu_6$) and second overtones (e.g., $3\nu_6$) are shown in yellow and light green, respectively. As mentioned before, we have restricted the RVC configuration space to vibrational states up to a maximum sum of quantum numbers of 3, i.e., third overtones and combination bands of four different vibrational transitions are not included. The fact that there is only one very weak second overtone at 1650 cm^{-1} and the absence of strong second overtones in Table 2 provide some evidence that this is a good approximation. Further analysis shows that, in this spectral region, the coupling between these higher overtones and other strong vibrational bands is relatively weak compared to the two or three mode combination bands, which are colored pink and gray, respectively. Finally, all types of hot bands are colored black.

As expected from Table 2, the ν_2 mode is the most intense vibrational transition by more than one order of magnitude. Although ν_2 and $\nu_3 + 2\nu_4$ have the same irreducible representation (A'), their coupling within VCI theory is virtually zero, but within RVC theory it is noticeable. This can also be seen by considering the intensities. VCI calculations yield an intensity of $469.9 \text{ km mol}^{-1}$ for ν_2 and 0.4 km mol^{-1} for $\nu_3 + 2\nu_4$. In contrast to that, the RVC results show a little less than two orders of magnitude difference in the intensities, see Figure 5. Moreover, there are several regions that are sufficiently separated to allow for independent investigations by different experiments.

A more detailed analysis of some spectral regions of the infrared spectrum of diazophosphane is provided in Figure 6. All of the strong bands shown in the different panels are fundamental bands of this near-prolate asymmetric top molecule. Since panel (a) shows two strong bands, all of the six fundamental bands are covered within this figure. Neither of the two vibrational modes in panel (a) can be assigned to a

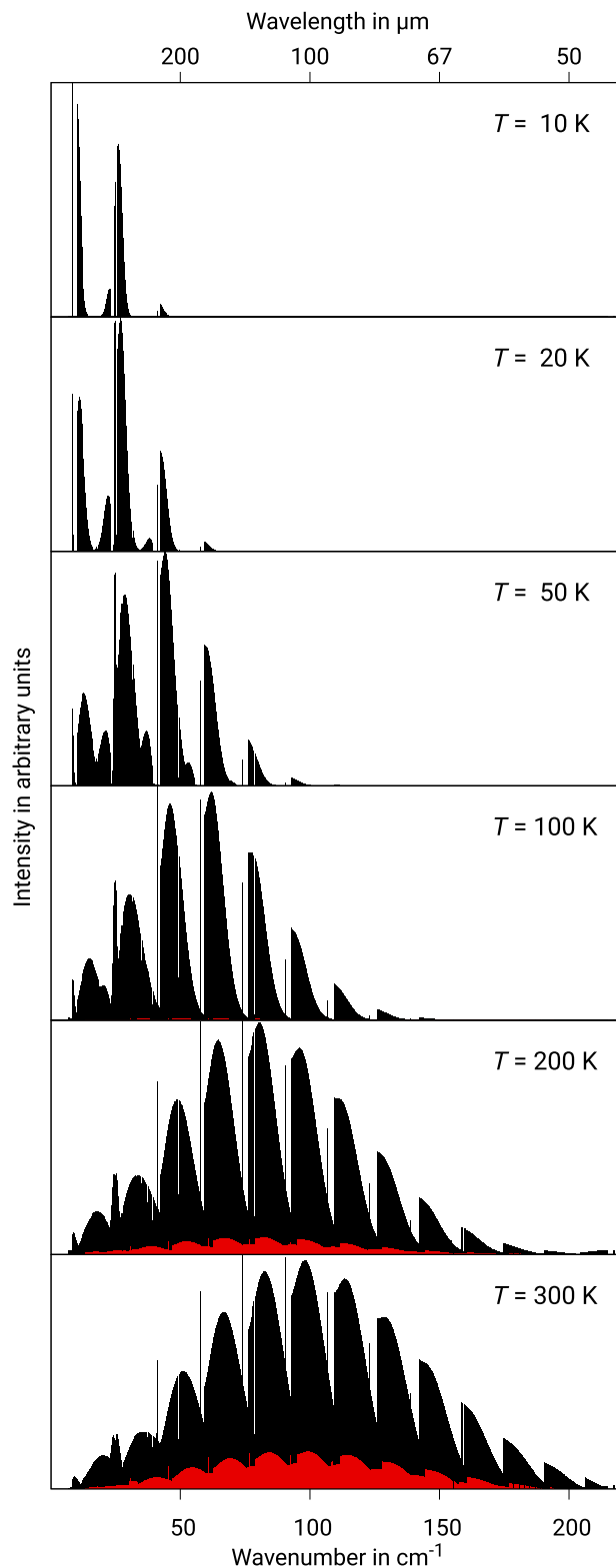


Figure 4. Vibrational ground-state stick spectrum of diazophosphane for different temperatures. Transitions from the vibrational ground state to the vibrational ground state are drawn in black. All hot band transitions are given in red. The maximum total angular momentum was set to $J = 75$.

typical asymmetric top band type. While the in-plane P–N≡N bending mode ν_6 shows a similarly strong change in the electric dipole moment along the A - and B -axes, the dipole moment of

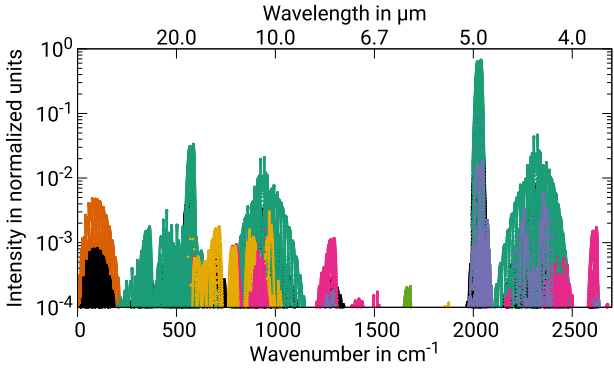


Figure 5. Overview of the rovibrational infrared stick spectrum of diazophosphane at a temperature of 300 K. Hot bands are colored black, the pure rotational spectrum is given in orange, fundamental bands in dark green, first overtones in yellow, second overtones in bright green (only visible at 1650 cm^{-1}). Combination bands of two or three different vibrational transitions are colored pink or gray, respectively. The maximum total angular momentum quantum number is set to $J = 75$.

the out-of-plane P–N \equiv N bending mode ν_5 changes only along the C -axis. However, the small spectral separation of the two bands of less than 100 cm^{-1} and the fact that they belong to different irreps lead to strong Coriolis-coupling and hence a lifting of the typical selection rules.

The P–N stretching mode ν_4 shows the expected A-type spectrum. However, it is subject to intensity borrowing due to coupling with the much weaker overtones $2\nu_5$ and $2\nu_6$. As discussed in Tschöpe et al. (2021) and Tschöpe & Rauhut (2023), this leads to the typical compression of the branch facing the borrowing bands, i.e., toward higher energies, in this case. Another typical example of an A-type pattern arises for ν_2 , which was to be expected since it is assigned to the N \equiv N stretching mode. Although there are combination bands coupling with ν_2 , this leads to only a small asymmetry. The H–P bending mode ν_3 in panel (c) and H–P stretching mode ν_1 in panel (e) show the expected B-type intensity pattern.

3.6. Hot Bands

The influence of hot bands on the low-frequency region below 600 cm^{-1} can be seen in Figure 7. Panel (a) shows the vibrational ground-state spectrum and the fundamental modes ν_6 and ν_5 , while panel (b) shows ν_4 . At a temperature of 300 K, there are three vibrational states with meaningful thermal occupations, which are 4^1 , 5^1 , and 6^1 . The hot bands of the pure rotational spectrum were already briefly discussed in Section 3.4. Considering the different transitions $4^1 \rightarrow 4^1$, $5^1 \rightarrow 5^1$, and $6^1 \rightarrow 6^1$ individually allow for two results: (1) the intensity pattern is mainly the same in all cases and (2) the intensity ratios seem to be in accordance with the thermal occupation ratios.

In contrast to that, the four transitions $0 \rightarrow 6^1$, $6^1 \rightarrow 6^2$, $5^1 \rightarrow 5^1 + 6^1$, and $4^1 \rightarrow 4^1 + 6^1$ at around 350 cm^{-1} show very different intensity patterns. Especially, the $5^1 \rightarrow 5^1 + 6^1$ band in pink is significantly shifted toward higher frequencies. This effect is even more pronounced for the next higher fundamental band at 440 cm^{-1} , where all bands have a very unique visual appearance due to the strong coupling. Moreover the $5^1 \rightarrow 5^2$ transition (pink) is at least as intense as the $6^1 \rightarrow 5^1 + 6^1$ transition (green), although the thermal occupation of 5^1 is lower than for 6^1 . Figure 7(b) highlights another common

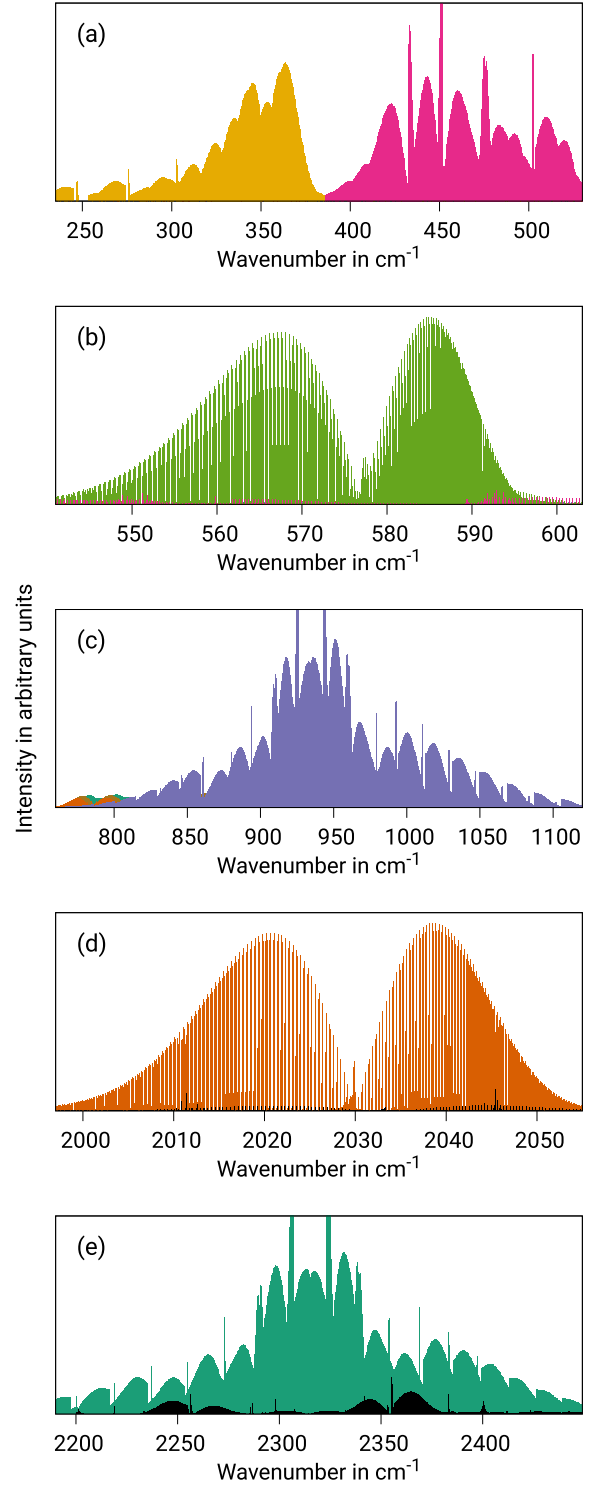


Figure 6. Infrared spectrum of the vibrational fundamental bands of diazophosphane at a temperature of 300 K. The maximum total angular momentum was set to $J = 75$. The modes ν_6 (yellow) and ν_5 (pink) are shown in panel (a), mode ν_4 (vibrant green) in (b), mode ν_3 (hazy blue) in (c), mode ν_2 (orange) in (d), and mode ν_1 (green) in (e). The y-axis scale range for the different figures varies.

phenomenon for hot bands, which is a significant shift in the band center. In the case of the $4^1 \rightarrow 4^2$ band (yellow), the transition is 20 cm^{-1} lower than for the fundamental transition $0 \rightarrow 4^1$.

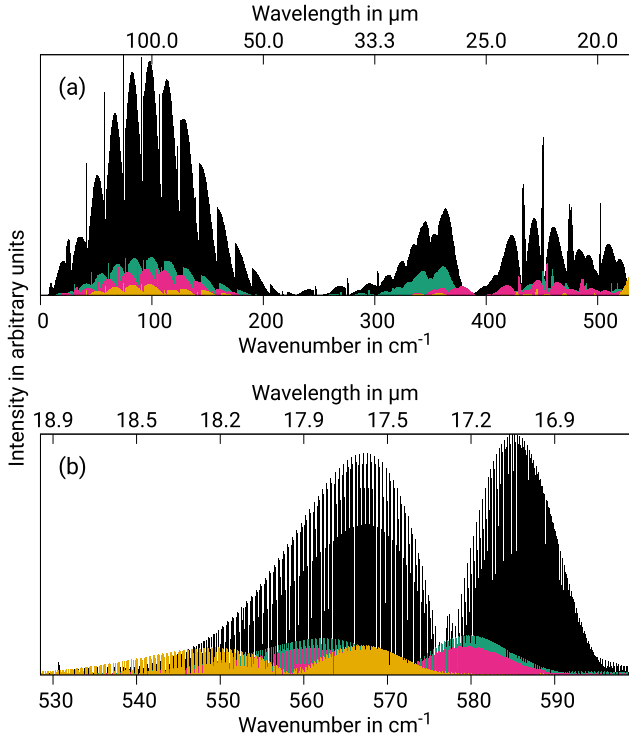


Figure 7. Infrared low-frequency stick spectrum of diazophosphane. This spectral region is split in two panels for better visibility because the band around 577 cm^{-1} is one order of magnitude stronger (see Figure 5) than the band in panel (b). For transitions drawn in black the initial vibrational state is the ground state. Hot bands for different vibrational transitions are given in different colors. Transitions initiated from vibrational state 4^1 , 5^1 , and 6^1 are colored yellow, pink, and green, respectively. The maximum total angular momentum was set to $J = 75$.

3.7. Spectroscopic Constants

Another way to analyze rovibrational characteristics besides comparing line lists and the visual appearance of spectra are spectroscopic constants. They allow to condense large line lists, which are obtained by experiments or simulations, into a small set of well-defined molecule-specific constants by using a model Hamiltonian. Computationally, these rotational and centrifugal distortion constants can be obtained by vibrational perturbation theory (VPT). For this reason, the PESs of HPN_2 and DPN_2 have been transformed to a quartic force field to obtain the force constants needed for VPT2 calculations. For diazophosphane, we have chosen the A-reduced Hamiltonian over its alternative, the S-reduced Hamiltonian similar to our previous studies, see Dinu et al. (2022) and Tschöpe & Rauhut (2023). Moreover, we followed the convention to use the I' orientation for this near-prolate asymmetric top molecule.

The results for HPN_2 are given in Table 3 and, for DPN_2 , they can be found in the supplementary material. Again, we provide a comparison between calculations based on a PES using the frozen core approximation and a PES obtained by all-electron calculations. Since diazophosphane is a near-prolate asymmetric top molecule, it has one very large rotational constant, i.e., A , and two rather small ones being very similar in size, B and C . The relative deviation between the fc and ae results are about 0.5%, which is similar to the findings in Schneider & Rauhut (2022). Although the quartic and especially sextic constants are several orders of magnitude smaller, the relative deviations are about the same as for the

Table 3
Spectroscopic Constants for the Vibrational Ground State of HPN_2

Parameter		ae	fc
A	[GHz]	254.46592	253.29347
B	[GHz]	5.94814	5.91260
C	[GHz]	5.80568	5.77117
Δ_J	[kHz]	2.298	2.295
Δ_{JK}	[kHz]	126.733	125.805
Δ_K	[MHz]	19.120	19.061
δ_J	[Hz]	54.842	54.748
δ_K	[kHz]	77.312	76.986
Φ_J	[Hz]	-0.002	-0.002
Φ_{JK}	[Hz]	0.432	0.430
Φ_{KJ}	[Hz]	-134.311	-135.313
Φ_K	[kHz]	-8.868	-9.050
ϕ_J	[mHz]	-0.048	-0.049
ϕ_{JK}	[Hz]	0.247	0.245
ϕ_K	[Hz]	378.121	378.626

Note. Watson's A-reduced Hamiltonian and I' representation is used for the VPT2 calculations. Comparison between results for the PES using the frozen core (fc) approximation and the all-electron (ae) correlation calculation. The rotational constants for the equilibrium geometry are $A_e = 254.98012\text{ GHz}$, $B_e = 5.94287\text{ GHz}$, and $C_e = 5.80751\text{ GHz}$ within the fc approximation and $A_e = 256.16949\text{ GHz}$, $B_e = 5.97837\text{ GHz}$, and $C_e = 5.84203\text{ GHz}$ for the ae correlation calculations.

rotational constants. In fact, in many cases, the difference is about 0.1%. However, it should be mentioned that, for the sextic constants, we do not expect that the small difference between our two simulations reflects the error margin of our method.

4. Summary and Conclusions

Within this work, high-level ab initio methods have been used for the first time to investigate the rotational and rovibrational spectra of diazophosphane. Explicitly correlated coupled-cluster calculations have been used to determine multidimensional PESs represented by an n -mode expansion up to fourth order. For each of the two isotopologues (HPN_2 and DPN_2), two PESs were determined. The first one uses the frozen core approximation relying on error compensation with respect to neglected contributions within the electronic energies and leads to vibrational frequencies that usually match nicely with experimental results. The second PES uses all-electron calculations, which have shown a better agreement for the spectroscopic constants in the past (Schneider & Rauhut 2022; Tschöpe & Rauhut 2023). To determine the vibrational and rovibrational frequencies and intensities, VCI and RVCI theory has been used. All simulations were performed with the MOLPRO program package of ab initio programs.

Theoretical results for the geometrical parameters of the equilibrium and vibrational averaging structures of HPN_2 and DPN_2 have been provided. Moreover, theoretical values for the partition functions within a temperature range between 10 and 800 K have been presented. In addition to that, we provided line list for more than 70 vibrational bands, which show neither Fermi nor Darling–Dennison resonances. However, it revealed a strong resonance with a leading coefficient for the VCI wave function of 0.71 for the combination bands $\nu_3 + \nu_5$ and $\nu_4 + \nu_5 + \nu_6$ at 1375 cm^{-1} for HPN_2 . In contrast to HPN_2 , the deuterated system shows even fewer resonances. The rotational spectrum was also studied for temperatures between 10 and 300

K, including hot bands. Moreover, we discussed the K_a quantum number dependence of the progressions. The rovibrational spectrum was analyzed with respect to the hot bands and vibrational quantum numbers. Furthermore, a discussion of the rovibrational infrared stick spectra was presented for all fundamental bands of HPN₂. Last, we provided the rotational and centrifugal distortion constants obtained by VPT calculations of the asymmetric top molecule. A comparison between results based on the all-electron PES with results obtained by frozen core calculations showed a relative deviation of about 0.5%.

These data should allow to guide observations of diazophosphane in astrophysical environments, like, for example, AGB star envelopes, as well as further laboratory studies. In particular, the spectral region between 300 and 550 cm⁻¹ appears to be fairly unique and thus characteristic for the molecule's identification.

We are grateful to Prof. X. Zeng for bringing this molecule to our attention. We thank the Deutsche Forschungsgemeinschaft (DFG; project Ra 656/23-3) and the Studienstiftung des deutschen Volkes for financial support. The authors acknowledge further support by the state of Baden-Württemberg through bwHPC and the DFG through grant No. INST 40/575-1 FUGG (JUSTUS 2 cluster). This publication was funded by the German Research Foundation (DFG) grant "Open Access Publication Funding/2023-2024/University of Stuttgart" (512689491).

Software: MOLPRO (Werner et al. 2020).

Data Availability

The data that support the findings of this study, i.e., potential energy surfaces and line lists, are available online on the ZENODO database: doi:[10.5281/zenodo.7628591](https://doi.org/10.5281/zenodo.7628591).

ORCID iDs

Martin Tschöpe  <https://orcid.org/0000-0001-9888-4577>
Guntram Rauhut  <https://orcid.org/0000-0003-0623-3254>

References

- Adler, T. B., Knizia, G., & Werner, H.-J. 2007, *JChPh*, **127**, 221106
- Agúndez, M., Cernicharo, J., Decin, L., Encrenaz, P., & Teyssier, D. 2014, *ApJL*, **790**, L27
- Agúndez, M., Cernicharo, J., Pardo, J. R., Guélin, M., & Phillips, T. G. 2008, *A&A*, **485**, L33
- Amyay, B., Fayt, A., & Herman, M. 2011, *JChPh*, **135**, 234305
- Bowman, J. M., Jr., Carrington, T., & Meyer, H. D. 2008, *MolPh*, **106**, 2145
- Bowman, J. M., Christoffel, K., & Tobin, F. 1979, *JPhCh*, **83**, 905
- Carter, S., Bowman, J. M., & Handy, N. C. 2012, *MolPh*, **110**, 775
- Carter, S., Wang, Y., & Bowman, J. M. 2017, *JPCA*, **121**, 1616
- Cherchneff, I. 2012, *A&A*, **545**, A12
- Christoffel, K. M., & Bowman, J. M. 1982, *CPL*, **85**, 220
- Clark, V. H. J., Owens, A., Tennyson, J., & Yurchenko, S. N. 2020, *QSRT*, **246**, 106929
- Czakó, G., Mátyus, E., & Császár, A. G. 2009, *JPCA*, **113**, 11665
- Darling, B. T., & Dennison, D. M. 1940, *PhRv*, **57**, 128
- Dinu, D. F., Tschöpe, M., Schröder, B., Liedl, K. R., & Rauhut, G. 2022, *JChPh*, **157**, 154107
- Dinu, D. F., Ziegler, B., Podewitz, M., et al. 2020, *JMoSp*, **367**, 111224
- Dunham, T., Jr. 1937, *PASP*, **49**, 26
- Endres, C. P., Schlemmer, S., Schilke, P., Stutzki, J., & Müller, H. S. P. 2016, *JMoSp*, **327**, 95
- Erfort, S., Tschöpe, M., & Rauhut, G. 2020a, *JChPh*, **152**, 244104
- Erfort, S., Tschöpe, M., & Rauhut, G. 2022, *JChPh*, **156**, 124102
- Erfort, S., Tschöpe, M., Rauhut, G., Zeng, X., & Tew, D. P. 2020b, *JChPh*, **152**, 174306
- Ferenc, D., & Matyus, E. 2019, *MolPh*, **117**, 1694
- Fermi, E. 1931, *ZPhy*, **71**, 250
- Ghellab, T., Baaziz, H., Charifi, Z., et al. 2019, *MRE*, **6**, 075906
- Harris, G. J., Viti, S., Mussa, H. Y., & Tennyson, J. 1998, *JChPh*, **109**, 7197
- Jacobs, H., Nymwegen, R., Doyle, S., Wroblewski, T., & Kockelmann, W. 1997, *Z. Anorg. Allg. Chem.*, **623**, 1467
- Kats, D., & Manby, F. R. 2013, *JChPh*, **139**, 021102
- Knauth, D. C., Andersson, B. G., McCandliss, S. R., & Warren Moos, H. 2004, *Natur*, **429**, 636
- Knizia, G., & Werner, H.-J. 2008, *JChPh*, **128**, 154103
- Lu, B., Shao, X., Jiang, X., et al. 2022, *JChS*, **144**, 21853
- Martin, J., Francois, J., & Gijbels, R. 1992, *JChPh*, **96**, 7633
- Mathea, T., Petrenko, T., & Rauhut, G. 2022, *JCoCh*, **43**, 6
- Mathea, T., & Rauhut, G. 2021, *JCoCh*, **42**, 2321
- May, A. J., & Manby, F. R. 2004, *JChPh*, **121**, 4479
- McGuire, B. A. 2018, *ApJS*, **239**, 17
- McKellar, A. 1940, *PASP*, **52**, 187
- Müller, H. S. P., Schlöder, F., Stutzki, J., & Winnewisser, G. 2005, *JMoSt*, **742**, 215
- Müller, H. S. P., Thorwirth, S., Roth, D. A., & Winnewisser, G. 2001, *A&A*, **370**, L49
- Neff, M., & Rauhut, G. 2009, *JChPh*, **131**, 124129
- Nikitin, A. V., Rey, M., & Tyuterev, V. G. 2017, *QSRT*, **200**, 90
- Peterson, K. A., Adler, T. B., & Werner, H.-J. 2008, *JChPh*, **128**, 084102
- Petrenko, T., & Rauhut, G. 2017, *JChPh*, **146**, 124101
- Pfeiffer, F., & Rauhut, G. 2014, *JChPh*, **140**, 064110
- Pflüger, K., Paulus, M., Jagiella, S., Burkert, T., & Rauhut, G. 2005, *Theor. Chem. Acc.*, **114**, 327
- Rauhut, G. 2004, *JChPh*, **121**, 9313
- Rey, M., Nikitin, A. V., & Tyuterev, V. G. 2017, *ApJ*, **847**, 105
- Santa Daria, A. M., Avila, G., & Matyus, E. 2021, *JChPh*, **154**, 224302
- Sarka, J., Petty, C., & Poirier, B. 2019, *JChPh*, **151**, 174304
- Schneider, M., & Rauhut, G. 2022, *JCoCh*, **44**, 298
- Schnick, W., & Lücke, J. 1992, *Z. Anorg. Allg. Chem.*, **610**, 121
- Schröder, B., & Rauhut, G. 2022, in *Vibrational Dynamics of Molecules*, ed. J. M. Bowman (Singapore: World Scientific), 1
- Simmons, J., Wang, X.-G., & Carrington, T. J. 2019, *JPCA*, **123**, 10281
- Smydke, J., Fabri, C., Sarka, J., & Császár, A. G. 2019, *PCCP*, **21**, 3453
- Špirko, V., Jensen, P., Bunker, P., & Čejchan, A. 1985, *JMoSp*, **112**, 183
- Swings, P., & Rosenfeld, L. 1937, *ApJ*, **86**, 483
- Tenenbaum, E. D., & Ziurys, L. M. 2008, *ApJL*, **680**, L121
- Tobias, R., Furtenbacher, T., Tennyson, J., & Császár, A. G. 2019, *PCCP*, **21**, 3473
- Tschöpe, M., & Rauhut, G. 2022, *JChPh*, **157**, 234105
- Tschöpe, M., & Rauhut, G. 2023, *MNRAS*, **520**, 3345
- Tschöpe, M., Schröder, B., Erfort, S., & Rauhut, G. 2021, *FrCh*, **8**, 1222
- Tyuterev, V. G., Barbe, A., Jacquemart, D., et al. 2019, *JChPh*, **150**, 184303
- Vidler, M., & Tennyson, J. 2000, *JChPh*, **113**, 9766
- Wang, X.-G., & Carrington, T., Jr. 2013, *MolPh*, **111**, 2320
- Watson, J. K. G. 1968, *MolPh*, **15**, 479
- Werner, H.-J., Knowles, P. J., Manby, F. R., et al. 2020, *JChPh*, **152**, 144107
- Yachmenev, A., Polyak, I., & Thiel, W. 2013, *JChPh*, **139**, 204308
- Yachmenev, A., Yurchenko, S. N., Ribeyre, T., & Thiel, W. 2011, *JChPh*, **135**, 074302
- Yurchenko, S. N., Amundsen, D. S., Tennyson, J., & Waldmann, I. P. 2017, *A&A*, **605**, A65
- Ziegler, B., & Rauhut, G. 2016, *JChPh*, **144**, 114114
- Ziegler, B., & Rauhut, G. 2018, *JChPh*, **149**, 164110
- Ziegler, B., & Rauhut, G. 2019, *JPCA*, **123**, 3367

Declaration of Authorship

Erklärung über die Eigenständigkeit der Dissertation

Ich versichere, dass ich die vorliegende Arbeit mit dem Titel *Extension of a VCI program for the calculation of rovibrational intensities* selbständig verfasst und keine anderen als die angegebenen Quellen und Hilfsmittel benutzt habe; aus fremden Quellen entnommene Passagen und Gedanken sind als solche kenntlich gemacht.

Declaration of Authorship

I hereby certify that the dissertation entitled *Extension of a VCI program for the calculation of rovibrational intensities* is entirely my own work except where otherwise indicated. Passages and ideas from other sources have been clearly indicated.

Stuttgart, den June 27, 2023

Martin Tschöpe